Three Dimensional Printing of Ceramic Molds with Accurate Surface Macro-Textures for Investment Casting of Orthopaedic Implants

by
Alain Curodeau

S.B., Mechanical Engineering, Université Laval, 1989.
M.S.M.E., Mechanical Engineering, MIT, 1991.

Submitted to the Department of Mechanical Engineering
in Partial Fulfillment of the Requirements for the Degree of

Doctor of Philosophy

at the

Massachusetts Institute of Technology

September 1995

Signature of Author _____
Department of Mechanical Engineering
September 28, 1995

Certified by _____
Emanuel M. Sachs
Associate Professor of Mechanical Engineering
Laboratory for Manufacturing and Productivity
Thesis Supervisor

Accepted by _____
Ain A. Sonin
Chairman of Graduate Committee

Three Dimensional Printing of Ceramic Molds with Accurate Surface Macro-Texture for Investment Casting of Orthopaedic Implants

by Alain Curodeau

Submitted to the Department of Mechanical Engineering on August 8, 1995
in partial fulfillment of the requirements for the degree of
Doctor of Philosophy in Mechanical Engineering

Abstract

Three Dimensional Printing is a solid freeform fabrication process that has extensive geometric flexibility. Intricate parts are built from powdered materials deposited in layers, and selectively joined with binder droplets from a continuous jet printhead.

One area of application is to generate accurate millimeter and sub-millimeter surface textures on ceramic parts. Used as molds, ceramic parts can transfer those accurate surface textures onto metal castings. An example of such application is for bone in-growth texture on cast orthopaedic prostheses.

This research established design rules and process control strategies to allow the production of functional orthopaedic implant with various porous textures from 3D printed alumina molds. The design rules outline the casting, printing and machine capabilities and limits with regard to the feature geometry, minimum size and accuracy that can be achieved effectively. Minimum mold protrusion size was constrained by the 200 μm primitive size while minimum cavities ≈ 150 μm relied on powder removal limitations. Mold dimensional integrity was achieved by accounting for the primitive size as tool offset and by developing drop placement control strategies.

An extensive analysis of the printhead was performed since it was found to be the major source of error in the process. Issues such as merged drops caused by air drag and induced charged caused by electrostatic crosstalk were compromising the integrity of the mold's small features. Physical models as well as simplified lookup tables were developed in order to predict merged drops and induced charge effects. It was found that merged drops could be delayed by either increasing the drop Reynolds number or selectively removing specific drops. Undesired induced charge was compensated by altering the charging voltage pattern according to inductive coefficient ratios that could be predicted or measured from drop position or charge information. As a result, printing accuracy was significantly improved in the range of ±5 to ±30 μm depending on the axis.

Casting conditions, related to metal head and freezing time, were also established to counteract metal surface tension and assure adequate mold filling of ≈350 μm cavity size. A variety of functional orthopaedic Co-Cr-Mo cast implants with 25 to 78% porous surface textures and 200 to 1000 μm pore size were produced successfully and submitted for evaluation against the FDA and ASTM standard requirements. Preliminary mechanical test on the textures exceeded easily both standards.

Thesis Committee from MIT: Dr. Emanuel Sachs, Chairman;
Dr. Michael J. Cima
Dr. Ian Hunter
from Johnson & Johnson Professional Inc.
Mr. Salvatore Caldarise

Acknowledgment

Cette thèse est dédiée à mes parents qui m'ont donné leur support inconditionnel depuis le tout début.

This thesis is dedicated to my parents who gave me their unconditional support from the very beginning.

I would like to thank Ely Sachs for giving me the opportunity and support to accomplish something I will be proud of all my life, and my committee members, Dr. Michael Cima, Dr. Ian Hunter and Salvatore Caldarise for their sensible advice and guidance.

This research would not have been the same without the valuable help provided by the accomplished engineering team at Johnson & Johnson Professional Inc. formed by:

Salvatore Caldarise, Tim Flynn, Dave Lasalle, Frank Matthews, Jim Oti, Deb Treacy, Brooke Weeden,... as well as the higher management who believed in the success of such a program.

This research is possible because of the contributions made by all the students who always gave the best of themselves. In the past six years, I interacted with so many fellow students, that I could not give each of them the credit they deserve. I would prefer to simply tell them: **Thank you everyone!**

Special thanks to the dedicated 3D printing staffs, Dave Brancazio and Jim Serdi who gave so much of their time and life to make the machine running day after day allowing others to pursue their own research.

To go through a Ph.D. has never been easy, but the support of my friends was an important condition for success. The lasting friendship I developed with the Canadian group Robin Côté, Denis Rancourt, John Keen, Paul Fieguth, ... and the Ashdown international crowd including Tay Kian Boon, Michel Kahan,... added up to the rich experiences I got from MIT. Special thanks to Judy Chen who has stood by me through the good and more difficult moments which were part of our everyday life in this demanding environment.

Table of Contents

List of Figures and Tables

Chapter 1: Introduction

Chapter 2: Orthopaedic bone ingrowth texture design

Chapter 5: 3D Printing Process Control

Chapter 6: Simplified error budget

Chapter 7: Conclusion

Appendices

Chapter 1: Introduction

1.1 Goal of the thesis

The goal of this thesis is to produce high temperature alloy castings with accurate surface texture suitable for orthopaedic applications directly from a 3D printed ceramic mold. The idea is also to develop an improved or a least equivalent bone ingrowth porous texture, generated by 3D Printing, compared to the actual Johnson &Johnson beaded texture showed in figure 1.2. Although this research is applied to the medical industry, it does not means it is not relevant to other applications. In fact, the medical application can be seen as a perfect test bench to evaluate the capabilities of 3D printing within stringent design specifications.

1.2 Background

1.2.1 Medical background

The use of surgical prosthetic devices, otherwise known as implants, is well known in various surgical applications, such as reconstructive surgery, for example, in the replacement of hip joint, knee or the like.

The most common procedure for securing hip and knee prostheses in bone is with polymethylmethacrylate (PMMA) cement. However, the polymeric cement is prone to long term deterioration. Most of the loosening related failures have been traced to cement degradation. Since the first demonstrations in the early 1960s that bone could grow into porous surfaces, various surface modification schemes, designed to improve fixation to implants, were introduced. Most of the work is centered around the development of porous surfaces by sintering layers of powder over the surface (see ref.2,6,7,9).

The use of porous surfaces for biologic attachment of implants by the ingrowth of bone offers a valuable alternative to acrylic bone cement as a means of fixation. It is well established that bone will infiltrate the pores of an inert porous system, provided the implant is initially stabilized and minimal movement occurs between the implant and bone. Several investigators have studied bone ingrowth into porous systems with different pore sizes and porosity. These studies indicate that the optimum pore size required for implant fixation remains undefined. There is limited fundamental information on the subtle variations of the host response to the different classes, types, and forms of materials.

There is also a lack of understanding of the effects of the host tissue on the implant and the anatomic site of implantation.

Although texture characteristics for biocompatibility is somewhat undefined, ASTM and the orthopaedic community recommend a range of design requirements within which performance and biocompatibility should occur (see ref. 1 to 30). Properties such as porosity, pore geometry and size, integrity and surface finish are some of the key factors addressed by those requirements. The final orthopaedic product should then comply with those standards unless proven inappropriate.

1.2.2 Manufacturing process

Making prostheses

Internal orthopaedic prosthesis or implants for knees and hips (see figure 1.1) are mainly manufactured from standard processes such as investment casting (lost wax) and forging of Cobalt-Chrome or Titanium alloys.

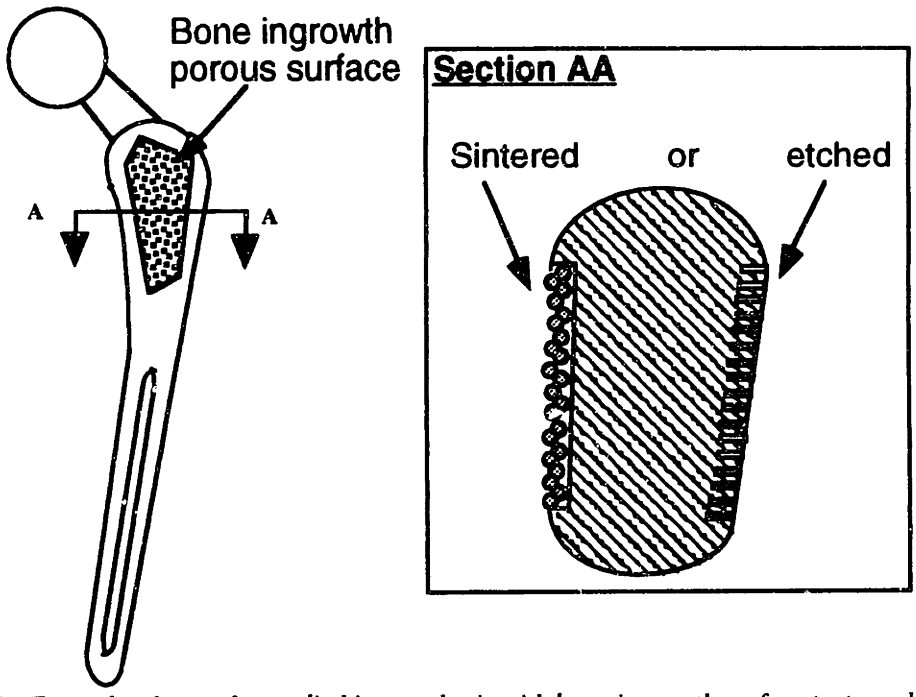

Figure 1.1: Example of an orthopeadic hip prosthesis with bone ingrowth surface texture shown in the section a) sintered beads, b) etched or EDM Electrical discharge machining.

In both cases, surface post-processing is required in order to create the necessary mirror finished surface and porous surface texture at selected locations on the prosthesis. Numerous surfacing techniques have been designed to attach or carve fine porous surface textures on cast or forged metal parts.

Sintering surface feature

One technique is to sinter small pieces of the same material on the surface of a cast prosthesis. In order to produce a porous surface on a Co-Cr casting (see figure 1.2), Co-Cr particles in 2 particle size ranges were used. The particles, produced by inert gas atomization of the alloy, are generally spherical in shape and initially held together by a binding material. This binder can be removed chemically later in the process. The spherical particles are bound to each other and to the solid substrate by sintering in a non-oxidizing atmosphere furnace. Sintering is the process whereby metal particles are heated in a controlled-atmosphere furnace to a temperature below its melting point, but sufficiently high to allow bonding (fusion) of the individual particles.

The entire casting is then solution annealed, "hipped" (hot isostatic pressing) and cleaned in order to generate a uniform material free of surface defects. The resulting surface porosity can be tailored by modifying the bead sizes and particle distribution.

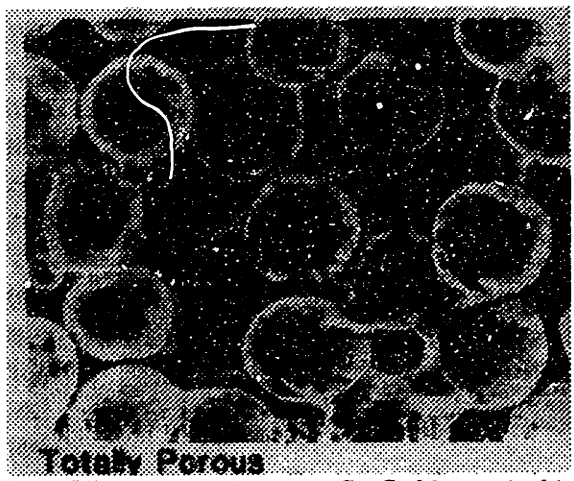

Figure 1.2: Standard 30-35% porous surface on a Co-Cr-Mo surgical implant. (see ref.2,3,4)

In the case of figure 1.2, three layers of normally distributed 250-300 μm diameter Co-Cr particles were sintered on the surface of a Co-Cr orthopaedic implant to give a 30-35% porous surface. Shapes other then spheres can also be used such as fine meshed wires in order to produce surfaces with different properties.

Electrical-discharge machining

Another way to produce surface texture on cast or forged orthopaedic prosthesis is with the process called "Electric Discharge Machining" or EDM (see ref.77,79). The EDM system consists of a surface textured tool and the workpiece, connected to a dc power

supply and placed in a dielectric fluid. When the potential difference between the tool and the workpiece is sufficiently high, a transient spark discharges through the fluid, removing a very small amount of metal from the workpiece or prosthesis surface. Two dimensional surface texture can then be produced on different material as long as this material is conductive. Similarly to EDM, electrochemical machining ECM can also be used in the same manner. The main difference is that instead of vaporizing the material with an electrical pulse, ECM uses very high dc current to erode the material atom by atom.

Chemical milling of surfaces and others

Other less common techniques could be used to give hard material a surface texture. For example, chemical machining CM is another process that makes use of chemical reagent, controlled to selectively attack different areas of the workpiece surfaces. Several other variations of manufacturing processes were also specially developed to produce distinct shapes into specific material, but their overall use is rather limited in the orthopaedic industry.

Limits of actual technologies

The common disadvantage of the above processes come from their post-processing nature. In fact, post processes should be minimized since they add production time and cost to the final product. In addition, due to the inherent lack of flexibility of such processes, attempts to modify their surface characteristics, such as pore size, often means either to substantially change the procedures or switch to a totally different process.

Overall, sintering and EDM are the most widely used processes for the production of bone ingrowth textures. Although those methods are very powerful, they have significant drawbacks that compromise the performance and quality of the parts they produce.

For example, sintering small particles on the surface of a prosthesis, requires high temperature heat treatments that reduce the physical properties of the prosthesis. Since the temperature needed for sintering is just below the melting point of the alloy, it is sufficient to affect the grain boundaries and also increase the grain size of the metallic structure. Thus, it is well known that for high temperature alloys, such as Co-Cr alloys, large grain size significantly reduce the fatigue strength (low strain high-cycle fatigue) of a prosthesis that need to endure dynamic cyclic loads.

On the other hand, electrical-discharge machining EDM of bone ingrowth texture comes also with its own peculiar features. What is commonly referred to as the "surface" finish left by EDM actually consists of two thermally affected, distinct layers of material known as the white layer and the heat affect zone. The white layer includes some particles

re-solidified on the surface and is so densely infiltrated with carbon that it has a separate and distinct structure, totally different from that of the original workpiece. Below the white layer is the heat affected zone and than the original parent material, unaffected by the EDM operation.

The material of the white layer, due to the ingress of carbon, always shrink more than the unaffected parent materials during the cooling process. As a result, this more highly tensioned surface eventually tear itself apart to relieve the pressure, creating series of microcracks at the surface of the material.

Those microcracks create local stress concentration site which acts as seed point for fatigue impair to spread throughout the part and eventually fracture the implant prematurely. Moreover, dynamic loads and shocks on the implant could eventually force the cracked surface to peel, fracture or break away from the parent material. In such event, the small hard particles would act as an abrasive inside the body, that could originate internal inflammation or damage the sliding joint. Secondary operation such as lapping or bead blasting (shot peening) is than necessary to stress relieve the surface. Implementing such an operation without damaging the tiny surface features is almost not feasible.

1.2.3 Proposed Approach

Solid freeform manufacturing

New manufacturing techniques involving computer aided manufacturing (CAM) process allow greater geometrical flexibility and selection of material. In a variation of standard investment casting, a desktop manufacturing technique could be used to produce ceramic molds, with embedded surface textures, directly from a CAD model (see figure 1.3 without embedded texture).

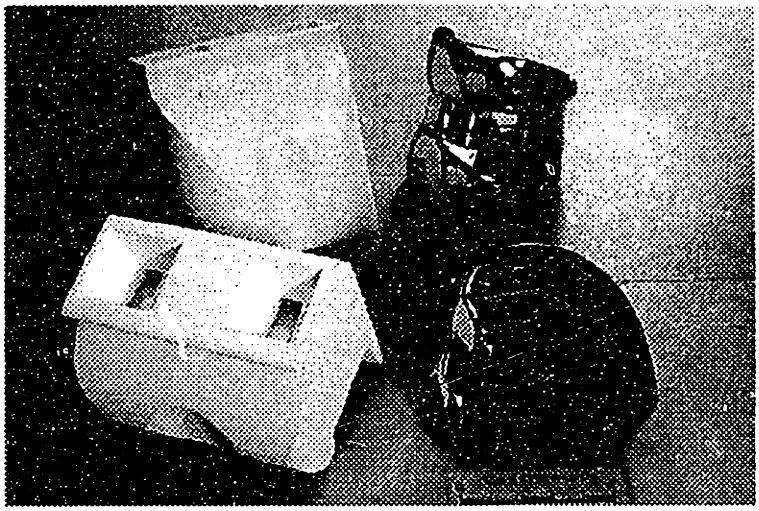

Figure 1.3: F75 Cobalt -Chromium casting of a knee implant made directly from a 3D printed alumina mold. showed on left.

Producing castings in such a way would represent a significant advantage over actual processes, by allowing more control over the various surface properties, and suppressing time consuming and detrimental surface conditioning post processes.

A preliminary investigation of the problem has shown that the "3D Printing" process has the ability to meet the basic requirements to produce ceramic molds with embedded surface texture suitable for orthopaedic prosthesis application (see figure 1.4 &1.5a & b).

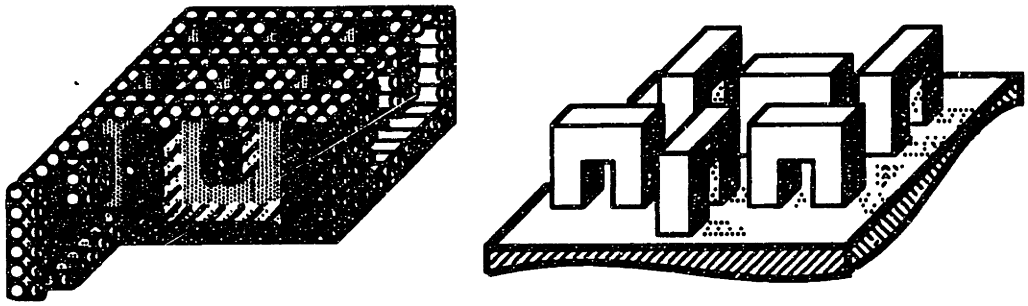

Figure 1.4 (left) Schematic of a mold surface texture showing the primitive size, (right) schematic of the resulting casting made from the mold on left.

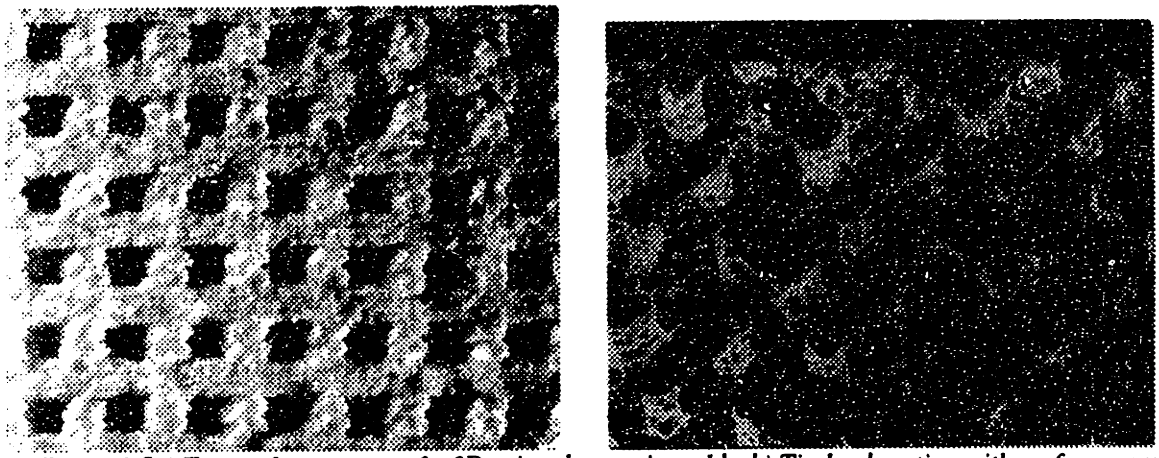

Figure 1.5a) Top surface texture of a 3D printed ceramic molds, b) Tin-lead casting with surface macro features 350 μm wide x 1000 μm long (produced from 3D Printed mold similar to figure a)).

One of the unique advantages of using 3D printing is the geometric flexibility which allows re-entrant shapes such as undercuts and overhangs within the surface texture. Such features can be used to give more attachment strength between the bone matrix and the prosthesis (see figure 1.6).

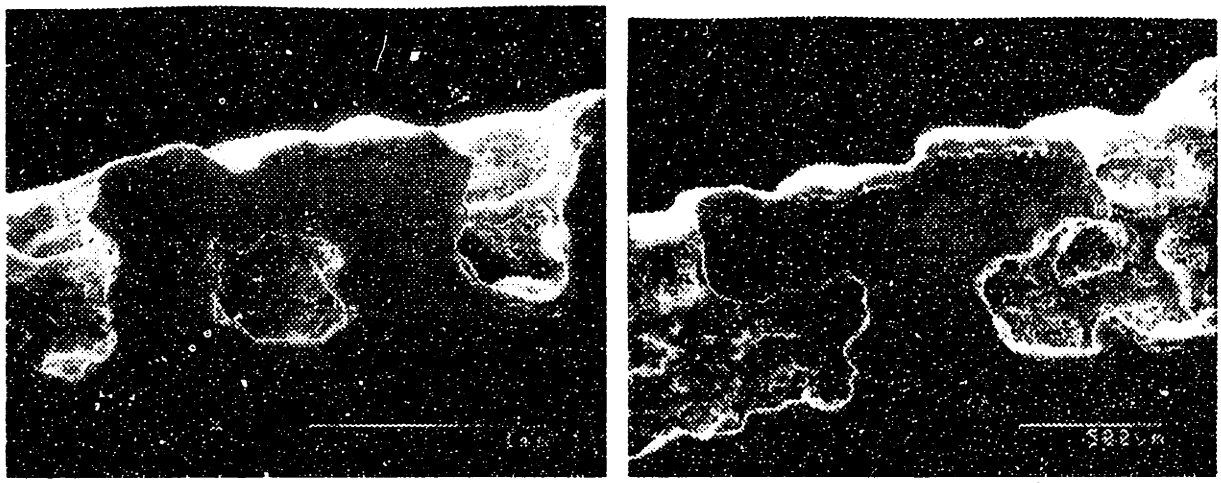

Figure 1.6: (Left) Cobalt-Chrome cast 1..2 mm Long overhang feature, (right) undercut.

Also, since it makes directly the ceramic mold with no need for special tooling or qualified labors, impressive reductions in production time and cost can be attained, permitting quick iterations for optimal product design.

Previous research

The object of on going research was to eliminate the need for detrimental heat or chemical surface treatments in order to keep the original physical properties of the cast or forged alloys. Another research objective was to develop a process with enhanced production flexibility while output quality is improved or at least maintained.

One solution was to apply flexible manufacturing methods, allowing accurate fabrication of random shapes, to build parts with integral surface texture in a single operation. This technology is already known as desktop manufacturing or solid freeform manufacturing, and consist in producing parts of any shape directly from a computer model without intervening steps. A lot of research effort has already been invested in the field of solid freeform manufacturing (see ref. 58) in order to apply emerging technologies such as: CNC machining, stereolythography, selective laser sintering SLA , laminated objet manufacturing LOM, 3D Printing, ... to various engineering tasks.

Along those lines, the orthopaedic industry has devoted an entire segment of their research to investigate the performance of various freeform processes in order to improve their manufacturing competitiveness. For example, a new efficient mold making technique has been developed around a stereolythography firable positive pattern of the desired part. The polymer object can be dipped in standard ceramic slurry and then fired out (QuickCast ™), replacing regular wax injection molded patterns. Although this technology seems promising, it is still limited by the long drying cycles of ceramic slurry, and restrained by the minimum achievable feature size; nevertheless it promises important improvements over prior methods.

Surface textures

On the other hand, none of the actual solid freeform manufacturing technologies have been designed to control surface texture. Controlling the surface characteristics of an orthopaedic prosthesis is key to optimize the performances of bone fixation and obtain quicker rehabilitation from the patient. The biological repercussions of surface characteristics could be better understood by the medical community. In fact, no manufacturing process really allow to easily produce various surface textures with a flexible range of surface design characteristics. Until recently, such medical experiments were confined to a modest number of surface texture designs, tightly linked with the surfacing process that produced them.

New research efforts

Before 3D Printing can be implemented in industry, a better understanding of the technology needs to be achieved. In fact, basic research on accuracy, repeatability, flexibility, process limits, and castability has to be conducted in order to optimize the machine performance and robustness. Likewise, applying 3D Printing to produce various surface textures for the orthopaedic industry is a unique platform to address most of the issues cited above, since it pushes the limits of the process by requiring control over feature size in the range of the actual machine resolution.

1.3 Research scope

1.3.1 Specific goals

- Understand design rules for successful orthopaedic implant.
- Understand the 3D printing process limitations on design.
- Understand the casting limitations on design.
- Unite the design rules-limitations-constraints.
- Fabricate sample macro-textures applied to bone implant application.

The goal of this research is to understand the possibilities allowing the 3D Printer to create metal castings with various functional textures directly from ceramic molds. To achieve that goal, different printed and cast texture designs will be evaluated according to their geometric and dimensional accuracy, mechanical properties, biocompatibility and manufacturing pitfalls. Process limitations will be analyzed by building a simplified error budget of the 3D Printer. Meanwhile, printing strategies such as offset compensation, feature snapping, patterns and line placement will be refined to optimize printing quality and accuracy.

1.3.2 Specifications

Orthopaedic requirements

The focus of this present research is to produce surface textures that provide an adequate site for bone ingrowth. The castings produced by 3D printing technology will have to comply with the specifications predetermined by the orthopaedic community including the orthopaedic surgeon group, the Food and Drug Administration (FDA), Johnson& Johnson Orthopaedic division and ASTM. Although many years and efforts of *in vivo* experimentation have been carried on, the precise requirements for successful bone ingrowth texture are still not well understood. Therefore, since nobody agrees upon a rigid set of standardized parameters, a range of acceptable characteristics has been defined in literature available from the different sources mentioned above.

The requirements for the bone ingrowth texture can be summarized as followed:

- Porosity	30 to 70% porous
- Pore size	50 to 1000 μm
-Thickness	250 to 1500 μm
- Shear strength	>25 MPa
- Tensile strength	> 30 Mpa
- Integrity, biocompatibility,...	

3D Printing Process requirements

Since surface textures require sub-millimeter surface features, resolution and accuracy are important parameters ensuring geometric and size conformity to the CAD model. Resolution is actually a limiting factor that needs to be quantified to determine the printability of very fine surface texture. Minimum sizes protrusion (positive features), cavity and radius of curvature will have to be estimated. These measurements will set the limits to what can and cannot be printed and cleaned from the unbound powder without altering the surface macro-texture integrity.

On the other hand accuracy of 3D Printing will be assessed from a drop placement error budget analysis along the three orthogonal axes of the machine. Since the printhead is the major contributing factor to the drop placement error, a special attention will be given for that component of the 3D printer. A set of simulation of the droplet motion will be computed and substantiated by experiments on a stationary printhead. The experiments will consist in controlling various printing conditions while the path of each droplet is monitored. The latter results will help to understand the different phenomena affecting the path of each droplet and to develop new control strategy. This new knowledge will be used to compensate for any undesired errors, and achieve better accuracy and parts conformity with the CAD model.

Casting requirements

Another set of requirements originates from the investment casting process itself. In fact, the mold design should conform to various casting rules necessary to sustain pouring stresses and yield quality castings; see partial listing.

- mold material should sustain high temperature
- mold feature strength
- minimum cavity dimensions
- minimum radius of curvature
- mold design
- Sprue and gate design

1.4 Methodology

To reach the goal of producing castings with functional surface texture, the following procedure is proposed in order to gather the required information necessary to conduct a complete analysis of the subject. Here is a list of the most important experiments intended to be accomplished; not necessarily in chronological order.

A) Literature review of orthopaedic bone implant design requirements and Co-Cr investment casting procedures.

B) Process control and accuracy will be addressed mainly by analyzing the printhead performance. The coupled effects of drag, induced charge and electrostatic repulsion-attraction on individual drop of binding material will be computed for different printing conditions and verified experimentally.

C) Design rules for printing ceramic mold with millimeter and sub-millimeter feature size will be obtained by analyzing geometric integrity and dimensional conformance.

D) Powder removal will be assessed to determine the minimum cavity width and depth from which powder can be removed effectively without destroying the fine printed features.

E) Casting design rules will be proposed to define the optimal casting conditions, mold dimensional limits and feature geometry and proportions, that will produce textured metal castings reliably without any defects.

F) Dimensional constraint of both ceramic mold and metal casting and others will be measured to complete the casting design rules.

G) CoCr texture samples will be produced and tested against the FDA and Johnson & Johnson standard specifications.

H) A simplified machine error budget of dimensional error sources will be computed in order to quantify the expected accuracy of the casting process with 3D printed mold.

1.5 Organization of this thesis

This thesis is organized as if we would start the design cycle of an orthopaedic implant in reverse order. Thus, we will start with the specifications set by the medical industry for porous bone ingrowth texture. The research exercise will be to verify the performance and limitations of our fabrication process within the dimensional window of opportunity for bone ingrowth texture. To be useful, our fabrication process (see figure 1.7) needs to achieve pore size in the order of 50 to 1000 μm with a preference for the 200 to 400 μm region. A porosity of 20 to 50% will also be targeted as well as a decent accuracy within ±50 μm is expected.

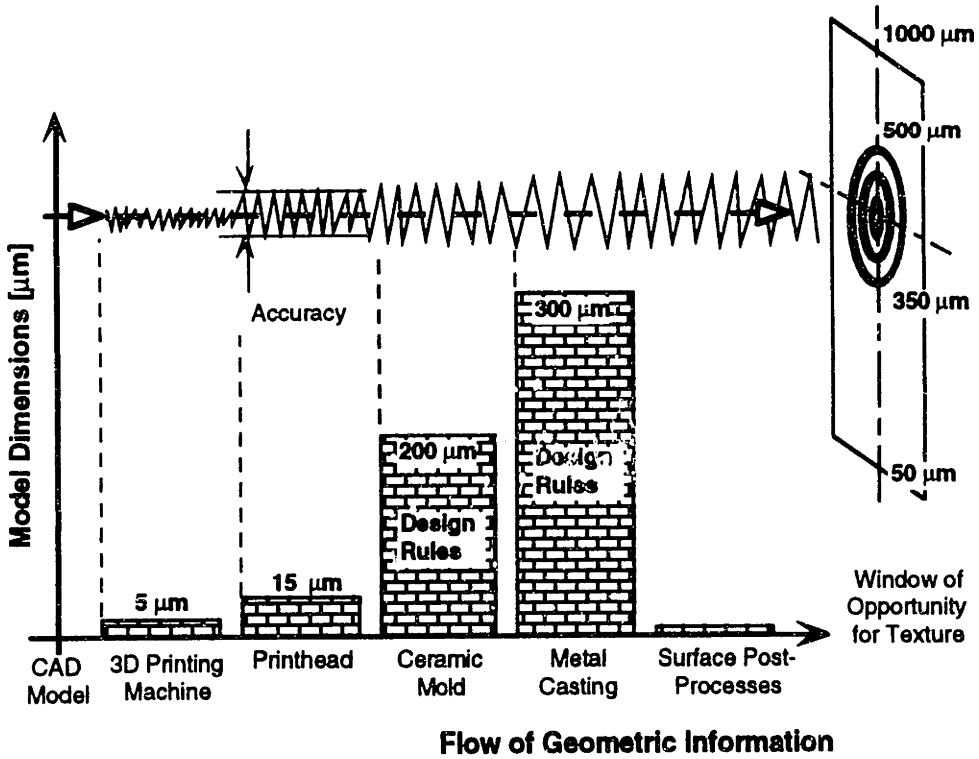

Figure 1.7: Thesis organization or summary of fabrication process for cast orthopaedic implants.

The performance of each fabrication step will be assessed by its minimum achievable feature size, accuracy and controllability. Those process characteristics (see figure 1.7) are represented into the flow of geometric information which control the dimensions from the CAD model up to the finish product. Starting by the casting process and going down to the CAD model, the flow of geometric information (see figure 1.7) will be analyzed in detail and optimized to achieve the best results. A set of design rules associated with each step will then be defined as a framework to help future design engineers to create new textures efficiently and accurately within the limits of the system.

Chapter 2:

Orthopaedic bone ingrowth texture design

2.1 Introduction

The research process started by proposing several texture designs with a broad spectrum of bone ingrowth surface characteristics. For economic reasons as well as to restrain the number of experiments, only a few texture designs were selected for the research.

Two goals had to be reached to collect the most information out of the texture samples:

1) evaluate bone ingrowth for a range of surface texture characteristic and
2) evaluate 3D printing capabilities for a range of feature geometry and sizes.

Since both criteria are consistent, both goal could be fulfilled from the same set of parts which resolved our limited resources problem. From those premises, six texture designs were chosen based on design requirements as well as on fabrication process capabilities described in the next sections. Those six designs were than 3D printed as ceramic molds and proceeded through powder removal, post dipping and casting process. Preliminary mechanical test were then conducted on the textured samples. Out of the six texture designs, only four were than selected to be used for the dog implant in-vivo experiments which will not be completed in this present research.

2.2 Design process & requirements

The process of developing new texture designs was done based on several factors. First, standard requirements defined by government and industry agencies to design and test textures had to be respected, such as:

- ASTM F04.03.02 "Standard Specification for Porous-surfaced Femoral Prostheses"
- ASTM F 1044 "Shear Test of Porous Metal Coatings".
- ASTM F 1147, 1160, 748, 981, ...
- ref[10,11,12,13,14,15]
- FDA (Food and Drug Administration), Guidance document for testing orthopaedic implants with modified metallic surfaces apposing bone or bone cement.
- Johnson & Johnson Professional Inc. standard requirement in accordance with the above standards.

Most of those requirements were in fact summarized in section 1.3.2 of this thesis.

Another criterion set within this research was to combine the benefits of two standard texture designs: the EDM'ed stud design which is also used by 3M inc, and the sintered beads design actually used by Johnson & Johnson Professional Inc (see figure 2.1).

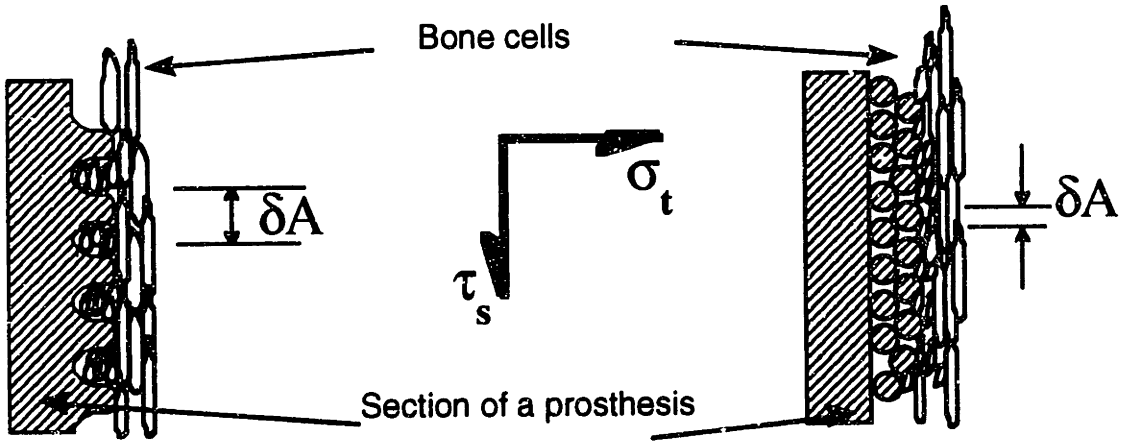

Figure 2.1: Comparison of bone attachment properties of a) 3M and b) Johnson & Johnson porous texture designs.

Both texture designs have their strong points which happen to become a weak point in the opposite design. First, the EDM stud design offers a large area for the bone cell to

grow in. As a result, the bonding interface, texture-bone matrix, performs better in shear mode τ_S compared to the sintered bead design which offers less shear area for the bone to grow. On the other hand, the stud design has no undercut or overhang features which would provide attachment in tension mode σ_T (see figure 2.1). Therefore, the stud design has almost no tensile attachment force compared to the sintered bead design which provide undercut features.

Thus, the idea was to combine both shear τ_S and tension σ_T characteristics into a single texture design which could be done on 3D printed parts (see figure 1.6). Table 2.1 presents a dozen texture designs with variable level of shear and tension characteristics.

Table 2.1: Preliminary 3D printing texture designs characteristics for bone ingrowth application.*

Design #	Pores size (µm)	Top porosity %	Bottom porosity %	Average porosity %	Tensile area %
1A	≈350	25	75	50	50
1B	≈350	25	62.5	43.8	50
2A	350-700	37.5	68.5	53.1	37.3
2B	≈700	37.5	62.5	50	37.3
3	350-700	41.7	58.3	50	27.8
4	≈350-1000	39	41	40	6
5	200,350-800	37.5	62.5	50	37.5
6	350-550	27.8	72.2	50	44.4
7A	200,350-800	33	78	56	56
7B	750	33.3	55.6	44.45	33.3
8	600	33.3	50.0	41.7	33.3
9	≈350	22.2	77.8	50	55.6
10	350-1000	67	30	49	11

*Theoretical data

The shear attachment area is controlled by the top porosity of the surface texture in which case a large porosity would give larger bone section, therefore better shear properties to the bond. The tensile attachments is associated with the number of undercuts and overhangs present inside the texture. A high percentage of tensile area would give better tensile properties to the bond. The optimum tensile property is reached however when an equal or larger shear area is also available. Since shear area becomes a tensile area at the points of attachment, the smallest section of the two would determine the break point in tension.

The porosity was subdivided into two classes: the top and bottom porosity. Both classes of porosity have consequences on the performance of a bone implant texture. The bottom porosity (and average porosity) represents the volume available for the bone cells to grow. The right combination of bottom porosity and pore size are key factors to promote bone ingrowth and assure proper irrigation of nutrients.

The twelve designs were subjected to a selection process based on design trade off between bone ingrowth requirements and fabrication process capabilities. The six chosen texture designs 4, 5, 7A, 8, 9 and 10 were selected based on their particular pore size, porosity and available tensile attachment area. The goal was to gather a range of texture characteristics in order to increase the probability of success of the bone implant experiment but also of the fabrication process. Two dimensional renderings of the six texture designs can be seen in Appendix A1.

Example of the four texture designs which were selected for the dog implant study are showed in figure 2.2 to 2.9. For example, figure 2.2, shows a unit cell isometric view of texture design #4 which was duplicated on a plane to form the actual cobalt-chrome-molybdenum casting in figure 2.3. The same thing can be said for design #5 (figure 2.4-2.5), Design #7A (figure 2.6-2.7) and design #10 (figure 2.8-2.9).

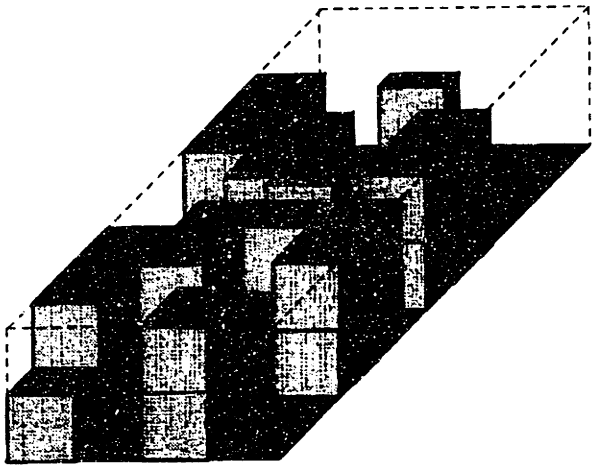

Figure 2.2: Unit cell schematic of design #4.

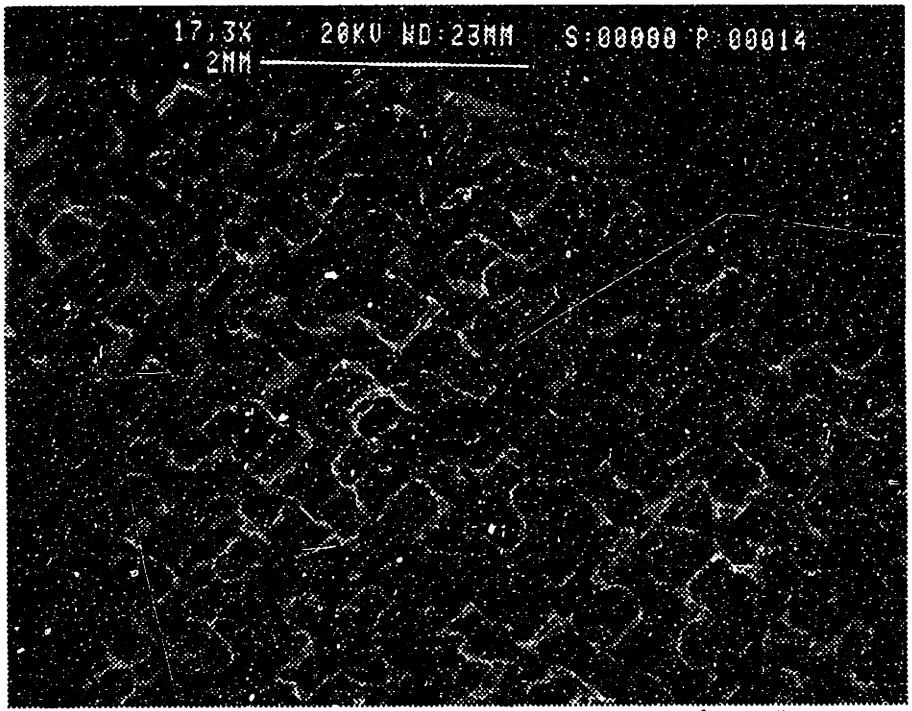

Figure 2.3: F75 Co-Cr-Mo casting of flat surface texture design #4.

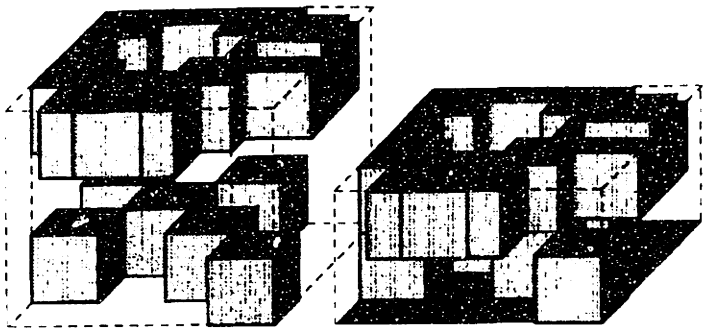

Figure 2.4: Unit cell schematic of design #5.

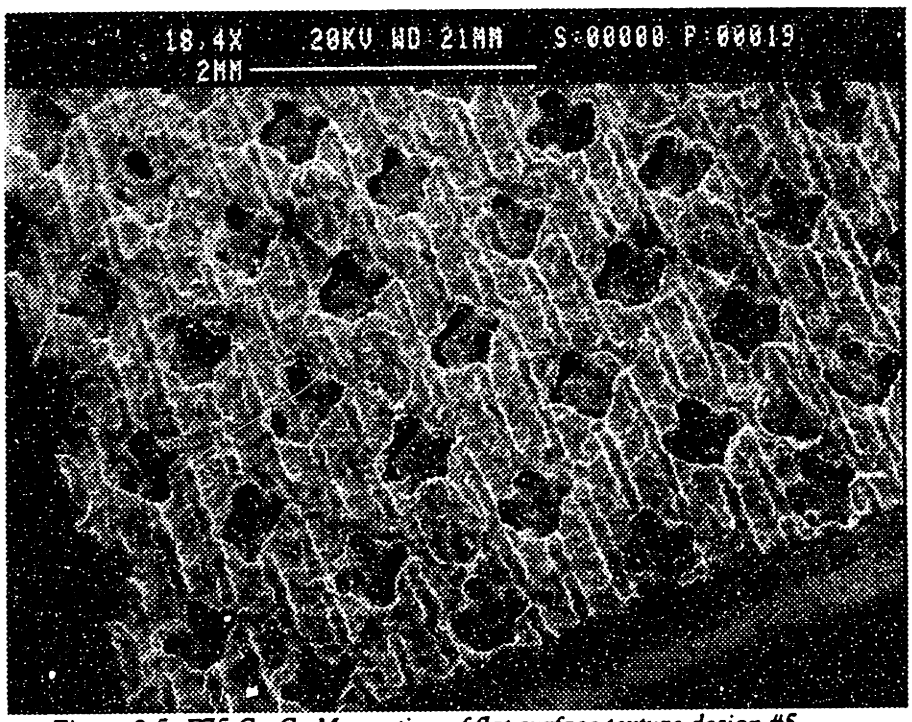

Figure 2.5: F75 Co-Cr-Mo casting of flat surface texture design #5.

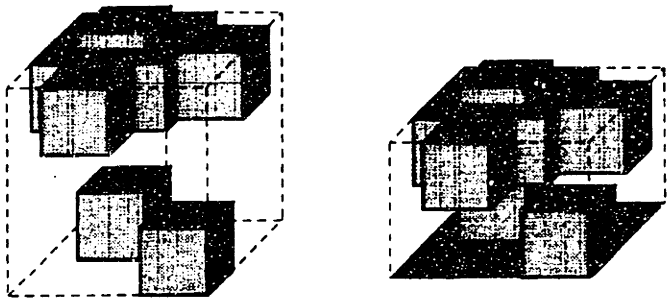

Figure 2.6: Unit cell schematic of design #7A.

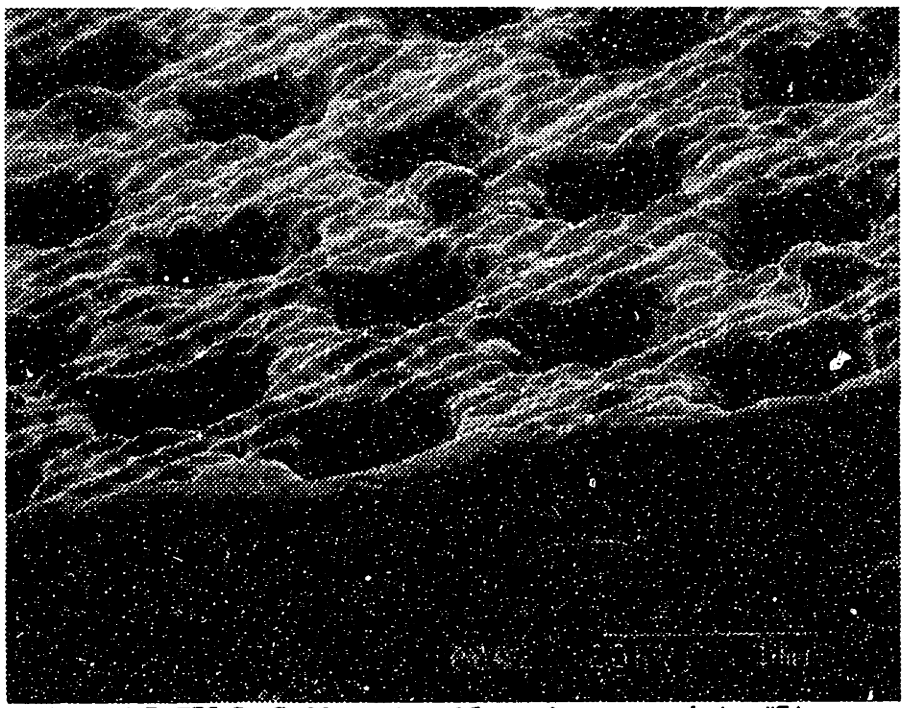

Figure 2.7: F75 Co-Cr-Mo casting of flat surface texture design #7A.

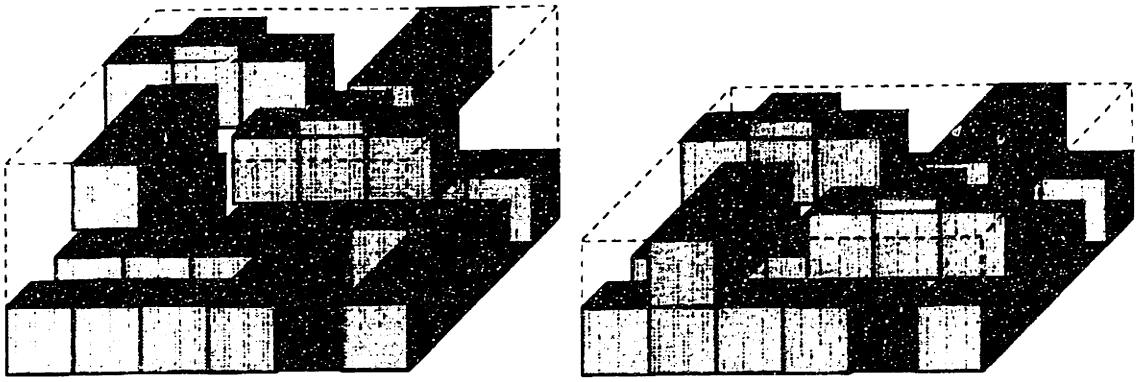

Figure 2.8: Unit cell schematic of design #10.

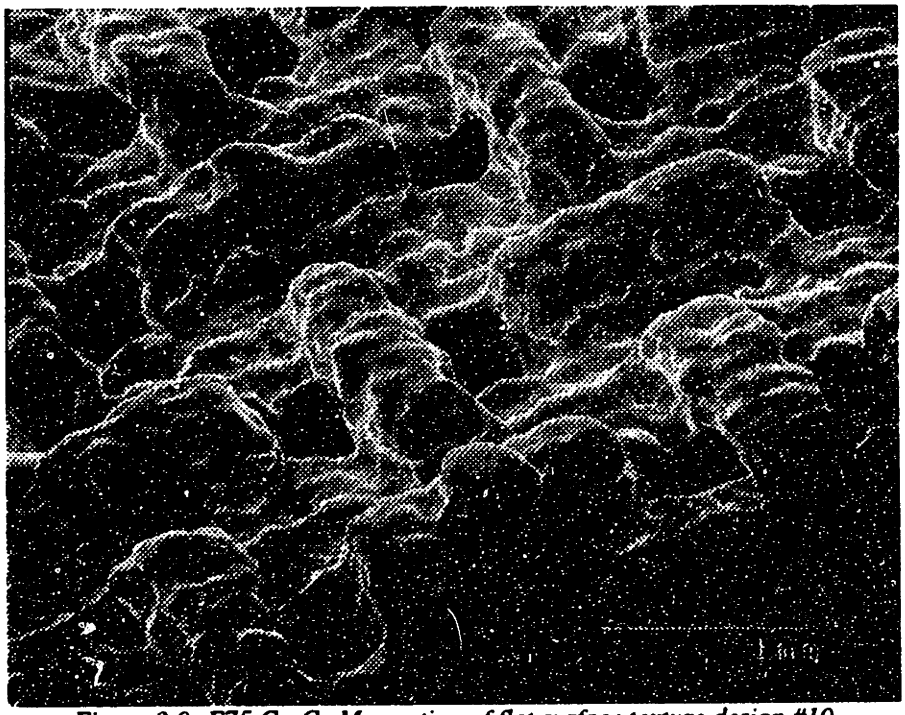

Figure 2.9: F75 Co-Cr-Mo casting of flat surface texture design #10.

2.3 Preliminary results and method

2.3.1 Six texture designs on flat surface

The six texture designs were rated in term of castability, printability and powder removal aptitude before being printed on a flat surface (see figure 3.9). This classification (see table 2.2) helped to predict potential problematic texture design and can be considered also in the final selection of the optimum texture. Number 1 is given for the best characteristics and 5 for the worst. The criteria were established from basic casting and printing rule of thumbs related to the geometry of the texture.

Table 2.2: Texture design classification in term of castability, printability and mechanical pull test.

Design#	Castability	Integrity & Powder removal	Pull test
4	1	1	MAX
5	3	4	MAX
7A	5	5	MAX
8	4	3	MAX
9	2	2	MAX
10	1	1	N/A

As it can be seen in section 3.4, all the surface texture could be printed and cast successfully on a flat surface out of F75 alloy. Although the castability and printability criteria seems irrelevant at this point, they can still have a meaning in term of fabrication process yield.

Standardized pull tests were conducted for five of the 6 texture since texture #10 was not available at that time. Figure 2.10 shows part of the Instron 1322 pull machine with the chuck in the upper part and the test sample below.

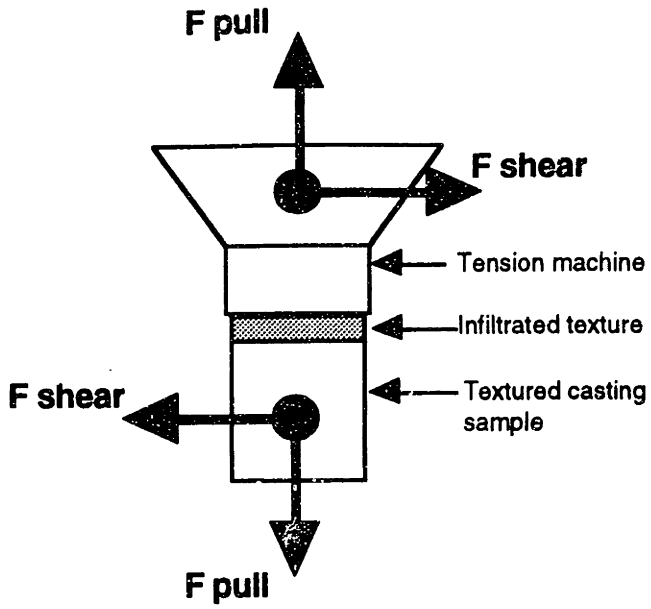

Figure 2.10: Texture pull and shear test simplified schematic.

The texture was bonded to a flat steel surface prepared for optimum bonding. Both surfaces were bonded with a 25 μm layer thickness of FM-1000 epoxy which has tensile strength of about 49 Mpa and peel strength of 10 kN/m. Since standard textures should sustain 20 MPa (FDA) and 30 MPa (J&J), epoxy is strong enough to conduct the pull test.

A thin 25 μm layer of epoxy was used in order to prevent epoxy to infiltrate to far inside the texture. For a valid pull test, epoxy should infiltrate in the texture without bonding to the substrate at the root of the texture. An example of the results is shown in graph of figure 2.11.

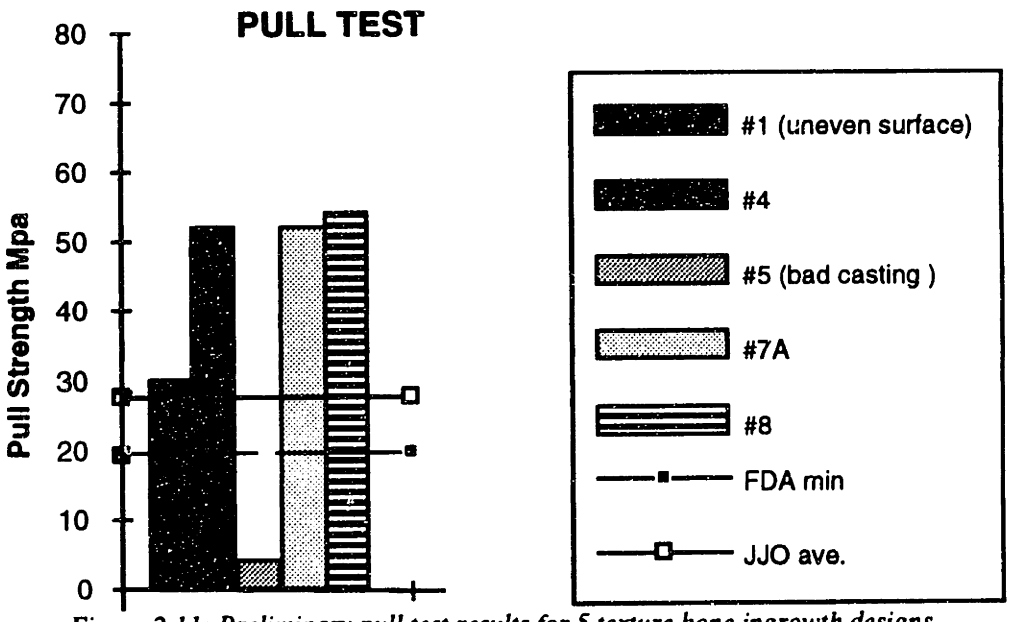

Figure 2.11: Preliminary pull test results for 5 texture bone ingrowth designs.

Texture designs #4, #7A and #8 significantly exceeded the required standards. Actually, the epoxy failed before any part of the texture could be detached from the substrate by the applied tensile force. The two results (design #1 and #5) which underscored compared to other samples were actually bad castings. In both cases, the textured surface was tilted (not orthogonal), as a result the epoxy could not infiltrate properly in the texture. Design #9 was done in a previous experiment such as the ones showed in figure 2.11 and again the epoxy failed before anything else. Since design #9 had a low top porosity, the epoxy infiltrated to the substrate and invalidated the test. However, since the initial results showed that even design #4, which has the lowest tensile area (6%), exceeded the standard, we believe that any other design including design #10 should behave the same.

We can then conclude that cast surface texture with a minimum of tensile area should exceed the tensile strength requirements without any problem.

It is also expected, since the pull test worked so well that the shear would react the same. Both mechanical tests are going to be redone to confirm the results when more cast surface textures will be made available.

2.3.2 Four texture designs for in-vivo dog implants

The in-vivo experiments had to be done on the femur of live dogs in which various texture implant would be installed for various time period (6, 12 and 24 weeks).(see figure 7.1 & 7.2 and figure 2.12)

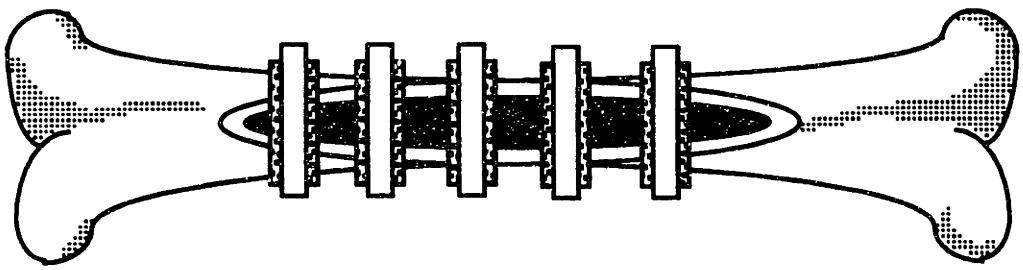

Figure 2.12 In-vivo experiment is done on a dog femur for periods ranging from 6 to 24 weeks.

To minimize the use of dog, only four texture designs had to be selected from the previous six. Since the mechanical test did not differentiate any design apart each other, the selection was done based on the range of pore size, porosity, castability as well as on the aesthetics of the texture. Since the dog implant appeared to be a more difficult shape to cast

(see section 3.4.2), the castability of the texture was a predetermining factor in the choice of the final four designs.

When presented to surgeons, they found that the surface textures were too smooth. A smooth surface would not induce bleeding upon installation of the prosthesis, which is thought to be an essential factor to initiate the process of bone ingrowth. Therefore, 350 x 350 x 175 µm studs have been added sparsely on all the surface textures as it can be seen in most designs presented earlier in figure 2.2 to 2.9.

Table 2.3 shows the final specifications for the four selected designs compared to the actual sintered bead texture used at Johnson & Johnson.

Table 2.3: Final specification for the four texture design used for the in-vivo experiments.

Design#	Pore size µm	Top porosity %	Bottom porosity %	Average porosity	Tensile area
4	350-1000	39	41	40	6
5	200,235-800	37.5	62.5	50	37.5
7A	200,350-800	33	78	56	56
10	350-1000	67	30	49	11
J&J	375-400	37.5-40	37.5-40	37.5-40	?

*Theoretical data

The individual performance of the in-vivo texture designs will be evaluated on five criteria:

- Time for osseointegration
- Depth of penetration of living cells (or histology)
- Pull out strength to remove the implant from the femur
- Shear strength
- General aesthetic of the texture

The final results should point out which texture or textures would provide the best performance on an actual prosthesis. All the results will be compared to a datum which consists in the regular beaded surface texture installed concurrently with the other implants, on which information is already available. The in-vivo results may also suggest the medical engineer to reevaluate the texture designs according to the performance revealed by the in-vivo experiments. Analysis of the results will not be completed in this particular research since the whole experiment will last at least for several months.

Chapter 3. Casting Process

3.0 Introduction

3.0.1 Goal

Orthopaedic implants such as the ones showed in the previous chapter are usually manufactured by standard investment casting and post-processing methods. Those methods have proved to provide adequate accuracy and efficiency for a wide range of precision casting such as turbine blades and orthopaedic prosthesis.

The goal of this research effort is not to try replace standard investment casting processes by the 3D printing process. Instead, the goal is to use the 3D printing casting advantages to complement the capabilities of conventional investment casting methods. For example, the surface texture showed earlier demonstrates the real advantage of 3D printing over any other technology. The as-cast surface texture with sub-millimeter feature size exhibits overhangs and undercuts which could not have been done directly from conventional casting technologies.

Thus, 3D printing could find a niche within the investment casting industry based on its geometrical flexibility, accuracy and feature size capabilities. In other instances, 3D printing could complement its capabilities with another process. For example, the texture capability of 3D printing can be combined to the surface finish capabilities of the lost-wax process. This technique can be used to procure very good surface finish as well as intricate surface textures in desired area on the casting. The mold would be obtained by merging a ceramic 3D printed textured segment onto a smooth wax pattern and then build the rest of the shell conventionally with ceramic slurry.

3.0.2 Challenge

From experience (see chapter 4), we know that we can produce 3D printed ceramic molds with accurate fine surface features. The question, however, is whether we can cast those molds with high temperature alloys reliably and without damaging the features. The fundamental principles of casting will be covered in order to understand the underlying concepts which govern casting quality. These concepts will be useful in order to direct our efforts to determine the best casting conditions. The casting experiments (see section 3.4-3.6) had addressed and answered the concerns about the dependability of the 3D printed mold.

Since conventional casting methods can not reproduce features as small as what we are expecting, another challenge may be to investigate mold filling of small cavities. As it will be showed in our experiments, the problem applies to 3D printed molds in some instance. As a result, different pouring techniques as well as more aggressive casting conditions were investigated.

3.1 Precision Investment Casting Process

3.1.1 Introduction

The thermo-physical properties of the 3D printed ceramic molds are similar to the mold produce with the more conventional precision investment casting process. Thus, understanding the capabilities and limits of the conventional molds will help us in assessing 3D printed ceramic mold own capabilities.

The investment casting process, also called lost-wax process, is the standard technique used to mass produce high precision castings. The sequence involved in investment casting are showed in figure 3.1.

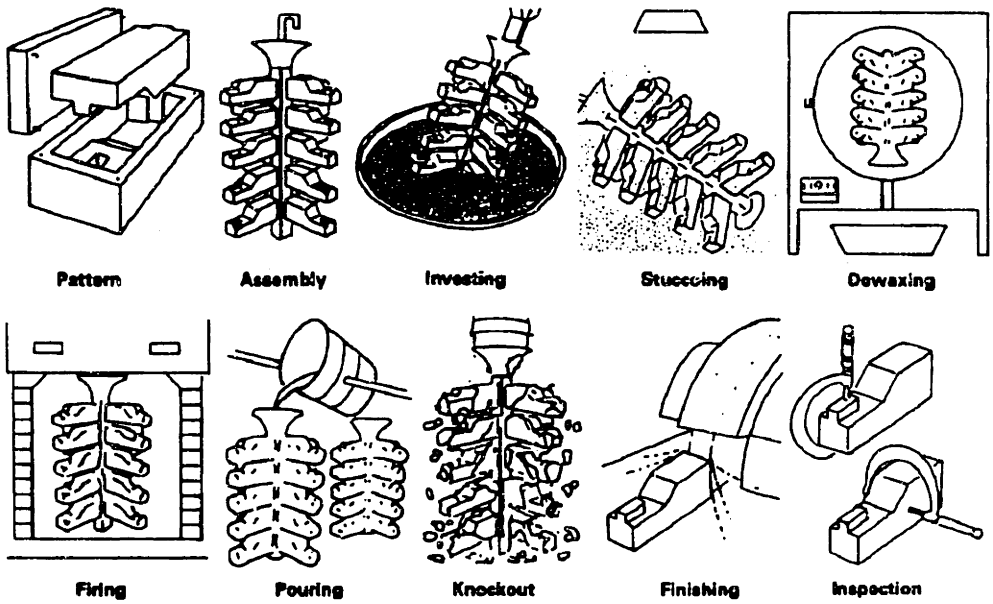

Figure 3.1 : Standard lost wax investment casting procedure

The pattern is made by injecting molten wax or plastic into a metal die in the shape of the desired model. The pattern is then dipped into slurry of refractory material, such as alumina, zirconia,... and bound with water based or alcohol based binders. The first coat also called prime coat is not structural. The very fine particles of the prime coat slurry are used to define the surface finish of the casting. After this initial coating has dried, the pattern is then coated repeatedly with thicker slurry material to increase the thickness of the shell (stuccoing). The one-piece mold is dried in air and heated in an inverted position to melt out the wax (dewaxing). The mold is then fired at high temperature to drive off the

water of crystallization (chemically combined water). After the mold has been poured and the metal has solidified, the mold is broken up and the casting is removed. A number of patterns can be joined to make one mold, called a tree, thus increasing the production rate.

3.1.2 Standard process capability

One of the capability of investment casting is to provide a good accuracy compared to other casting processes. As with the conventional processes, the actual variation which might be expected will vary with the casting size and configuration and, to a lesser degree, with the alloy being cast. For a given process, the tolerance which can be met on a specific dimension has two components: precision and accuracy. (see figure 3.2).

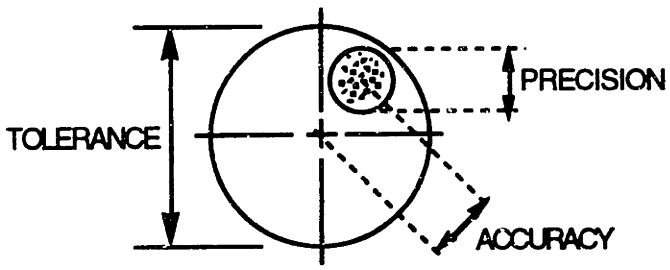

Figure 3.2: Component of tolerance

Precision relates to the variation inherent in the process. Measurements taken on identical castings produced with one process and foundry variables held constant will reveal the scatter within the process (precision). Comparison of the average of such readings with the intended dimension shows accuracy.

Tolerances are affected by several factors:

- *Casting Process:* Different casting processes produce different levels of precision.
- *Configuration/Dimension Type:* Complex shapes may not contract after solidification as predicted. Cored holes especially may not contract as predicted. These affect accuracy as does warping of thin sections during cooling.
- *Casting weight/Dimension Length:* Variation has been showed to increase with weight at constant dimension and with dimension at constant weight.
- *Process Control:* Greater variation in process variables increases the variation to be expected in the castings. These include wax injection temperature and pressure, and mold and metal temperatures at pouring among many.
- *Dimensional Upgrading:* Tighter tolerances can be met by using techniques such as fixturing, gauging, straightening, coining and machining.

Some general comparisons of the dimensional capabilities of the processes can be made. Figure 3.3 shows typical linear tolerances for the sand, resin shell and investment casting processes. Larger dimensions appear to have less variation with resin shell process. However, the investment casting process should be considered for large casting when thin wall thicknesses or relationships between small features are more important and for more intricate parts.

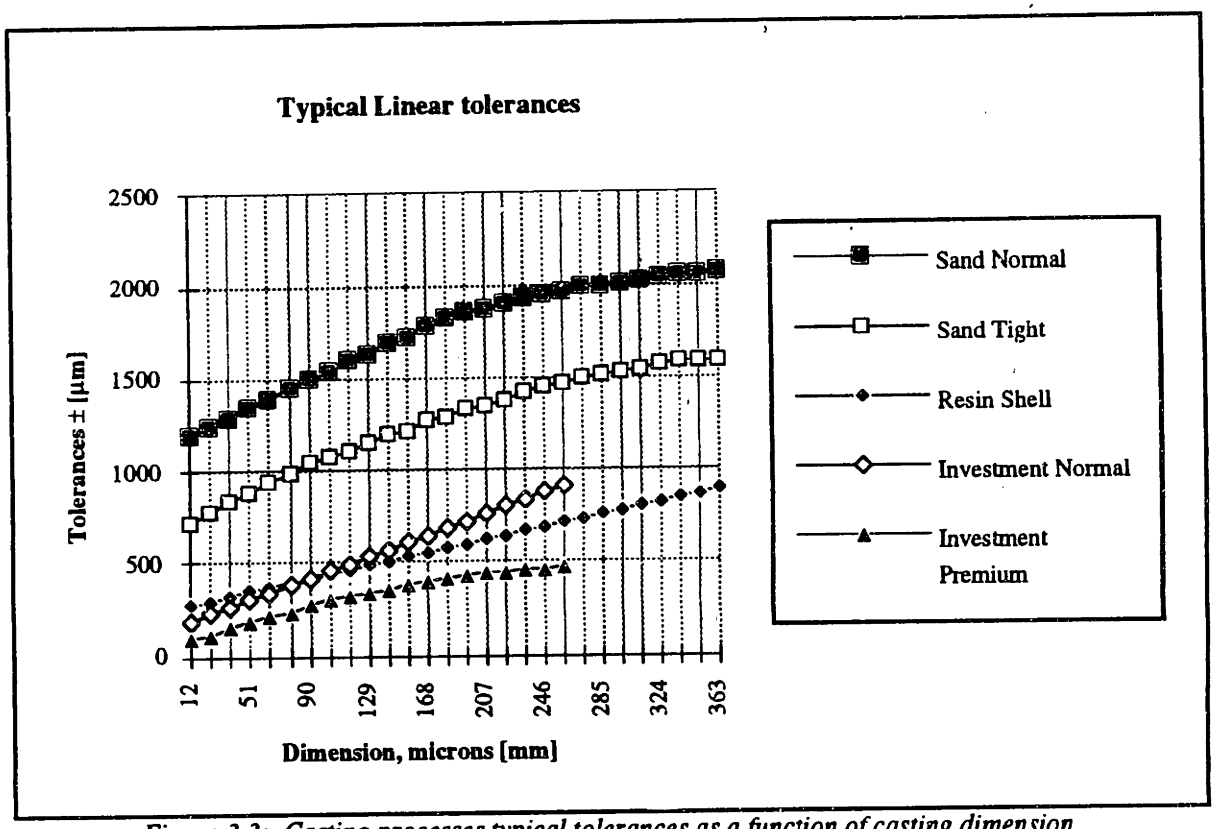

Figure 3.3: Casting processes typical tolerances as a function of casting dimension.
* From the same sources as table 3.1

Other limits related to the minimum and maximum weight and size which can be produced with different casting process can be compared (see table 3.1).

Table 3.1: Normal Limits of Casting Size

PROCESS	MINIMUM WEIGHT	MAXIMUM WEIGHT
Solid mold	0.01 lb (2g)	1 lb (0.5 kg)
Investment casting	0.01 lb (5g)	100 lbs (50 kg)
Resin shell	0.5 lb (0.25 kg)	10 lbs (5 kg)
Sand	1 lb (0.5 kg)	20000 lbs (10 Mg)

PROCESS	MINIMUM DIMENSION	MAXIMUM DIMENSION
Solid mold	0.020 in (0.5 mm)	3 in (75 mm)
Investment casting	0.030 in (0.75 mm)	15 in (400 mm)
Resin shell	0.125 in (3mm)	15 in (400 mm)
Sand	0.25 in (6 mm)	150 in (3.8 m)

[] "Steel Castings Handbook, Supplement 3", Steel Founders's Society of America, Rocky River, OH,pp 13,14 (1980)
[] "Steel Castings Handbook", 5th Ed., Steel founders's Society of America, Rocky River, OH, pp12-16 (1980)
[] "Investment Casting Handbook 1980", p162

In summary, those results suggest that 3D printed molds could handle a wide range of casting weight varying between 5g to 50 kg. The tolerance, although process and machine dependent, should match closely or surpass the one showed in figure 3.3 (Investment casting premium) because of the fewer geometry transfer and precision nature of the 3D printer. Tolerances of about ±125 μm. for dimensions up to 2.5 cm. and ±50 μm. per cm. for dimensions over 2.5 cm., represent the normal capabilities of the investment casting process.

One ambiguous point, however, is about the minimum dimension or feature size. It seem that conventional investment casting can not achieve dimensions smaller than 750 μm. This characteristic will have to be improved, since we are targeting casting feature of 350-400 μm size. On the other hand, this limit may be caused by the dimensional constraints prescribed by the wax pattern rather then on the ceramic mold and metal infiltration characteristics. This dimensional limit should then be part of the research effort in order to understand the cause(s).

3.1.3 Description of standard CoCr investment casting methods for producing orthopaedic prostheses.

This section provides a brief description of the actual process of manufacturing cast orthopeadic implants out of Cobalt-based alloy.

Preparing the pattern and the mold

The first steps in the process of casting orthopeadic implants are quite similar to the ones described in the previous section on investment casting:

- produce the tooling for the wax pattern
- injection mold the wax pattern
- create the silica-alumina shell around the pattern (prime + 7 coats)
- melting the wax out of the mold
- preheat the mold between 750° to 950° C.

The mold preheat is subject to change depending on the shape and dimension of the part being cast.

Melting

The next step is to prepare the metal for pouring. Figure 3.4 shows a standard procedure to bring the metal to its desired temperature.

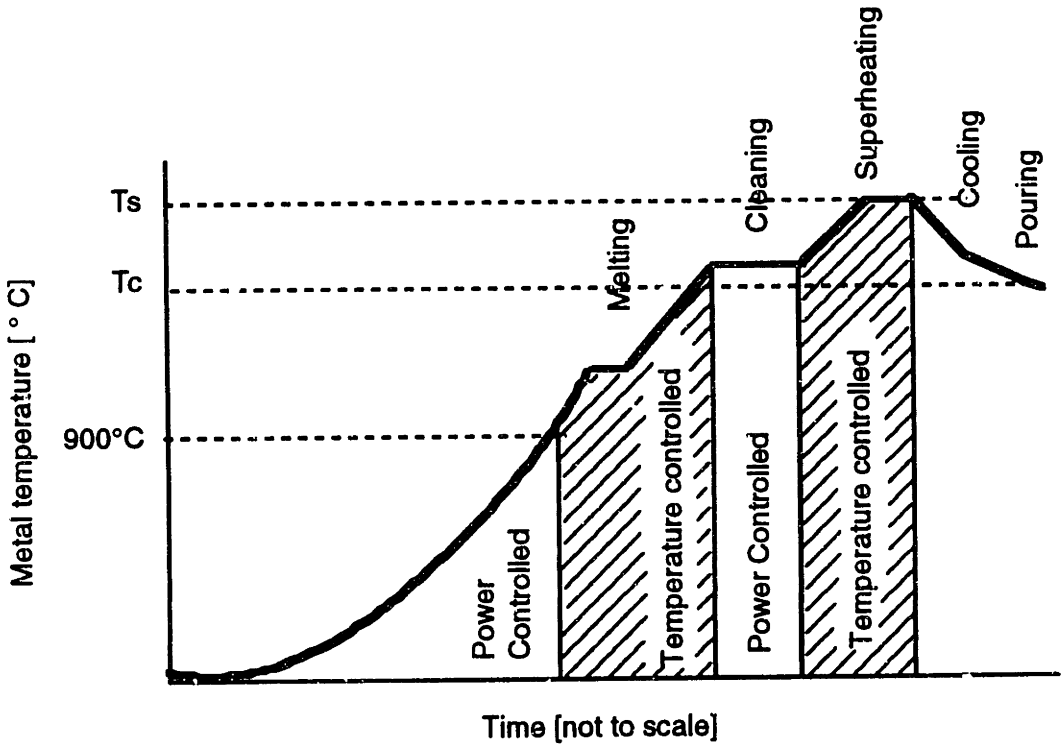

Figure 3.4: High temperature alloy melting procedure.

The graph shows how the induction melting and superheat are being closed-loop controlled in order to have an efficient and stable melting curve. As we can notice, the superheat temperature of the metal, as it is poured, is slightly lower. This decrease is mainly due to the fact that power in the induction coil is shut off prior to pouring the metal. The melting is done inside a controlled atmosphere chamber. Air and oxygen is rarefied by constantly injecting argon or similar inert gas in the chamber.

Pouring & solidification

The metal is then poured by tilting the crucible over the mold sprue. The mold is air cooled for a few minutes and then the shell is knockout with a vibrating pneumatic hammer or by hand. Sand blast is used to remove the last pieces of ceramic sticking to the surface of the casting.

Post-processing

The risers and gating system is then trimmed off the casting. Several steps of grinding and polishing (buffing wheel) with different grades of abrasive give almost the final finish to desired area of the prosthesis

For prostheses which require bone ingrowth surface texture, another set of post processing operations are needed. For example, the Johnson & Johnson prostheses exhibit a surface texture made of three layer of sintered cobalt-chrome sphere (distribution of 500 to 550 μm diameter). Conventional sintering techniques for bonding large powder particles to cobalt-chromium alloys typically involve sintering temperature that are 90 to 95% of the melting point of the substrate. Sintering leaves a binder residue which need to be remove chemically afterwards.

After sintering and debinding, the cast prostheses undergo hot isostatic pressing (Hipping) in order to close the pores inherent to casting and sintering heat treatments. As a result, the tensile and fatigue properties of the casting are significantly improved.

Finally, the casting is solution annealed in order to re-dissolve the carbides that precipitated at the grain boundaries. Since cast cobalt-chromium-molybdenum alloys are carbide strengthened this operation optimizes the strength and homogeneity of the prosthesis material.

3.1.4 Advantage of using 3D Printing

Three dimensional printing offers several advantageous characteristics which distinguishes it from other casting processes. The first advantage that comes to mind is its short cycle time. Figure 3.5 compares the steps required from the point where the technical drawings (or CAD model) are completed. The standard lost-wax investment casting process consists in several steps which involve time, effort and capital. For example, tooling is the major bottleneck as far as capital investment and process delays are concerned. It can take months and several thousands of dollars before the first tool is developed and functional. Even after the tools are made, other steps in the cycle can be time consuming. For example, each drying cycle of the ceramic shell is one day. Seven coats and seven days are required to form the completed shell. From concept to final product, a new knee design would require over a year before the first casting is produced.

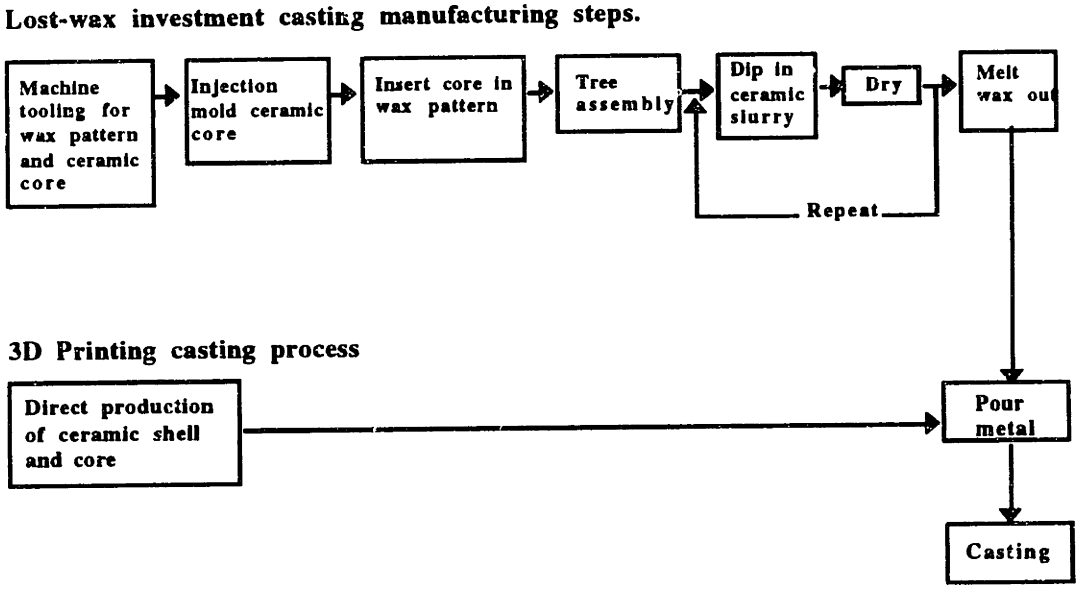

Figure 3.5: Standard lost-wax casting cycle compared to 3D printing casting cycle.

On the other hand, 3D printing could have produced prototypes of similar parts in a matter of days.

Because of the nature of 3D Printing, tight tolerances can be achieved on the ceramic molds and as a result on the casting themselves. The enhanced accuracy of 3D printing is mainly due to two process characteristics: control of drop placement and minimum transfer of dimensional information. The printing nature of 3D printing allows to locate the droplets, which form the mold material, very accurately on the ceramic powder bed independently of the mold dimensions. Furthermore, since 3D printing directly produce

the mold with the right dimensions, it eliminates the three shape transfers (tooling, wax pattern, shell making) involved with the lost-wax process. Each transfer introduces a lost of dimensional accuracy which does not occur in the case of 3D Printing.

Other advantages of 3D printing are related to its geometrical freedom and accessible feature size. In fact, 3D printing can generate sub-millimeter features in various shapes with overhang and undercut geometry. This unique feature is not available on any other standard casting processes. This advantage distinguishes 3D printing casting process from others. As a result, it extends 3D printing field of application beyond the rapid prototyping functions.

3.2 Fundamentals of Metal Casting

3.2.1 Introduction

The investment casting process provides the ability to produce accurate castings with thin wall and intricate small features. The limit of the process is determined by the achievable accuracy and smallest feature size that can be cast repeatedly without defect.

The casting accuracy depends on the material system metal-ceramic mold and casting conditions used, such as level of superheat temperature and mold temperature. On the other hand, three major physical phenomena determine the minimum castable feature size: the metal fluidity, surface tension and cooling rate.

The metal fluidity mainly relies on the metal composition and level of superheat temperature. Its effect on the casting integrity is inter-related to the metal cooling rate. In fact, the metal cooling rate and fluidity determine how far the metal can infiltrate in the mold before it starts freezing. The freezing time t_s can be calculated from the initial metal pouring conditions and mold conditions. The casting engineer has several alternatives in order to control the cooling rate and obtain a good casting. These options will be discussed in the section on freezing time.

The metal surface tension is the force that the casting pressure needs to counteract in order to fill small cavities. It introduces a direct limitations to the size of the feature since only a limited pressure is allowed in the molds.

The casting parameters may affect the casting quality on different front. In the next section, we will attempt to separate the parameters and determine the pattern in which they affect the casting quality.

3.2.2 Mold material

The raw materials for precision casting molds fall into three major categories: binders and catalysts, refractory filler, and additives. Some additives control the rheological properties and the wetting characteristics of the slurries. Others impart increased strength, better collapsibility and other desirable properties to the mold and core. In the case of 3D printing, additive are added separately to the binder and the powder in order to control gelling, foaming, binder stability,...

The 3D printed molds are made of refractory alumina powder bound by a water-based binder, colloidal silica. As we can find in Jim Bredt Ph.D. thesis ref.[90], the colloidal silica used for 3D Printing (Nyacol 9950) has 100 nm silica particle size with a solid

loading of 50% by weight (33% by volume) from Nyacol Corp., Ashland, MA. This solution is diluted and additives are added to control the solid content, stabilize the suspension and prevent foaming and algae development. Standard lost wax molds produced using colloidal silica binders are usually air-dried under carefully controlled conditions. In the case of 3D printing, the binder is gelled instead as it collides in the powder in order to prevent bleeding into unprinted region of the powder bed. To prevent bleeding, a catalyst containing acid is incorporated in the ceramic powder. (for more details on binder-powder interaction see J. Bredt Ph.D. thesis ref.[90]).

30 μm average alumina powder was used as the refractory filler to create the structure of the mold. This standard material is used only for high precision investment casting because of its cost compared to other refractories.

Table 3.2: Physical Properties of Common Refractories

Refractory	Melting Point [F & (°C)]	Density [Kg/m3]	Thermal Expansion [$x10^{-6}$ $mm/_{mm\ K}$]
Fused Silica	3110F (1710°C)	2070	0.015
Zircon	4600F (2538°C)	4650	0.23
Chromite	3800F (2093 °C)	4400	0.27
Alumina	3720F (2050 °C)	4000	0.7
Olivine	3400F (1875 °C)	3320	0.8
Quartz	3110F (1710 °C)	2660	1.4
Mullite	2820-3326F (1550-1830 °C)	3120	0.4
Kyanite	2415F (1325 °C)	3620	0.4

Alumina has a relatively low thermal expansion coefficient which allows accurate reproduction of pattern dimensions. In fact, high thermal expansion coefficients magnify the effect of mold temperature variations on casting dimensions and increase the incidence of mold fracturing and spalling. The high metal temperatures of the cobalt-based alloy requires also the use of mold refractories having high melt temperatures.

The comparison table 3.2 shows the properties of different refractory fillers. Although alumina does not seem to be the best choice at first, when all the considerations, such as mold reactivity with the metal, cost, availability and thermal expansion are considered, alumina precludes over others.

The 3D printed molds are made with almost exactly the same chemistry as what is used in the high precision investment casting industry. The difference occurs in the manner the ceramic shell is built and the particular way binder and ceramic filler are combined. As a result, the thermo-physical properties of the 3D printed ceramic shell are more or less equivalent to what is in use in the industry actually. The experiment described in the next

section 3.8 will demonstrate those similarities by producing high precision Cobalt-Chrome Co-Cr casting from the 3D printed mold material.

3.2.3 Metal composition

Two different metal alloys were used to conduct the various investment casting experiments; 60Sn-40Pb tin-lead alloy and ASTM F75 Cobalt base alloy. The first alloy (i.e. tin-lead) was not really designed for investment casting because of its poor mechanical properties. As showed in the alloy label, it is made of 60% tin (Sn) and 40% lead (Pb). It is more known for its electrical properties as a soldering material with low melting point eutectic $T_m \approx 183°C$. In fact, we used this alloy because of its low melting point and good fluidity. It allowed us to test prove the integrity and dimension of our mold models before going for the expensive process of casting with the F75 alloy.

The Cobalt-base alloy or more precisely the ASTM F75 alloy was developed for the biomedical industry for application such as orthopaedic implant. Implant materials must meet exacting requirements if the device is to perform its function successfully for extended periods of time. These requirements include biocompatibility, mechanical strength, corrosion, wear and fatigue resistance, and approval by various regulatory agencies. In general, the cobalt-base alloys are easy to work with in the foundry and exhibit good casting properties including:

- Good fluidity compared to other high temperature alloys
- Relatively low melting points
- Freedom from dissolved-gas defects
- Low alloy losses due to oxidation

The nominal composition of our two alloys is showed in table 3.3.

Table 3.3: Metal composition [weight %]

Alloy / %	C	Mn	Si	Cr	Ni	Fe	Mo	Co	Pb	Sn
ASTM F75	0.35	1.0	0.40	27-30.0	1.00	1.5	6.0	bal	-	-
40-60 Pb-Sn	-	-	-	-	-	-	-	-	40	60

Metals Handbook Vol.1 10th edition, Properties and Selection Irons, Steels and High Performance Alloy, ASM international

The nominal metal composition was used to calculate the **molten** density of the two alloys. The molten density is necessary since it enter in the calculation of the metal pressure head inside the mold. The density was then calculated by using the molten density (see table 3.4) of the basic elements forming both alloys.

Table 3.4: Element density @ melting point [kg/m^3]

Element	C	Mn	Si	Cr	Ni	Fe	Mo	Co	Pb	Sn
Density	2260	5390	2526	6290	7910	7036	9520	7750	10665	7010

Metals Handbook 9th edition, Volume 15 Casting (TA 459 .A5171 1978 V.15)

The rule of proportions was then used to calculate the densities as follows:

$$\rho_{Pb-Sn} = (0.4x10665) + (0.6x7010) \equiv 8472 \ {}^{kg}/_{m^3}$$

$$\rho_{F75} = (0.0035x2260) + (0.01x5390) + (0.004x2526) + (0.28x6290) + (0.01x7910) + (0.015x7036)\ldots$$
$$+ (0.06x9520) + (0.6175x7750) \approx 7370 \ {}^{kg}/_{m^3}$$

3.2.4 Metal surface tension effects

The main parameter which determines the minimum feature size that can be cast adequately is the metal surface tension σ [mN/m]. Surface tension has the dimensions of force per unit length. The surface tension σ is a property used to describe certain phenomena that are observed at the interfaces between a gas and a liquid or like in our case gas-liquid-solid (air-metal-mold). Data for molten metal surface tension are scarce.

By comparing the experimental surface tension data of Ni-Co and Fe-Co @ 1600 °C and the one of the element Co and Cr, we notice a definite consistency of their value. From those premises, we could evaluate the **surface tension of the F75** alloy to be in the vicinity of **1800 mN/m**. The value was taken a little higher considering that skin effect (or oxidization) can only increase the surface tension of molten metal in air. We will rely on the same rules to evaluate the **surface tension of Pb-Sn to be about 560 mN/m**.

Table 3.5: Surface tension [mN/m]

Element or alloy	Surface tension [mN/m]
Cr @ melting point	1700
Co @ melting point	1870
Mo @ melting point	2250
Sn @ melting point	613
Pb @ melting point	468
Ni-60% Co @ 1600 °C	1775-1800
Fe-Co @ 1600 °C	1775

Handbook of physico-chemical properties at High Temperatures
The Iron and Steel Institute of Japan, Special issue No. 41 (TA418 .52 .H36 , 1988) p. 150 & 155

Experimentally we observe that surfaces resist deformation. This resistance can be explained by considering the intermolecular forces within the liquid. As seen in figure 3.6, surface tension effects occurs in the small cavity where pressure attempt to bend the liquid meniscus to infiltrate the cavity with metal.

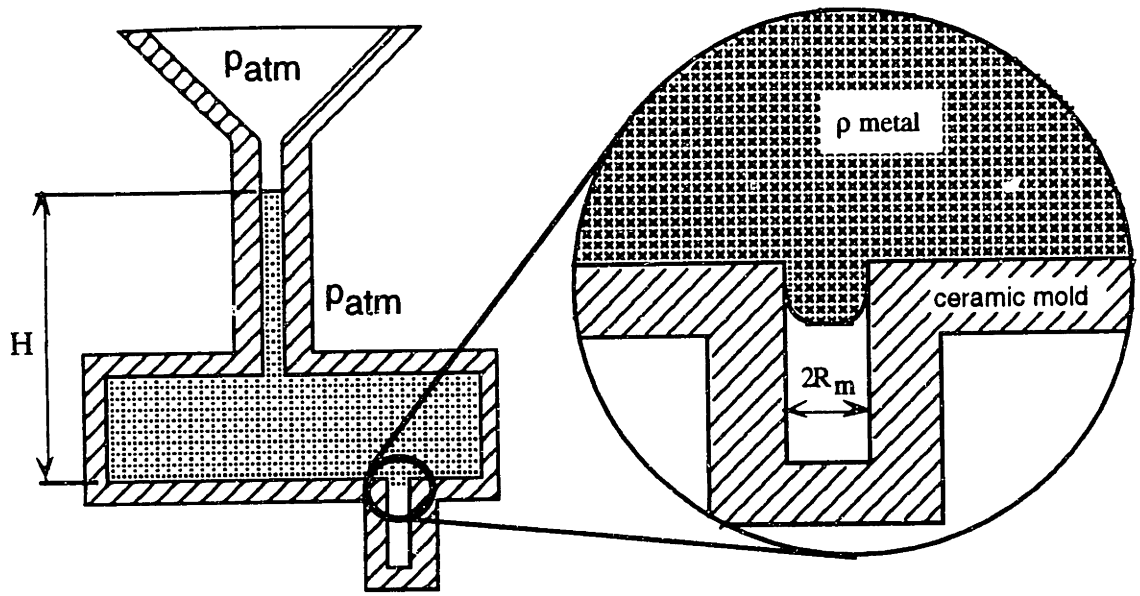

Figure 3.6: Investment casting of a mold with a small cylindrical cavity of radius R_m.

The shape of the liquid metal surface that is in contact with the alumina and air is determined by the relative value of the surface energy. Specific liquid-solid combinations are classified as wetting or nonwetting depending on the contact angle between the liquid and solid surfaces. Most casting alloys will present nonwetting characteristic on alumina molds, which means that the angle θ of contact is always >90°. Very little information is available on the contact angle of high temperature alloys on alumina. As a result, it was not possible to find the contact angle for our material systems; ASTM F75 and SnPb with alumina. However, available data for alloys resembling our F75 alloys are showed in Table 3.6.

Table 3.6: Contact angle [θ]

Liquid and solid mat'l in contact + Temp. [°C]	Contact angle [°] (non-wetting)
Ni-60% Co on Al_2O_3 @ 1600 °C	115° - 120°
Fe-Co on Al_2O_3 @ 1600 °C	135° - 138°

Handbook of physico-chemical properties at High Temperatures
The Iron and Steel Institute of Japan, Special issue No. 41 (TA418 .52 .H36 , 1988) p. 175-176

Those results show the non-wetting characteristics of such alloys on alumina at high temperature (i.e. ≈ 1600° C) with values of θ varying between 115° and 138°. The following data was used to build the force balance control volume (figure 3.7a) around the meniscus showed in figure 3.6. The direction of the surface tension force per meter σ is then determined by the contact angle as showed in figure 3.7a. As expected, the surface tension linear force goes against the molten metal pressure P_m.

Minimum castable feature size

The minimum feature size that can be cast or in other words infiltrated by the metal is determined by the radius R_m for a given molten metal pressure P_m . The minimum feature size would be in this case a cylindrical stud with diameter $D_m = 2R_m$. The value of R_m is determined for the equilibrium conditions of the metal surface at the surface of contact between the metal and the mold.

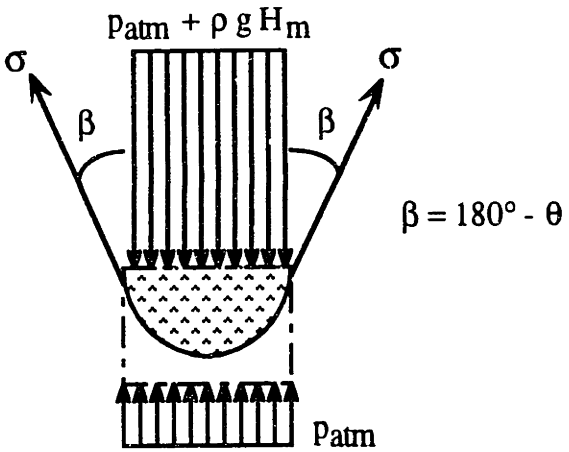

A) Control Volume for smooth ceramic mold.

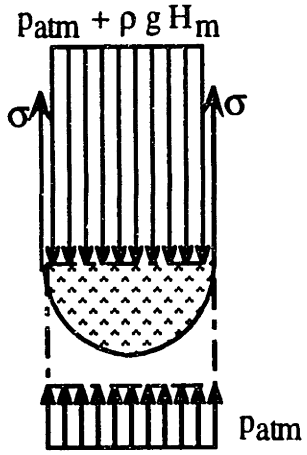

B) Control Volume for rough ceramic mold worst case (β=0).

Figure 3.7: Force balance control volume around the meniscus of radius R_m from figure 3.6.

One can assume with a sufficient degree of accuracy that the capillary pressure P_σ (caused by the surface tension σ) added to the excess pressure of gas in the mold ΔP_g is equalized by the pressure of the molten metal P_m (equation 3-1).

$$P_m = P_\sigma + \Delta P_g \quad [N/m^2] \qquad (3\text{-}1)$$

The pressure of the metal is determined by the expression

$$P_m = P_{atm} + \rho_m \, g \, H_m \qquad (3\text{-}2)$$

where P_{atm} is the ambient air pressure 101.3 kPa [kN/m^2]
ρ_m is the metal density in [kg/m^3]
g is the acceleration due to gravity 9.81 [m/s^2]
H_m is the height of the column of metal creating the pressure [m]
(if the pressure is external the H_m indicates the relative height of the equivalent column of metal being poured).

The value of the capillary pressure P_σ opposing the penetration of the metal into the mold is determined by the Laplace equation

$$P_\sigma = \sigma \cos(\beta)\left(\frac{1}{R_1}+\frac{1}{R_2}\right) \qquad (3\text{-}3)$$

where σ is the surface tension of the metal [N/m]

$\beta = 180° - \theta$

R_1 and R_2 are the radii of curvature of the surface of separation between the liquid and the solid phases in two perpendicular directions.

In our case $R_1=R_2=R_m$, and equation 3-3 takes the form

$$P_\sigma = \frac{2\sigma\cos(\beta)}{R_m} \qquad (3\text{-}4)$$

In many case, taking into account hysteresis of wetting and also the fact that the mold surface is irregular, we may assume that an angle of contact θ=180° ($\beta = 0°$). Then from equation 3-4 we obtain

$$P_\sigma = \frac{2\sigma}{R_m} \qquad (3\text{-}5)$$

If the pressure of the gases in the casting mold is equal to atmospheric pressure ($\Delta P_g = P_{atm}$) because of the porosity level of the mold, then from equation 3-1, 3-2 &3-5 we obtain

$$R_m = \frac{2\sigma}{\rho g H_m}$$

$$\text{or} \quad R_m = \frac{a^2}{H_m} \quad \text{where} \quad a = \left(\frac{2\sigma}{\rho g}\right)^{1/2} \qquad (3\text{-}6)$$

where a is the capillary constant characterizing the ability of a given alloy to fill capillary tubes. Therefore, the minimum feature size $2R_m$ that can be cast from a molten metal head H_m is determined by equation 3-6.

The later value of R_m is valid for small pore size where the meniscus forms a spherical shape. Another case that can be evaluated is when the metal front forms a cylindrical shape instead, such as along all the linear or square edges of the mold. For this condition, the value of R_1 can be defined as R_{edge} while $R_2=\infty$. This would transform equation 3-6 into:

$$R_{edge} = \frac{\sigma}{\rho g H_m} \qquad \text{or} \quad R_{edge} = \frac{a^2}{2H_m} \qquad (3\text{-}7)$$

where R_{edge} is the minimum radius defining the edges of our casting. For simplification R_{edge} happens to be equal to $R_m/2$.

Minimum radius & expected surface finish

Along the same line, the casting surface finish can also be determined by the value of the minimum radius R_m. The grains composing the surface layer of the mold are in fact not close together and have a gap between them. On the basis of this observation (Lyashchenko 1965 ref [43]) proposed an estimate picture of the structure of the surface layer of a mold consisting of granular materials. The diagram of the structure (see figure 3.8) as a whole is made of three assumptions:

1) the grains of sand are spheres of the same radius R_S;

2) the grains of sand are distributed uniformly in the surface layer of the mold. The centers of neighboring grains in the section of maximum clearance are at a distance $2\varphi R_S$ from each other, where φ is the coefficient characterizing the closeness of packing of the grains of sand in the surface layer of the mold;

3) the maximum penetration of the metal between grains is along the X-X axis (see figure 3.8) the farthest from both grains of sand. In first approximation we may assume that the meniscus formed at that point is a segment of a sphere.

Three different types of configuration can occur on the surface of the castings, depending on the degree to which the metal penetrates between the grains of sand and assuming no mechanical pick up of the grains (see figure 3.8)

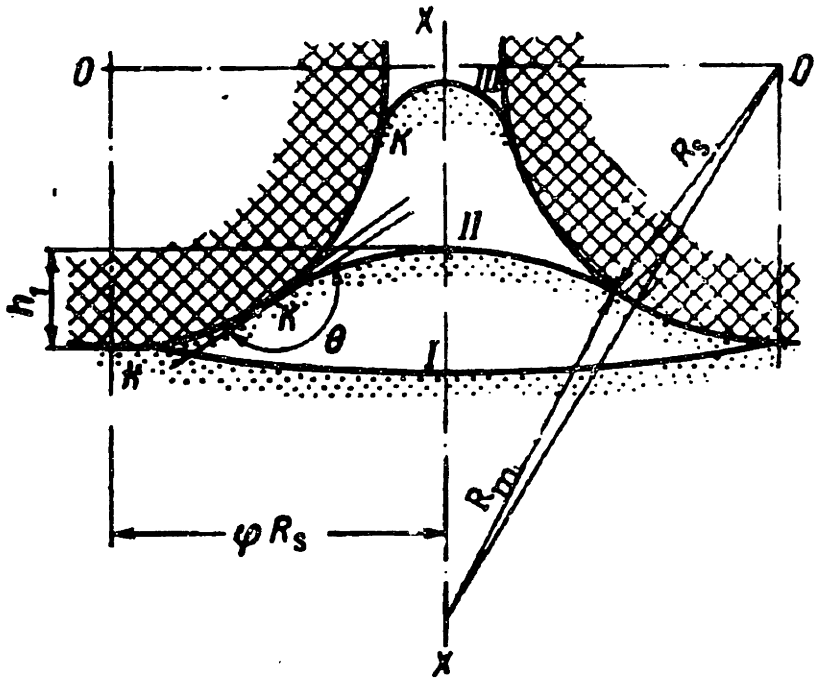

Figure 3.8: Schematics showing the height of the surface irregularity on the casting caused by surface tension effects.(from ref [44])p.225)

Configuration I: Metal does not penetrates the mold; shallow depressions are formed on the surface of the metal. This type of configuration on the surface is sometimes called gaseous roughness of the surface (Obolentsev, 1961 ref.[44])

Configuration II: The protrusions on the surface have slightly sloped sides, making a smooth profile of the microtexture. In this case the metal penetrates to a shallow depth between the grains of sand.

Configuration III: The protrusions have steep slopes; the micro texture has peaks. This type of configuration is characteristic of deep penetration of the metal into the surface pores of the mold.

On the basis of figure 3.8 we can derive by geometry the following equation for configurations II and III:

$$h_1 = R_s + R_m - \sqrt{R_s^2 + R_m^2 - 2R_s \cdot R_m \cos\theta - (\varphi \cdot R_s)^2} \qquad (3\text{-}8)$$

where h_1 is the height of the irregularities on the surface of the casting, provided the model has no surface irregularities [m]

R_S is the radius of the ceramic grains

R_m is the radius of the meniscus at the front edge of the metal which penetrates the pores of the mold [m]

θ is the angle of contact between the metal and the grains [$\theta > 90°$]

φ is the coefficient of packing closeness of the grains [$\varphi > 1$]

As mentioned earlier, in many cases if we consider the grains porosity and irregularities, we may assume $\theta = 180°$ to obtain a simpler version of equation 3-8 as:

$$h_1 = R_s + R_m - \sqrt{(R_s + R_m)^2 - (\varphi \cdot R_s)^2} \qquad (3\text{-}9)$$

An interesting characteristic of the model can be used to evaluate whether or not the metal will capture ceramic grains on the casting surface. This phenomenon is called also grain mechanical picking. The condition for grain mechanical picking occurs when the point of contact k (see figure 3.8) is above the 0-0 axis. From figure 3.8, we can conclude that mechanical picking will occur only for:

$$\varphi \cdot R_s > R_s + R_m \qquad (3\text{-}10)$$

or if we combine equation 3-10 & 3-6, the final condition for grain mechanical pickup is:

$$\varphi > 1 + \frac{2\sigma}{\rho g H_m R_s} \qquad (3\text{-}11)$$

The above results are based on the assumptions made earlier that the grain of powder are spherical and uniformly distributed. We can assume the 3D printed ceramic mold to follow those assumptions with one exception. The calculated value of h_1 represented the best surface finish that can be achieved on the machine as opposed to the one we get at this

moment. In fact the surface of the mold is not uniform because of the step effect between layers and groves between printed lines. In fact, the groves formed between printed lines can easily overcome the value of h_1. More research will have to be done in order to eliminate those groves, nevertheless this task is not part of the objective of this present research.

Example

Say we cast our ASTM F75 Cobalt base alloy into a 3D printed mold with the following condition:

ρ_m=7370 kg/m^3 is the density of the molten metal
H_m = 0.30 m is the pressure head of the molten metal
σ = 1.790 N/m is the surface tension of the metal
2 R_S = 30 μm is the ceramic grain diameter
θ=180° is the contact angle between the molten metal and the ceramic mold.
φ = 1.5 is the closeness packing factor

From equation 3-6, the radius of the meniscus at the front edge of the metal is R_m = 165 μm which give a minimum castable feature size of $2R_m$= 330 μm. The edges of the casting should have a radius R_{edge}= 83 μm. The height of the irregularities (equation 3-9) for the best achievable surface finish is h_1 = 5.3 μm or peak to peak of ± 2.7 μm. Then finally, no grain mechanical pickup is to be expected since our value of φ =1.5 is not larger than 6.5 according to the condition of equation 3-11.

3.2.5 Metal freezing time

Theory

The metal freezing time t_s is an important characteristic which helps casting designers to evaluate the probability of success of a particular casting method and mold arrangement. The time constant t_s is a good estimate of the time allowed in a process to fill a mold cavity before freezing occurs. As far as filling the mold macro-surface texture is concerned, t_s represents also the period available for pressure to build up in the case of conventional investment casting.

The value of t_s depends on several factors associated with the metal properties, the mold properties as well as the mold design. In order to determine the freezing time t_s of a casting, we must first know about the design of the mold. The two most important

parameters are the mold cavity surface area A and volume V. The value of A is associated to the available mold surface through which heat can be dissipated. Therefore, a larger surface *A* should make the casting solidify faster. On the other hand, the volume V of the casting is proportional to the amount of heat stored in the metal.

The heat to be dissipated is the superheat above the freezing temperature and the latent heat of fusion. Let the pouring temperature be T_p and the solidification temperature be T_1. The pouring temperature is also defined as the superheat temperature T_{SH} which is predetermined somewhere above the melting point temperature T_{mp}. The interface metal-mold temperature assumes that the mold surface is raised from an initial temperature T_0 to temperature T_1 and remains at T_1 during solidification. Since the melting point temperature T_{mp} is a good estimate of the interface temperature, we will define $T_1 \approx T_{mp}$. Thus, the heat Q_{metal} to be dissipated is:

$$Q_{metal} = \rho_{metal} V_{mold}\left[L_{metal} + C_{metal}\left(T_p - T_1\right)\right] \quad \text{[Joule]} \qquad (3\text{-}12)$$

where ρ_{metal} is the liquid metal density [kg/m^3]

V_{mold} is the volume of the mold internal cavity [m^3]

L_{metal} is the metal latent heat of fusion [Joule/kg]

C_{metal} is the specific heat of the liquid metal [Joule/(kg K)]

$T_p = T_{SH}$ is the metal pouring temperature [K]

$T_1 \approx T_{mp}$ is the solidification or interface temperature [K]

Then the heat to be dissipated Q_{metal} should be equated to the heat Q_{mold} to be absorbed by the mold in a time t:

$$Q_{mold} = A_{mold} \frac{2K_{mold}\left(T_1 - T_0\right)\sqrt{t}}{\sqrt{\pi \alpha_{mold}}} \quad \text{[Joule]} \qquad (3\text{-}13)$$

where A_{mold} is the surface area of the mold cavity [m^2]

K_{mold} is the thermal conductivity of the mold [Watt/(m K)]

T_0 is the initial temperature of the mold [K]

t is the time elapsed to transfer the amount of heat Q_{mold} [s]

α_{mold} is the thermal diffusivity [m^2/s]

Q_{mold} is in fact the average heat transferred through the surface of the mold between t=0 and t=t considering a semi-infinite mold thickness (or Dirichlet boundary conditions see ref [86]).

The thermal diffusivity α_{mold} can be determined by:

$$\alpha_{mold} = \frac{K_{mold}}{C_{mold}\,\rho_{mold}} \quad \left[\mathrm{m}^2/\mathrm{s}\right] \qquad (3\text{-}14)$$

where C_{mold} is the specific heat of the mold [Watt/(m K)]
ρ_{mold} is the mold density [kg/m^3]

then we find for t=ts

$$t_s = B\left(\frac{V}{A}\right)^2 \qquad (3\text{-}15)$$

Which is also called the Chvorinov's rule, where B is the mold constant equal to:

$$B = \left\{\frac{\rho_{metal}\sqrt{\pi\alpha_{mold}}\left[L_{metal} + C_{metal}\left(T_p - T_1\right)\right]}{2K_{mold}\left(T_1 - T_0\right)}\right\}^2 \qquad (3\text{-}16)$$

Hence, the freezing time is proportional to (volume/area)^2 of the casting or riser. Chvorinov tested this relation for a wide variety of casting shapes and weights and found good agreements.

Material Thermo-Physical property data

The freezing time calculation requires a good knowledge about several process parameters related to the mold and metal thermo-physical conditions.

The ceramic mold material used for this research was kept the same for all our experiments. The molds were made out of alumina powder bound with silica. The thermo-physical properties of the mold are mainly determined by the alumina content, since it makes for more than 95% of the mold material. The alumina material alone can exhibit a wide range of thermo-physical properties depending on the material porosity, trace elements, manufacturing process and others (see appendix B1). The properties, showed in table 3.7, are based on the material which approaches the most our mold material characteristics.

Table 3.7: Alumina mold Al_2O_3 high temperature physical properties.

Al_2O_3 Mold Material Properties	**DATA**
100% dense alumina $\rho_{Al_2O_3}$	3980 kg/m^3
Mold density ≈45% dense alumina ρ_{mold}	≈ 1790 kg/m^3
Specific heat of mold C_{mold} @ 1100 °C	≈ 1255 J/(kg K)
Thermal conductivity of mold K_{mold} @ 1100°C	≈ 1.5 Watt/(m K) App. B1
Thermal diffusivity of mold α_{mold} @ 1100 °C	≈ 6.67x10^{-7} m^2/ s
Melting point of Al_2O_3	2072 °C

* Data from reference 31, 32, 37

In this research, two alloys were used to conduct the various experiments on the molds. First, a tin-lead 60%Sn-40%Pb alloy was used to test prove the molds integrity and dimensions. In fact Sn-Pb alloy is more forgiving in terms of castability compared to our other CoCr alloy because of its low surface tension and melting temperature.

The other alloy is a variation of the alloy ASTM F75 which is a cobalt Co based alloy with other major elements such as Chrome Cr, Molybdenum Mo and others. The F75 is the standard alloy used for the cast orthopaedic prosthesis at Johnson & Johnson Professional Inc. and elsewhere. The real test for this research will to successfully infiltrate the F75 alloy into the intricacies of our surface textured molds.

The following table 3.8 & 3.9, shows the physical properties of both alloys which will allow us to calculate the freezing time of our particular casting.

Table 3.8: Tin-Lead alloy 60%Sn-40%Pb physical properties.

Tin-Lead 60%Sn-40%Pb Metal Properties	**DATA**
Sn-Pb density ρ_{SnPb} (see previous section for calc.)	8472 kg/m^3
Specific heat of SnPb C_{SnPb}	≈ 190 J/(kg K)
Latent heat of fusion SnPb L_{SnPb}	≈ 45x10^3 J/kg
Melting point of SnPb T_{mpSnPb}	230-250 °C
Superheat temperature range of SnPb $T_{SH,SnPb}$	270-450°C

Table 3.9: Cobalt based alloy F75 high temperature physical properties.

ASTM F75 Metal Properties	**DATA**
F75 density ρ_{F75} (see previous section for calc.)	7370 kg/m^3
Specific heat of F75 alloy @ 1200 °C	≈ 750 J/(kg K)
Latent heat of fusion F75 L_{F75}	≈ 312x10^3 J/kg
Melting point of F75 T_{mpF75}	1315-1345 °C
Superheat temperature range of F75 $T_{SH,F75}$	1425-1595°C

Most alloys physical properties seen above could be found directly in metal handbooks except for the latent heat L_{metal}. The latent heat L_{metal} is the energy absorbed or released by a material at its melting point while no real temperature change occurs in the material. This energy can also be defined as the excess enthalpy necessary to be remove in order to make the transition from the liquid to the solid phase. The heat content of a material is termed its enthalpy H [Joule/kg]. The total enthalpy of m_i kilogram of material i is:

$$(H_i)_{total} = m_i H_i \qquad (3\text{-}17)$$

For a mixture of materials, the total enthalpy is the sum of the individual enthalpies:

$$H_{total} \equiv \sum_i m_i H_i \qquad (3\text{-}18)$$

This latter expression represents a rough estimate of the enthalpy of a mixture of material. However, since the elements of our mixture (Co, Cr, Mo elements 27, 24, 42) are in the same region of the periodic table, they have similar individual latent heat. This means that the attraction forces between individual elements which define the latent heat are also within the same order of magnitude (see table 3.10).

Therefore, the total latent heat of fusion L_{metal} of an alloy can be roughly estimated by summing the proportional effect $\Delta H_{i,fusion}$ of each element forming the alloy:

$$L_{alloy} \approx \sum_i m_i \, \Delta H_{i,fusion} \qquad (3\text{-}19)$$

The latent heat L_{F75} and L_{SnPb} were then determined from the value of Table 3.10.

Table 3.10: Enthalpy of fusion of pure metals.

Pure metal sample	Latent heat of fusion $\Delta H_{i,fusion}$ x10^3 J/kg
Cobalt Co	275
Chrome Cr	404
Molybdenum Mo	390
Iron Fe	247
Nickel Ni	298
Manganese Mn	235
Tin Sn	59.2
Lead Pb	23.0

Data from: CRC Handbook of Chemistry and Physics,
David R. Lide, 76th edition 1995-96, p. 12-172 & 12-173

For example the estimate latent heat of fusion of 60%Sn-40%Pb would be:

$$L_{Sn-Pb} \approx 0.6 \times 59200 + 0.4 \times 23000 = 45 \times 10^3 \frac{Joule}{kg}$$

Calculation example

For example, say we are casting a small smooth surface cylinder 9 mm in diameter and 20 mm long (no surface texture) with our F75 alloy. First we need to determine the volume and surface of the internal cavity of the mold which will form our small cylinder. Then we need to determine the level of superheat we want to give to our metal to be poured. Finally using the properties as tabulated above we calculate the freezing time t_s to be:

$$A = 5.65 \times 10^{-4} m^2$$

$$V = 1.27 \times 10^{-6} m^3$$

$$T_p = T_{SH} = 1510°C$$

$$T_0 = 600°C$$

$$B = 4.33 \times 10^6$$

$$t_s = 4.33 \times 10^6 \left(\frac{1.27 \times 10^{-6}}{5.65 \times 10^{-4}} \right)^2 = 21 \text{ seconds}$$

To complete our example, if macro-texture is added to the mold surface, than the surface area A will be typically increased 2 to 3 fold for a new A = 1.7x10^{-3} m^2 while the volume V slightly decreases by about 10% to V=1.14x10^{-6} m^3.

$$A = 1.7 \times 10^{-3} m^2$$
$$V = 1.14 \times 10^{-6} m^3$$
$$T_p = T_{SH} = 1510°C$$
$$T_0 = 600°C$$
$$B = 4.33 \times 10^6$$
$$t_s = 4.33 \times 10^6 \left(\frac{1.14 \times 10^{-6}}{1.7 \times 10^{-3}} \right)^2 = 2 \text{ seconds}$$

The fact of adding surface texture expand the surface area A of the mold cavity and slightly reduce the volume. This translates into a faster cooling rate which may produce cold shuts if the wrong process is selected of if casting parameters are not controlled properly. Some experiments will describe this effect in the section 3.2.6.

Chvorinov's rule assumes a 1 dimensional heat transfer problem, which is not the case when thin 2D features are on the inner surface of the mold. However, it is not our intent to calculate exactly the freeze time of the casting. Instead, we are interested in the bulk freezing time of the entire casting which we believe has a direct proportional relationship to the mold filling capabilities.

3.2.6 Casting parameters and their effect on castability

Introduction

Casting thin-section molds involves compromising about the casting conditions which will provide adequate surface and microstructural properties, and casting reliability. In fact, casting parameters used to promote a desirable design characteristics often conflict with another desired effect. The following sections present the complexity of deciding which casting conditions shall be used, since all the parameters are somehow interrelated.

Superheat temperature

Because the concept of "superheat above the freezing point" provides an approximate index of fluidity for many commercial alloys, it should be possible to use any one of a variety of alloys to pour the same casting satisfactorily, simply by maintaining constant superheat above the respective freezing points. This has been adequately proved commercially. It should be emphasized, however, that variation in pouring techniques or gating must be taken into account. For example, a drossy metal (easy to oxide metal such

as aluminum or titanium) with an elaborate gating system must naturally be poured with a greater superheat.

To determine the proper pouring temperature for a new casting, i.e., one which has not been poured in any alloy, a pilot casting is necessary. The following empirical rules apply to the selection of test temperatures:

1- For fairly intricate castings of light sections (1 cm. and under), test temperatures are usually from 167 to 278 °C above the liquidus.

2- For heavy castings such as machine bases, the range is 56 to 167°C above the liquidus.

The pouring temperature of an alloy is determined partly on the basis of the thickness of the section to be poured. Metal is usually poured at the lowest possible temperature, to reduce the likelihood of casting defects from gas, dross, metal-and-mold reaction, and other deleterious effects that depend on temperature and time at temperature. However, in pouring thin sections, it is often necessary to increase pouring temperature, in order to prolong the time interval between pouring and solidification.

Mold material and its surface characteristics

The higher the thermal conductivity of the mold and the rougher its surfaces, the lower the fluidity of the molten metal becomes. Heating the mold improves fluidity, however it slows down solidification of the metal which generates coarser grains in the casting and lower strength.

Friction between molten metal and mold may seriously hinder mold filling. It becomes increasingly troublesome as the ratio of mold surface to metal volume increases, a condition that is characteristic of thin-wall castings. A high ratio promotes premature freezing in thin sections.

Mold permeability

Mold permeability partially provides for the release of entrapped gases and play an important part in the determination of wall thickness. If the permeability is too low for the amount of gas present, a gas seam or gas lock can result. In addition, but less common, the high density (low permeability) mold extracts heat from the metal more rapidly and may set the casting before the mold is filled.

3D printed molds exhibit high permeability since the molds are between 50% to 65% porous. This high permeability combined with a rather rough surface, compared to lost-wax casting, make the casting subject to oxidation and fusion. (see next section for fusion)

Mold temperature

Usually, a cooler mold results in a better casting surface finish, because of the faster freezing of the metal skin and the elimination or at least reduction of chemical reactions that may take place at the interface of the metal and the investment. However, this same cooling effect reduces the chance of filling extremely thin sections. Consequently, it may be necessary to relax the surface finish requirements in order to obtain the thin wall desired.

Minimum mold section

Published rules and suggestions regarding the minimum thicknesses to which cast sections can be designed are in conflict, because they are based on different points of view. Some tables are intended to prevent an increase of casting cost because of thinner section. Others consider the actual limits of the process, rather than cost, but often fail to define the applicable processing conditions.

Because so many aspects of design (such as the area of thin-wall section, its proximity to a gate, and the availability of heavy sections to conduct molten metal to it) have an influence on the actual minimum wall obtainable for any particular casting, recommendations have limited usefulness when applied to a specific part. They do, however, provide the casting designer with a starting point, by familiarizing him with minimum thickness that normally can be produced efficiently.

In designing for minimum wall thickness, the fluidity of the alloy and its ability to flow in the mold are important considerations. Of almost equal importance is the solidification range of the alloy in relation to proper feeding of a section. The surface area of exposed molten metal and the feeding distance are also important in determining the castability of thin sections.

Table 3.11 shows typical minimum-wall-thickness relations for a tube 1.5 in. long produced from various metals by investment casting.

Table 3.11. Typical Minimum Section Relations for a Tube 1.5 In. Long Produced from Various Metals by Investment Casting

Metal	Min. wall, mm
Carbon steel	1.5
Series 300 stainless steel	1.25
Series 400 stainless steel	1.65
Aluminum alloy	1.25
Magnesium alloy	1.25
Aluminum bronze (10% Al)	1.5
Beryllium copper	1.0
Cobalt-chromium alloy	1.25

From "How to Design and Buy Investment Castings", Investment Casting Institute, 1960, p.132

These recommendations reflect the experience of the industry as a whole. Although these minimum thicknesses may be subject to modification, the relative mold-filling capabilities of the different metals will remain as indicated in the table.

Pouring speed and metal head

The slower the rate of pouring the molten metal into the mold, the lower the fluidity becomes because of faster rate of cooling. On the other hand, if the rate of pouring is too high the metal flow may become turbulent and entrap gas which creates undesired porosity in the casting. Furthermore, if fine features, such as a thin core or texture, are being poured, high flow velocity may break those mold features.

The higher the metal head or mold pressure, the more probable metal penetration can occur. The metal head should be determined based on the minimum section-thickness in the mold. The smaller the section, the higher head of metal needed.

Factor affecting the fluidity

Fluidity depends on two major factors: the intrinsic fluid properties of the molten metal and casting conditions. The properties usually thought to influence fluidity are viscosity, surface tension, the character of the surface oxide film, inclusion content, and manner in which the particular alloy solidifies.

Casting conditions that influence fluidity include the mold configuration, physical measures of the fluid dynamics of the system, such as liquid static pressure drops, mold surface characteristics, heat flux, rate of pouring, and degree of superheat.

Gating

The gating system is the conduit network through which liquid metal is delivered to the mold. For example, gating design can be used to control the mold filling time and as a result minimizing metal turbulence and mold erosion.

The gating system should be designed such that the metal never splatters inside the mold. For example, if the diameter of the entrance of the mold is small in proportion to the volume of metal that must pass through it. Thus, the metal can break into separate streams and trickled down to various points on the periphery of the plate section. Such separated streams oxidized rapidly and resulted in misruns, cold shuts, and "BB shot". (The BB-shot defect refers to drops of molten metal that separate from the main body of fluid metal, freeze prematurely, and fail to fuse with the main body of metal on recontacting it). A possible solution is to redesign the gating system and make reservoir or place the ingate at the bottom of the mold cavity. In this way the splashing and oxidation accompanying top gating are avoided.

Risers

Riser size is determined by two factors: first the freezing time of the riser must exceed that of the casting, at least to some extent, and second, the riser must supply sufficient feed metal to compensate for the liquid-to-solid shrinkage.

Summary

Here is a simplified list of casting conditions which should guide our casting investigation of thin-section surface macro-texture casting.

- The lowest superheat T_{SH} should be used: as the freezing time permits.
- Mold temperature chosen according to the required grain size within the limits assuring good metal fluidity.
- Keep the metal pouring rate at the lowest end to prevent porosity and mold damage.
- The head of metal should be the minimum required to fill thin cavities and prevent metal penetration.
- Packing density of mold powder should be maximized to prevent metal penetration and oxide fusion.
- Design of the mold thin-section geometry should respect the basic rule of heat transfer otherwise cold shuts will occurs.
- others...

3.2.7 Casting defects

Here is some definitions of terms used in the previous section.

Misruns and cold shuts

A misrun casting is one which lacks completeness due to failure of the metal to fill the mold cavity. There may be a smooth round-edged hole through the casting wall or one or more extremities may be only partially filled out. A cold shut casting is one in which a definite discontinuity exists due to imperfect fusion where two streams of metal have converged. This defect may have the appearance of a crack or seam with smooth, rounded edges.

For example, if the metal section is too thin for the area involved, freezing may occur before the metal had the time to fill the entire cavity. Such failure mode can be prevented by taking into account the laws of metal flow and solidification. If the designer cannot thicken the section, the only recourse is to increase melting and pouring temperature or modify the chemistry to develop better metal fluidity.

Fusion

Many metal oxides have an affinity for silica and react with it at relatively low temperature. The fusion of oxide and silica results in rough finish which requires additional cleaning. If fused oxide-silica system penetrates into the mold, then ceramic grain can be trapped in the metal matrix. Design is a contributing factor as well as mold surface roughness. For example, contributing factor are sharp corner, overhang or protruding sections, thin core when they are surrounded by a heavy metal section. If the surface is bruised, rough, abraded, or loose, an abnormal fusion or penetration can also result.

Since fusion is a temperature related chemical reaction, the speed of reaction increases as temperature increases. A design which creates an unusually high temperature in any part of the core or mold will produce maximum fusion tendency.

Any condition that promotes excessive porosity of the mold surface can cause fusion. Low density ceramic mold caused by improper distribution of the grains increase the ease with which the metal oxide can adhere to the ceramic surface. Such low density mold are also characterized by high permeability since density and permeability are related. Low fluidity and/or low moldability will result from mold porosity which, in turn promotes ready access to the metal oxides during pouring and solidification.

Hot tears

Hot tears are another form of metal unsoundness developed during or at the end of freezing in the casting. Some casting alloys have little tendency to hot-tear, whereas others hot-tear easily. Contraction stresses produced by resistance of the mold or other portions of the casting may becomes large enough to cause rupture (tearing) of the casting. For example, if a reduced section is connected to a bulky one by a gradual section transition, as opposed to abrupt, the tear might not occur. The incidence of tearing is reduced by having uniform distribution of metal thickness. Hot tears are common to the higher carbon (>0.40 wt%) cobalt alloys and can be avoided with alloy chemistry adjustments, less rigid mold materials, and slower cooling rates from the casting temperature. Wrapping molds in selected areas with an insulating material often reduces hot tears and without altering the solidification of the total system.

Other sources of metal oxidation

Oxidized metal may be a direct result of the melting procedures or furnace practice. This includes possible oxide pickup from refractories and the obvious effects of excessive oxygen and/or excessive humidity at elevated temperature.

3.3 Exploring potential high temperature pouring processes

The casting research effort is to investigate promising pouring processes and determine which one will provide the best cast surface texture quality. The quality is based on the capability of the process to fill the sub-millimeter cavities forming the surface macro texture of the mold. The standard processes (described in section 3.1.1) as well as casting conditions were proven unsuccessful to cast very small features reliably. Therefore, the challenge is to push further the limits of standard casting processes and conditions in order to cast successfully fine surface textures.

Because of cost concerns, only a few promising casting process will be evaluated. But first, we should list and describe existing or experimental processes which could meet our requirements based on their individual characteristics.

3.3.1 List of potential casting techniques

First, the easiest way to cast our 3D printed mold would be to used the conventional open **air melting** & crucible tilting method since the equipment is already available. This method is possible since the ASTM F75 alloy does not contain reactive elements such as titanium, aluminum, tantalum,.. To reduce slag and oxidation, the melt could be done under **controlled atmosphere** where an inert gas is constantly iniected in the melting chamber. A derivative of this technique is to conduct the melting and pouring under complete **vacuum atmosphere.** This latter technique although more complex and expensive would minimize the effects of oxidation and trapped gases in the mold cavities.

If mold filling is problematic, **centrifugal casting** could be used in order to increases the metal head and break the metal surface tension. With centrifugal casting however casting conditions such as metal temperature and mold temperature are difficult to control. Another casting method which create an increased metal head is the forced **vacuum casting**. This process also know as counter- gravity casting creates a vacuum in the mold and sink the mold upside down into the crucible in order to fill the mold. This method is superior than many other casting techniques such as centrifugal concerning the controllability of the casting conditions.

Finally, an experimental casting method involving the **vibration** of the mold inside a conventional air-melt casting technique may improve the castability of thin section. In this case, vibration would be used to break the metal surface tension instead of using a higher

metal head. Although vibration casting as potential, there is concern whether it would damage fragile thin mold sections.

Beginning in section 3.4, casting experiment on 3D printed mold will be described in details. The used of some of the latter processes was evaluated in order to determine the appropriate casting method which will yield casting with accurate surface macro-textures with good reliability.

3.4 Experiment with standard investment casting methods

The first set of experiments were developed to verify the castability of a textured mold with standard air-melt casting process.

3.4.1 Experiment #1: tin-lead

Tin-lead alloy was used first to test proof the integrity of the 3D printed molds. Because of its low melting point and ease of use, we were able to perform several trials to get the conditions right. Two casting configurations were used in this experiment (see figure 3.9): flat texture on a circular disk and texture wrapped around a small diameter cylinder.

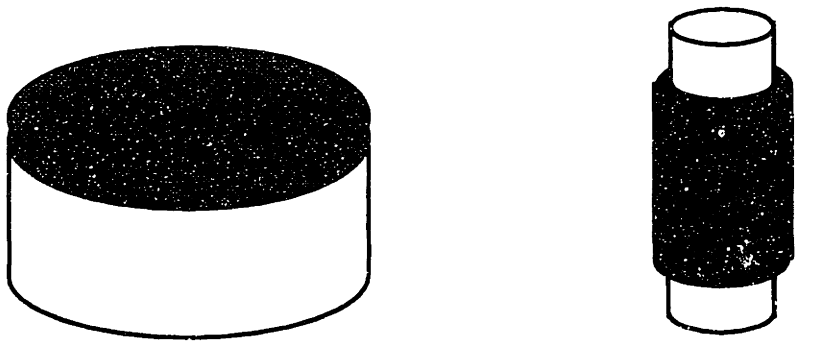

Figure 3.9: Casting designs for the pull test part and dog implant with texture location showed on shaded area.

In the first configuration, the surface texture was located at one end (see gray area on figure 3.9) of a 22mm (7/8") diameter x 10mm high disk. This configuration was used to generate the samples for the mechanical pull test experiment described in chapter 1. Most of the casting experiments were done with identical surface texture as showed in figure 3.17.

In the second configuration, the surface macro-texture was wrapped around a cylinder to form a 9mm diameter x 20mm long casting. This casting has the required dimensions for the dog implant the in-vivo texture evaluation. The texture used in this case was a simple mesh (as showed in figure 3.17)with 350μm pore size, which had a casting difficulty level comparable to our other texture geometry.

The molds were arranged for pouring as showed in figure 3.10; the sprue and gate were built along the same axis and the mold was located right at the end of the assembly.

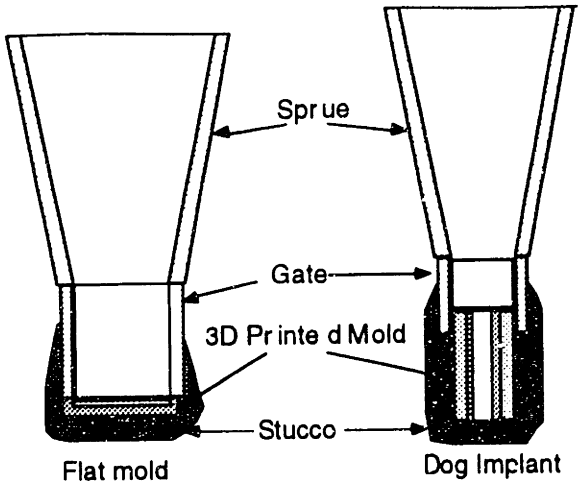

Figure 3.10: Gating assembly for both mold configuration.

Casting conditions

The experience was performed with rudimentary equipment. The metal was melted inside a small graphite crucible by a band heater located around the periphery of the crucible. The metal superheat temperature was controlled by a PID closed loop temperature controller within ± 20 °C. On the other hand the mold temperature was roughly preheated by a propane torch. The initial casting conditions were then:

Superheat temperature	$T_{SH} \approx 300°$ C
Mold temperature	$T_0 \approx$ range between 25° to 600°C (no exact value)
Flat mold volume	$V_1 \approx 1.9 \times 10^{-6}$ m^3
Flat mold surface	$A_1 \approx 7.25 \times 10^{-4}$ m^2 (smooth)
	$A_1 \approx 1.4 \times 10^{-3}$ m^2 (with texture)
Dog implant volume	$V_2 \approx 1.27 \times 10^{-6}$ m^3
Dog implant surface	$A_2 \approx 5.65 \times 10^{-4}$ m^2 (smooth)
	$A_2 \approx 2.12 \times 10^{-3}$ m^2 (with texture)

According to the minimum pore size (350 μm, R_m = 175 μm) the metal head H_m required to fill the pore with tin-lead should be ≈ 8 cm (or 3 inches) according to equation 3-6.

The metal freezing time (eqt. 3-15) for the flat mold configuration should vary between 3 to 5 seconds when no mold preheat is performed ($T_0 \approx 25°C$) and up to several minutes when mold is 200°C and over (minimum $T_{SH} = 300°C$).

The case of the dog implant is different since the particular geometry would make the metal freeze time to 0.5 second when no mold preheat is applied ($T_0 \approx 25°C$) and 28

seconds for $T_0 \approx 200°C$ and $T_{SH} \approx 300°C$. A decent freezing time value of about 5 seconds would be obtained for $T_0 \approx 175°C$ and $T_{SH} = 300°C$. Since the mold temperature is difficult to controi, another possibility would be to avoid preheat and increase the superheat T_{SH} to a value of about 500°C. However, this temperature is out of the range of our set-up capabilities.

(Tin-lead) Flat texture results

The first tin-lead casting of the flat surface was done for:

-metal head $H_m = 10cm$ (4inch)
-superheat $T_{SH} = 300°C$
-no mold preheat $T_0 = 25°C$.

The casting resulting from such casting conditions were not satisfactory. The metal was penetrating in only 1/3 of the mold cavities. It seemed that the metal front was freezing prematurely, preventing the metal from penetrating in the small cavities. Our estimate freezing time of 3 seconds proved to be insufficient. The value 3 seconds is the estimate freezing time of the entire casting. Hence, we should presumed that the freezing time of the metal front which defines the surface texture is some value shorter. However, the freezing time of the entire casting is a good indicator in order to compare two different casting conditions.

After several trials and errors, the casting conditions which gave us a good yield was the following:

-metal head $H_m = 12$ cm (5 inch)
-superheat $T_{SH} = 300°C$
-mold preheat $T_0 = 80\text{-}140°C$. estimate

The mold preheat would give us a metal freezing time varying between 5 to 7 seconds. This figure is not exact since the temperature of the mold could not be determined exactly. The slight increase in the metal head H_m was necessary to prevent defect which appeared randomly on the textures. Figure 3.11 shows an example of a successful tin-lead cast of the "Velcro" surface texture.

Figure 3.11: Successful tin-lead "Velcro" macro-texture. casting

(Tin-lead) Dog implant results

Because of its geometry, the dog implant was very difficult to cast without any defects. Out of dozens of attempts to cast the dog implant, only one trial succeeded and could not be repeated. The good casting was achieved for the following extreme conditions:

- metal head H_m = 30 cm (≈12 inch)
-superheat T_{SH} = 450° C
- mold preheat T_0 = 80-140°C estimate

It appeared that the right casting conditions for the metal head H_m, superheat temperature T_{SH} or mold temperature T_0, were out of the limits imposed by our equipment. If the mold preheat temperature was too high combined with elevated superheat temperature, the metal would penetrate between the ceramic grains of the mold. On the other hand, if the preheat was kept low (T_{SH}≈ 250-300°C), then the mold would not fill.

Two solutions to solve the problem were considered:

1) One, to prevent metal infiltration the metal had to freeze rapidly. Therefore the superheat temperature T_{SH} should be kept low. This action would decreased also the fluidity of the molten metal as well. As a result a higher head would be necessary to push

the metal inside the mold cavity. However, our actual set-up could not provide a higher metal head H_m.

2) Second, low superheat temperature T_{SH} and low head H_m are adequate to fill 350µm pore size as seen in the case of the flat mold. However, the way the gating system delivers the metal to the dog implant casting might be at fault. In fact, because of the very small section of the dog implant mold, the metal may become turbulent and splatter into drops which produced an accelerated cooling rate of the metal front. Therefore, the problem might be fixed by modifying the gating system.

The first solution was tested in section 3-5 by increasing the metal head using centrifugal casting. Additional experiments were also done to verify if metal oxidation would create a skin effect at the metal front.

The second affirmation was tried in the next experiment with cobalt chrome alloy this time. Although it is a different metal then tin-lead, as we will see the results were similar.

3.4.2 Experiment #1.2: cobalt-chromium

The same experiment as in 3.4.1 was performed with the F75 alloy at the Johnson & Johnson facilities. The metal was melted in a crucible surrounded by a controlled inert gas atmosphere. Pouring was done by a conventional tilt crucible design.

According to equation 3-6, the required metal head of F75 alloy necessary to fill a 350 μm cavity is about ≈30 cm (12 inches). The exact casting conditions, although proprietary, are in the vicinity of the following values:

-metal head $H_m \approx 30$ cm
-superheat temperature $T_{SH} \approx 1510°C$
-mold temperature $T_0 \approx 600$ and 750°C

(F75) Flat texture results

According to equation 3-15 for the above data, the freezing time of the flat texture should be around 8 seconds. Based on our experience with the tin-lead casting this number seemed suitable. As a matter of fact it was, since most of the flat texture casting came out with very good quality. Only a few castings (5%) had to be rejected which is a sign that the casting conditions were favorable. SEM pictures of all the textures cast with those casting conditions can be seen in chapter 2, figure 2.2 to 2.9.

(F75) Dog implant results

The same casting conditions as above were used for the dog implant as well. The freezing time in this case is a mere 1.5 seconds (based on above data), which is not a good sign to start with. Our concerns were quickly confirmed since the results were as disastrous as in the case of the tin-lead casting for identical molds.

The metal head H_m was then increased to as high as 36 cm without any success. As mentioned earlier, the gating design may be the source of the problem. Two gating design were then developed to attempt solving the problem (see figure 3.12).

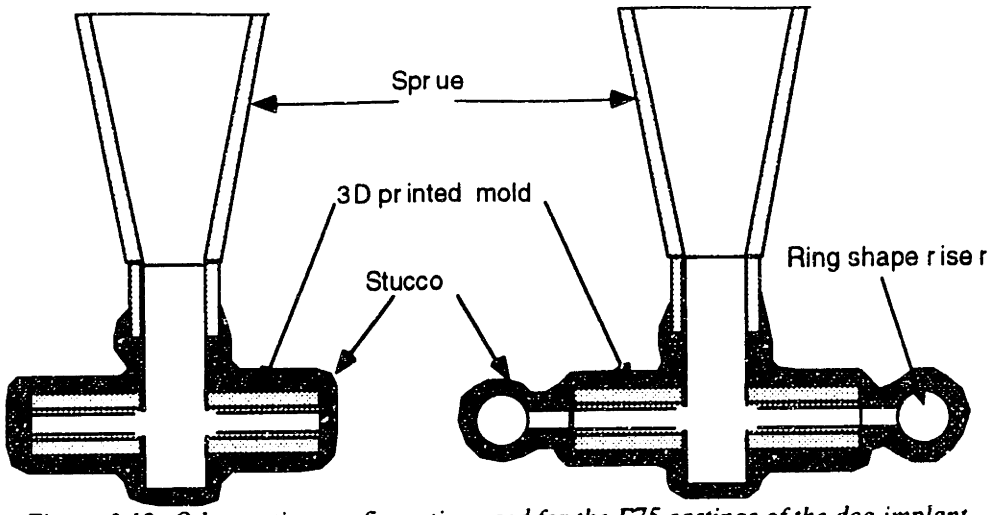

Figure 3.12: Other gating configuration used for the F75 castings of the dog implant.

One of the design was developed in order to decrease the turbulence of the metal flow as it enters the textured mold (see figure 3.12 left). The other one was designed to reduce turbulence as well but also to increase slightly the freezing time (riser effect) and allow an escape route for hot gases. The concept was to create a ring connecting the four molds, inside which all the metal front would meet.

Both designs were cast with values of H_m of 20 and 36 cm without any more success. The metal would freeze too quickly. Those results could be interpreted as followed:

i) the metal front forming the texture was freezing even before the pouring was completed. Therefore the pressure did not have the time to build up inside the mold.

ii) High superheat and mold preheat are needed to increase the freezing time.

Observation i) suggest that the pouring method as well as the gating design should be revisited. It would involved testing other casting technique described in section 3.3. Moreover, since the experiment was done on a production casting unit, the metal superheat T_{SH} and the mold preheat could not be modified at will.

3.5 Experiment with centrifugal CoCr casting method

This experiment was to focus on creating complete F75 dog implant casting only, since the flat texture could be cast with the standard casting methods. Three different experiments addressing three different casting issues were designed to find the cause of our casting defects.

#2.1 Higher metal head H_m and higher mold preheat
#2.2 Different gating, higher head and mold preheat

These casting methods allowed more flexibility over the choices of different casting conditions. However, we shall say beforehand that this particular centrifugal casting equipment did not allow a precise control over the casting parameters. Nevertheless, we will try to get the best results according to the circumstances.

3.5.1 Experiment #2.1: Higher metal head

This experiment was designed to evaluate the effect of increasing the metal head to an extreme on the mold filling. The mold preheat temperature was also a variable considered in the experiment. The goal was to determine if for a minimum mold preheat, extreme metal head alone could fill the thin surface texture cavities. The following casting conditions were used:

- metal head rotation adjusted to create 50g and 100g on the casting. Those values are equivalent to about 50 cm to 100 cm of metal head inside the mold.
- mold preheat $T_0 \approx 750$ and 950°C
- metal superheat $T_{SH} \approx$ 1450-1500°C (rough)

To prevent metal infiltration, the superheat temperature T_{SH} was kept to a minimum. In any case the superheat temperature must have been on the low end, since the metal had to sit a few seconds in the crucible before being forced in the mold. The mold preheated at $T_0 \approx 750$°C had a estimate freezing time of about 2 seconds and for $T_0 \approx 950$°C of 5 seconds.

The casting process generated several rejects for both mold preheat temperature and metal head. It was found that 100g was damaging the fine texture on the mold as the metal

hammered the mold at high velocity. However, a few runs at 50g generated almost complete casting with very few defects for both mold preheat temperatures. In all cases, no metal penetration could be observed on the surface of any casting produce with the metal superheat temperature $T_{SH} \approx 1450\text{-}1500$ °C. Even though the casting were not perfect, it was still the best casting we had produced up to this point. Figure 3.13 shows one of these castings; notice the discontinuities in the mesh of the texture.

The reason for these defects was believed to originate from two probable effects:

i) cold shut due to fast cooling rate,

ii) or thin undercut cavities were filled with loose powder which was not removed by the powder removal process.

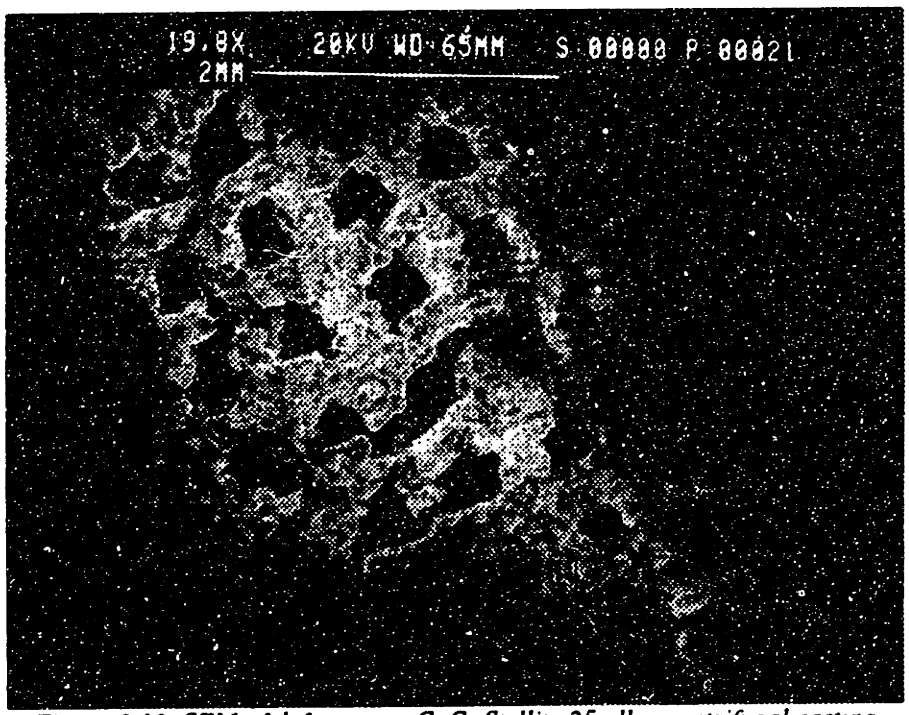

Figure 3.13: SEM of defects on a CoCr Stellite 25 alloy centrifugal casting.

A closer inspection of the shape of the discontinuities could lead us to the cause of casting defect. If the metal front shows a rough surface with multiple peaks, this could means the defect is due to powder that was trapped in the mold cavity. If, on the other hand, the metal front is smooth and spherical it means the cooling rate must have been to fast and a cold shut was generated. Figure 3.14, shows an enlarge view of one of these defects.

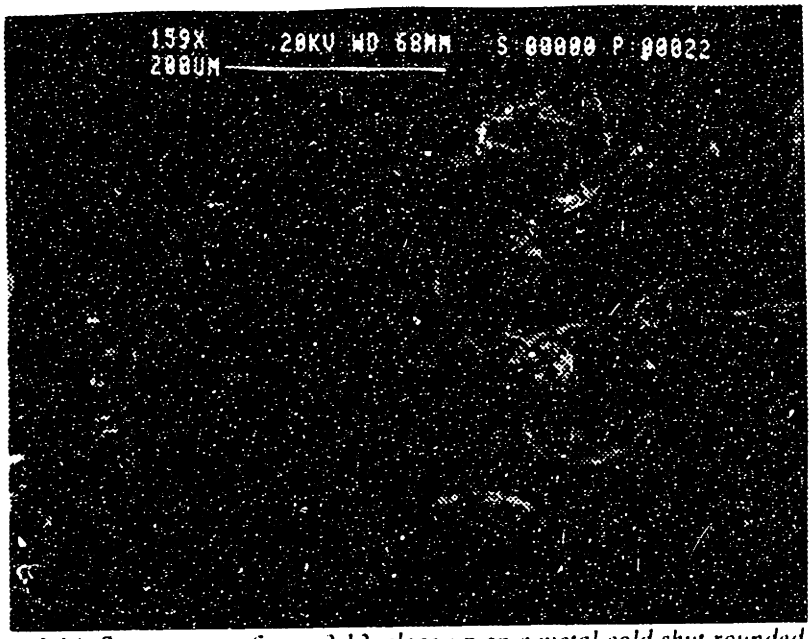

Figure 3.14: Same part as figure 3.13, close-up on a metal cold shut rounded edge.

We can see very quickly that the metal front is spherical which suggest an excessive cooling rate.

From those observations, we can conclude that pressure alone can not be used to force the molten metal inside the small cavities because of the mold limited strength. The next experiment is to evaluate if for similar conditions as in this case, we can counteract the short freezing time by improving the gating design.

3.5.2 Experiment #2.2: Different gating design

Only one gating design was investigated in this experiment (see figure 3.15). The gating was arranged such as it would significantly slow down the metal velocity just before it enters the mold. The metal would then enter the mold in a more laminar fashion and may improve the casting overall quality.

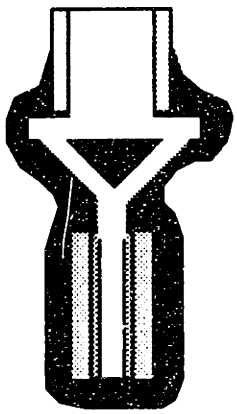

Figure 3.15: Proposed gating design for the centrifugal casting process.

The same casting conditions as in experiment #2.1 were used without any more success. The casting showed similar defects which could be attributed to accelerated cooling rates.

Crucible contamination of the alloy was also pointed out as a potential source of casting defect. The crucible could in fact react with the metal to create inclusion or other chemical constituents which could affect the fluidity of the alloy. But since the same phenomenon could be seen for different crucible material, the contamination problem was ruled out.

3.5.3 Summary

In summary, we can conclude from the two last experiments that:

1) Metal head should be kept on the high end in order to fill the mold with relatively low metal superheat. This method would limit metal penetration because a metal skin would form faster on the surface of the mold.

2) Pouring technique can have a beneficial effect on the final casting results. In fact, the method to fill the mold with centrifugal casting seemed to give superior results for the specific case of the dog implant. It would seem that a faster pouring rate improves the chances of success.

3.6 Experiment with counter-gravity casting

3.6.1 Introduction

Counter-gravity casting (see figure 3.16) is known as an excellent method of filling thin sections. The counter gravity casting process starts by inserting a ceramic shell assembly inside a air tight chamber. The inverted sprue of the mold assembly is then dipped directly in the heart of the crucible. The vacuum created inside the chamber, pulls up the molten metal inside the mold cavities.

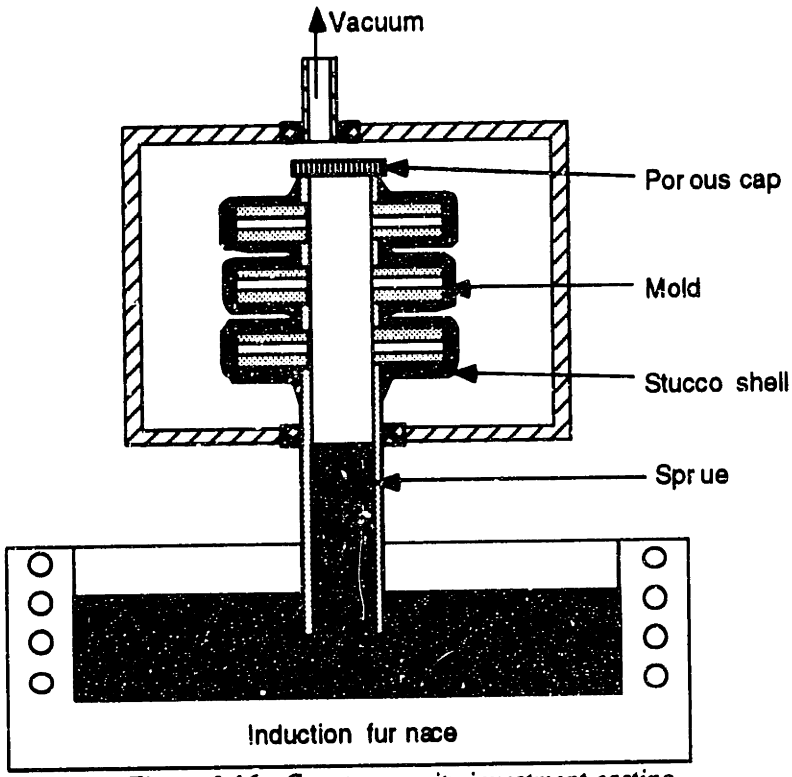

Figure 3.16: Counter gravity investment casting.

The metal superheat temperature is usually kept very low such that metal solidification begins within a fraction of a second. This last detail is very important to prevent metal penetration through the pores of the ceramic mold. The ceramic shell material (stucco) is produced almost similarly then for conventional investment casting. The only small difference is related to the actual pore size and porosity of the stucco shell which were optimized for this specific process.

3.6.2 Experiment #3.1: Counter-gravity casting of CoCr dog implant

Goal

The goal is still to produce dog implant casting without any defect. To achieve this goal we need to fill the small cavities of the mold without any misrun or cold shuts. Another issue that came out from the previous casting experiment was about the oxidation on the casting surface. Therefore, this experiment will attempt to compare the oxidation level for different superheat temperature and with or without protective atmosphere.

The equipment used in this experiment was provided at the production facility of Hitchiner gas turbine division.

Casting parameters

Except for the metal superheat temperature and atmosphere control, we had to rely on standard parameters predetermined by Hitchiner's proprietary look up table. Parameters such as vacuum level and hold time and mold temperature were determined based on the casting sizes and metal superheat values.

The fixed casting parameters involved in the Hitchiner standard procedure were:

-Mold @ constant temperature ≈ 1120°C ± 20°C (2050 F) for 1 hour

-Vacuum procedures:

Step #1: Vacuum level for 2 to 2.5 s ≈ 20 in-Hg (66.7 kPa)

Equivalent metal head H_m: ≈ 47 cm (19 inch) of F75

Step #2: Vacuum level for 90 s. ≈ 15 in-Hg (51 kPa)

Equivalent metal head H_m: ≈ 70 cm (28 inch) of F75

Two vacuum levels were used to fill the mold. The first one, shorter and more gentle, is used to bring the metal front in or near by the mold cavities. The second vacuum level, 25% lower, is applied for a longer period in order to give enough time to the metal to solidify in the mold but not in the sprue. The rational behind the two vacuum levels is to minimize the metal front velocity as it enters the mold. This procedure would prevent mold damage due to excessive impact of the metal on the mold walls.

Note, the vacuum equivalence in cobalt-chromium metal head H_m for standard pouring technique are much higher then the expected 30 cm. This suggest that the metal fluidity is expected to be low.

Five distinct casting conditions were tested with the counter-gravity casting process. The conditions can be read as followed:

- Metal superheat temperature T ± 10°C:

Exp #3.1a	1535°C (2800 F) cooled in air
Exp#3.1b	1510°C (2750 F) cooled in air
Exp#3.1c	1535°C (2800 F) cooled in protective atmosphere hexamine (MgO)
Exp#3.1d	1510°C (2750 F) cooled in protective atmosphere hexamine (MgO)
Exp#3.1e	1482°C (2700 F) cooled in protective atmosphere hexamine (MgO)

Using equation (3-15) the freezing time estimate varies between 15 and 18 seconds. According to the freezing time seen previously those ones seemed quite high.

Once the molds were cast, they let cool down in two different manner: air cooled and a "so-called" controlled atmosphere of hexamine. The hexamine protective atmosphere was created by enclosing the mold underneath a bell-shape cover and burning hexamine to deplete the air of its oxygen. The procedure is supposed to reduce the oxidation of the castings.

Casting results

The dog implant casting came out with very good quality (see figure 3.17). Few castings had to be rejected (5%) because of cold shuts, misruns or mold damages. The superheat range as well as the protective atmosphere did not have any effect on either the casting quality nor the level of oxidation (see results in Appendix B2). In fact, a greenish chromium oxide layer could be seen on almost every casting produced.

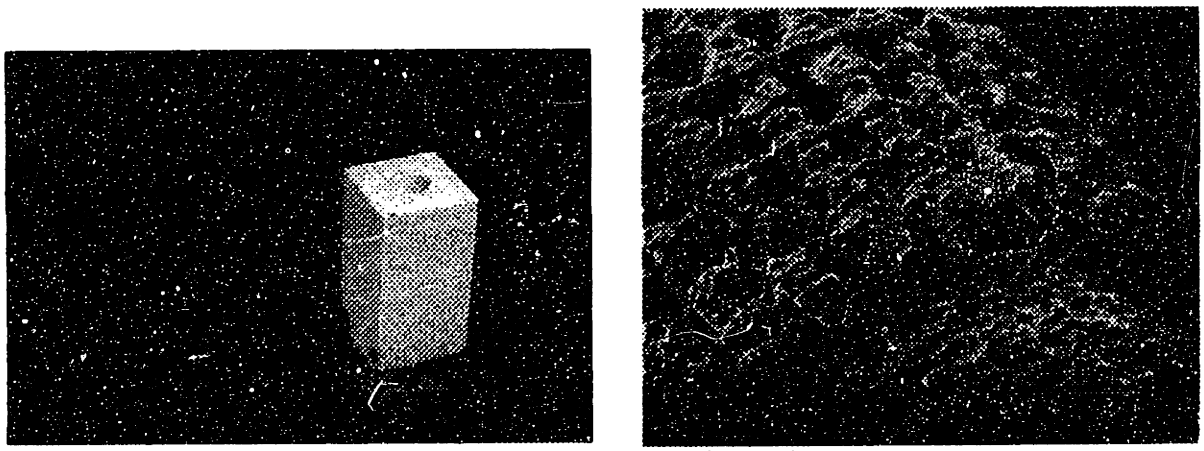

Figure 3.17: CoCr casting of dog implant.

Although the quality was high, most casting exhibited some minor flaws such as metal penetration and mechanical grain pick up. The metal penetration could be expected since the freezing time and metal head were quite substantial. However, since the occurrence of metal penetration is low, decreasing the metal superheat by 10-15°C and the vacuum level as well should solve the problem.

On the other hand, grain mechanical picking was more generalized to all the casting. Two causes of mechanical pick up were presented earlier in this chapter: high metal head combined with loose packing density, and fusion of the metal oxide on the ceramic grain. Both causes are likely to occur according to the casting condition we used. The common factor of both is that they originate from the roughness of the mold surface finish (see section 3.2.4 ,3.2.6 and 3.2.7).

The corrective measures to prevent grain picking is to reduce the surface roughness of the mold. Several options could be investigated to reduce the surface roughness and improve packing density of the mold. Current research is done on improving packing density by evaluating the use of bi-modal grain size distribution or different powder shapes such as spherical.

A promising solution is to post-dipped the 3D printed mold in diluted slurry of refractory material. On top of improving the surface finish of the molds, this technique could be used to strengthen the bonds between the ceramic grains. This post-dipping procedure could be in fact the equivalent of the prime coat used as first layer on investment casting wax pattern.

The methods to solve the mechanical picking problem will not be discussed any further in this research since it involves creating new mold material systems. However, post-processing surfacing methods applied to the casting in order to make up for the problem were covered in section 3.7.

3.6.3 Experiment #3.2: Estimate casting limits with counter-gravity casting

Another experiment was designed to determine a safe range of mold and casting dimensions within which surface texture could be produced accurately and repeatedly for our particular material system; i.e. 3D printed alumina mold and ASTM F75 alloy. Two major questions needed to be answered:

- Can metal infiltrates small mold cavities?
- Will the pouring stresses damage small surface texture features?

A mold with fine features of dimensions pushing the limits of the processes was designed (see figure 3.21 & 3.18) to answer those questions. The mold has a very deep and thin cavity in order to test metal infiltration. In addition, a very long and thin mold section was used to test the mold resistance to metal pouring stresses. Both features had exaggerated dimensions compared to regular surface texture in order to define a safe window of casting operation.

An experiment is successful only if a set of casting with the mold feature, such as described above, can be produced with a sufficient yield. If so, it means that parts with surface-textures within the dimensional limits set by the experiment could also be produced repeatedly. The design of the part can be seen in figure 3.18.

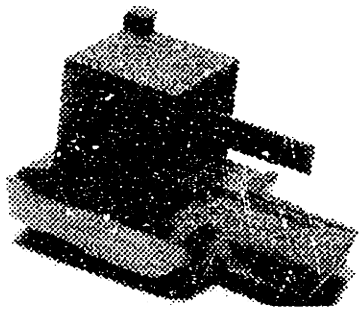

Figure 3.18: Test sample to evaluate metal infiltration and mold damage caused by pouring stresses.

On the ceramic mold (figure 3.21 top), we can see a very thin and long cavity (0.350mm W x 2.500mm H x 10mm L). This cavity has an exaggerated aspect ratio length to width of about 25, in order to get to push the limits of metal infiltration. The length of metal which infiltrates inside the cavity can be measured in order to indicate the maximum distance metal can infiltrate in the mold. The experimental length of metal infiltration L_{exp} can be divided by the width of the cavity W to determine the maximum aspect ratio L_{exp}/W

allowing casting integrity. A design rule can then state a specific range of mold cavity (or casting protrusion) aspect ratio which would insure casting quality.

The same part was also used to determine a safe range for mold protrusion aspect ratio L/W. Actually, since mechanical stress is what causes mold damage and casting failure, the ratio L^2/HW^3 represents more adequately the problem. In fact the ratio L^2/HW^3 is proportional to the stress at the base of a cantilever beam (Length L, width W and Height H) with uniformly distributed load.

Figure 3.21 top, shows a very thin mold section in the shape of a thin cantilever beam, with a stress aspect ratio $L^2/HW^3 = 450$ [$1/mm^2$] (L/W =20). Any aspect ratio smaller than 450 would experience a lower stress, thus if a fin with a 450 stress aspect ratio sustains successfully pouring stresses, we will conclude that any lower values should do as well. For example, maximum stress aspect ratio used for textures in this research had a ratio $L^2/HW^3 \approx 35$ [$1/mm^2$]. Results of the experiments can be seen in Appendix B3.

Results

It was found that all the mold cavities filled without any defects, which means that the geometrical aspect ratio L/W = 25 is not even large enough to prevent metal infiltration. From this result we can then define the following design rule:

• Mold cavities with a section (0.35mm W x 2.5 mm H x 10 mm L) with aspect ratio L/W ≈ 25 or lower can be repeatedly infiltrated with ASTM F75 alloy with the pouring conditions mentioned in section 3.6.2 with a T_{SH} = 1535°C.

Other results showed that only one out of sixteen fins was not properly cast. In other words, only one fin broke due to pouring stresses for a yield of 1/16 or 6% defects. This preliminary result can be used to say:

• If a positive mold features with stress aspect ratio L^2/HW^3 smaller than ≈ 450 [$1/mm^2$] is exposed to metal pouring stresses with the conditions described in section 3.6.2, than an adequate casting yield should be obtained.

This result is preliminary since it was done on a limited number of casting i.e. 16. More accurate figures can be achieved in the future by analyzing the casting defect rate spread over more runs.

3.7 Casting surface post-processes

3.7.1 Introduction

A significant amount of efforts is invested in the postcasting operations of investment cast parts. Once the mold has been poured with metal, a certain amount of post-processing is required before obtaining the final product. The two major post-processes are used to break the shell and remove the ceramic core, and clean the casting surfaces. Other post-processes such as surface grinding, polishing and heat treatment will not be discussed since they are not relevant to surface textures.

3.7.2 Leaching the mold

The mold as well as the ceramic cores need to be removed in order to free the casting from any foreign ceramic material. The method used to remove most of the shell is relatively straight forward. Using a vibrating pneumatic hammer , most of the shell can be knock out. However, small ceramic pieces located in confined area as well as the ceramic cores can not be removed in this manner. In this case, the reluctant little pieces can be dissolved out.

The part can be submerged in a 30%wt solution of sodium hydroxide NaOH, and boiled for about 2 to 3 hours in ambient pressure at about ≈100 °C. This method removes most of the ceramic shell and core on the casting. However, even after 2-3 hour of treatment the very small cavities forming sub-millimeter surface macro texture will not be completely cleared from their small ceramics cores. In order to remove those small pieces, the casting may be vibrated inside an ultrasonicater for about 30 minutes in distilled water. Adding surfactant (soap) to the distilled water may help to keep the particles in suspension in water. The parts can then be dipped once more in the NaOH solution and the procedure can be repeated until all the surface features are cleared from the ceramic. If the leaching solution needs to be more potent, an additional 5%wt of potassium hydroxide KOH can be added.

Here is a summary of the procedure:

1) boiling 30% wt NaOH solution @ ambient pressure (5% KOH optional)*
*Caution: Solution reacts violently with aluminum.
2) Immerse in the solution the cobalt-chromium casting for 2-3 hours
3) Ultra-sonicate the casting in distilled water for 30 minutes
4) Repeat step 2) and 3) until the ceramic is completely removed.

If the ceramic mold has been post-dipped in colloidal silica more than once, the mold material might be much harder to remove. It means that it might take more cycles or even have to use more than one batch of fresh NaOH solution before the ceramic can be removed. For example, an experiment was done with 3 post-dips which required two batches of NaOH-KOH and about 10 cycles of ultrasonic bath and NaOH immersion. The cavity had dimensions (7mm L x 2.5mm H x 0.35 mm W).

3.7.3 Cleaning the casting surface

The surface of the casting as it comes out of the leaching process have a dull greenish color due to a layer of chromium oxide. In addition, a closer look at the casting surface reveals mechanical pick up of ceramic grains (see figure 3.19a &b).

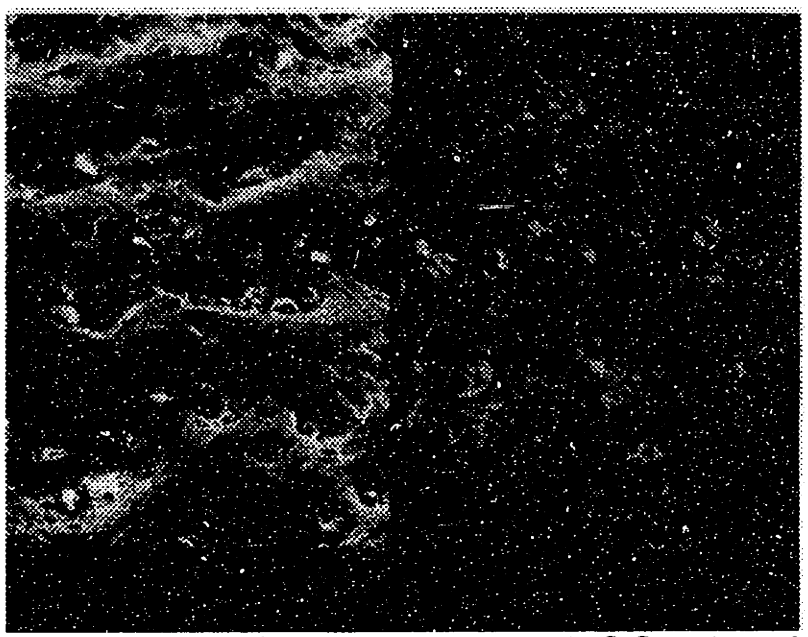

Figure 3.19a: Scanning electron microscope image of a CoCr casting surface. Grain of ceramic are revealed on the right using back scattering.

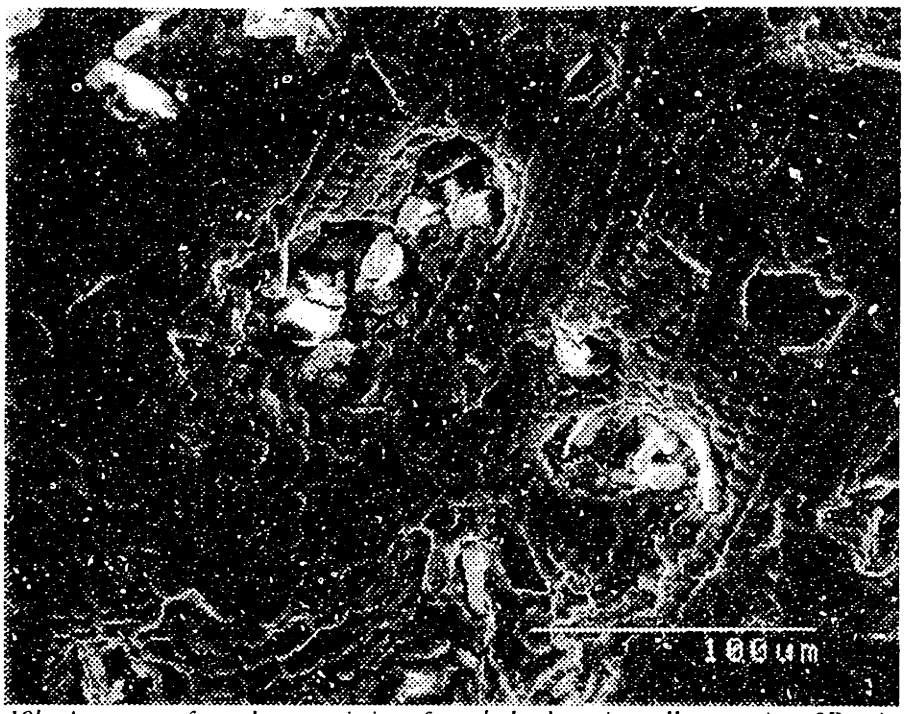

Figure 3.19b: As cast surface characteristics of a cobalt-chromium alloy cast in a 3D printed mold.

This kind of surface characteristics are unacceptable for orthopeadic application, since no oxide layer nor foreign abrasive particles can be tolerated at the interface bone-prosthesis.

A simple method to remove both oxide layer and ceramic inclusion is sand blasting. Figure 3.20 shows the effect of sand blasting a cobalt-chromium surface with aluminum oxide sand 425 grit size propelled through a suction blast nozzle.

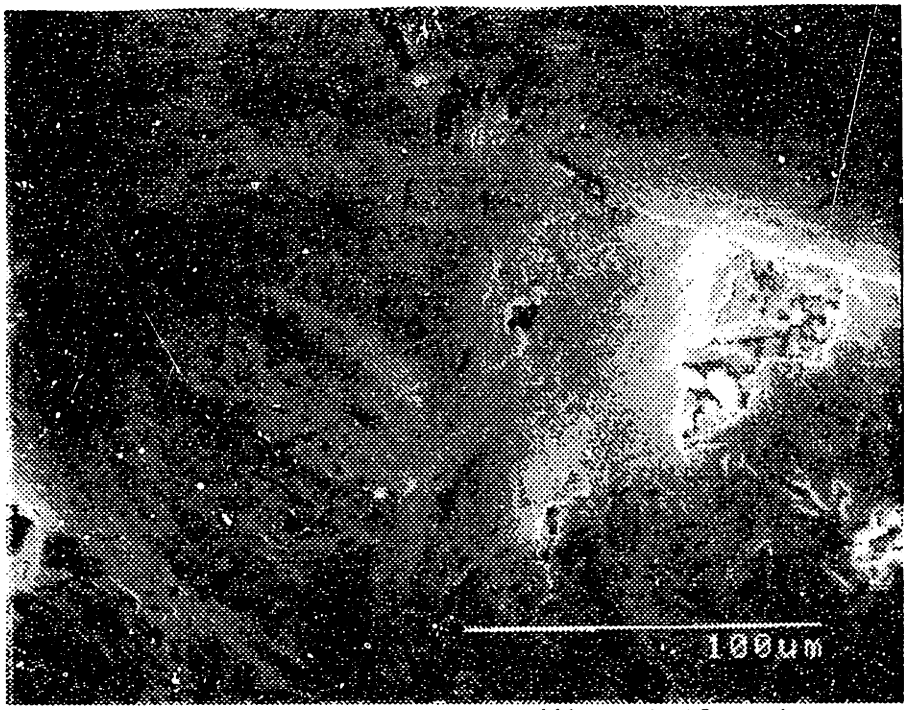

Figure 3.20: Same surface as figure 3.19, after sand blast with 425 grit aluminum oxide.

Although the result look satisfactory, the orthopaedic industry would like to stay away from sand blasting since the process itself can cause ceramic inclusion in the metal. Moreover, our surface textures have undercuts that could not be cleaned by the sand casting process since the sand can not reach that region of the texture.

Therefore, other processes involving caustic solution or acids were designed to accomplish the cleaning task. The process* that has been optimized for this particular application can be read as followed:

1) Kolene Kastech Ceram-x [K4E] @ 650°C for 15 minutes - 4 volts (reduction voltage).

2) Cold water quench/ rinse

3) 80 vol% H_3PO_4 with 20 vol% H_2SO_4 @ 150°C for 10 minutes

4) Cold water rinse

5) 10 cycles of Alko @ 220°C for 10 minutes, hot water quench, ultrasonicater rinse.

*Proprietary material of Kolene Corporation, 12890 Westwood ave. Detroit, MI 48223

The procedure makes use of proprietary chemical compounds. However the basic concepts in the procedure can be illustrated from conventional processes. The first step involves electrolytic pickling of the casting in order to remove some amount of the oxide layer. A cathodic current is used in order to speed up the process. It is one of the fastest

way to remove layers of rust or oxide, but involves risk of damaging the part itself. (so it should be used carefully). Then, a cold water quench help to crack the remaining brittle layer of oxide as well as attempting to break ceramic grains inclusions into smaller particles. A gentler acid cleaning is then used to remove another layer of oxide and free the casting from loosely attached particles. The final step is an alkaline descaling process (using probably a solution of sodium hydroxide or others) which is slower than the previous processes, but attack only the oxide without affecting the metal. This procedure gives the castings their final shinny look and removes the remaining oxide and weakly attached particles from the metal.

3.8 Casting dimensions vs. mold dimensions

3.8.1 Introduction

The dimensional relationship between the ceramic mold and the casting needs to be characterized in order to have the ability to predict casting dimensions right from the design level. Dimensions are mainly determined from the metal shrinkage compared to the mold dimensions. Linear shrinkage should be the same for all the axis of the part since the metal is isotropic. The casting dimensional accuracy on the other hand, depends on the mold accuracy itself which is different for each axis.

3.8.2 Castings dimensional analysis

The following experiment was done to verify the dimensional relationship between the 3D printed mold and the casting. The shrinkage value for the cobalt-base alloy ASTM F75 is expected to be in the vicinity of 2.75% linear according to Johnson & Johnson's data. Twenty of the part showed in figure 3.21 were measured both as a mold and as a casting to statistically evaluate their average dimension and accuracy.

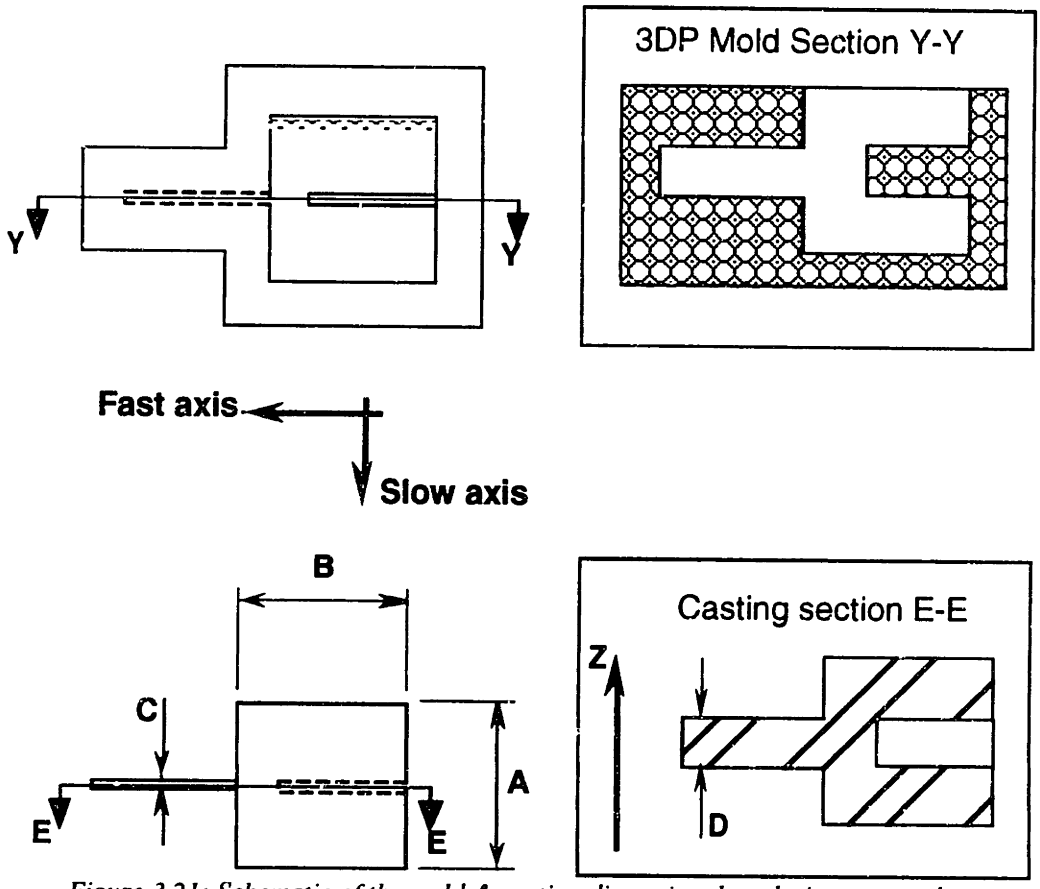

Figure 3.21: Schematic of the mold & casting dimensional analysis test sample.

Four important dimensions were measured on the part, see dimension A, B, C, D. Dimension A and C corresponds to the slow X axis of the machine. Dimension B is along the fast Y-axis and D along the piston Z axis of the machine.

Measurements A, B, C, and D were measured optically using a microscope and precision linear displacement slide. Statistics of the various measurements can be seen in table 3.12. The shrinkage value was calculated as followed:

$$\%Shrinkage = \frac{(\text{Mold dimension X}) - (\text{Casting dimension X})}{(\text{Mold dimension X})} \times 100\%$$

The value of shrinkage can be seen also in table 3.12. Notice the spread in the value for each dimension which in principle should all be the same.

Table 3.12: F75 Cobalt-Chromium alloy casting dimensional statistics (over ≈ 20 parts)

	Mold [mm]	**Casting** [mm]	**Shrinkage** [%]
Dimension **A**	9.77 ± 0.026	9.71 ± 0.029	0.6
Dimension **B**	9.68 ± 0.023	9.73 ± 0.060	-0.5
Dimension **C**	0.33 ± 0.019	0.35 ± 0.021	-6
Dimension **D**	2.52 ± 0.030	2.46 ± 0.008	2.44

* See Appendix B4 for experimental data

The discrepancy in shrinkage value can be explained in figure 3.22 based on the surface characteristics of the 3D printed molds. In fact, because of the layer by layer nature of the process, the sides of a printed part has regularly spaced surface ripple corresponding to the layer thickness used. For example, if we take dimension A which was measured along the slow axis.

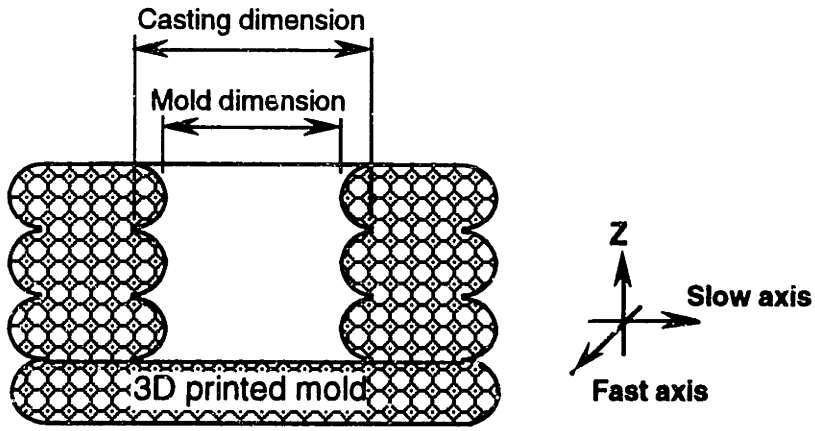

Figure 3.22: Cross section of 3D printed mold showing discrepancy between mold and casting measurement of the same feature.

The dimension A measured on the mold corresponds to the distance between the peaks of the ripple on both side of the mold cavity; to give a smaller dimension than expected. Dimension A, as measured on the casting with a caliper, will correspond to the distance between the bottom of the ripple to give a larger dimension than expected.

If we attempt to compensate for the ripple by assuming its amplitude to be about 100 μm, we would get:

$$\%\text{Shrinkage on A} = \frac{(9.77 + 2 \times 0.100) - 9.71}{(9.77 + 2 \times 0.100)} \times 100\% \approx 2.6\%$$

which is very close to our 2.75% expected shrinkage within 0.15%. Same concept can be applied to dimension C where the calculated shrinkage of -6% is exaggerated since the ripple dimension (≈100μm) is significant compared to the fin total thickness (≈ 350 μm). However, if we try to apply the same rule to dimension B, it will not work because of error sources such as merged drops and bi-directional printing which affect the mold surface roughness in the plane perpendicular to the fast Y axis. Those errors will be discussed in the process control section chapter 5.

At last, the dimensional analysis of dimension D showed a nice fit ≈ 2.44% with the expected shrinkage value of 2.75%. It was no surprise since the piston Z axis of the 3D printer defines this surface with a roller acting as the reference of the machine. The layer surface is also the smoothest surface with an RMS value in the vicinity of 300-500 μin (7-12 μm). Therefore, the shrinkage value ≈ 2.44% is also reduced by the effect of small surface ripples of similar amplitude (≈7-12 μm).

In conclusion , the values calculated from this preliminary study, all secondary affects accounted for, agree with the expected shrinkage measured on regular investment casting. Therefore, we can say that the expected shrinkage of 2.75%, which was measured over several samples in industry, should be applied for the cobalt-casting in 3D printed mold as well.

Note

It was noticed that the casting surface, defined by the mold surface showed in hatches in figure 3.21 top, is always rougher than the surface on the opposite side. This effect is probably due to powder ejection problem which are discussed in Tailin Fan Ph.D. thesis ref.[93].

3.8.3 Pore size dimension

The dimension of importance, considering our goal to produce surface macro-texture for orthopaedic application, is the pore size. The dimensions of the pore size will be measured to verify whether the size are within the initial specifications. Shrinkage calculation will not be performed in this case since first, it was covered in the previous section and second, since the pore size are small, shrinkage would be within the measurements noise. In any case, the pore size will be measured for both 3D printed molds and castings. Different texture designs were produced, but only design #5 will be discussed in detail. It would be redundant and lengthy to analyze each design. However, casting measurement results for other designs are available in Appendix B7.

Top surface pore size

The definition of pore size is not clear because the shape, distribution and orientation of the 3D printed pore is quite different from the sintered bead surface texture. Therefore, we will define a pore size in term of minimum, maximum, average diameter and surface area of pores in the three orthogonal plane of the 3D printer. The pore will be segregated into two classes: the top surface and bottom surface pores. The top surface pore can be seen readily by looking at the top of the texture (see figure 3.23b), while a cross-section of the texture should be done to see the bottom pores (see figure 3.23b and 3.24).

Figure 3.23a &b, shows the picture of design #5 and a schematic of one of its top surface pore.

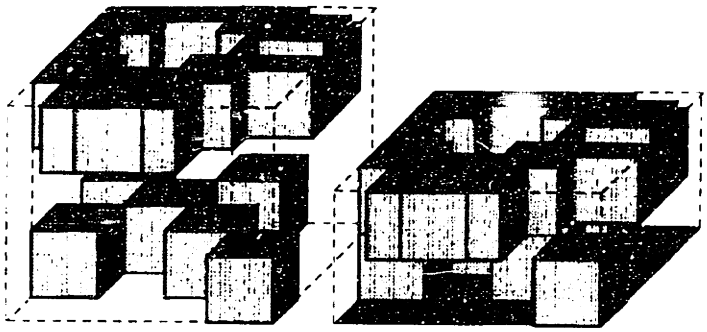

Figure 3.23a: Casting design #5 unit cell isometric view schematic.

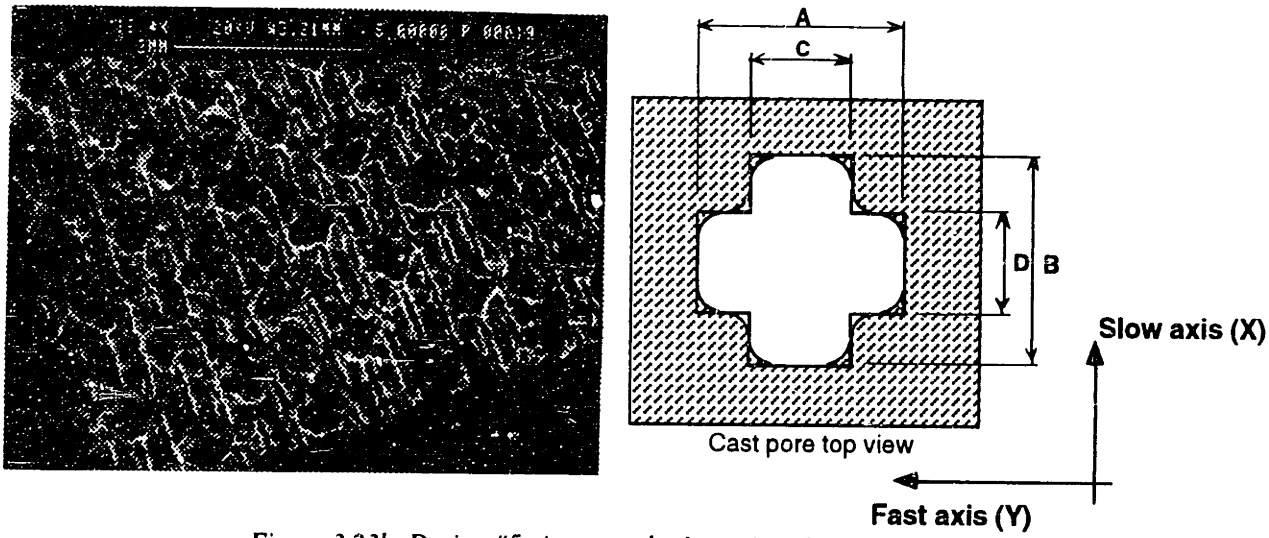

Figure 3.23b: Design #5 picture and schematics of a top surface pore.

The expected dimensions of the mold top surface pores were obtained from the printing offsets along the slow X-axis $\Delta offset_X$ = 15 μm and fast Y-axis $\Delta offset_Y$ = 20 μm (see section 4.2 for calculations) results in table 3.13. The mold features A, B, C and D were measured from a SEM picture of a top cross section of design #5 ceramic mold showed in figure 3.24 (see table 3.13).

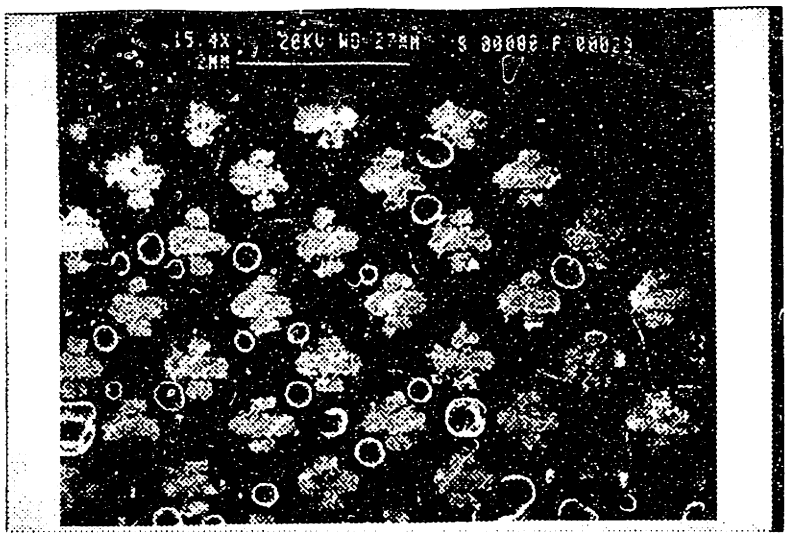

Figure 3.24: Top cross section of design #5 3D printed ceramic mold.

Table 3.13: Design #5 mold : top surface expected and measured pore dimensions:

Dimension	A [mm]	B [mm]	C [mm]	D [mm]
Expected	0.760	0.695	0.380	0.345
Mold	0.741 ± 0.023	0.666 ± 0.036	0.301 ± 0.048	0.285 ± 0.034

Data in Appendix B6

The dimensions of the cast pores were measured from an image analysis apparatus which gave the minimum, maximum, average diameters and area of the top surface pores. The minimum dimension corresponds to dimension D in figure 3.23b, while the maximum dimension is the diagonal line across dimension A. The average cast pore diameter is calculated as the diameter of a circle with surface area equivalent to the actual cast pore. Table 3.14 shows the dimensions obtained for the top surface pore both as a mold feature and as a cast feature. The mold dimensions were actually obtained or derived from table 3.13.

Table 3.14: Design #5, top surface pore size measurements (mold-casting)

Dimension [mm]	Minimum dimension	Maximum. dimension	Average dimension	Area [mm^2]
Mold	0.345	0.769	0.709	≈ 0.395
Castings	0.456 ± 0.035	0.603 ± 0.035	0.526 ± 0.035	0.231 ± 0.032

Data in Appendix B7

The casting dimensions are higher than the mold dimensions whereas the opposite is expected. This can be explained by the peculiarities of the image analysis software which uses difference in brightness and contrast to define the contour of a feature and measure its various dimensions. Since the top surface of the texture is not perfectly ground flat, the contrast between holes and solid was not adequate. As a result, no crisp delimitation could

be drawn around the cast pores. This virtual effect changed the dimensions by measuring additional shaded or brighter regions which were not part of the pores to be measured.

More accurate measurements were achieved on the bottom pore measurements.

Bottom surface pore size

The same analysis as above was done on a cross section of the texture design #5. The expected dimension were obtained from the same printing offset as for the top surface pores while the mold dimensions E and F were measured from a SEM photograph. See schematic in figure 3.23a and 3.25 and dimension results in table 3.15.

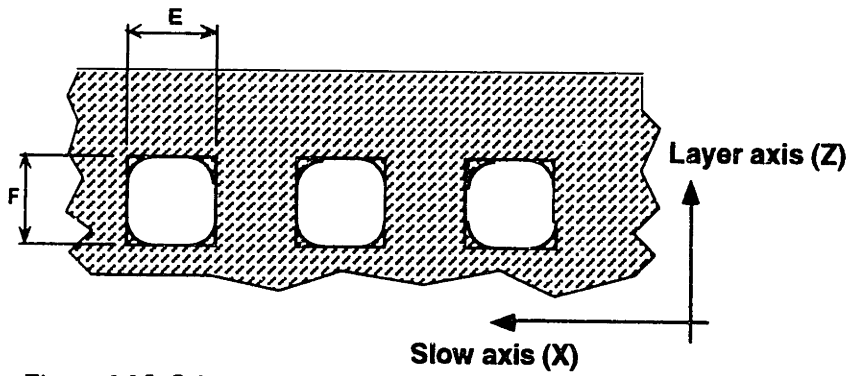

Figure 3.25 Schematic of casting cross section XZ of texture design #5.

Table 3.15: Cross section XZ of 3D printed ceramic mold features dimensions

Dimension	E [mm]	F [mm]
Expected	0.345	0.340
Mold	0.285 ± 0.034	0.323 ± 0.025

The minimum cast pore dimension corresponds to dimension F in figure 3.25 and the maximum dimension corresponds to the length of a diagonal line ≈45° across the pore section. The average pore diameter is calculated as the diameter of a circle with a surface area equivalent to the actual pore area (see table 3.16). The mold dimensions were obtained or derived from table 3.15.

Table 3.16: Design #5, Cross section XZ pore size measurements (mold-casting)

Dimension [mm]	Minimum dimension [mm]	Maximum. dimension	Average dimension	Area [mm^2]
Mold	≈0.323	≈0.480	≈0.386	≈ 0.106 ± 0.011
Castings	0.288 ± 0.042	0.396 ± 0.042	0.335 ± 0.042	0.093 ± 0.025

* Data in Appendix B7

Since the cast texture had to be sectioned in the XZ plane with a cutting wheel, the surface created around the pore was flat, shinny and free of oxide. As a result a much

better contrast could be obtained between the pores and the metal. Thus, the measurements are by far more consistent with the expected dimensions.

However, the casting dimensions are consistently smaller than the mold dimensions. If we take in account a linear 2.75% shrinkage, the dimension still do not get quite to the actual casting dimension. The other aspect to account for is the minimum casting radius that was calculated in section 3.2.4 as a function of metal surface tension. The radius was measured between 50 and 100 μm which is in agreement with our earlier estimate calculations. With this in mind, there is good fit between the expected and measured pore size considering also the noise in the measurements.

For additional experimental results on different texture designs, please look at Appendix B7.

In conclusion, we have showed a strong dimensional relationship between the ceramic mold and metal casting. The mold as well as the casting have dimensional limits which depends on the physics of the metal and ceramic materials. Rules of thumb for minimum mold feature size where also determined to help evaluate the range of design possibilities. Finally, we have showed that shrinkage as well as minimum casting radius should be accounted for when calculating for expected pore sizes.

Chapter 4:
3D Printed Ceramic Mold Characteristics

4.1 Introduction

In order to obtain accurate castings dimensions, it is important to understand first the methods to obtain the right dimensions on the ceramic mold. Just like a machine tool, 3D printing has a tool offset which needs to be compensated for. The tool offset depends on the primitives size which should be determined for the three orthogonal axis of the machine. The resolution of the machine is another important factor which will limit the printed features to a specific minimum size. This minimum size depends not only on what can be printed but also what feature size can survive powder removal stress among other things. Mold shrinkage will not be considered as a problem in our application, since the textures are relatively small and made of a few primitives only, which do not shrink significantly during the firing step.

4.2 Mold dimension control with tool offset compensation

4.2.1 Introduction

The process of generating textures on metal castings is done by creating a negative of the required features in the 3D printed ceramic mold. The ceramic features can be defined as positive feature (or protrusion) when created by an aggregate of primitives, or negative feature (cavity) when surrounded by a group of primitives. Both features are used extensively in order to form textured molds for investment casting. In order to obtain accurate dimensions on both type of features, tool offset should be compensated for.

4.2.2 Tool offset on mold cavity

A simplified mold cavity is showed in figure 4.1.

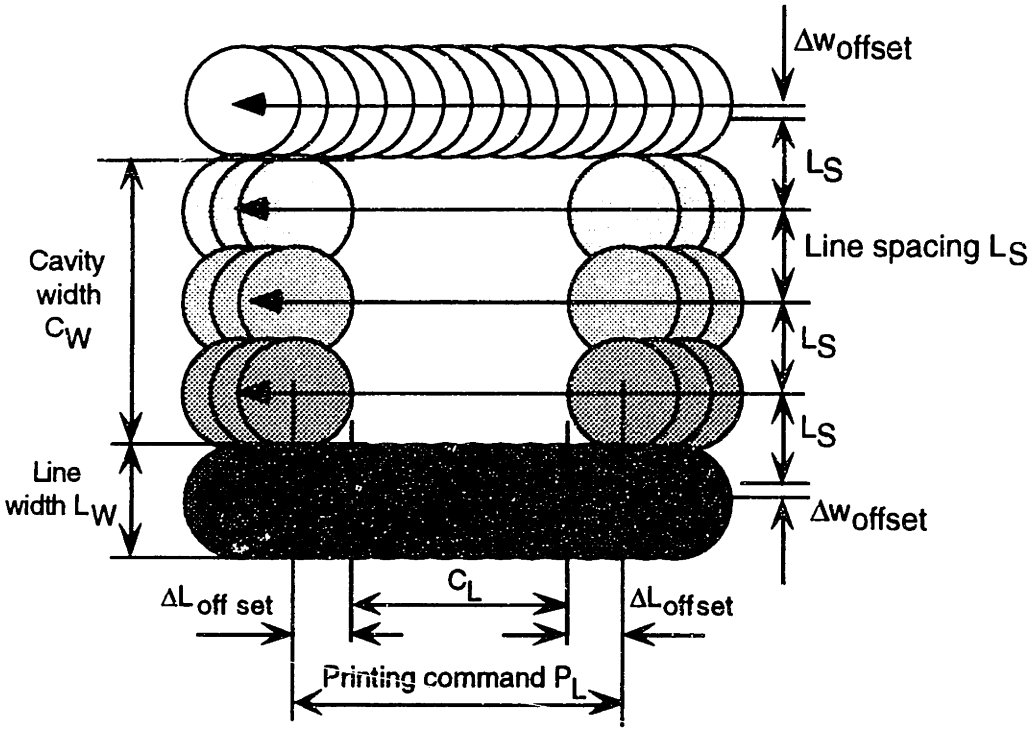

Figure 4.1: 3D Printed mold cavity with n=3 lines removed.

The schematic shows the top surface of a ceramic mold cavity in the plane XY, which corresponds to the powder bed plane (or fast and slow axis plane). In our example, the cavity has a width C_w and length C_L which was formed by eliminating n=3 line segments made of a certain number of drops determined by the print command $P_{command}$. The exact width C_w of the cavity is determined by the following expression:

$$C_w = (n+1)L_s - L_w + 2\Delta w_{offset} \qquad (4\text{-}1)$$

where n is the number of line segment removed
L_s is the line spacing: typical value = 175 µm
L_w is the printed line width
Δw_{offset} is the slow X axis offset [µm]

In the latter expression, we assumed that line spacing is constant except at both extremities where an offset Δw_{offset} can be added to the line spacing L_s. To determine the

value of C_w, all the parameters but one are readily available. In fact, the line width L_w needs to be measured prior to applying equation 4-1.

The graph of figure 4.2 was generated from a set of experiments where the cavity width C_w was measured for a range of Δw_{offset} varying between 0 and 40 µm (see figure 4.6) . The value of L_w can be determined from equation 4-1 when the offset is set to 0.

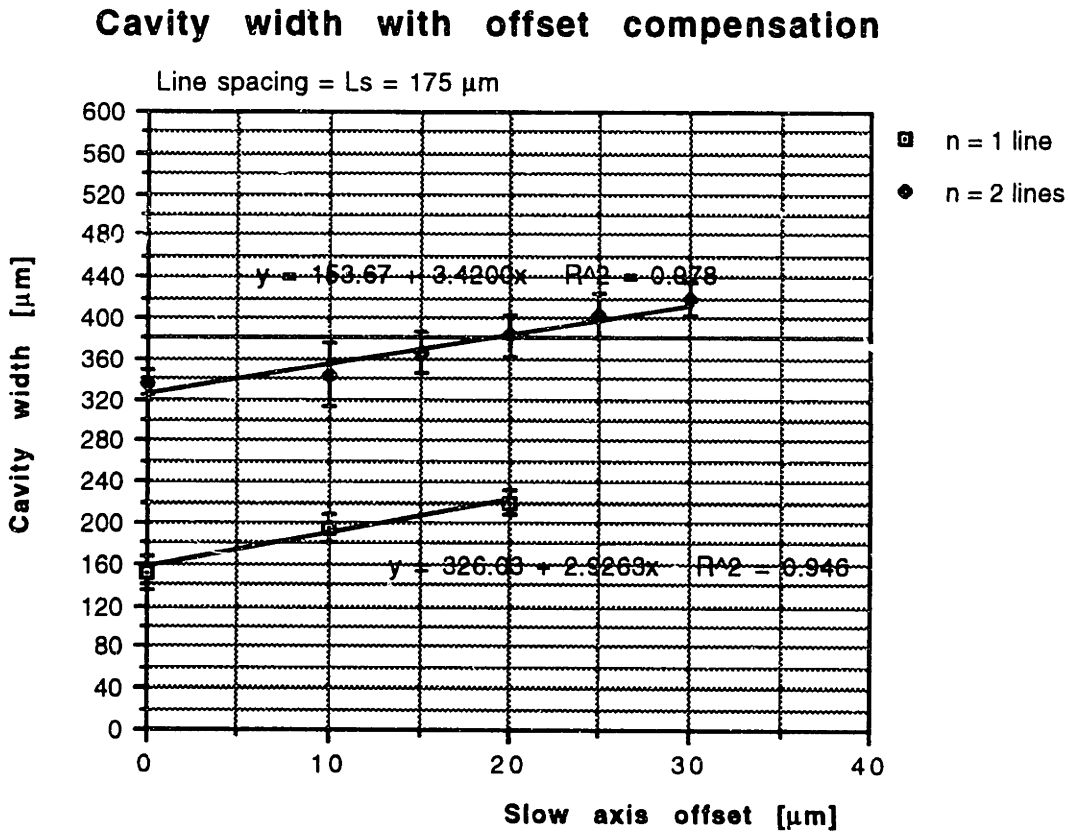

Figure 4.2: Cavity width for n=1 and n=2 removed line segments for various offset values. Data in Appendix B5

According to the graph 4.2, the cavity width C_w should be ≈ 325 µm when the offset Δw_{offset} is 0. Then, according to equation 4-1, the primitive width L_w is equal to ≈ 200µm, result that was confirmed in Jim Bredt's Ph.D. thesis ref[90]. From then on, the value L_w=200µm can be used to predict the width C_w for different offset Δw_{offset} value. The results obtained from equation 4-1 follows the linear interpolation shown on the graph (figure 4.1) within the measurement noise.

On the other hand, the length C_L of the cavity (along the fast axis) can be determined by the following expression:

$$C_L = P_{command} - 2\Delta L_{offset} \qquad (4\text{-}2)$$

The cavity length was printed along one-scanning direction only in order to achieve the best accuracy. The value of the offset ΔL_{offset} is determined from the graph of figure 4.3.

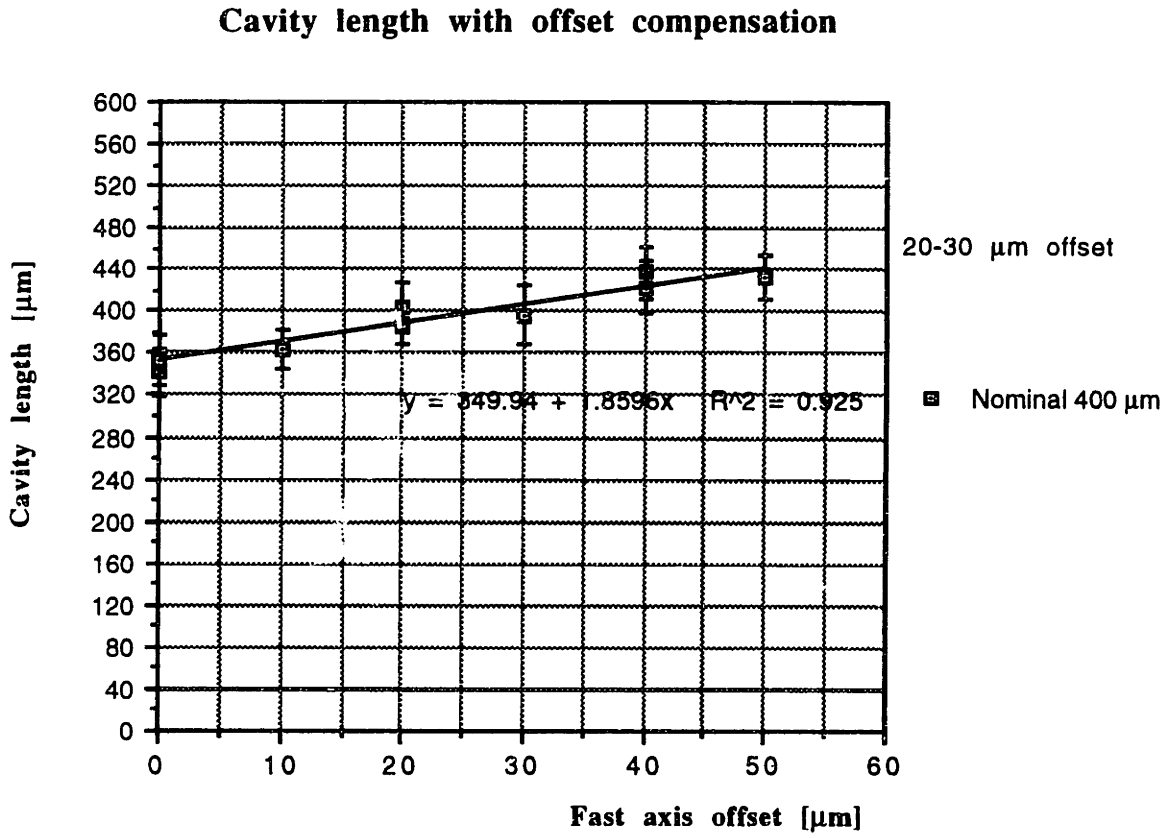

Figure 4.3: Cavity length for print command P_L=400µm for various offset values. Data in Appendix B5

For example, if a length C_L= 400µm is targeted, according to the graph of figure 4.3 an offset $\Delta L_{offset} \approx 26$ µm should be applied. Therefore, the print command P_L that will provide a length $C_L \approx 400$ µm should be $P_L = 452$ µm, since ΔL_{offset} has to be compensated on both sides of the cavity.

However, since the resolution of the fast axis is 10µm, ΔL_{offset} should be rounded off to either 20 or 30 µm. In this case, the command P_L would become 440µm or 460µm for a respective cavity length $C_L \approx 390$ or 410 µm.

The offset ΔL_{offset} = 20-30 µm is smaller than the 100µm expected offset due to the 200 µm primitive size. This apparent inconsistency can be explained from the air drag effect on the drops which reduce the expected length of a given printed line (see section 5.10.4).

We now have considered the tool offset for the fast Y-axis and slow X-axis. The last offset to be determined is the piston Z-axis offset ΔZ_{offset}. A similar experiment than the one showed in figure 4.1 was performed in the Y-Z plane. The height of the cavity C_H along the Z-axis can be expressed by:

$$C_H = (m+1)Lay_S - Lay_T + 2\Delta H_{offset} \qquad (4\text{-}3)$$

where m is the number of layers removed to form the cavity
Lay_S is the layer spacing: typical value = 170 or 180 µm
Lay_T is the printed layer thickness
ΔH_{offset} is the piston Z axis offset [µm]

This latter equation assumes that the layer thickness Lay_T is the same whether the layer is at the top or bottom of the cavity. This assumption is valid as long as C_H is two to five layer thick. For larger value of C_H, equation 4-3 should be modified to compensate for the different bottom and top layer thicknesses.

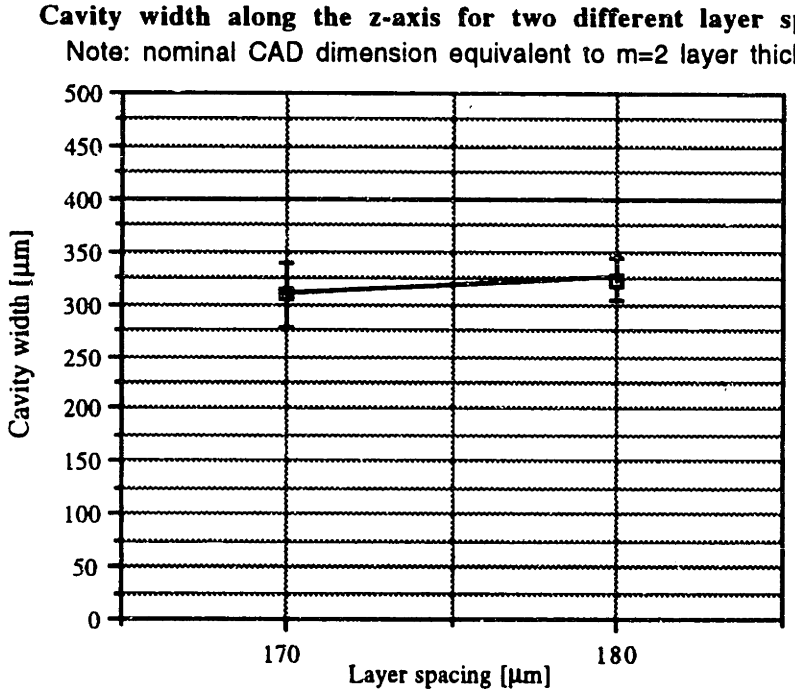

Figure 4.4: Cavity height for m=2 removed layer thickness (Offset ΔH_{offset}= 0 µm).

Following the same procedure as for the dimension C_W, the layer thickness Lay_T needs to be determined first. Using the graph of figure 4.4, for m=2 removed layers and using a layer spacing Lay_S=170 μm and offset ΔH_{offset} = 0 μm, the cavity height C_H was measured at ≈310 μm. Using this result in equation 4-3, we can determine that the layer thickness Lay_T is ≈200 μm. This latter result can now be used in order to predict the height C_H of a cavity for various printing conditions.

The cavity width, length and height C_W, C_L and C_H can now be accurately determined respectively from equation 4-1 to 4-3. The same principles can be used for protrusions which need however some minor modifications to the equations.

4.2.3 Tool offset on mold protrusion

The same principles of tool offset can be used for protrusion dimensions defined as the width P_W, length P_L, and height P_H. A similar experiment (see figure 4.6) as above was done for printed protrusions. The result were very noisy since merged drops and induced charge effect were deforming the small protrusions. As a result, the cavity offsets, which in principle should be the same as for the protrusion, will be used. The accuracy of the cavity offsets is in fact better since the material surrounding the cavity could absorb most of the detrimental effects caused by merged drops and induced charge.

First, equations 4-1 to 4-3 needs to be modified as followed:

$$P_w = (n-1)L_s + L_w + 2\Delta w_{offset}$$

$$P_L = P_{command} - 2\Delta L_{offset} \qquad (4\text{-}4)$$

$$P_H = (m-1)Lay_S + Lay_T + 2\Delta H_{offset}$$

where n is the number of line forming the protrusion
L_S is the line spacing 150-180 μm
L_W is the line width ≈ 200 μm
Δw_{offset} is the slow X-axis offset 0-30 μm
$P_{command}$ is the printing command along the fast Y-axis
ΔL_{offset} is the fast axis offset ≈ 20-30 μm
m is the number of layer forming the protrusion
Lay_S is the layer spacing 170-180 μm
Lay_T is the layer thickness ≈ 200 μm
ΔH_{offset} is the piston Z-axis offset 0-20 μm

The above equations and parameters are valid for printing colloidal silica binder in alumina powder using the standard printing conditions as described in chapter 5. Any changes in the materials system may require some modification of the values cited in the list of parameters.

The set of equation 4-4 is very useful to produce accurate dimensions on a mold by allowing feature snapping of basic printed primitives to the specific shapes of a CAD model. This task can be accomplished by adjusting the various offset values within reasonable limits.

Offset values along the slow and piston axis should be used carefully. It is advisable to keep them as close as possible to 0. Small offsets in the range of -30 to +30 μm can be used, but may cause delamination or even binder bleeding along the fast or piston axis, depending on the sign and magnitude of the offset. Bleeding is likely when a protrusion made of two or three line segments is used. In this case, if a negative offset Δw_{offset} is applied, bleeding can occur more readily since the tiny protrusion can not absorb the excess binder like a bulkier part could. The limit of binder content should be calculated beforehand in order to prevent such bleeding (see section 4.4.1).

Delamination is another problem that occurs when the offset is too large (positive). Line offset can be used along the slow axis without any significant effects on the bulk properties of the ceramic part. However when used on the piston Z-axis, it affects the full layer which may create delamination. Therefore, it would be advisable to used only a negative ΔH_{offset} (from uniform layer spacing) in order to prevent delamination within the permissible range preventing bleeding.

On the other hand, the fast axis offset should be kept constant to a value of 20 or 30 μm. The length of a printed segment can then be specified by the print command $P_{command}$ only.

4.3 Mold minimum feature size

4.3.1 Introduction

The minimum feature size that can be produced by the 3D printer is of two types: protrusions (or positive features) and cavities (or negative features). The minimum positive feature size is defined by the primitives size or in other words, the size of single drops and lines of drops forming the building blocks of the parts. The minimum negative feature size can be smaller as it is determined by the need to remove powder to define the feature.

Both types of feature needs to sustain handling stresses in order to be used effectively in our casting application. Therefore, design rules will be identified to determine the minimum feature size based on its resistance to the various stresses inherent to the process.

4.3.2 Minimum cavity size

The minimum cavity size is associated with the ability of removing the loose powder out of the cavity. Two methods of powder removal were evaluated: dry removal and wet removal

Powder removal process

Dry removal consists in using a gentle air jet which is directed to the part in order to blow the loose powder away from the main part and cavities (see figure 4.5b).

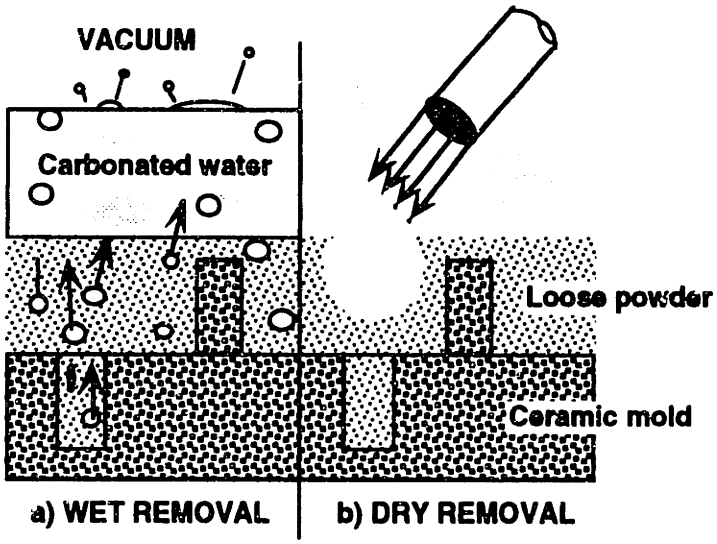

Figure 4.5: Powder removal methods

With wet removal, the entire part has to be submerged in carbonated water. Then a vacuum is created above the carbonated water in order to release the carbon dioxide gas originally dissolve in the water. A procedure was designed to optimize the effect of a given batch of carbonated water. The procedure is:

1) Submerge the ceramic part with loose powder in carbonated water inside vacuum chamber.
2) Build up vacuum ≈29-30 in-Hg in the storage secondary tank which is connected to the vacuum chamber. As the vacuum is built up in the storage tank, the vacuum chamber remains at atmosphere pressure because the valve between storage tank and chamber is in closed position.
3) Create vacuum in the chamber for 1 to 2 minutes by turning on the valve to the vacuum storage tank. Then close the valve.
4) Repeat cycle 2) and 3) twice until the carbonated water runs out of gas.

The bubbles created by the action of the vacuum lift up the powder from any cavity in the part. An alumina surfactant such as (Sodium Pyrophosphate) can be dissolved in the carbonated water in order to delay settlement of the loose powder on the part.

Experiment

An experiment was designed in order to determine the minimum cavity dimension from which 30μm alumina loose powder can be removed. A test part with a range of cavity width varying between 150 and 400 μm and depth varying between 175 to 1800μm was printed (see figure 4.6)

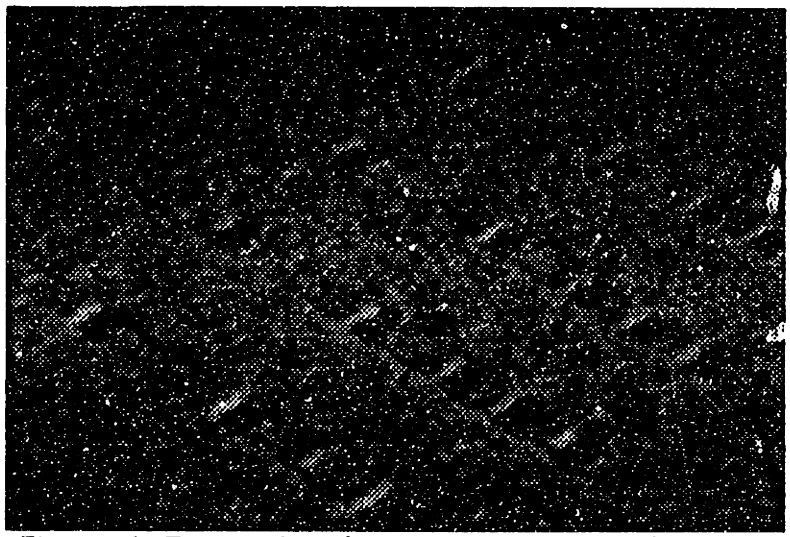

Figure 4.6: Test sample to determine minimum cavity dimensions.

Some of the parts were then subjected to dry removal while others were subjected to wet removal. Two initial powder bed conditions were used in the experiment. The layers forming the test part were either kept dry before printing or were sprinkled with a mist of water to increase the powder cohesion forces and reduce the ballistic effect of the printing drops.

Results

The results showed that wet powder removal was superior to the dry powder removal process for cavities deeper than 1000 μm and also for parts that were printed with mist. In fact, with the dry process, it was almost impossible to remove the powder even for the larger cavities (400μm W x 400μm L x ...) when mist was used on the powder bed.

The best results were obtained for wet removal. The smallest and deepest cavity (150μm W x 400μm L x 1800 μm Deep) could be cleared from all its loose powder when no mist was used on the powder bed. If mist was used, the wet powder removal process could cleared a cavity no smaller then (350 μm W x 400 μm L x 1800 μm Deep). The compaction effect of the mist and binder bleeding causing an increased strength of the powder bed can be attributed for the decrease of powder removal capabilities.

In summary, we can say that:

1) When mist is used, the minimum cavity dimension is about (350μm W x 400 μm L x 1800μm Deep) for a ratio width to depth W/D = 5 or a width equivalent to 11 grain of powder (11x30μm). Therefore, any cavity with a ratio W/D < 5 and width > 12 grain size should be easily cleaned from their loose powder.

2) When mist is not used, the minimum cavity dimension is about (150μm W x 400 μm L x 1800μm Deep) for a ratio W/D = 12 or a width equivalent to 5 grain of powder (5x30μm). Therefore, any cavity with a ratio W/D < 12 and a width > 5 grain size should be easily cleaned from their loose powder.

Note on other powder removal method

Ultrasonic water bath can also be used to remove loose powder from mold cavities. However, it should be used very carefully since it can easily damage small mold features. One possible method is to damp the vibration in order to have gentler shock waves reaching the part. The vibrations can be reduced by submerging the mold inside one or even two self contained plastic beakers. Than, the part can be sonicated for periods of 15 to 30 seconds and inspected for damage. This method is not recommended for small mold feature since it is difficult to control reliably the strength of the vibration.

4.3.2 Minimum protrusion size

Another experiment was designed to evaluate the damage caused on small protrusions (positive features) by the two powder removal processes. This experiment will help determine the design rule for the minimum feature size that can sustain powder removal stresses. Although we know that the ceramic tensile strength is about 10 to 20 MPa, this experiment is necessary due to the non-uniform stress inherent to the powder removal process.

Experiment

Again a test part was designed with protrusion 1 to 2 line primitives wide (200 to 400 μm), 400μm long and heights varying between 1 and 10 layer thickness (170 and 1800μm) (see figure 4.7). The protrusion sizes cover a ratio height to width H/W between 0.5 to 10 which is sufficient considering the fact that the highest H/W ratio used on textures is about 2 or 2.5 .

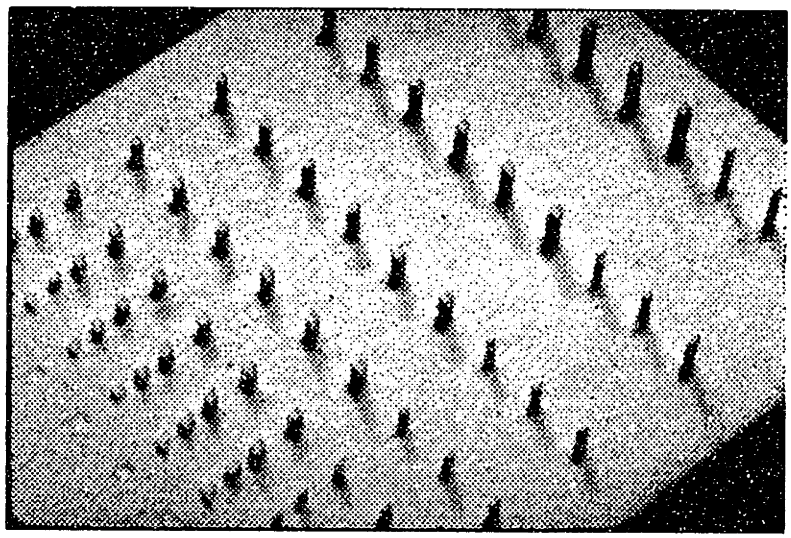

Figure 4.7: Test sample to determine the minimum protrusion size that will sustain powder removal stresses.

Four powder bed conditions were used in this experiment:

1) Layer thickness = 170 μm dry powder removal
2) Layer thickness = 170 μm wet powder removal
3) Layer thickness = 180 μm dry powder removal
4) Layer thickness = 180 μm wet powder removal

The sample parts were subjected to one of those conditions, and statistics of the damage occurring to the protrusions were compiled as a percent defect of a set with a given stress aspect ratio H^2/LW^3. Since the studs were damaged from mechanical stress, the stress ratio H^2/LW^3 is a good parameter to compare different studs dimension performance. In fact, the stress ratio H^2/LW^3 is proportional to the stress at the base of a cantilever beam, much like our stud features (see figure 4.7), with uniformly distributed load.

Results

The results can be summarized in the two following graphs (figure 4.8 and 4.9). Graph of figure 4.8 was done for protrusions made of a single line primitive (or 200 µm wide) while graph of figure 4.9 was done for protrusions made of a combined 2 line primitives or (≈ 350 µm wide).

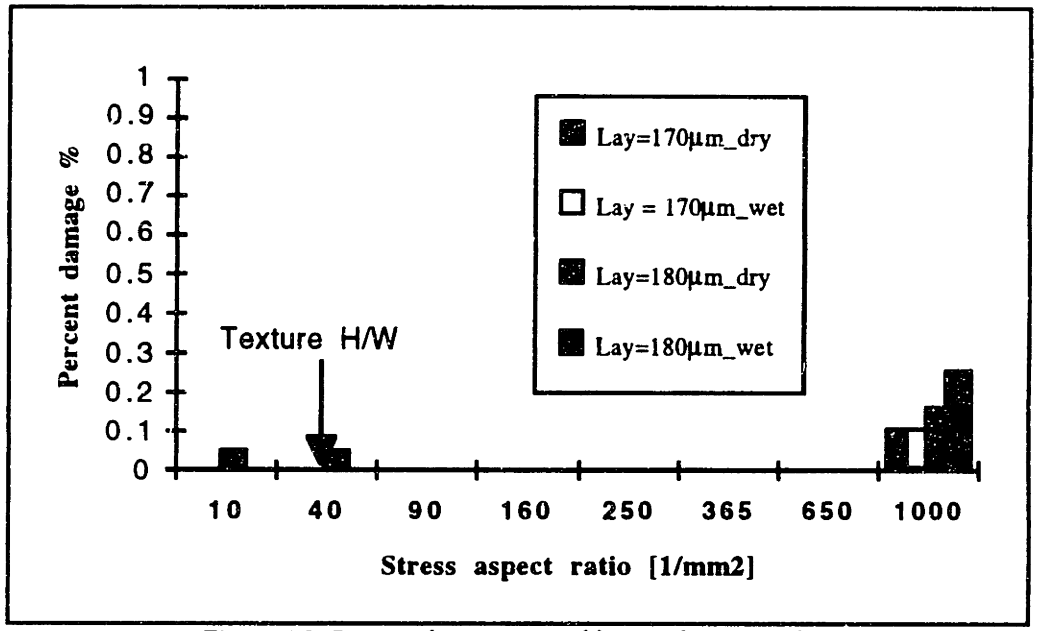

Figure 4.8: Percent damage caused by powder removal on 200 µm W x 400 µm L x Height ceramic studs.

Figure 4.8 shows that protrusion with a section 200 µm wide x 400 µm long can sustain with almost no defect powder removal stresses up to a ratio H^2/LW^3 of 1000. For ratio H^2/LW^3 of 1000, between 10 and 20% of the protrusion were damaged. A small percentage ≈4-5% of the smaller features were also damaged. Those feature were in fact weaker since they were made with layer thickness of 180 µm. The protrusions made of 170µm layer thickness were stronger than the protrusions made of 180µm layer thickness

because of their higher binder content. No significant difference was noticed between dry and wet powder removal as far as defect percent is concerned.

Figure 4.9 shows the results for protrusions with a section 350 μm Wide x 400 μm Long. In this case, no defects were seen up to a ratio $H^2/LW^3 \approx 200$ where the same observations as in figure 4.8 could be made about the powder removal method.

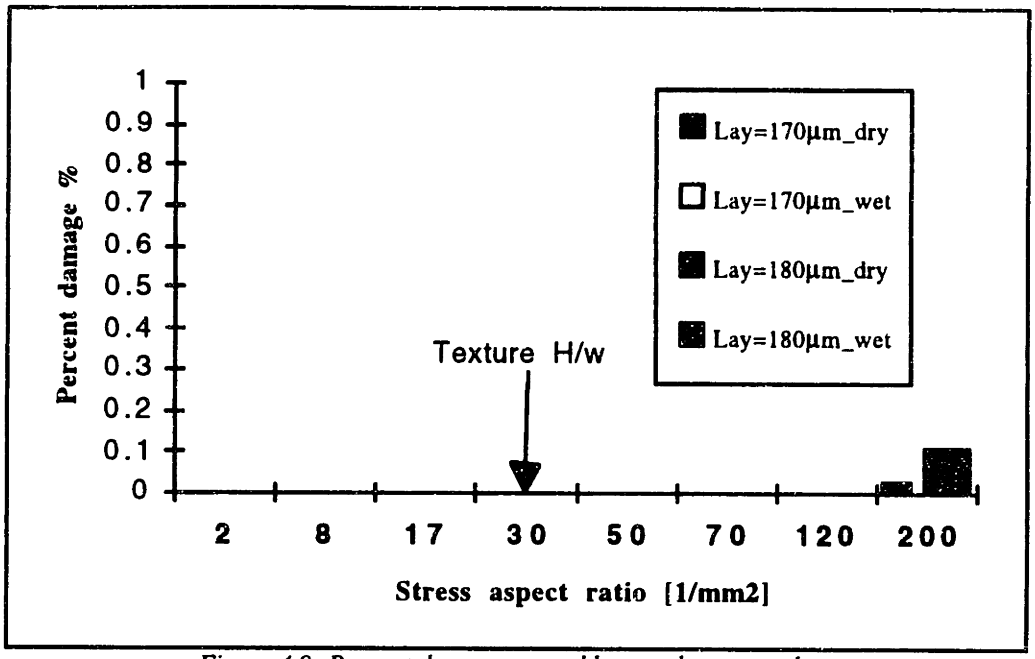

Figure 4.9: Percent damage caused by powder removal on 350 μm W x 400 μm L x Height ceramic studs.

However, the results in figure 4.9 clearly showed (≈ 10% damage) that studs made of 180 μm layer thickness reached their break point at $H^2/LW^3 \approx 200$ [1/mm^2]. However, no significant damage was produced on the stud made of 170 μm layer. As a result, we can not really conclude the limit for those latter studs other than saying that they can sustain at least H^2/LW^3 up to 200.

In both figure 4.8 and 4.9, some of the highest studs were broken by other means than the powder removal itself. In fact, some of the test samples were displaced by the rush of bubbles and settled on top of studs of other parts. Such stud damage can be seen in figure 4.9 for the 170μm_dry layer characteristic.

The feature size of the surface macro-textures used in this research were well within the limits of maximum stress ratio. In fact, since most of the features are interconnected with each other reduces even more the risk of mold damage.

In summary:

1) Protrusions with a section 200μm wide by 400 μm long can sustain powder removal up to a stress ratio $H^2/LW^3 \approx 1000$ [$1/mm^2$] without any significant defects.

2) Protrusions with a section 350μm wide by 400 μm long can sustain powder removal up to a ratio $H^2/LW^3 \approx 200$ [$1/mm^2$].in the case of 180 μm layer thickness without any significant defects. However, the limit for 170 μm layer thickness was not reached. Thus, for 170 μm layer, we can at least tell that studs with the above section should sustain at least $H^2/LW^3 \approx 200$ [$1/mm^2$] or probably much higher.

3) The two types of powder removal process have about the same detrimental effects, but wet removal is more efficient.

4) Thinner layer thickness make stronger protrusions because of higher binder content.

Those results are conservative since each feature was standing on its own as opposed to interconnected together into a structure as in the case of most texture. However, the values offer a reference on which the designer can rely.

4.4 Other mold characteristics

4.4.1 Binder content calculation

In order to make crisp surface macro-texture, it was very important to control the amount of binder printed in the powder bed. Moreover, since the line spacing was not always kept uniform, we needed a method to evaluate the optimum printing parameters to prevent bleeding and achieve the best results.

The following expression (equation 4-5) was used to evaluate the degree of saturation of the powder bed.

$$S = \frac{Q}{L_S \cdot Lay_S \cdot (1-\varphi) \cdot v_{y,scan}} \qquad (4\text{-}5)$$

where S is the saturation level (75 to 90%) depending on the powder composition
Q is the binder flow rate [m^3/s]
L_S is the line spacing (170-180 μm)
Lay_S is the layer spacing (150-180μm)
φ is the powder bed packing density in percent (typical 0.35-0.65)
$v_{y,scan}$ is the printhead scanning speed [m/s]

Any printing parameter combinations which give a saturation S over 100% would cause bleeding. The saturation represents the ratio of the volume of printed binder to the volume of the powder bed porosity available to hold the amount of liquid. A saturation S=100% would mean that all the porosity have been filled with binder material.

Most texture printed in this research were done with a saturation level of about 80%. To obtain such a saturation level, the scanning speed $v_{y,scan}$ was adjusted accordingly. For example, for a line spacing of 175μm, a layer spacing of 175μm, a flow rate of 1 ml/min (1.67×10^{-8} m^3/s) and a powder bed packing density of 45%, the scanning speed required to achieve 80% saturation was 1.24 m/s.

4.4.2 Effect of drop printing density: edge effect

One phenomena that is easily forgotten in printing droplet is the different drop density along a printed line. In fact, if a straight line is printed with uniformly spaced droplets, the resulting line segment will have a smaller drop density at both ends of the line. (see figure 4.10).

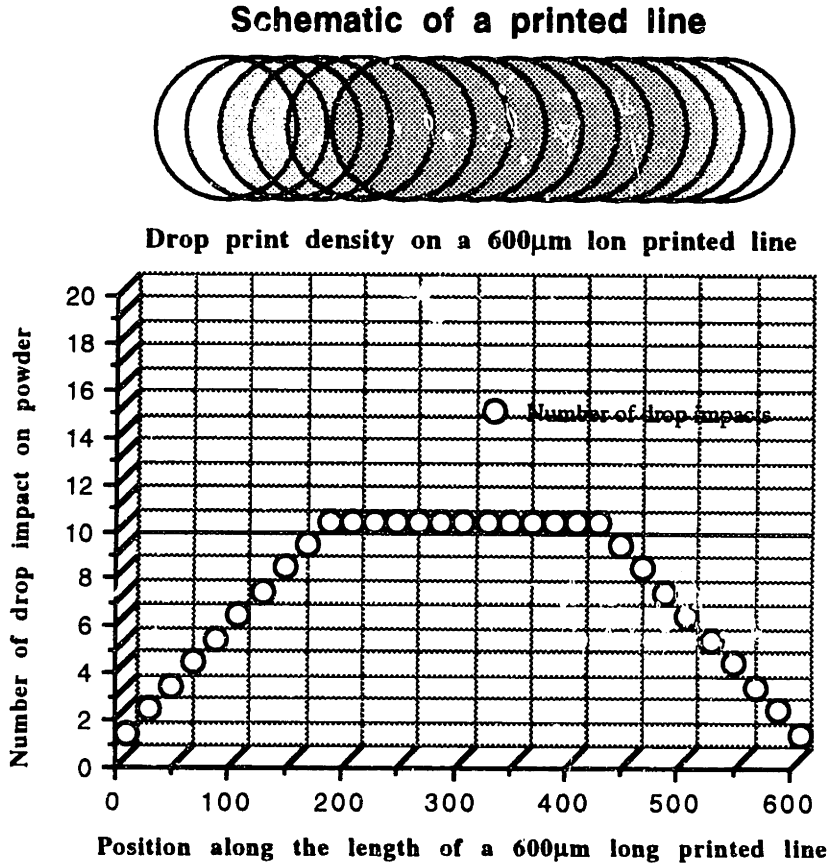

Figure 4.10: Drop print density along a 600 µm long printed line.

For example, the graph of figure 4.10 was done for a printhead traveling at 1.5 m/s with a drop generation rate of 76300 Hz, for a drop spacing on the powder bed of ≈20µm. The effect of print density can be seen on a cross-section of a ceramic mold (see figure 4.11). The ends which get between 1 to 9 drop impacts are not as compacted as the middle section which get an average 10 drops impact along its length. Therefore, the top surface of both ends curls up, making the surface of the textured mold rougher then expected (see figure 4.11). The number of drop impacts can be calculated by dividing the primitive size

by the drop spacing. For example, in our case a primitive of 200 μm and a drop spacing of 20 μm gives an average drop impact on the powder bed of $^{200\mu m}/_{20\ \mu m/drop} \approx 10$ drops. Since the primitive size is about 200 μm, the length of the transient at both ends is also 200 μm.

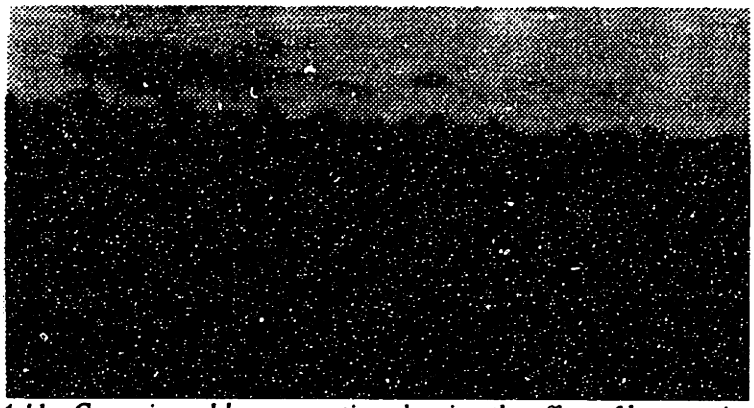

Figure 4.11: Ceramic mold cross-section showing the effect of lower print density at the ends of a printed line (see top of the part).

The ripples amplitude created at both ends of the top surface of the ceramic mold are in the range of 50 to 70 μm. The effect can be counteracted by controlling the drops density along the length by printing wave form patterns instead of straight lines. Another approach would be to decrease the drop spacing in order to make the effect smaller, since the powder compaction would reach a steady state faster.

4.4.3 Post-dipping

Colloidal silica

Post-dipping is a post-process used on 3D printed ceramic molds to increase the strength of the molds. After initial firing, the ceramic part still do not have enough strength to sustain handling and casting stresses.

Post-dipping is done by submerging the part in a solution of colloidal silica similar to the one being printed through the nozzle. After dipping for a few minutes, the part has to be drained of the excess binder and dried. The part is then fired at about 1000°C to soften the silica particles and strengthen the existing silica-alumina structure. The cycle can be repeated several times, although one post-dip is sufficient for the casting application. An excessive number of post-dipping cycles may cause clogging of small cavities and make it harder to leach out the ceramic from the metal casting. Therefore more then one post-dip cycle should be used only if necessary.

The drying procedure may cause the silica particles to migrate at the surfaces of the ceramic part instead of being uniformly distributed throughout the part. However, this effect is negligible on the surface macro-textures and may even be favorable to increase the strength of the small ceramic features and improve surface finish as well.

Other post-dipping possibilities

Just as a side note, post-dipping could also be used to improve the surface finish and overall casting quality. First, post-dipping can be used to fill the small gaps or steps which are characteristics of a layer based manufacturing process. A thicker solution of slurry carefully formulated with refractories in suspension, could improve surface finish without affecting the accuracy or clogging small cavities. Such solution is under development at the company Ashland chemical Inc..

Second, post-dipping could be used as an equivalent to the prime coat used on wax patterns for investment casting. In fact, a particular post-dipping solution could prevent casting oxidation and could even control the grain size of the casting. In fact, a nucleating agent (grain refiner), such as cobalt compounds in the form of aluminates, silicates, titanates, and oxides in amount ranging from about 0.5% to 10% by weight, can be added to the slurry.

A judicious combination of those materials could be added to our basic colloidal silica post-dipping solution in order to improve the overall casting quality.

Chapter 5: 3D Printing Process Control

5.0 3D Printing: Process Control

The ability to print accurately sub-millimeter surface texture relies heavily on the level of control on the various components of the 3D printer. A set of design rules related to the control of the 3D printing machine can be defined in order to improve the quality and accuracy of the printing process.

5.1 Drop Placement Accuracy

The goal of process control is to identify the main sources of error and develop methods to reduce their effect or simply eliminate them in order to improve drop placement accuracy. Of all the components forming the 3D printing machine, the printhead is the most complex system and as a result the major error source along the X-Y axes (see schematic figure 5.1). In fact, its reliable operation depends on the control of several parameters which can significantly vary over time.

In order to deal with such complexity, standard continuous-jet printing controller the position of the drops by referring to an exhaustive look-up table built in their ROM (Read Only Memory). These look-up tables are made of thousand of data points which relates different combinations of printing parameters to a precise drop position for a specific printhead design only. Although look-up tables work in principle, they are very limited in practice. For example, the number of parameters in the table has to be limited, otherwise the dimension of the matrix reaches sky-high proportions. For example, a small scale look up table using only 7 different parameters with 10 levels of variation each would require 10^7 = 10 millions experimental data points! Imagine 20 levels of variation ? The logistic of such an amount of experimental data points is truly overwhelming as far as experimentation time is concerned and computer power needed to deal efficiently with that much information.

Thus, our goal is to eliminate as much as possible the need for a look up table since it is cumbersome and probably not necessary for our process. Therefore, in order to adequately predict drop position from a given set of printing parameters, we will need to achieve a considerable level of understanding of the printhead physics. The task will be to take apart all the sub-systems of the printhead and develop a suitable physical model which

fits their dynamics well. If the physical model do not provide a satisfactory accuracy, then empirical methods using experimental measurements will be investigated.

Those models will be the building blocks which provide a means to estimate the drops position and accuracy. The design rules associated with the process control will refer to the expected accuracy and printing quality. Those rules will give the users an idea about the dimensional conformity of small printed features such as surface textures.

In the next sections, the printhead will be described part by part and their characteristics will be explained with physical models validated by experimentation. The model will be designed in order to help predict the printing command for different printing conditions. This exercise should also provide insights on future possible improvements for the printhead design. Clearly, sources of error other than the printhead, such as the scanning Y-axis speed controller, contributes also to the error along the Y-axis. However, unlike the printhead, motion control as well as other major error sources are better understood and well documented. Therefore, the core of this chapter will cover the printhead theory and process control development which will make the printhead a more precise and controllable building tool.

5.2 The Printhead And Its Sub-Systems

5.2.1 Introduction

The printhead chosen on the actual 3D printer delivers the drop continuously as opposed to on demand or as needed. This technology is known as "continuous-jet printing". The control of this continuous sequence of drops is done by electrostatically charging the drops in order to either deflect them in a drop catcher or precisely locate them on the powder bed. Figure 5.1, shows the different sub-systems of our printhead assembly.

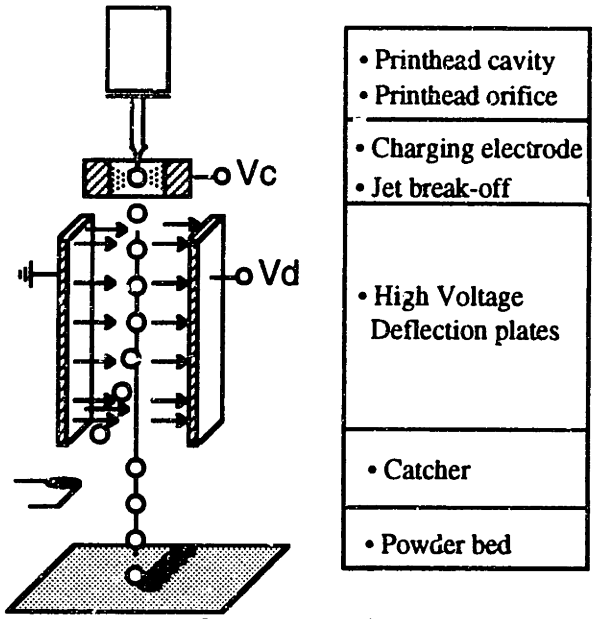

Figure 5.1: Printhead description

The stream of drop originates from an orifice located at the bottom part of a resonating assembly. The resonating assembly is driven by a piezo resonator glued on the external part of the resonator. A liquid jets is generated by forcing a liquid at high pressure through a nozzle with a circular openir ..xed on the resonating assembly. After exiting from the nozzle, the jet travels through the air in the form of a continuous laminar flow cylinder. This continuous part of the jet disintegrates into a train of droplets at a well-defined point, the break off point.

The jet generated from the piezo-resonator assembly break up into drops at the charging electrode level. A potential V_c is applied for drop formed in order to electrostatically charge each individual drops. Then the charged drops go through an electric field generated within the deflection cell by the potential V_d. At this point, the drop

are being deflected parallel to the field lines according to the polarity and magnitude of the charge they hold. The charge on each drop is like a piece of information which defined where the drop will land. For some charge level, the drops are deflected in the drop catcher. While other charge level would position the drops on the powder bed.

5.2.2 Machine Axes and drop label conventions

In this chapter, we will refer to the three axis of the printhead on a regular basis; the axis convention is showed in figure 5.2.

Axes convention

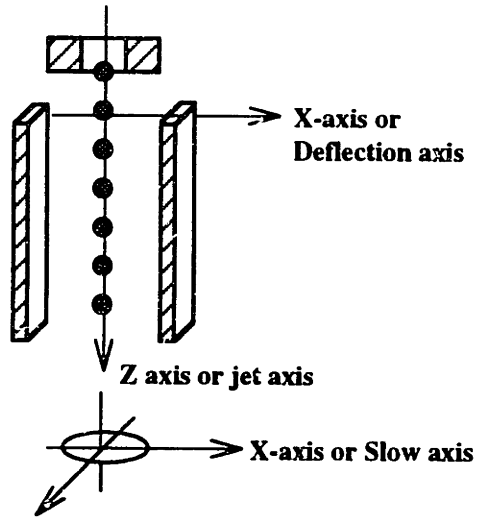

Figure 5.2: Axis description of the printhead system.

The axis which coincides with the jet center line is the Z-axis or stream axis. As a reference to the powder bed the Z-axis is also the piston axis which define the thickness of the powder layers.

The X-axis or deflection axis is perpendicular to Z-axis and parallel to the electric field lines created inside the deflection cell. When referred to the machine the X-axis is also called the slow axis of the machine.

Finally, the Y-axis is the scanning axis generally perpendicular to the X-axis. The Y-axis is also referred to as the fast axis of the 3D printer.

Drop label convention

The drop label convention is also important to define in order to follow the different theories about drop charging and drop interaction. The convention refers to two distinct printing instant: the charging (figure 5.3a) and the drop deflection inside the deflection cell (figure 5.3b)

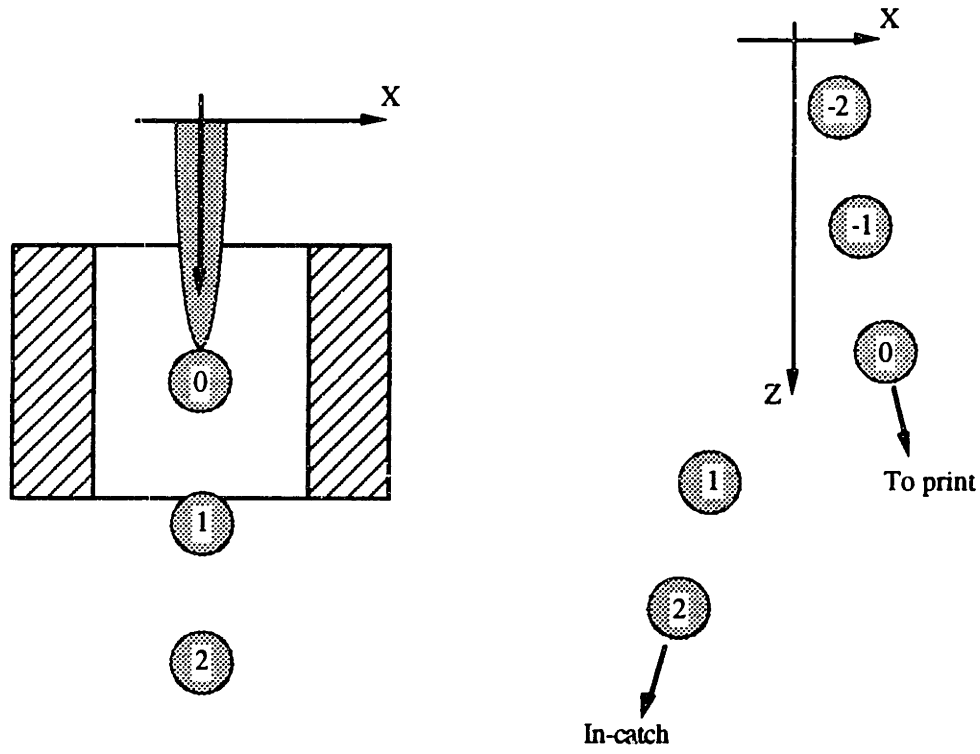

a) Inside charging cell b) Inside deflection cell and below

Figure 5.3: Drop labeling convention used in this thesis

When we refer to drop charging inside the charging electrode, the drop on the edge of breaking off from the stream or in other words the drop being charged is always drop #0 (see figure 5.3a). The drops preceding drop #0 are labeled in ascending fashion as drop #1, drop #2, ...

When we refer to drop deflection, most of the interaction occurs at the transition between the last in-catch drops and the leading printing drops (see figure 5.3b). In this case, drop #0 is always the first drop to be printing out of a sequence of drops. The other drops to be printed are following drop #0 with descending label as drop #-1, drop #-2, .. On the other hand, drop #1, drop #2, ... are the trailing drops of an in-catch (not print) sequence. Drop #1 being the last drop of the sequence to be in-catch.

5.2.3 Printhead Type & Design

The printhead used in this research was a resonating cavity continuous-jet type printhead. It was manufactured by Dyconix which is now part of Scitex company. The assembly is normally operated at its natural frequency which varies between 60 and 80 kHz. Resonance is obtained by adjusting the vibration frequency in order to optimize the magnitude of the signal coming from the piezo pickup also glued on the resonator surface.

The rest of the printhead design including the charging electrode, deflection cell and drop catcher was completed at MIT by Chris Shutts (see Chris Shutts' Master thesis ref[98]). Figure 5.4 shows the most important dimensions which appears in various calculations further down.

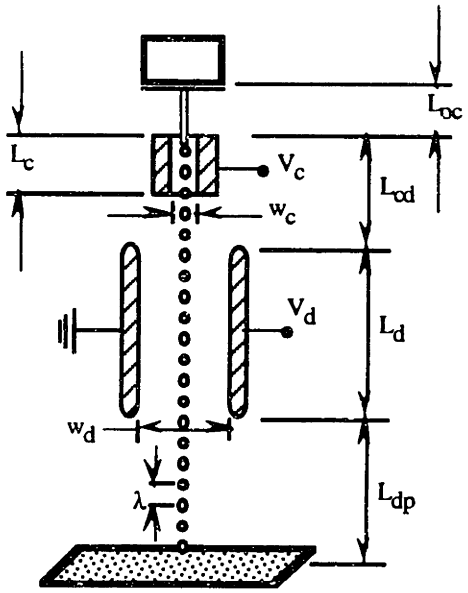

L_{oc} ≈	1	mm
L_c =	3.05	mm
L_{cd} =	4.06	mm
w_c =	450	μm
r_d =	0.6	mm
L_d =	9.7	mm
w_d =	1.5	mm
L_{pd} ≈	16	mm

$-150\ V < V_c < +150\ V$

$-2500\ V < V_d < +2500\ V$

$150\ \mu m < \lambda < 250\ \mu m$

Figure 5.4: Printhead layout

The accuracy of the above dimensions varies according to which surface they refer to. In fact, some of the surfaces were electroplated which leave at least a 12 μm layer on the surface. Therefore, dimension such as w_c or w_d may not be as accurate as other dimensions which depends on the milling machine accuracy only. (which is about ± 20 μm)

5.2.4 Printing Process Characteristics

Printing characteristics

The feature which characterizes our printing process compared to other ink-jet printing devices is the raster scanning nature of our drop lay out. In fact, instead of printing

characters, we print a continuous sequence or line of drops. Our process prints most of the drops in long packs while only a few drops are discontinuously deflected away from the stream in the case of continuous-jet printers.

As a result, we will not be able to use guard drops, the same way it was described in the IBM paper ref[63,56], in order to prevent detrimental effects from aerodynamic drag. Instead, techniques such as selective drop removing may just perform the same as it is described at the end of this chapter.

Printing issues

Among the printing issues which compromise the accuracy and conformity of sub-millimeter surface features with the CAD model, two of them can be considered as major; drop merging and induced charge.

Induced charge occurs when drop #0 is being charged by the charging electrode. However, the charge on previously charged drops also affect the final charge of drop #0. Since the charge is directly related to the deflected position along the X-axis, it affects the drop placement accuracy and will change the dimension or even integrity of the texture if not compensated for.

Drop merging occurs at the leading edge of a train of drops since the first drop of the train (or drop #0) experiences a larger drag force relative to the following drops. Several leading may merge into a single bigger drop depending on the printing conditions. This larger drop may seriously compromise the conformity of small printed features.

Developing drop placement error compensation strategy

One goal of this research was to develop printing conditions which will prevent undesired effects in order to restore or improve the quality of sub-millimeter printed features. Those methods as well as the theory related to them will be described in details. Their performance will also be assessed in order to determine the final improved accuracy and print quality that could be achieved on the 3D printer.

Error Budget

A simplified error budget of the 3D printing machine will help the designer to understand the accuracy limits of the process. Also, since the accuracy of the machine is different along each axis, the error budget will help to orderly classify the error sources. At the same time, it provides a tool which can be used to determine the impact of specific printing conditions along any particular axis of the printer.

5.3 Experimental Measuring Instruments

In order to evaluate the proposed physical models as well as the error compensation methods, the following experimental set-up was designed to help measure various parameters.

5.3.1 Description of experimental set-up

The experimental set-up was designed to replicate as close as possible the environment of a printhead mounted on the 3D printer (see figure 5.5).

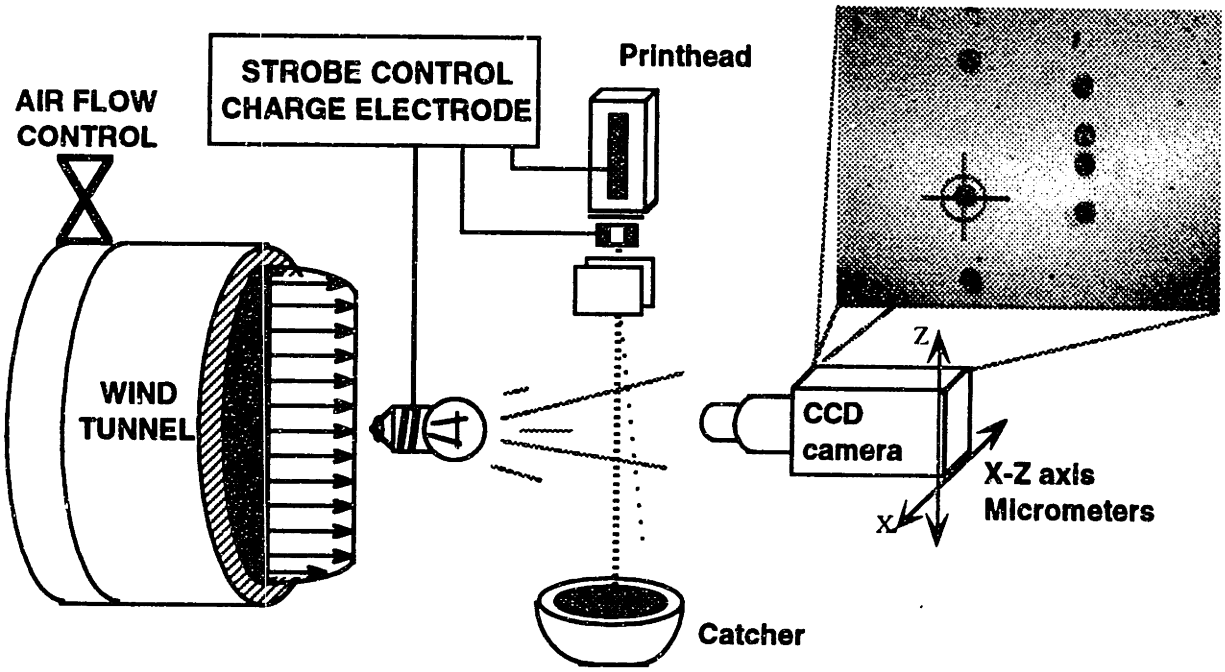

Figure 5.5: Simplified schematic of the printhead experimental set-up.

Printhead environment

The printhead was actually mounted on a stationary structure in order to provide a stable reference for our high precision drop position measurements. A function generator (Wavetech; accuracy ±30 ppm) was used to drive the piezo-resonator with a sine wave signal set at the natural frequency of the printhead. The charging voltage V_c applied at the charging electrode was determined by the electronic controller (see description below). On the other hand, the deflection plate potential V_d was established by a high voltage power supply (Bertan Model 205B-03R) which has a 0 to 2kVolts range with an accuracy of ±0.1% and repeatability of 0.01%.

Scanning speed simulation

The printhead scanning speed $v_{scan,y}$ was simulated by a wind tunnel blowing a laminar air flow toward the printhead along the fast Y-axis. The flow rate Q_{rot} was controlled by a pressure regulator and measured with a rotameter located between the regulator and the tunnel. The air rotameter was calibrated for flow rates up to 0.004 m^3/s. The average speed $v_{scan,y}$ inside the pipe was measured as a flow rate Q_{rot} in the rotameter by the following formula:

$$v_{scan,y\,(rel)} = \frac{Q_{rot}}{A_{pipe}} \qquad (5\text{-}1)$$

where A_{pipe} is the area of the pipe section of diameter Ø = 44.5 mm or ($1^3/_4$").

The rotameter (Omega, model FL4613-V) has an accuracy of ±2% over its full range of operation. This means that a typical air flow of 1.5 m/s generated by a flowrate of Q_{rot}= 0.0023 m^3/s in a pipe of section A_{pipe} = 0.0016 m^2 can be controlled within ± 0.03 m/s.

A stack of 30 mm long x Ø5mm straws were inserted at the inlet of the 1m long wind tunnel in order to reduce the turbulence and create an approximate laminar flow at the exit of the pipe.

Stream visualization

The stream of drops were visualized using a strobe light flashing in the background towards the drops and CCD camera. The light source was chosen to be an infrared LED (Light Emitting Diode) because of its power compared to normal LED, short time response, small size and immunity to surrounding light sources in the room. The LED strobe was fixed to the CCD camera structure. This design assures that when the camera was moved in order to measure a new position, the strobe light was kept in the field of view.

The camera, mounted on a X-Z precision positioning table, was used to measure accurately the drops positions. In fact, the camera could be moved along each axis while the position was monitored by precision micrometers (±2 μm). The reference position (0,0) of the camera assembly was defined as the lower X-Z edge of the deflection cell. The reference position was re-initialized before every experiment since the relative position of the equipment was not secured. A thin cross hair placed on the TV screen provided the user reference point from which all the measurement were done by centering the crosshair on the feature being measured.

One issue was about the interaction between the LED strobe light and the air flow. Since the LED is physically located in the path of the air flow before the drops, it may have introduced undesired turbulence which could have compromised the validity of our experiment. Therefore, the LED was shaped into a much smaller and oblong form in order to reduce its effect on the laminar flow. We know for a fact, that if the Reynold's number for an oblong body can be kept below $\approx 1x10^4$, then the laminar flow would just open up along the body and close some distance behind. Our LED was transformed into an oblong body 4 mm long. The calculation for our experimental conditions predicted a Reynolds number of:

$$60 < Re_L < 600$$

where $$Re_L = \frac{v_{scan,y} L}{\gamma_{air}}$$

$v_{scan,y}$ is the relative air flow velocity or scanning axis speed=0.25-2.5 m/s

L is the length of the oblong LED= 4mm

γ_{air} is the kinematic viscosity of air $\approx 1.7x10^{-5}$ [m^2/s]

which means that the air flow stays laminar and closes back quickly behind the LED without disturbing the flow at the drops. An adequate distance of 20-25 mm (5x LED length) was given between the LED and the stream to make sure that the air flow wake closes on itself before the LED.

5.3.2 Electronic controller

The electronic controller was designed with the capability of charging a sequence of drops with different very accurate charge levels. The progression of a drop sequence could also be captured on a TV monitor at different time interval with the help of a synchronized strobe light commands. A schematic of the controller is showed on figure 5.6; a detailed electronic circuit is also available in Appendix C1.

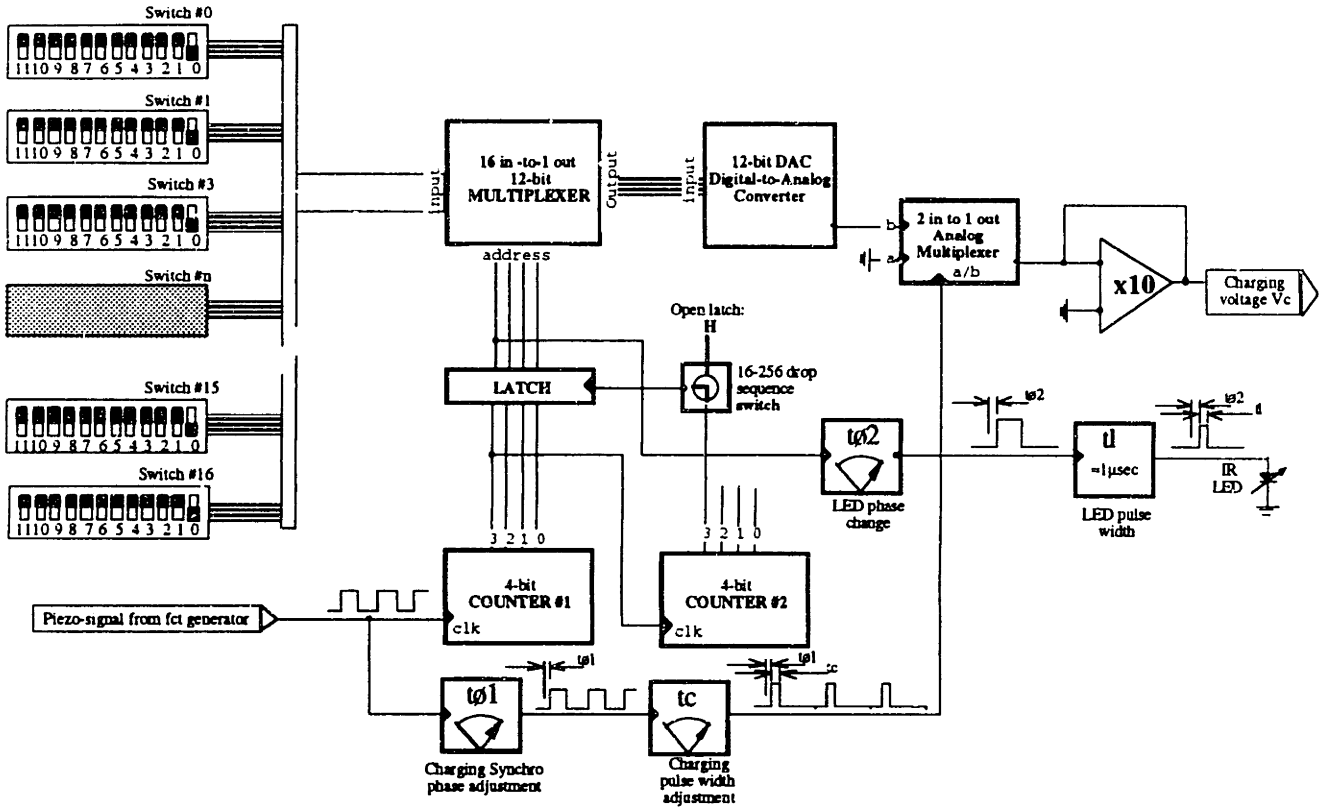

Figure 5.6: Simplified schematic of the printhead experimental controller.

Six different controls were provided:

i- Number of drops in sequence 16 or 256

ii- LED strobe synchronization adjustment with the piezo-resonator signal

iii- Drop charging pulse width adjustment.

iv- Charging pulse synchronization adjustment with the piezo-resonator signal

v- Sixteen 12-SPST DIP switches controlling 16 consecutive charging voltages.

vi- Various calibration potentiometers.

i- Number of drops in sequence

The drops were controlled in sequences such that their motion could be frozen in space by stroboscopic effect. In other words, the controller was cycling the same charging voltage information repeatedly. Two different mode were available: 16 and 256 drops. For example, if the 16 drop sequence was selected, then the voltage on drop #1 of a sequence would be the same for drop #17, #33, #49,...and so on.

The 256 drop sequence had a slightly different mode of operation. In this case, only sixteen different voltages were also available. Therefore, the 15 first drops of every sequence would get their individual charging voltage. However, the charging voltage of the 16th drop would remain locked constant for the next 240 drops, before cycling again. This procedure was used mainly to aerodynamically isolate a sequence of 16 drop from each other.

ii- LED strobe synchronization

The strobe pulsed signal is generated directly from the rising edge of our piezo-resonator signal. One possible adjustment is to vary the phase between the piezo and the strobe signal. The effect of such a phase change was to give the impression to look up or down the Z-axis along the stream. This trick would allow the user to measure the deflected position X of all the drops for a given Z position. It also provided a means to align the drops of a sequence by inspection. In fact, by changing the phase, if all the drop pass by the same point on the TV screen (cross hair), they form a straight line.

The strobe signal is a 1 μs pre-adjusted pulse. A pulse is generally generated for every drop sequence by triggering on the first drop of the sequence. The 1 μs pulse width was chosen based on the piezo-frequency and the light intensity required by the CCD camera.

iii- Drop charging pulse width adjustment.

The charging pulse width had to be determined from the piezo-resonator frequency. A method to determine the pulse width is described in the drop charging section below. This adjustment was done initially and kept constant for all the experiments.

iv- Charging pulse synchronization adjustment

The charge synchronization is a very important feature which makes sure that each drop gets its full expected charge. The charge synchronization adjustment changes the phase between the piezo and the charging voltage pulse dedicated for each drop. A proper charge will be induced on the drops only for a specific phase relationship between the two signal (piezo vs. charging) This phase relationship drifts in time as the control parameter

are intentionally changed or not. Therefore a constant supervision of this control should be done.

The method to find the phase relationship is rather simple. Looking at the stream below the deflection cell, the operator changes the phase relationship from 0° to 360°. Along the way, the stream will reach a maximum deflection (plateau) which corresponds to our desired phase relationship. The operator should verify on a regular basis, if the maximum deflection conditions is still satisfied by wobbling the phase knob CW and CWW.

v- Sixteen 12-SPST DIP switches voltage information

Sixteen DIP switches are arranged one beside each other on the controller board. Each switch represents the voltage information that is sent to a specific drop in the sequence. The switches are labeled from #0 to #15 as a reference to drop #0 to #15 in the drop sequence. The switches are indirectly connected to a DAC (Digital-to-Analog-Converter) through a digital multiplexer. In other words, the electronic circuit reads the information of each switch successively and sends the information to the DAC. The voltage information is encoded as a 12-bit number where each bit is represented by one of the 12 SPST actuators on the DIP-switch. A 12-bit number can represent by itself 2^{12} or 4096 different voltage level within a predetermined voltage range. The accuracy of a DAC is specified as ± %x LSB where %x is the fraction of the last bit (bit #0) which defines the error. For example, if the voltage range is 10 V and the DAC error is $\pm 1/2$ LSB, it means we can control the voltage from 0V to 10 V with a resolution of $10V/4096$ = 2.44 mVolt and an accuracy of $0.5/4096$ x 10 V = ±1.22 mVolt.

The DAC was configured as a bipolar converter in order to deflect drops on both side of the jet stream axis. The voltage range was set at -10V to +10V for a resolution of 4.88 mVolt and accuracy of ±2.44 mVolts. The voltage is then sent to an analog multiplexer which routes the voltage to a 10x amplifier when the write pulse t_c triggers the gate of the multiplexer.

vi- Various calibration potentiometers.

Other calibration knobs (not showed in simplified schematic) were also used to compensate for amplifier offset or calibrate the DAC reference voltage. Those adjustments were all done only once when the board was first tested.

5.3.3 Charge collector instrument

The charge collector instrument is designed to measure the average charge level q_n of drops. The instrument operates by catching the desired charged drops onto a conductive drop collector. As the drops collide on the collector, they release their charge q_n into the electronic circuit. The rate (coulomb/s) of charge q_n transferred to the circuit is prescribed by the number of drops per second landing on the collector. This flow of charge creates a current signal i which is sunk into the circuit and converted into a voltage signal by the first amplifier stage.

The first amplifier stage (OPA111) is designed as a current-to-voltage converter and concurrently as a low pass filter (see figure 5.7). The OPA111 is a low input bias (1 pA max) current operational amplifier which means it will virtually not corrupt our small input current signal.

The task of the filter is to remove the high frequency harmonics caused by the discharge of discrete drops as they collide on the collector. The effect of removing those high frequency is to transform our pulsed current signal such that only the DC component remain. The conversion of the current signal i_d into a voltage signal V_{inter} can simply be done by:

$$V_{inter} = R1 \times i_d = R1 \times q_n \times f_{drop} \qquad (5\text{-}2)$$

where R1 is the Op-Amp feedback resistance.

q_n is the charge on each drop #n

f_{drop} is the number of drops landing on the collector per second.

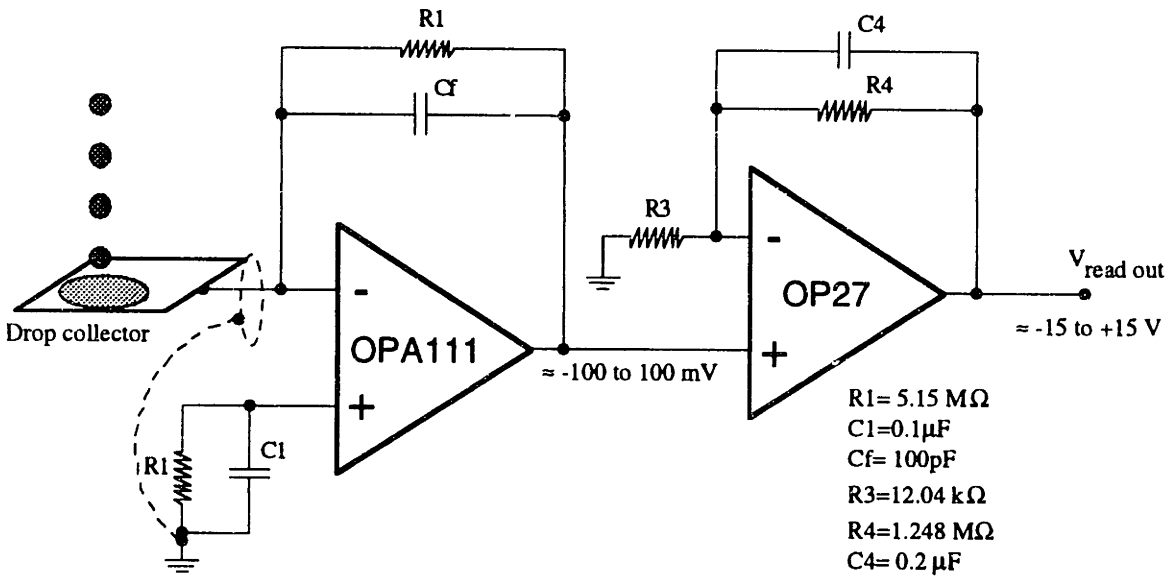

Figure 5.7: Charge collector simplified schematic.

Temperature compensation is also provided (bottom left figure 5.7) to compensate for the resistance fluctuation of R1.

The second stage (OP27) is designed as a standard high precision bipolar amplifier with gain G (see equation 5-3 below) adjusted to amplify our voltage signal in the range ±15 V.

$$G = \frac{R4}{R3} + 1 \qquad (5\text{-}3)$$

The signal V_{inter} had to be amplified such that it could be measured accurately with a standard voltmeter. The second stage acts also as a low pass filter to complete the work started by the first stage. Finally, we can relate the average drop charge $\bar{q}_n$ to the output voltage $V_{read\ out}$ by combining equation 5-2 and 5-3, to give:

$$\bar{q}_n = V_{read\ out} \frac{R3}{R1 \times f_d \times (R3 + R4)} \qquad (5\text{-}4)$$

Using the values showed in figure 5.7 and a drop frequency f_d= 76300 Hz, the expected accuracy from the circuit is about ±10 mV on the output voltage $V_{read\ out}$. This converts into a charge q_n accuracy of ± 2.4×10^{-16} coulomb. A typical drop charge is about 3.0×10^{-13} coulomb, which is ≈1250 time larger than the error.

5.3.4 Other experimental measurement procedures

Measuring binder flow rate

The binder flow rate was measured with a calibrated 2 ml measuring cylinder. The time required to fill the cylinder was recorded several times with a chronometer. The average flow rate Q [ml/min] could than be easily calculated by:

$$Q = \frac{2\ ml}{t_{min}} \qquad (5\text{-}5)$$

or

$$Q = 6 \times 10^{-7} \left(\frac{m^3 \cdot \min}{ml \cdot s} \right) \times \frac{2\ ml}{t_{min}} \ [m^3/s] \qquad (5\text{-}6)$$

The overall accuracy of the flow rate measurements depends mainly on the time measurement accuracy which is about ±1 s. For a typical flow rate of 1.2 ml/min this would translates as $\pm Q = 0.012$ ml/min or ±1% error.

Parameters assumed constant

Diverted stream

Throughout most of the experiments, the stream was assumed to be centered in the charging electrode. If the stream was off-centered or making an angle with the orifice axis, then the experiment was aborted and the printhead was either repositioned, cleaned or simply replaced. More details about printhead maintenance are given in Chris Shutts master thesis (see ref[98]).

Others

Other parameters such as binder temperature, density, and surface tension, orifice diameter,... and other parameters which could have an effect on the experiments were assumed constant. In any case, the effect of most of these parameter is minimized since all the experiments were done in a short period of time and in the same temperature controlled room.

5.4 Drop formation

The droplet formation parameter of a continuous printhead are mainly determined by the piezo resonator frequency f , binder density ρ_{liq} and flow rate Q , and orifice diameter d_0 of the printhead.

5.4.1 Jet speed, drop mass, drop spacing

The jet exit velocity u_0 can be determined from the mass conservation expression by the relation :

$$u_0 = \frac{4Q}{\pi d_0^2} \qquad (5\text{-}7)$$

For typical values of f, Q , d_0 and ρ_{liq} as showed below:

f=77000 Hz

Q= 1.2 ml/min

d_0= 45 μm

ρ_{liq} = 1180 kg/m^3

the exit droplet velocity would be u_0= 12.5 m/s.

Since we know the initial drop speed u_0 and the time lapse between each drops $1/f$, we can now derive the initial drop spacing λ_0 with:

$$\lambda_0 = \frac{u_0}{f} \qquad (5\text{-}8)$$

As a matter of fact, the same expression can be used to determine the drops spacing away from the nozzle assuming we know the value of u_z. Most of the time u_z is unknown, therefore since the drop spacing λ_z can be measured more easily, equation 5-8 would become more useful in the form.

$$u_z = f\lambda_z \qquad (5\text{-}9)$$

Also, since we know the flow rate and the number of drops generated per second, we can determine the drop volume by:

$$\text{Drop Volume} = \frac{\pi D^3}{6} = \frac{Q}{f} \qquad (5\text{-}10)$$

which give a diameter D of:

$$D = \sqrt[3]{\frac{6Q}{\pi f}} \qquad (5\text{-}11)$$

and a drop mass of:

$$m_d = \frac{\rho_{liq} Q}{f} \qquad (5\text{-}12)$$

If we complete the example for our typical values of f, ρ_{liq}, Q, and d_0: then the corresponding typical drop formation parameter would be:

$\lambda_0 \approx 165\ \mu m$

$D \approx 80\ \mu m$

$m_d \approx 3.0 \times 10^{-10}\ kg$

5.5 Drop charging

In order for the computer to control the jet position along the X-axis, the droplets must be charged electrostatically. A charge is applied to a drop as the drop passes through an electrode centered about the jet axis at the nominal stream breakup point. The amount of charge is determined by the relative voltage level applied to the charge electrode. That level is approximately proportional to the amount of deflection desired along the X axis.

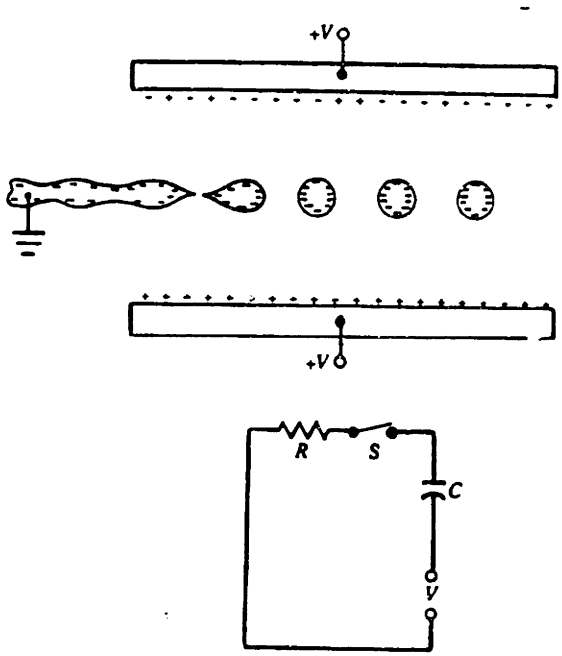

Figure 5.8: (a) Schematic of drop charging, (b) Equivalent electrical circuit.

A stream of binder at the point of breakup located between two parallel-plate electrodes located is shown in figure 5.8 (a) , with the equivalent electrical circuit as in Fig 5.8(b). The conductive binder stream is grounded. The forming drop acts as one plate of capacitor C_1 between the stream and the electrode. When a voltage of the polarity shown is applied to the electrode, a negative charge is induced on the drop and is retained after breakoff until the drop impinges on the powder.

5.5.1 Charging theory

The charge electrode geometry, preferred in this research, was the parallel plate design as opposed to a cylindrical design. Although parallel plates is less efficient, it facilitates

stream alignment, breakup point adjustment and start up procedures since it has an easy access from the side to view the stream of drops with a strobe light.

The magnitude of the droplet charge is determined by the capacitance between the liquid stream center electrode and the conductive charging electrode. For a parallel plate configuration with a center conductor of diameter small compared to the plate spacing, the capacitance is:

$$C = \frac{2\pi \varepsilon_0 \lambda}{\ln\left(\frac{4w_d}{\pi d_0}\right)} \qquad (5\text{-}13)$$

See ref[66] page 316

where ε_0 is the permittivity of free space =8.81 pF/m

λ is the drop spacing [m]

w_d is the charging electrode plate separation [m]

d_0 is the printhead orifice diameter [m]

Notice that the droplet capacitance (and thus the charge on the droplet) is a function of the stream wavelength λ. Changes in the excitation frequency and particularly in the jet velocity will change the charge on the droplet. The charge induced on a single droplet by the applied voltage V_c is:

$$q = -CV_c \qquad (5\text{-}14)$$

where C is the capacitance given by equation 5-13.

This simplified model, although not a rigorous solution to the drop charging problem, proved useful in indicating general trends.

Generalized drop charging model: Using the method of image

In order to improve the accuracy of our drop charging model and also to generalize for non-ideal printing conditions, a more sophisticated charging model is proposed. The model is based on the determination of the electric field around the stream inside the charging cell in order to compute the capacitance of the system. Once the capacitance is known for a particular set of printing condition, the charge induced on the drops can be calculated using equation 5-14.

However, since the configuration of the stream of drops inside the charging cell significantly changes with the flowrate, piezo resonator frequency and amplitude, and stream alignment, it becomes extremely difficult to model the electric field accurately. Even

though numerical methods were used to solve for the electric field in 2D or 3D, the accuracy would not be improved since the shape of the stream itself is not even known accurately. Therefore, simplifying the model with an analytical approach for simpler geometry is sufficient, considering the uncertainty about the stream shape.

The arrangement electrode- stream can be modeled into more or less simpler geometry as showed in figure 5.9 depending on the desired level of complexity.

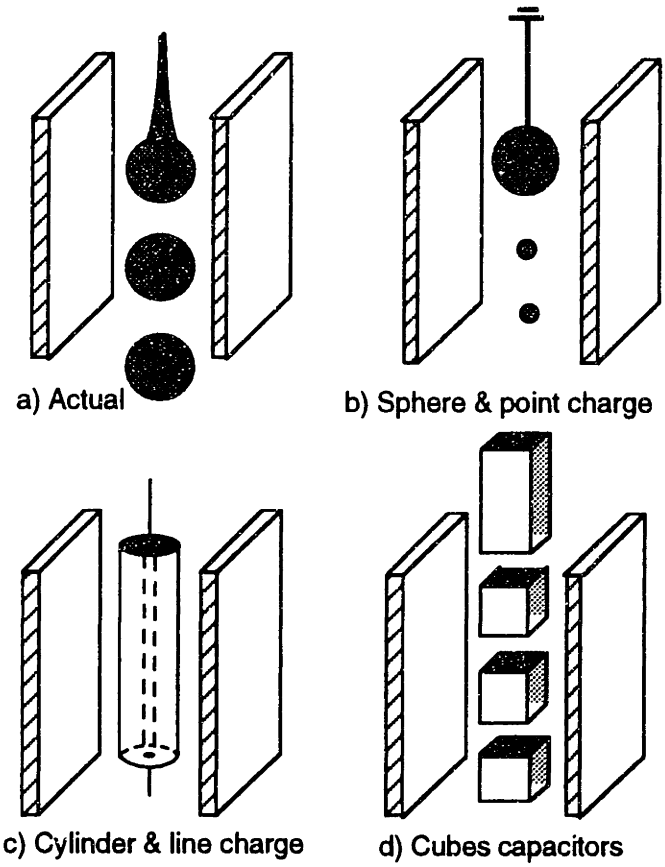

Figure 5.9: Electrode-Stream model a) Actual shape b) Sphere & point charge c) cylinder& line charge d) cubes. capacitors

From the proposed alternatives, the cylinder and line charge model (Figure 5.9c) was preferred since it provided the potential to account for stream misalignment while offering a better fit with the actual stream geometry. Nevertheless, mathematical expressions were also developed for the sphere and cube models and showed as example in Appendix C2 & C3.

Cylinder & line charge model

The main assumption of this model is to approximate the shape of the stream, in the vicinity of the break off point, as an infinitely long cylinder with diameter equal to the average jet width. Assuming the jet to be a continuous charged cylinder allows us to simplify the problem into a two-dimensional model (see figure 5.11). The capacitance of the charging cell will then be defined as a capacitance per unit length of cylinder [Farad/m] .

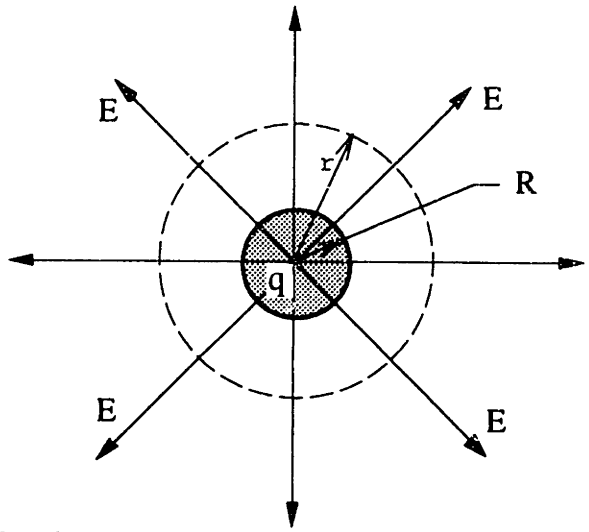

Figure 5.10: Two-dimensional electric field around the stream cross section.

The electric field around a cylinder (see figure 5.10) is equivalent to the electric field around a line charge and can be formulated by the following expression:

$$E = \frac{q'}{2\pi \varepsilon_0 r} \qquad (5\text{-}15)$$

where:

q' is the charge per unit length [Coulomb/m]

ε_0 is the permittivity of free space [8.81 pF/m]

r is the distance from the line charge (not necessarily the center of the cylinder) [m]

R is the average stream radius ($\approx$ drop radius)

The charging electrode itself is modeled as two parallel infinite planes in order to neglect edge effect on the electric field. The radial electric field E of the stream cross section is altered by the two conductive plane of the charging cell (see figure 5.11). In fact, the electric field bends from its radial direction to intersect the charging cell orthogonal to its surface. This field configuration satisfies the boundary condition stating that an electric

field must terminate perpendicular to the surface of a perfect conductor (assuming stream & electrode are good conductors).

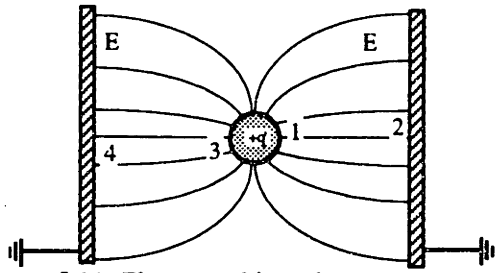

Figure 5.11: Electric field inside the charging cell.

The electric field E can not be determined anymore with the simple equation 5-15 because of its new symmetry. However, a clever method "Methods of images" (introduced by W. Thomson, Papers on electrostatics and magnetism, p.73) can be used in order to simplify the system into a simple interaction between multiple line charges.

The method of images concerns itself with the problem of point or line charge in the presence of boundary surfaces, for example, conductors either grounded or held at fixed potential. It is then possible to infer from the geometry of the situation that a small number of suitably placed charges can simulate the required boundary conditions. The replacement of the actual problem with boundaries (figure 5.11) by an enlarged region with image charges (see figure 5.13) but no boundaries is called the method of images.

In order to apply the method of images, we will have to apply the fixed potential V_c on the stream instead, and keep the charging electrode grounded. This transformation is valid since the charging electrode and the stream are equivalent to two interchangeable plates of a capacitor.

The method of images states that the field between a conducting plane and a line charge must be the same as between two line charges of equal and opposite charge separated by double the distance between plane and given line charge (see figure 5.12).

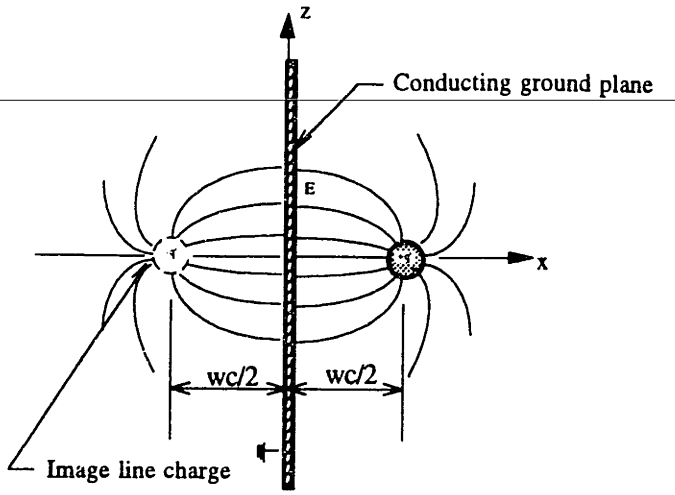

Figure 5.12: Method of image for a single line charge facing an infinite grounded conducting plane.

As a result, the case of a line charge between parallel grounded metal planes requires two infinite sequences of images which are summarized in figure 5.13, giving signs as well as locations of the charges.

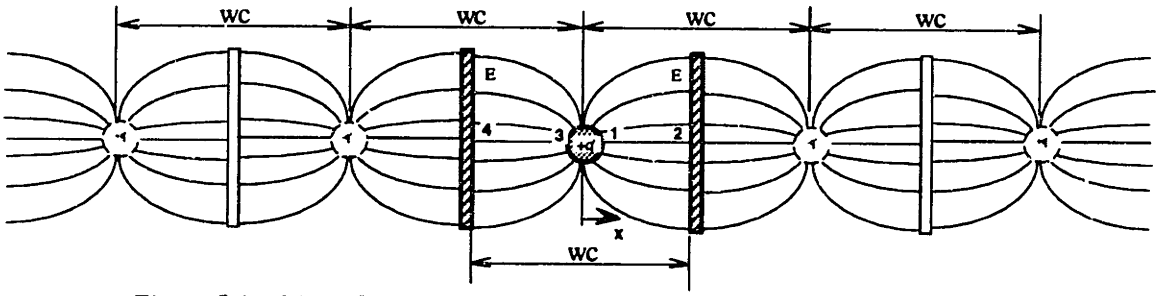

Figure 5.13: Method of images to determine electric field between point 1 and 2.

The electric field from each image E_n contributes additively to the total electric field E situated between point 1 and 2 independently of the two conducting plate forming the charging electrode.

$$E_n = \frac{q'}{2\pi\varepsilon_0(nw_c - x)} \qquad (5\text{-}16)$$

$$E = \sum_{n=-\infty}^{\infty} \frac{(-1)^{n+1} q'}{2\pi\varepsilon_0(nw_c - x)} \qquad (5\text{-}17)$$

The potential difference V_{12} between point 1 and 2 is then a line integral of the electric field from 1 to 2 (see equations 5-18). The X-axis reference coincides with the jet axis to

make point 1 equal to half the diameter of the stream d/2 and point 2 equal to half the charging cell gap $w_c/2$.

$$V_{12} = \int_{\frac{d}{2}}^{\frac{w_c}{2}} E_{12}\, dx = \frac{q'}{2\pi\varepsilon_0} \sum_{n=-\infty}^{\infty} \left[(-1)^{n+1} \ln\left(\frac{w_c\left(n - \frac{1}{2}\right)}{n w_c - \frac{d}{2}} \right) \right] \qquad (5\text{-}18)$$

When equation 5-18 is developed into a series, it gives

$$V_{12} = \frac{q'}{2\pi\varepsilon_0} \left[\ln\left(\frac{w_c}{d}\right) + \ln\left(\frac{2w_c - d}{d}\right) - \ln\left(\frac{3w_c}{2w_c + d}\right) - \ln\left(\frac{4w_c - d}{3w_c}\right) + \ln\left(\frac{5w_c}{4w_c + d}\right) + \ldots \right] \qquad (5\text{-}19)$$

where the linear capacitance C' of the charging cell can be read as

$$C' = \frac{2\pi\varepsilon_0}{\left[\ln\left(\frac{w_c}{d}\right) + \ln\left(\frac{2w_c - d}{d}\right) - \ln\left(\frac{3w_c}{2w_c + d}\right) - \ln\left(\frac{4w_c - d}{3w_c}\right) + \ln\left(\frac{5w_c}{4w_c + d}\right) + \ldots \right]} \qquad (5\text{-}20)$$

The logarithmic series converged rapidly after about 20 terms, however if accuracy is less important, then equation 5-20 reduces to:

$$C' \approx \frac{2\pi\varepsilon_0}{0.244 + \ln\left(\frac{w_c}{d}\right)} \qquad (5\text{-}21a)$$

for value of $w_c >> d$.

An interesting point to make is to compare equation 5-21a to the capacitance of a cylindrical charging electrode with an inner diameter $d_c = w_c$ (equation 5.21b).

$$C' = \frac{2\pi\varepsilon_0}{\ln\left(\frac{w_c}{d}\right)} \qquad (5.21b)$$

In fact, both equations are very similar. With as difference the constant ≈ 0.244 which reduces slightly the capacitance of the parallel plate design because of its weaker electric field.

This equation suggests that the charging cell capacitance depends essentially on the ratio $\frac{w_c}{d}$. The lowest the ratio $\frac{w_c}{d}$, the higher is the capacitance C', which is an important characteristics for a charging electrode in order to minimize the charging voltage V_c for a

given drop charge q. A lower charging voltage V_c is less taxing on the signal amplifier stage of the printhead controller, which in return help to condition the voltage signal with improved timing and accuracy.

For example, the charging cell designed by Chris Shutts (see master thesis ref[98]) (gap w_c=0.00045 m) with an average stream size of about d=80 μm has a linear capacitance of ≈ 28 pF/m for a gap to stream ratio $\frac{w_c}{d}$ of 5.6. The calculation can be repeated for other ratios to give the graph of figure 5.14.

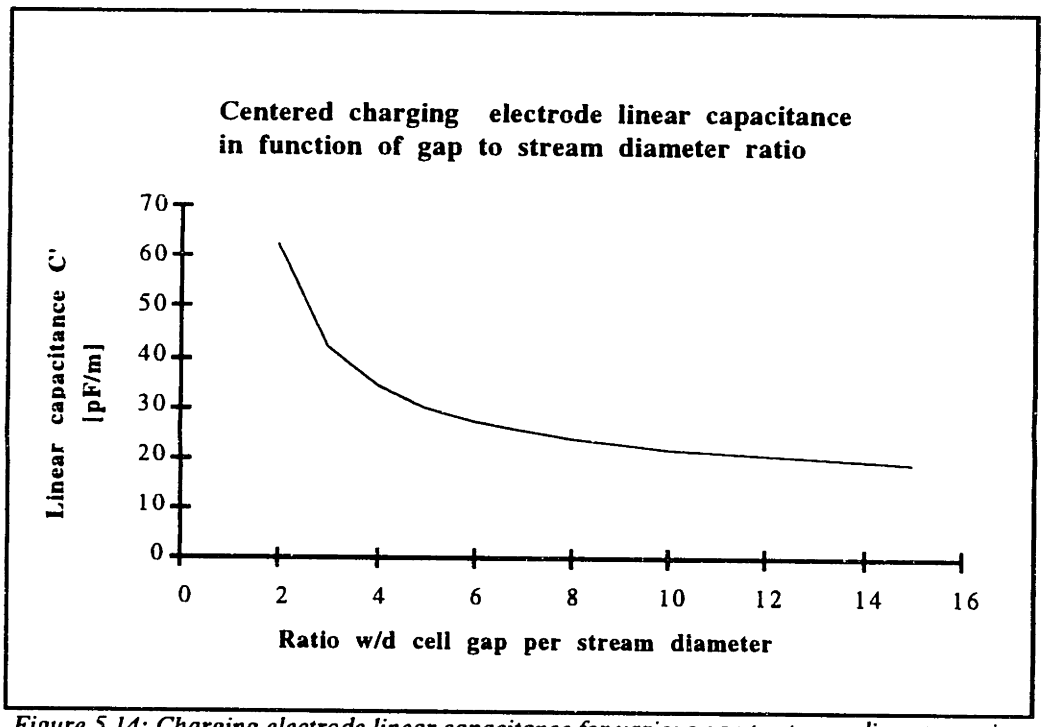

Figure 5.14: Charging electrode linear capacitance for various gap to stream diameter ratio.

At this point there is no need to compare this result with the experimental one, since another effect called "induced charge" affects the final charge of a particular drop (see section on induced charge).

Off-centered stream

The above derivations were done for a stream of binder positioned in the middle of the charging electrode. However, in practice the stream is not always centered in the charging electrode. Using the same approach as for the centered case, a new formulation was developed for the case of an off-centered stream (see figure 5.15).

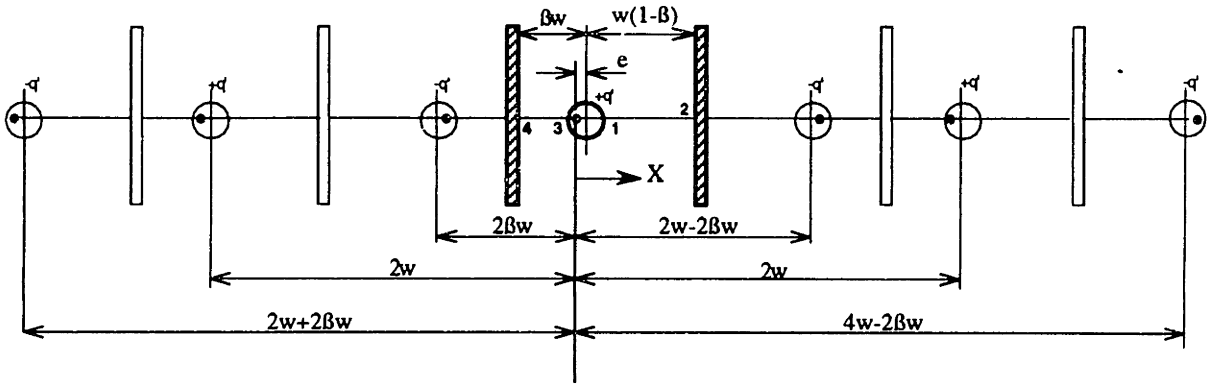

Figure 5.15: Images line charges and limits of integration for the off-centered stream.

This investigation should confirm the sensitivity of the level of charge, transferred to a drop for a given charging voltage V_c, to stream alignment relative to the electrode. The factor of alignment ß is a dimensionless position within the charging electrode where ß =0.5 is in the center of the cell while ß= 0 and 1 correspond respectively to the left and right edge of the cell.

A new concept called "polarization" needs to be discuss for the case of an off-centered stream. In fact, because the images are no longer distributed symmetrically on both side of the stream, the equivalent line charge q of the stream is no longer centered in the middle of the stream cross section (see figure 5.16). In fact, the equivalent charge is shifted by an amount *e* toward the closest edge of the electrode because of polarization effect.

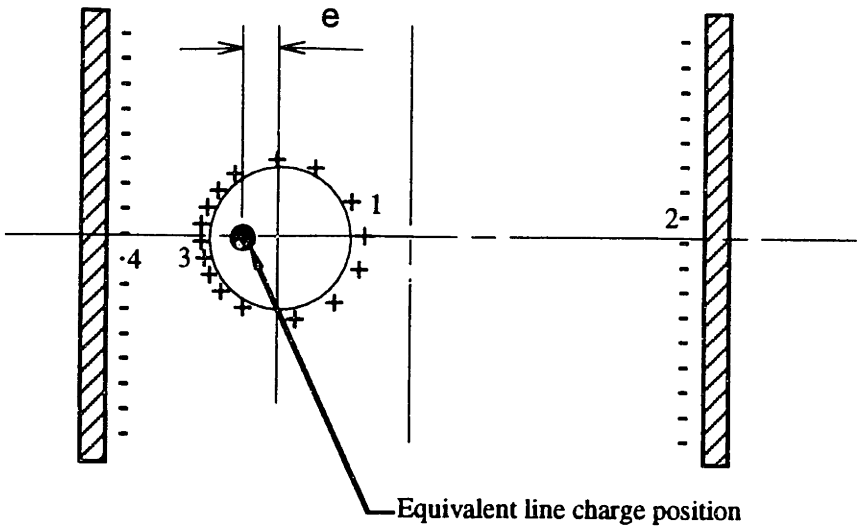

Figure 5.16: Polarization of the stream inside the charging electrode.

The value of e needs to be estimated beforehand since it is needed in the following equations to locate each image charge. The problem is purely geometric, and refers to the electrostatic rule which requires the field lines to terminate perpendicular to the surface of a conductor. Figure 5.17a shows two stream cross sections which represents the actual stream and its nearest image. The idea is to find the radius c of the circle which crosses both stream cross sections at right angle at point $p1$ and $p2$ (see figure 5.17a).

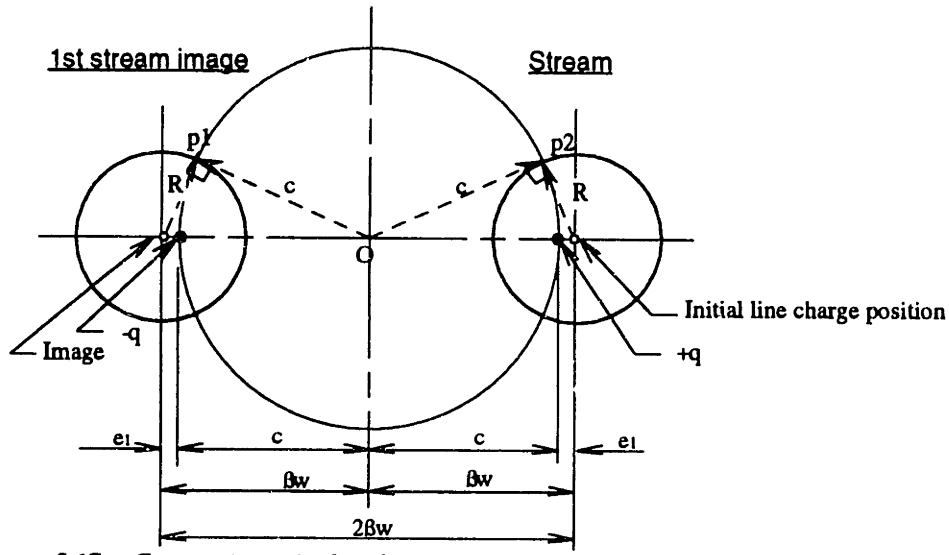

Figure 5.17a: Geometric method to determine the point of line charge equivalent. (First step)

In fact, it was proved (see ref[70]), that the E field, between two line charges or infinite cylinders of equal and opposite charges, is formed of a family of arc segments. Each arc segment has a center of curvature located on an orthogonal line crossing midway

between the two line charge. One of those arcs which has a center of curvature halfway between both charges ^{+}q and ^{-}q forms a complete circle of radius c. Once the radius c has been determined with Pythagore's theorem then the equivalent line of charge offset e_1 is determined by:

$$e_1 = \beta w_c - \sqrt{(\beta w_c)^2 - R^2} \qquad (5\text{-}22)$$

The final offset e needs to be calculated iteratively, since several image charges affect the position of the equivalent line charge (refer to figure 5.15). The calculation should be repeated for the next closest image with a total separation distance corrected with the previous offset e_{n-1} (see figure 5.17b).

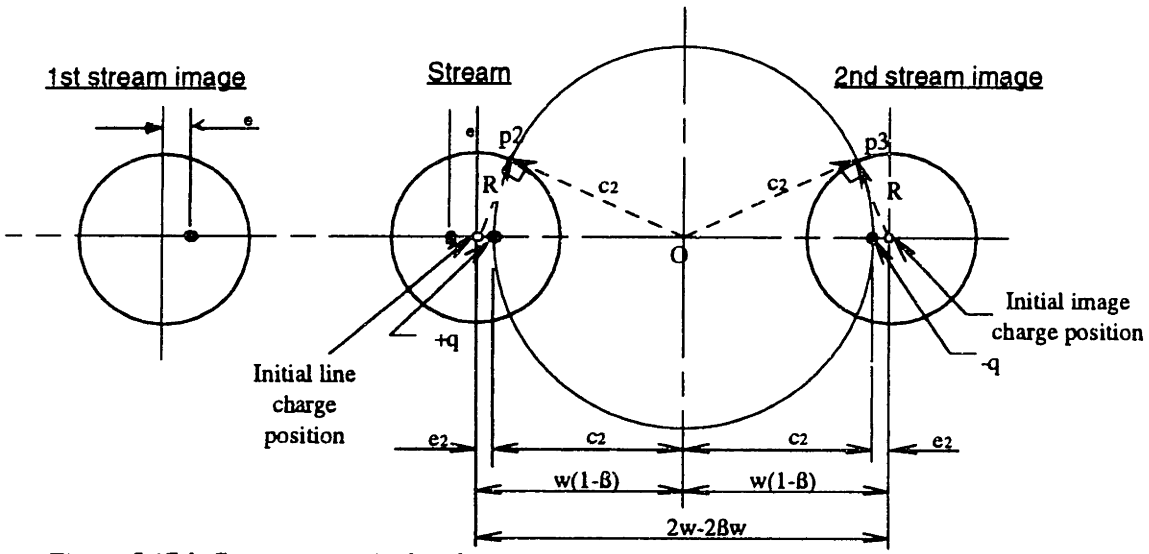

Figure 5.17:b Geometric method to determine the point of line charge equivalent. (Second step)

The series converges very quickly within 1 percent for the 6 first images. For simplicity, the expression can be simplified for its first two iterations which yields an acceptable accuracy (see next equation).

$$e \cong e_1 - e_2 + e_3 - \ldots$$
$$e \approx w_c(1-2\beta) + \sqrt{(\beta w_c)^2 - R^2} - \sqrt{[w_c(1-\beta)]^2 - R^2} \qquad (5\text{-}23)$$

Using the method of image for figure 5.15, we can now determine the electric field inside the charging cell by adding the electric field effect of all the images as before:

$$E = \frac{q'}{2\pi\varepsilon_0}\left[\sum_{i=2n}\frac{(-1)}{iw_c - x} + \sum_{j=2n+1}\frac{(+1)}{w_c(j+1) - 2\beta w_c - 2e - x}\right]$$

(5-24)

for n = -∞ to +∞

Now, we have to integrate E either for V_{12} along the line 1 to 2 or V_{43} along 4 to 3. Since the drop can have only one fixed potential, V_{12} and V_{43} are necessarily equal. The integration limits can be defined as:

Integration limits

$$1 \equiv \frac{d}{2} - e \qquad 2 \equiv w_c(1-\beta) - e$$

$$3 \equiv -(\beta w_c + e) \qquad 4 \equiv -\left(\frac{d}{2} + e\right)$$

The calculation of the drop potential V_c can be determined by either of the following expressions.

$$V_{12} = \frac{q'}{2\pi\varepsilon_0}\left[\sum_{i=2n}(-1)\ln\left(\frac{iw_c - w_c(1-\beta) + e}{iw_c - \frac{d}{2} + e}\right) + \sum_{j=2n+1}(+1)\ln\left(\frac{(j+1)w_c - 2\beta w_c - e - w_c(1-\beta)}{(j+1)w_c - 2\beta w_c - e - \frac{d}{2}}\right)\right]$$

(5-25a)

or

$$V_{43} = \frac{q'}{2\pi\varepsilon_0}\left[\sum_{i=2n}(-1)\ln\left(\frac{iw_c + \beta w_c + e}{iw_c + \frac{d}{2} + e}\right) + \sum_{j=2n+1}(+1)\ln\left(\frac{(j+1)w_c - \beta w_c - e}{(j+1)w_c - 2\beta w_c - e + \frac{d}{2}}\right)\right]$$

for n = −∞ to +∞

(5-26b)

In both case, the value of C' can be read as :

$$C' = \frac{2\pi\varepsilon_0}{\left[\sum_{i=2n}\ldots + \sum_{j=2n}\ldots\right]}$$

(5-27a)

The summation should be done for values of n up to 6 or 8 for sufficient accuracy. A linearization of this problem has been completed in Jim Bredt PhD thesis (see ref[90] Appendix) to reduce the latter expressions to:

$$C' \cong \frac{2\pi\varepsilon_0}{\ln\left[5\left(x - x^2\right)\frac{w_c}{d}\right]} \qquad (5\text{-}27b)$$

where x is the relative position of the jet which can be estimated by:

$$x \cong \frac{\beta - \frac{d}{10w_c}}{1 - \frac{d}{5w_c}} \qquad (5\text{-}28)$$

The accuracy of this expression is subject to the approximation of the linearization including only the five first terms of the summation, and the implicit approximation that the cylindrical geometry accurately represents the shape of the jet in the vicinity of the break off point. When the jet is centered (i.e. ß = 0.5), the expression simplifies to:

$$C' \approx \frac{2\pi\varepsilon_0}{0.2231 + \ln\left(\frac{w_c}{d}\right)} \qquad (5\text{-}21c)$$

Equation 5-21c is similar to equation 5-21a with the exception of the constant 0.2231 which is 0.244 in equation 5-21a. This slight difference comes probably from the linearization done to derive equation 5-21c. Therefore, the constant 0.244 should be more accurate.

If we plot the linear capacitance C' as a function of stream alignment ß, we notice that for ß = 0.4 and 0.6 the linear capacitance will change by about 3%. However, if the stream exceeds those limits than linear capacitance can change by as much as 50 % (see figure 5.18).

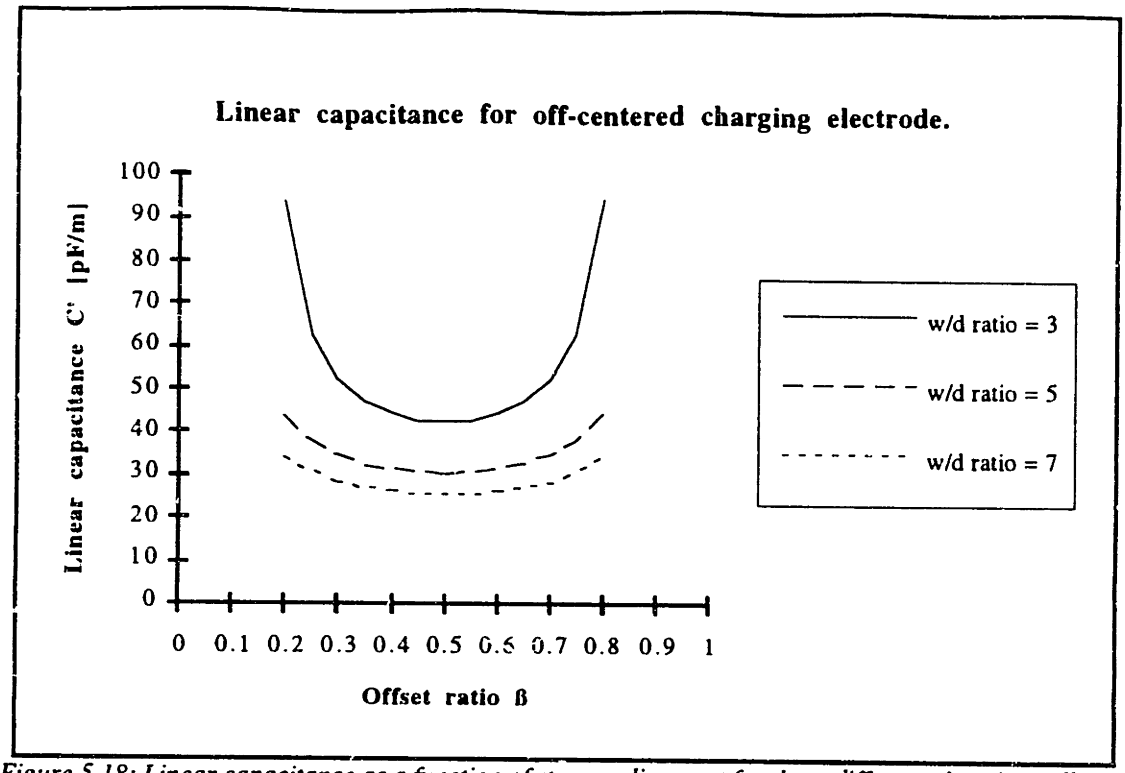

Figure 5.18: Linear capacitance as a function of stream alignment for three different charging cell gap.

It can be seen also from the graph that as the charging cell to stream ratio w/d is increased, the capacitance C' is less sensitive to stream alignment ß. This phenomenon can be attributed to a lower stream polarization level as the ratio or distance between the stream and electrode is increased.

Charge on drops

The amount of charge q remaining on a single drop after break off is proportional to the linear capacitance C', the charging voltage V_c and the drop spacing λ:

$$q = -C'V_c\lambda = C'V_c\frac{4Q}{\pi d_0^2 f} \qquad (5\text{-}29a)$$

where V_c is the charging voltage [V]
Q the flow rate [m3/s]
d_0 is the jet orifice diameter [m]
f is the piezo resonator frequency.

If charge mass ratio is preferred it can be calculated from equation 5-29b. After inspection of equation 5-29b, it may seem that charge/mass ratio is independent of the flow

rate Q. This observation is inaccurate since the capacitance per unit length depends on the stream diameter which in turn is a function of the flow rate and piezo resonator frequency.

$$\frac{q}{m} = -\frac{C'V_c\lambda}{m} = -\frac{4C'V_c}{\rho\pi d_0^2} \qquad (5\text{-}29b)$$

The capacitance C_e of the charging electrode on a single drop, as opposed to the linear capacitance C', is described by the following expression:

$$C_e = C'\lambda \qquad (5\text{-}30)$$

The capacitance C_e was measured by deflecting a single drop every 16 drops out of the main stream. The charge on the drops was measured using the charge collector instrument. Only one drop every 16th was used in order to eliminate induced charge effect. The following graph (figure 5.19) shows the experimental results compared to the model.

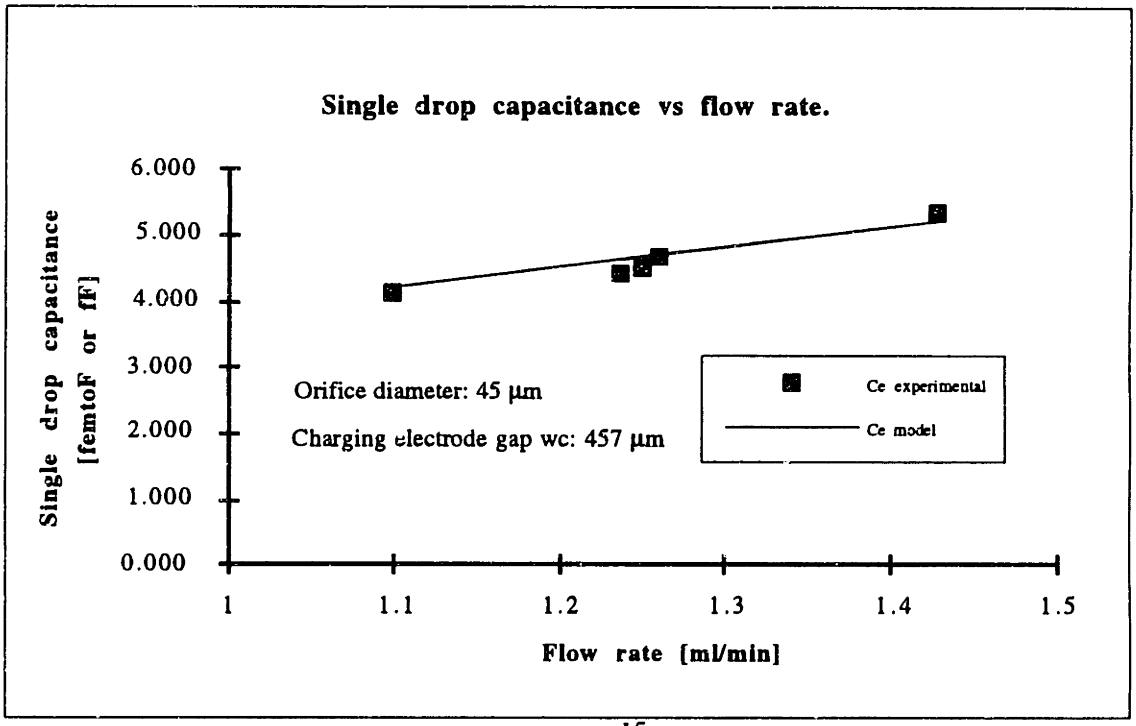

Figure 5.19: Charging cell capacitance [fF or $1x10^{-15}$F] on a single drop for various flow rate.

For more accurate results, the average stream diameter value d used in the capacitance model was computed by normalizing the drop diameter over the drop spacing distance with the following expression.

$$d \approx \frac{2\,D_d^2}{\lambda} \qquad (5\text{-}31)$$

When using the above expression for the average stream size d, the capacitance model agrees with the experiment within 4%. One must consider however that the experimental results themselves contain their own source of error.

Charging synchronization & phase control

A discrete voltage level V_c must be present on the charge electrode for each drop formed. This level must be applied for a sufficient interval prior to drop breakoff for the charge to build up to its desired value; this level must also be maintained until the drop breaks off. When proportional deflection requires a change in the voltage level to a different value for the next drop, the voltage must not change until after the first drop has broken off from the stream.

The timing control between the charge voltage pulse V_c relative to the drop formation cycle is called synchronization. Synchronization makes sure that the correct timing relationship is maintained by adjusting the phase $\emptyset_s$ of the voltage pulse to coincide with the instant of stream breakup (see figure 5.20). The break up instant can be measured from the piezo resonator signal since drop formation has a direct phase relationship with the piezo signal. The synchronization setting $\emptyset_s$ is then defined as the time or phase angle measured from a precise point (rising edge of TTL in this case) on the piezoelectric driving signal waveform.(see figure 5.20)

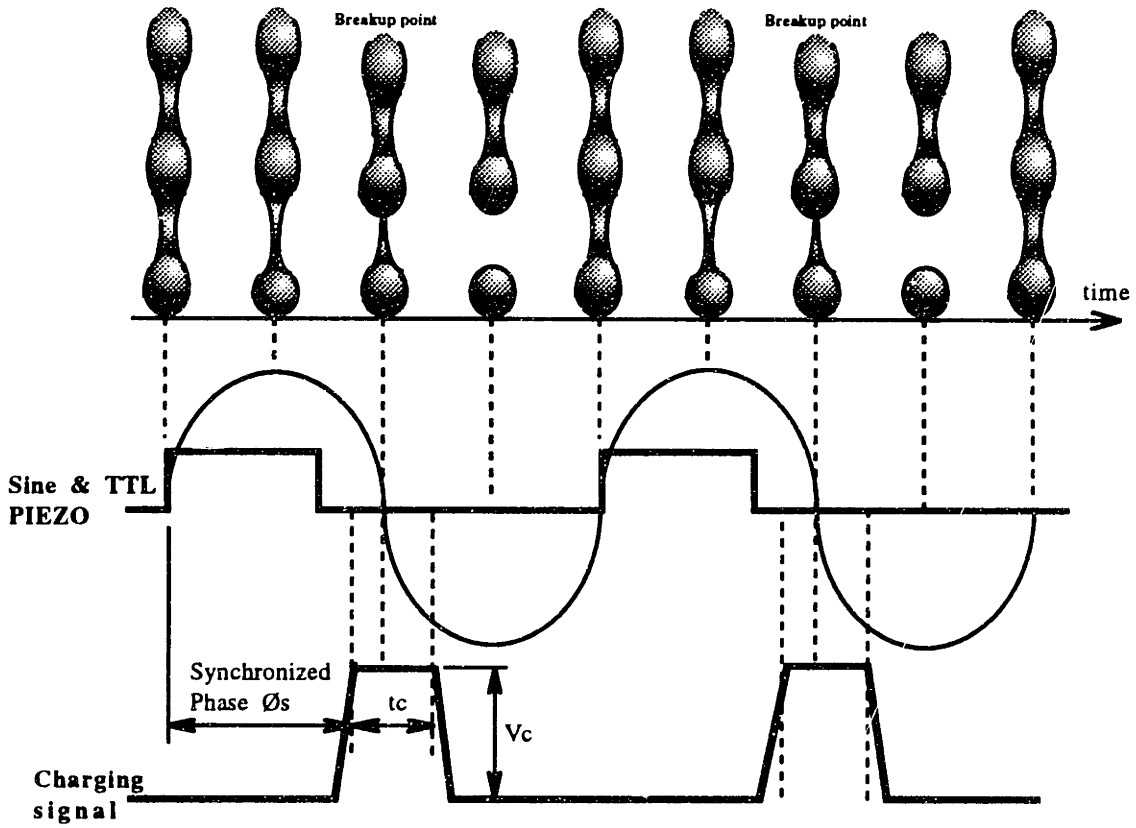

Figure 5.20: Timing diagram of charge synchronization with respect to printhead resonator frequency.

The sine wave and TTL piezo signal comes from a function generator which is preset to the printhead resonator frequency. The phase relationship between the sine wave driving signal and drop formation cycle is not necessarily the same as the one showed on figure 5.20. In other words, breakoff can occur almost anywhere relative to the sinusoidal cycle depending on the conditions.

The charge pulse width t_c is determined from the piezo resonator period T, the charging time constant t_{RC} of a droplet as well as the slew rate V_{SR} of the voltage amplifier driving the charging cell. Since we want to control the charge on each individual drop, t_c needs to be smaller than the period T = 1/f or preferably T/2=1/2f to prevent charging interference. On the other hand, t_c needs to be larger than the time constant t_{RC}; a typical charging time constant is about 5 to 10 nanoseconds. The slew rate V_{SR} of an amplifier corresponds to the rate at which the output voltage can be amplified. [Op-Amp. used in research had a 150Volt/μs slew rate].

For example, if the piezo resonator frequency is 80 kHz and the maximum and minimum charging voltage are +120 and -50V respectively. The maximum charging pulse width t_c would be:

$$t_c \leq \frac{1}{2f} - \frac{2\Delta V_{max}}{V_{SR}} - t_{RC} \cong \frac{1}{160000} - \frac{2\times 170}{150\times 10^6} - 10\times 10^{-9} \cong \ 4\ \mu \text{ second}$$

For the purpose of this research, two different methods were used in order to make sure that the synchronization was performed properly. The first one was done by charging the entire stream with a sequence of short voltage pulses as in figure 5.20. Then, the phase $\emptyset_S$ of the charging signal was varied until a maximum deflection was achieved. The stream deflection was monitored visually using the experimental set-up described earlier.

Another method was to charge the entire stream with the same short voltage pulses as in the previous method, but this time the average charge on the drops was measured instead. By deflecting the drops onto the charge collector instrument (see experimental set-up section 5.3.3), a voltage signal proportional to the drop charge was monitored as the phase $\emptyset_S$ was varied. Proper synchronization was obtained as the voltage read from the instrument was maximized.

Both synchronization methods are equivalent as far as accuracy is concerned or ease of automation. A method to automate the charging synchronization using a visualization technique is described in Chris Shutts master thesis (see ref.98).

Although the timing of the charge voltage pulse can be controlled electronically with sufficient accuracy, stream breakup time varies with binder temperature and pressure and

with drop generator drive voltage, all of which have long-term variations. The correct timing relationship can be maintained by periodically adjusting the phase $\emptyset_S$ of the voltage pulse to coincide with the instant of stream breakup.

Flow rate stability window

Reliable drop charging is possible only for a range of stable printing conditions represented by the right combination of orifice size, flow rate and piezo resonator frequency.

To obtain a stable synchronization a specific range of printing conditions have been measured experimentally by Rayleigh [see ref 66]. It consists of a range located on both side of the Rayleigh stream configuration. The generally accepted range is:

$$3.5 < \frac{\lambda}{d_0} < 7.0 \qquad (5\text{-}32)$$

However, when the liquid stream is stimulated at a uniform frequency near the natural frequency of the droplet stream, a very stable and uniform droplet frequency results. The jet natural frequency is defined as the Rayleigh's frequency:

$$f_n = \frac{u_0}{4.51 \times d_0} \quad \text{where} \quad \frac{\lambda}{d_0} = 4.51 \qquad (5\text{-}33)$$

where d_0 is the printhead orifice diameter, u_0 is the jet exit velocity and λ is the drop separation.

Most of the flow rates used in this research had a configuration ratio $\frac{\lambda}{d_0}$ either smaller or equal to the Rayleigh's ratio of 4.51. This range, although mostly dictated by the Scitex resonator printhead assembly, proved to be better adapted to our printing requirements since it minimizes drop ballistic effects on the powder bed.

Sensitivity to break-off location

As mentioned before, the breakup point of a particular stream may change position as the binder temperature or pressure and drop generator drive voltage shift in time. However, the charging electrode capacitance also changes along its length because of electric field edge effects.

Therefore, drop charging depends on the location of the break up point within the charging electrode. For a parallel plate cell configuration, the maximum charging should occur in the center. It is therefore very important to keep this distance constant throughout the printing session in order to keep drop charging repeatability.

A simple experiment was done on a charging cell with a length to gap ratio L_c/w_c of 6.67 in order to measure the effect of breakup position on the drop charging level. The entire stream of drops excited at its normal frequency f=76300 Hz was charged with a constant voltage V_c= 80 V. The flow rate was also kept constant at Q=1.2 ml/min through an orifice of diameter d_0 = 45μm. (Drop spacing = 165 μm)

Concurrently, the breakup position was varied by slowly changing the amplitude of the piezo resonator driving signal. As the break up position was changed, the charge on the drops was monitored with the charge collector instrument. The results showed that optimum charging was obtained in the middle of the charging cell. The experiment showed also that the charging level could deviate by as much as 2% from the maximum reading.

The charging electrode should appear infinitely long (large ratio L_c/w_c) within the range of expected excursions of the stream breakup point. Otherwise, variations in charging efficiency and induction interaction effects may become unacceptably large.

For more accurate charging, it is then recommended to keep the breakup position constant, near the middle of the charging electrode. Other research have showed that it may be even better to keep the breakup point one third up instead of half way. This way, since the breakup point would be slightly higher inside the charging cell, it would be less affected by the deflection cell strong electric field.

Charging problem with satellite droplets

A stream of drops does not always breakup into a uniform sequence of equal size drops. In fact, a liquid jet breaking up into drops tends to form satellite droplets interspersed among the main drops of the stream. Depending upon various conditions, satellite separation can occur on the fore side of the droplet first, on the back side first, at both ends simultaneously or no satellites at all.

The satellite interaction time, defined as the time between the break-offs of the two ends of a satellite, allows a momentum transfer between the satellite droplet and a main drop of the stream. This transfer alters the velocity of the satellite so that it merges with a main drop: Satellite separation occurring first on the fore side of the droplet results in rear-merging satellites; separation first on the back side causes a forward-merging situation.

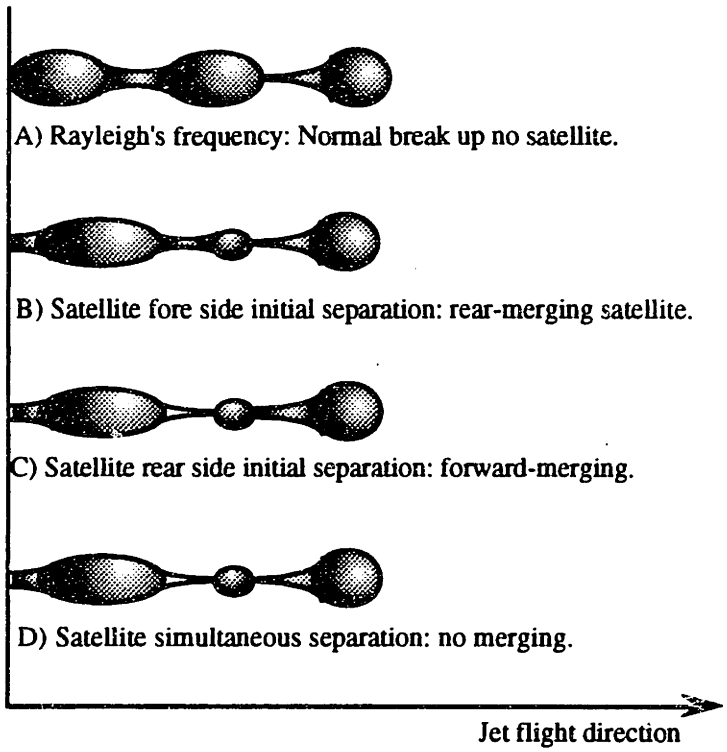

Figure 5.21: a) No satellite break off, b) fore side break off causing rear-merging, c) back side break off causing forward-merging. d) Simultaneous break off: no merging.

At the charging point, each satellite droplet received a charge proportional to the charging voltage pulse V_c targeted for the preceding main drop. Therefore, if the satellite and the previous main drop merge together (forward-merging figure 5.21c), the charge to mass ratio of the combined drop should not differ from the case where no satellite occurred (see figure 5.21a)).

The charge to mass ratio is in fact a direct measure of the amount of deflection experienced by a charged droplet. In order to keep the printing accuracy , we should avoid any change in charge to mass ratio. Case A) and C) showed in figure 5.21 are therefore acceptable and equivalent printing condition, since they do not affect the expected charge to mass ratio.

However, in the case of rear-merging (figure 5.21b)), since the satellite and the following drop have been charged from a different charging pulse, they do not necessarily share the same characteristics. It was even measured experimentally that rear-merging can lower the expected charging level by as much as 5 to 6% depending on the respective charging voltages. This charge decrease effect could be partly attributed to the additional induced charge effect caused by the previous main drop nearby the satellite about to break on its back side. After the fore side of the satellite had snapped, the main drop is free to induce a charge of opposite polarity on the satellite. After the back side is broken the

satellite end up with a lower charge due to induced charge. The merging of this satellite with the following drop would then produce a drop with a lower charge then expected.

Another explanation would be that the satellite of case B) was partially charged because of charge timing uncertainty. Both explanations are conceivable but it is not clear at this point which one is the most probable.

Finally, the case of figure 5.21d is clearly to be avoided, since the satellite, which has a large charge to mass ratio, will not merge and be deflected much farther then other drops. In this event, the satellite droplet will probably accumulate somewhere on the printhead or machine and ultimately cause printing failure.

The solution to the satellite drop problem is to use the right set of piezo resonator signal amplitude and frequency in order to get no satellite as in case A) or forward-merging satellite as in case C). Methods to control satellite droplet have been investigated in the past, and can be found in the IBM references under "Satellite Droplet Formation in Liquid Jet" ref.[63].

Minimum & maximum admissible charge

In order to fix the limits of a charging electrode, it is possible to estimate the maximum and minimum charge that can be transferred on the surface of a single conductive drop .

Since the electric forces generated by the charge on the surface of the drop counteracts surface tension, the drop will disintegrate if the charge becomes too large. This effect was originally treated by Rayleigh (1882) who found the limiting charge q to be

$$q = \sqrt{64\pi^2 \varepsilon_0 r^3 \sigma} \qquad (5\text{-}34)$$

where r is the drop radius and σ the binder surface tension.

For example, assuming the binder to have a surface tension similar to water [7.28e-2 N/m] and a droplet 80 µm in diameter; the maximum charge a droplet could hold before exploding would be 5×10^{-12} coulomb. This latter charge level is larger than the maximum admissible charge related to excessive mutual electrostatic repulsion. It was found (IBM ref[63]) that excessive drop charging causes the drops to repulse each other and disperse the stream into a spray. This limit can be estimated by the following empirical relation:

$$q_{max} = 1.05 \times 10^{-3} \frac{u_0 \, d_j \, \lambda^2}{z_i} \text{ coulombs} \qquad (5\text{-}35)$$

where u_0 is the jet velocity [m/s]

d_j is the jet diameter [m]

λ is the drop spacing [m]

z_i is the distance from breakup to the point at which the average deflection is one drop diameter.

For example, using d_j =45 μm, u_0 = 12 m/s, λ = 160 μm and z_i = 4 mm, the maximum charge q_{max} for stream stability would be about 3.5 x 10^{-12} coulomb.

The total charge present on the surface of a droplet is determined by the excess or lack of electrons (or ions) compared to the neutral level. The minimum charge that can differentiate a neutral drop from a charged drop is one electron charge [1.6026x10^{-19} coulomb]. Knowing the number of electrons for a particular charge can guide us in the design of the charging electrode control electronics, more precisely the digital to analog converter DAC signal generator.

For example, a typical charging electrode induces about 4.5x10^{-13} coulomb on a single drop when a +120 volt charging voltage is applied. This charge represents a total of 2.8 millions electrons in excess on the droplet. If 120 volts represents the maximum voltage used for this printing application, then a total of 2.8 millions control step of 43 μVolts can be used on the charging electrode. Therefore, the best DAC accuracy that will control single electrons would be a 21-bit DAC ($2^{21} \approx$ 2 millions steps); a higher value would be useless. For practical reason however, a 12-bit DAC gives the required accuracy as far as drop positioning is concerned. In that case, each control unit [29mVolts] would induced a total of 680 additional electrons on each single drop.

5.5.2 Induced charge

Introduction

The charge on a forming drop is influenced not only by the charge electrode potential but also by the charges on previously formed drops. This phenomenon called "induced charge" can alter the expected charge on a drop by as much as 20% depending on the conditions.

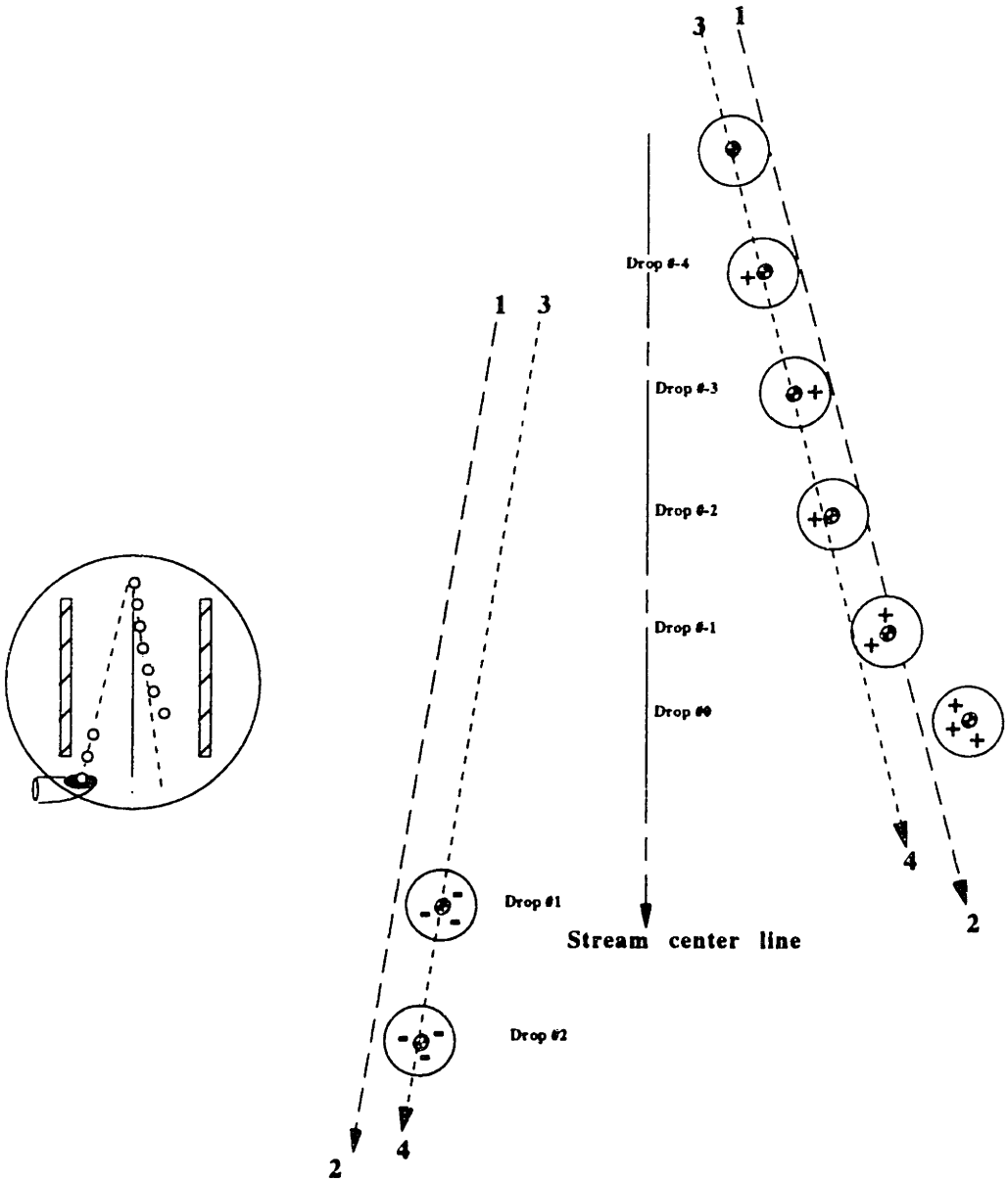

Figure 5.22: Induced charge effect on leading drops and following drops inside deflection cell.

The effect of induced charge on the drop placement accuracy are unacceptable since a 20% error on the charge translates into 20% positioning error. The characteristic shape of a

sequence of printing drops with uncompensated induced charge can be seen in figure 5.22. Induced charge occurs inside the charging electrode, but its effect can be seen only once the drops have traveled through the deflection cell.

Figure 5.22 shows a typical example of what induced charge does to a stream of charged drops. First, if induced charge could be tuned down, then both in-catch (on left) and printing drops (on right) would follow a flight paths similar to line 1-2 showed on the graph (see figure 5.22). However, for long sequence of equally charged drops, a steady state induced charge will always cause an overall decrease of the average drop charge. Therefore the in-catch (left) and printing drops (on right) sequence follow a smaller deflection path similar to lines 3-4 instead (see figure 5.22).

The charge decrease can be physically explained by the charge polarity of the nearby drops and charging electrode. In fact, the drops, ahead of the drop #0 being charged, have a polarity opposite to the polarity of the charging electrode. This opposite polarity counteracts some of the charges induced on drop #0 by the charging electrode itself, decreasing by the same token the expected charging level from the electrode.

Another induced charge effect can be seen at the transition between in-catch drop (drop #1) and leading printing drops (drops #0,#-1,#-2). Since the charge differential between the in-catch and printing drops is relatively important, the charge induced by the trailing in-catch drops on the 2 or 3 leading printing drops is notable. For example, the charge on drop #0 can be increased by as much as 20% of its original value. The characteristic shape of a stream showing significant induced charge is showed in figure 5.22. The three leading drops are forming a characteristic hook shape pointing away from the drop catcher since they hold a higher charge than other drops in the stream. The charge on the leading drop #0, #-1 and #-2 was in fact increased since the in-catch drops have a polarity opposite to the one of the printing drops. Consequently, the preceding drops have the same polarity as the charging electrode, which actually increases the charging potential of the electrode.

Modeling induced charge

Hence, the goal of this section is to develop a better understanding of induced charge in order to predict and counteract its effects.

The induced charge interaction between droplets is through the inter-droplet capacitance (see figure 5.23).

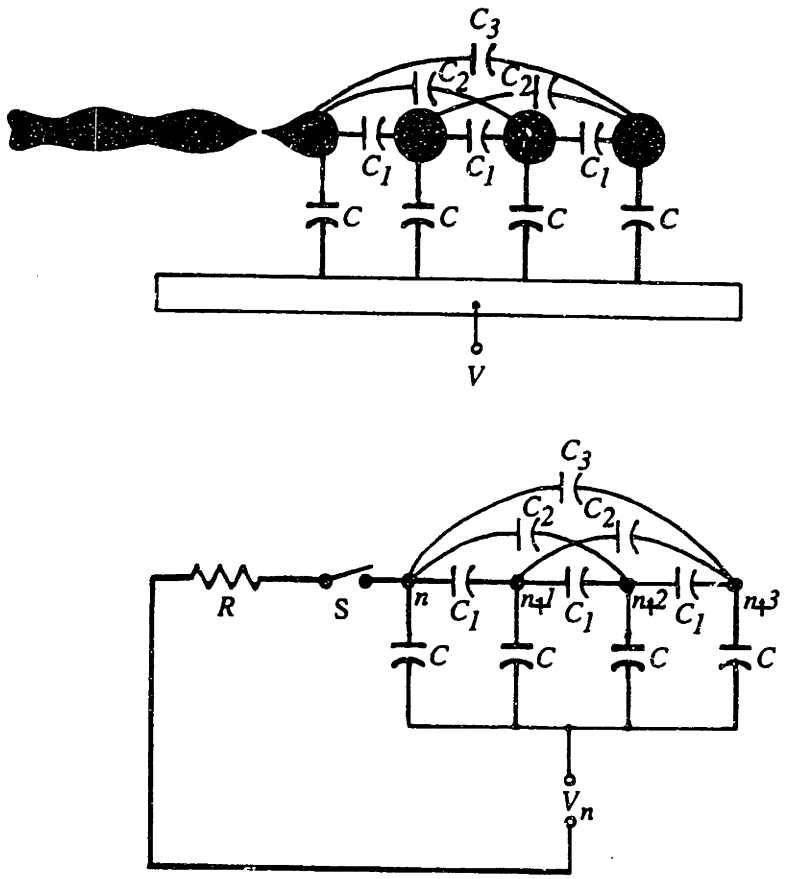

Figure 5.23: Drop charging schematic with induced effects of the three previous drops.
(Principle of non impact printing, Jerome L. Johnson p.318 ref[66])

Node n represents the droplet being formed and charged. Nodes $n+1$, $n+2$, and $n+3$ represent the three previously charged droplets having charges q_{n+1}, q_{n+2}, and q_{n+3}. The capacitance between each droplet and the charging electrode was given by equation 5-26 & 5-30 in the previous section. Capacitors C_1, C_2, and C_3 are the inter-droplet capacitance; R is the fluid resistance in the unbroken stream, and S represents the switch which opens when the droplet separates from the stream.

The charge q_n on the droplet n, is the sum of the charges on the four capacitors connected to node n.. Calculating the capacitance between several drops and two conductive planes, involves the modeling of a complex electric field which can be done

adequately only through numerical methods. Therefore, simplification methods were developed in order to estimate efficiently the charge q_n as a function of the charging voltage $V_{c,n}$ as well as the charge on previous drops.

Model with cubes

The simplest method used to estimate induced charge is by modeling the drops as cubes, where each face of the cube is considered as one plate of a capacitor (see figure 5.24).

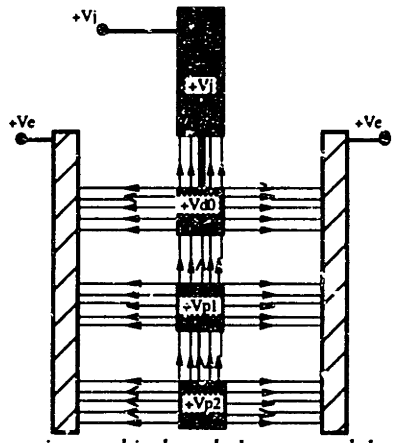

Figure 5.24: Charging and induced charge model with cubes.

This simple method is not accurate since the geometry of the drops and electric field are too much deformed from the reality. Although it is a good first order estimate of the induced charge effect, it should not be used to predict drop charge for accurate printing. The nice feature about this model is that it combines the charging and the induced charge in the same model, which is not the case for the other model described below. The cube model is described in more details in Appendix C3 and comparison results are given later in this section.

5.5.3 Theoretical model of induced charge (Method of images)

A better approach is to model the drops as spheres and point charges (see figure 5.25).

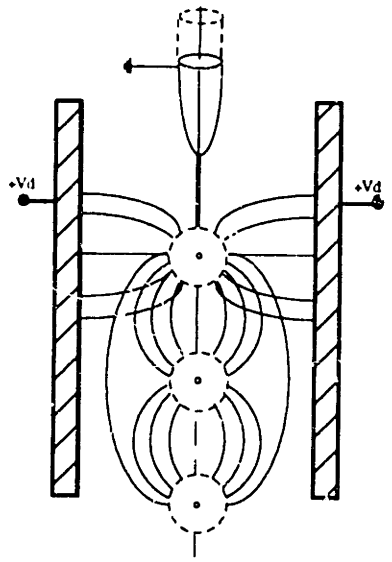

Figure 5.25: Induced charge model with sphere and point charge.

This model is concerned with the charge induced by the preceding drops in addition to the charge induced by the electrode. The calculation of the charge induced by the charging electrode has been covered in a previous section. On the other hand, the charge induced by the preceding drops needs to be evaluated from the polarization level caused by their own electric field on drop #0. In fact, the preceding drops act as a second charging electrode which charge drop #0 proportional to their own charge q_1 and q_2.

A simple method to estimate polarization is done with the method of images (see section 5.8.1 for more details). This time, we must compute the image of a point charge inside a conductive sphere or drop. The basic theory is developed in Appendix C4.

We assume that the charge $q_{0,electrode}$, induced by the charging electrode for a voltage V_c, was computed using equation 5-26. To compute the charge induced by the preceding drops #1 and #2, we need to know the values of q_1 and q_2. A method will be described later on to compute q_1 and q_2, but for now we assume to know their values.

The first step is to define the exact model geometry and sequence of calculation. The model geometry consists in a conductive grounded sphere #0, the size of a drop, followed by another sphere #1 with charge q_1. The last entity situated one drop spacing away from drop #1 is a point charge which is a simplified representation of drop #2 .(see figure 5.26)

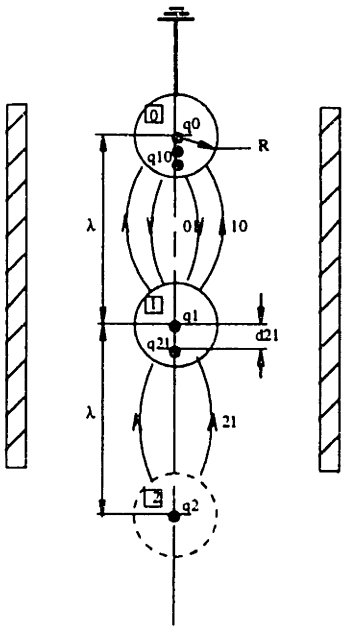

Figure 5.26: Sphere and point of charge schematic.

It could be helpful to read section 5.8.1 beforehand in order to understand the details of the calculations of a point charge image inside a conducting sphere.

We first start by computing the image charge and position of point charge q_2 in drop #1. The image charge $q_{21}^{1,0}$ has a polarity opposite to charge q_2 and is located inside drop #1 at a distance $d_{21}^{1,0}$ from the center of charge q_1 towards q_2. The values of $q_{21}^{1,0}$ and $d_{21}^{1,0}$ are derived from the equations developed in Appendix C4, as followed:

$$q_{21}^{1,0} = -\frac{R}{\lambda} q_2 \qquad (5\text{-}36)$$

$$d_{21}^{1,0} = \frac{R^2}{\lambda} \qquad (5\text{-}37)$$

Since drop #1 is isolated, its total charge q_1 must remain constant. Therefore, the new charge $q_1^{1,1}$ at the center of drop #1 must become:

$$q_1^{1,1} = q_1 - q_{21}^{1,0} \qquad (5\text{-}38)$$

To clarify the notation, the superscript on any charge q or distance d corresponds to the iteration step at which it was computed. The subscripts indicate on and from which drop the image charge was created. For example, $q_{21}^{1,3}$ is an image charge where 21 means

that it was created from drop #2 in drop #1. The 1,3 means that its was 3th image charge calculated within the 1st iteration (see section 5.8.1 for more details)

The next step is to calculate the effect of drop #1 on drop #0. Drop #1 is now modeled as two point charges $q_1^{1,1}$ and $q_{21}^{1,0}$ acting on drop #0 from their respective positions. For the moment, drop #0 is modeled as a conductive sphere with charge q_0. Using the same method, both point charges $q_1^{1,1}$ and $q_{21}^{1,0}$ create their respective image $q_{10}^{2,0}$ and $q_{10}^{2,1}$ inside drop #0 at different position $d_{10}^{2,0}$ .and $d_{10}^{2,1}$ (see equations below)

$$q_{10}^{2,0} = -\frac{R}{\lambda} q_1^{1,1} \qquad d_{10}^{2,0} = \frac{R^2}{\lambda} \qquad (5\text{-}39)$$

$$q_{10}^{2,1} = -\frac{R}{\lambda + d_{21}^{1,0}} q_{21}^{1,0} \qquad d_{10}^{2,1} = \frac{R^2}{\lambda + d_{21}^{1,0}} \qquad (5\text{-}40)$$

Since drop #0 is connected to ground through the unbroken stream, the total charge q_0 can change. Therefore the charge located in the center of drop #0 remains q_0. The first hint of induced charge can be seen as the new total charge $q_0^{2,2}$ is computed by adding to the expected charge q_0 the value of $q_{10}^{2,0}$ and $q_{10}^{2,1}$.

$$q_0^{2,2} = q_0 + q_{10}^{2,0} + q_{10}^{2,1} \qquad (5\text{-}41)$$

In order to improve the accuracy of our induced charge effect estimate, two more image charge iterations should be done. These additional iterations will make sure that polarization has reached an equilibrium level.

The third step is to consider drop#0 as three point charges q_0, $q_{10}^{2,0}$ and $q_{10}^{2,1}$ inducing their image charge into drop #1 which is at its turn a sphere with a centered total charge q_1. (see equation below) It should be noticed that the image charge $q_1^{1,1}$ and $q_{21}^{1,0}$ calculated earlier on are no longer needed at this point.

$$q_{01}^{3,0} = -\frac{R}{\lambda} q_0^{2,2} \qquad d_{01}^{3,0} = \frac{R^2}{\lambda} \qquad (5\text{-}42)$$

$$q_{01}^{3,1} = -\frac{R}{\lambda - d_{10}^{2,0}} q_{10}^{2,0} \qquad d_{01}^{3,1} = \frac{R^2}{\lambda - d_{10}^{2,0}} \qquad (5\text{-}43)$$

$$q_{01}^{3,2} = -\frac{R}{\lambda - d_{10}^{2,1}} q_{10}^{2,1} \qquad d_{01}^{3,2} = \frac{R^2}{\lambda - d_{10}^{2,1}} \qquad (5\text{-}44)$$

$$q_1^{3,3} = q_1 - q_{01}^{3,0} - q_{01}^{3,1} - q_{01}^{3,2} \qquad \text{centered} \qquad (5\text{-}45)$$

Then, back again to drop #0, the 4 point charges of drop #1 induce a set of image charges which should provide the equilibrium charge condition between the drops and the electrode from the following expressions.

$$q_{10}^{4,0} = -\frac{R}{\lambda} q_1^{3,3}$$

$$q_{10}^{4,1} = -\frac{R}{\lambda - d_{01}^{3,0}}\, q_{01}^{3,0}$$

$$q_{10}^{4,2} = -\frac{R}{\lambda - d_{01}^{3,1}}\, q_{01}^{3,1}$$

$$q_{10}^{4,3} = -\frac{R}{\lambda - d_{01}^{3,2}}\, q_{01}^{3,2}$$

$$q_0^{4,4} = q_0 + q_{10}^{4,0} + q_{10}^{4,1} + q_{10}^{4,2} + q_{10}^{4,3}$$

The total charge remaining on drop #0 after break off should be close to the estimate value $q_0^{4,4}$. The expected charge q_0 calculated from the charging electrode equations should be corrected with the charge induced by the two previous drops #1 and #2, which is:

$$q_{induced} = q_{10}^{4,0} + q_{10}^{4,1} + q_{10}^{4,2} + q_{10}^{4,3} \qquad (5\text{-}46)$$

Induced charge can be formulated as a function of drop radius R, drop spacing λ, and charge q_o, q_1, q_2 and a geometric factor K_{geo}.

$$q_{induced} = \text{Induced\_Charge}\left(R, \lambda, q_o, q_1, q_2, K_{geo}\right) \qquad (5\text{-}47a)$$

If we solve equation 5-46 for q_1 and q_2, induced charge can be estimated from the following expression:

$$q_{induced} \approx -\frac{R}{\lambda} q_1 + \frac{R^2}{\lambda^2 + R^2} q_2 \qquad (5\text{-}47b)$$

One important point to notice here is that induced charge is affected proportionally to the square of the distance from a particular preceding charged drop.

Since we assumed that the electrode conductive planes do not reduce the electric field strength between drops, the model is likely to over evaluate the induced charge effect. When compared to experiment, a geometric coefficient K_{geo} can be used to adjust the calculation for a specific charging electrode and flow rate. This factor compensates for the

part of the electric field which was cut by the parallel plane of the electrode. The geometric factor K_{geo} remains constant for a specific flow rate and when used properly improves the accuracy of induced charge estimate to within one percent.[≈1%]

Model assumptions

The polarization model implies that the effect of the electrode and the induced charge produced by the drops are independent and can be treated separately. One assumptions is that most of the induced charge effect is coming from the two nearest preceding drops of the stream; drop #1 and #2. We assumed also that the electrode did not significantly affect or reduce the electric field between the drops. A geometric factor K_{geo} was introduced in order to compensate for the electric field reduction between drops. This coefficient can be determined as a function of the flow rate and drop spacing. Finally, in order to apply the theory of image properly, the ratio charging electrode gap w_c over drop diameter d is assumed to be > 10 and the ratio drop spacing λ over drop radius R should be >4.

Estimating q_1 and q_2

The charge q_1 and q_2 on the preceding drops can be determined by a method referring to the polarization model. As mentioned before, induced charge can be formulated as a function of drop radius R, drop spacing λ, and charge q_o, q_1, q_2 and a geometric factor K_{geo} (see equation 5-46).

The values of R, λ and q_0 can be evaluated from standard expressions, however q_1 and q_2 needs to be evaluated differently since they have themselves been subjected to induced charge effects.

Because the model is to evaluate the induced charge on the leading drop of a sequence of printing drops, drop #1 and #2 are as a result two in-catch drops. Therefore, drop#1 and #2 have the same charge and induced charge level. The induced charge level is the same because drop #1 and #2 are the last of a long sequence of in-catch drops holding the exact same charge.

The steady state induced charge for a sequence of in-catch drops can be calculated by using expression 5.47 iteratively. The resulting induced charge converge rapidly to a steady state within 4 iterations or in other words 4 drops. The charge of drop #1 and #2 can then be calculated by adding the charge produced by the electrode (equation 5-28) to the steady state value of the induced charge (equation 5-46 iteratively).

The iteration starts by calculating the initial charge value q_0 on the drops produced by the charging electrode alone for an applied in-catch voltage V_{cc}.

Step 1: $q_0 = \text{Charge\_Electrode}(d, w_c, V_{cc}, Q, f, \beta)$ see equation 5-26, 5-28

This value is used as initial charge condition for the three in-catch drops:

Step 2: $q_{ind} = \text{Induced\_Charge}(R, \lambda, q_o, q_0, q_0, K_{geo})$

Then the same expression can be iterated as:

Step 3: $q_{ind,(k+1)} = \text{Induced\_Charge}(R, \lambda, q_o, (q_0 + q_{ind,(k)}), (q_0 + q_{ind,(k)}), K_{geo})$

where k is the iteration number.

Step 3 can be repeated about 4 times before reaching a steady state value. The final step is to add the charge value of step 1 and the steady state induced charge of step 3 to give:

Step 4: $q_1 = q_2 = q_0 + q_{ind,(4)}$

As mentioned before, now q_0, q_1 and q_2 can be used in equation 5-46 to evaluate the induced charge on the leading printing drop #0.

Summary

This technique is more accurate than in the case of the cube model. However, the geometric coefficient K_{geo} which changes with flow rate Q and drop spacing λ needs to be measured experimentally for different printing conditions. Therefore, a simplified lookup table of K_{geo} as a function of flow rate and drop spacing is necessary

This method works well for predicting the induced charge on the leading drop #0 or the steady state induced charge on a long sequence of drop with equal charge. The polarization model is better suited to evaluate induced charge on drop #0 for on-off printing, in which case a distinct charge transition occurs between in-print and in-catch drops. Therefore, this model is not intended to be used for proportional deflection printing because it does not have a sufficient accuracy to cope with such fine charging adjustments.

Inductive coupling coefficient approach.

In order to provide fine positioning capabilities using proportional deflection, a more accurate charging model was needed. Since charging is characterized by several variables, which are difficult to measure accurately and vary over time, it is not practical to use a model based solely on the physics of the system. One alternative is to develop an empirical model which combines most varying phenomenon into a few coefficients. This new empirical technique is based on the use of inductive coupling coefficients.

If we refer back to figure 5.23, the charge on droplet n is the sum of the charges on the four capacitors connected to node n:

$$q_n = -C_e V_{c,n} - \alpha\, q_{n+1} - \beta\, q_{n+2} - \gamma\, q_{n+3} \qquad (5\text{-}48)$$

where C_e is the effective capacitance of all the path to node n and α, β, and γ are inductive coupling coefficients. Note that since the polarity of $V_{c,n}$ and q_n are of opposite sign, the coupling terms α, β and γ act to reduce the charge q_n on the droplet. Only three preceding drops are necessary since it will be demonstrated later that the forth inductive coupling coefficient and above can be neglected (≈ 0.000025 and smaller).

The charge on each of four successively charged droplets can be found from equation 5-48 in term of the potential $V_{c,n+i}$ applied to the charging electrode. If several uncharged droplets precede the formation of droplet n+3, there will be no coupling effects upon its charging, then:

$$q_{n+3} = -C_e V_{n+3} \qquad (5\text{-}49)$$

similarly:

$$\begin{aligned} q_{n+2} &= -C_e V_{n+2} - \alpha\, q_{n+3} \\ &= -C_e V_{n-2} + \alpha\, C_e V_{n+3} \end{aligned} \qquad (5\text{-}50)$$

and:

$$\begin{aligned} q_{n+1} &= -C_e V_{n+1} - \alpha\, q_{n+2} - \beta\, q_{n+3} \\ &= -C_e V_{n+1} - \alpha\left(-C_e V_{n+2} + \alpha\, C_e V_{n+3}\right) - \beta\left(-C_e V_{n+3}\right) \\ &= -C_e V_{n+1} + \alpha\, C_e V_{n+2} + \left(\beta - \alpha^2\right) C_e V_{n+3} \end{aligned} \qquad (5\text{-}51)$$

Equation 5-48 then becomes (see ref. 66):

$$q_n = -C_e V_n + C_e\left[\alpha V_{n+1} + \left(\beta - \alpha^2\right) V_{n+2} + \left(\alpha^3 - 2\alpha\beta + \gamma\right) V_{n+3}\right] \qquad (5\text{-}52)$$

Typical values of the coupling coefficients from the 3D printing printhead operated at the Rayleigh's frequency are: α=0.12, β=0.04 and γ=0.005. Since the last inductive coupling γ is relatively small, we can assume that only the three preceding drops have a significant inductive effect on the drop being charged.

Equation 5-49 through 5-52 give the charge on each of the four droplets when the applied potential has not been adjusted to compensate for the induction coupling from the preceding droplets. The next section will cover the strategy to compensate for induced charge effect by adjusting the charging potential in order to get the desired charge on each droplet.

Sensitivity to parameters

Although inductive effects caused by the preceding drops can not be completely eliminated, it can be reduced or compensated for by using the right set of printing parameters. Induced charge can be reduced by increasing the drop spacing. Drop spacing can be increased by either increasing the flow rate or decreasing the piezo resonator frequency. Referring to Coulomb's law, induced charge will be reduced proportional to the square of the distance between the drops.

Finally, induced charge can be reduced by decreasing the charging electrode gap w_c. A narrower charging cell gap will block some of the electric field present between the drops and reduced the crosstalk between drops. This latter approach has to be used carefully since a narrower gap makes charging more sensitive to stream alignment and less reliable as far as flooding is concerned.

After induced charge has been reduced to a minimum, it still need to be compensated for in order to achieve a good printing quality. Next section covers the methods that should be used for each charging model described in this section.

5.6 Induced charge compensation method

5.6.1 Introduction

The goal of induced charge compensation is to established the charging voltage $V_{c,n}$ that will provide any particular drops *n* of the stream with the desired charge. The desired charge is defined as the charge that will make the bulk of the stream follow a flight path similar to line 3-4 showed on figure 5.22. Line 3-4 which represents the flight path of charged drops with steady state induced charge included was chosen as our standard reference for practical reasons. In fact, since line 3-4 represents a stable steady state charge level, drop charge can be measured as a drop position with standard optic or inductive instruments.

Since the steady state induced charge (line 3-4 figure 5.22) is considered as our reference stream position, induced charge compensation will be used only for the first few printing drops (drop #0, #-1, #-2). As it can be seen in figure 5.22, the induced charge effect is amplified for the first few leading printing drops. This amplification, as explained in the introduction of this section, is due to the important charge differential between the in-catch and printing drops. Since the charge on the in-catch drops #1, #2 is usually much higher than on the printing drops, a larger charge is induced on drop #0,#-1,#-2 as a result. However, the effect of in-catch drops rapidly decreases for the next printing drops #-3, #-4,.. following in the stream.

Since each induced charge model approached the same problem differently, they will require a different compensation strategy. Each strategy will be evaluated experimentally in order to establish their respective accuracy for different printing conditions .

5.6.2 Simple approach using method of image model

The goal of this compensation scheme is to align the leading drops #0,#-1 and #-2 with the rest of the printing drop sequence. As we know, the rest of the printing sequence has a charge which is affected by the steady state induced charge. In order to align the printing drops, they should all have the exact same charge. Thus, the compensation scheme will have to determine the new charging electrode potential $V_{c,0} + \Delta V$ which will restore the desired total charge on the drop #0,#-1,...

Say, the in-catch drops are charged from a charging voltage V_{cc} and the printed drops are originally charged with a uniform voltage V_{cp}. According to the charging theory, if a

potential $V_{cp,n}$ is applied to the charging electrode, a charge q_n should be induced on drop #n:

$$q_n = \text{Charge\_Electrode}\left(d,\ w_c,\ V_{cp,n},\ Q, f, \beta\right) \quad \text{(see equation 5-28)}$$

n = 0,-1,-2,... [printing drops]

The same can be said about the in-catch drops:

$$q_m = \text{Charge\_Electrode}\left(d,\ w_c,\ V_{cc},\ Q, f, \beta\right) \quad \text{(see equation 5-28)}$$

m = 1, 2, 3,... [in - catch drops]

Then we need to calculate the steady state induced charge for both drop sequences. These charges have to be calculated iteratively as followed (follow method section 5.5.3):

$$q_{n,(st.ind,k+1)} = \text{Induced\_Charge}\left(R,\lambda,q_n,(q_n + q_{n,(st.ind,k)}),(q_n + q_{n,(st.ind,k)}),K_{geo}\right)$$

$$q_{m,(st.ind,k+1)} = \text{Induced\_Charge}\left(R,\lambda,q_m,(q_m + q_{m,(st.ind,k)}),(q_m + q_{m,(st.ind,k)}),K_{geo}\right)$$

k ≈ 4 - 5 iterations

n ≡ [printing drops]

m ≡ [in - catch drops]

Now the total steady state charge of most of the printing drop sequence is:

$$q_{n,st} = q_n + q_{n,(st.ind)}$$

This charge represents the target charge for all the drops of the printing sequence in order to align them similar to line 3-4 in figure 5.22.

However, the charge on drop #0 is:

$$q_0 = q_n + \text{Induced\_Charge}\left(R,\lambda,q_n,(q_m + q_{m,(st.ind)}),(q_m + q_{m,(st.ind)}),K_{geo}\right)$$

which is usually a higher value than $q_{n,st}$. Therefore, drop #0's charging voltage $V_{cp,0}$ need to be modified in order to compensate for the additional induced charge of drop #0. This can be done by determining the charge difference between drop #0 and the rest of the sequence as:

$$\Delta q_0 = q_{n,(st.ind)} - \text{Induced\_Charge}\left(R,\lambda,q_n,(q_m + q_{m,(st.ind)}),(q_m + q_{m,(st.ind)}),K_{geo}\right)$$

then the compensation charging voltage $\Delta V_{cp,n}$ is computed from the standard charging expression:

$$\Delta V_{cp,0} = \frac{-\Delta q}{C'\lambda} \qquad (5\text{-}53)$$

which give the final compensated charging voltage $V_{cp,0}$ for drop #0 in order to align it with the rest of the stream.

$$V_{cp,0} = V_{cp} + \Delta V_{cp,0} \qquad (5\text{-}54)$$

Such a charging voltage will restore the charge on drop #0 to $q_{n,st}$. The same method can be used to calculate the compensated charging voltage for drop #-1 and -#-2. However, a simple interpolation between drop #0 and drop #-3 would be almost as accurate.

The charging voltage for the other drops (i.e. drop #-3 , -4, ...) remain constant at a value $V_{cp,n}$ which corresponds to flight path 3-4 in figure 5.22.

Note: if the stream needs to be straighten by using a reference charging voltage $V_{straight}$ other than ground, than the reference voltage $V_{straight}$ should be directly added to the charge voltage $V_{cp,n}$ before the beginning of the calculation.

It is important to mention that the above method is valid only for on-off printing (straight lines) where the print drops are grounded or proportionally deflected with a constant charge. Otherwise, if a finer printing resolution is needed, the inductive coefficient ratio method should be used instead.

5.6.3 Compensation method using inductive coefficient ratio model

A simpler and more accurate approach to compensate for induced charge effect is to use the inductive coefficient ratios. This method should be used for accurate drop positioning or special drop sequencing to prevent drop merging. The prerequisite is to have a data bank or a simple look up table of the inductive coefficients as a function of flow rate and piezo frequency. An experiment to build the look up table will be described also later on in this section.

The method was made user friendly, by converting all the different drop charges q into charging voltages V which is more intuitive and easier to manipulate in the control software.

The convention used in this method refers to two different types of charging voltages; the command and the virtual voltage control. The virtual potentials V_n,V_{n+1}, V_{n+2}, V_{n+3},...previously described are the potentials required to achieve the desired droplet deflection when ***none of the adjacent droplets are charged.*** A set of primed command potential V'_n,V'_{n+1}, V'_{n+2}, V'_{n+3},...are now introduced which are the potentials required at the charge electrode ***to compensate for the effects of charged adjacent droplets***.

Charging voltage convention:

Virtual charging voltage V_n

- V_n is the potential which induced a charge q_n when none of the adjacent droplets are charged.

Command voltage V'_n (real voltage applied to the charging electrode)

- V'_n is the potential which induced the same charge q_n while compensating for the effect of induced charge.

First, it is important to note that this model allows the exact control of the charge on each drops. The case described below does not make full use of the model extended possibilities, since it is designed to print straight line segment only. In other words, all the drops part of a printing sequence have the exact same charge. In the case where particular charging pattern are necessary, the method is slightly different and will be covered in more details in next section.

This method relies also on the measurement of a proportionality factor which is basically a calibration procedure done for each individual nozzle of a printhead. The result

of these measurements is to provide the machine controller with a mathematical expression which relates the command voltage V'_n to a deflected stream positions at the powder bed level.

Aligning the leading drops with following drops

The goal of this compensation method is to align all the printing drops along the stream position defined by the command voltage $V'_{cp,ss}$, where "ss" stands for steady state. The command voltage $V'_{cp,ss}$ was determined by using the mathematical expression which relates the command voltage to a desired stream position. When the command voltage $V'_{cp,ss}$ is applied, it gives to the drops the virtual effect of a charging voltage V_{cp} when no adjacent droplet are charged.

Most of the drops (i.e. drop #-3, #-4,...#-N) charged with the command voltage $V'_{cp,ss}$ are already aligned at the right deflected position. When drops are aligned, it means they have identical charge q_{cp} or in other words the same virtual potential V_{cp}. However, because of excessive induced charge caused by the preceding in-catch drops, drop #0, #-1 and #-2 do not have the same charge q_{cp} or virtual potential V_{cp}.

Therefore, we need to determine the command voltage $V'_{cp,n}$ (n=0,-1,-2) that will give the drops the same virtual charging effect V_{cp} as the rest of the drops in the sequence. The command voltage can be calculated by using equation 5-48 as:

$$\begin{aligned} q_0 &= -C_e V'_{cp,0} - \alpha q_1 - \beta q_2 - \gamma q_3 \\ -C_e V_{cp} &= -C_e V'_{cp,0} - q_{ic}(\alpha+\beta+\gamma) \\ -C_e V_{cp} &= -C_e V'_{cp,0} + C_e V_{ic}(\alpha+\beta+\gamma) \\ V'_{cp,0} &= V_{cp} + V_{ic}(\alpha+\beta+\gamma) \end{aligned} \qquad (5\text{-}55)$$

where $q_0=q_{cp}$ is the desired charge on drop #0

C_e is the charging electrode capacitance.

$q_1=q_2=q_3=q_{ic}$ are the charges of the three trailing in-catch drops #1,2 & 3.

α, β & γ are the known inductive coefficient ratio.

V_{ic} is the steady state virtual potential of all in-catch drops #1,..,#N

The only known variables at this point are the printing command voltage $V'_{cp,ss}$, the in-catch command voltage $V'_{ic,ss}$ and the three inductive coefficient ratio α, β & γ. However, according to equation 5-55, we need also to know the values of the virtual potential V_{cp} and V_{ic}. Since we are printing straight lines the value V_{cp} can be calculated with the same equation 5-55 as:

$$q_{cp} = -C_e V'_{cp,ss} - \alpha\, q_{cp} - \beta\, q_{cp} - \gamma\, q_{cp}$$

$$-C_e V_{cp} = -C_e V'_{cp,ss} + C_e V_{cp}(\alpha+\beta+\gamma) \qquad (5\text{-}56)$$

$$V_{cp} = V'_{cp,ss}\,\frac{1}{(1+\alpha+\beta+\gamma)}$$

where the bulk of the drops are charged with the same charge level q_{cp}.

Similarly, in-catch drops are also charge with the same constant charge level q_{ic}. Therefore, V_{ic} can be calculated by the equation:

$$V_{ic} = V'_{ic,ss}\,\frac{1}{(1+\alpha+\beta+\gamma)} \qquad (5\text{-}57)$$

Thus, if we combined equation 5-55 & 5-56 in 5-57 we end up with the command voltage $V'_{cp,0}$ for drop #0:

Drop #0 command charging voltage

$$V'_{cp,0} = \frac{1}{(1+\alpha+\beta+\gamma)}\left[V'_{cp,ss} + V'_{ic,ss}(\alpha+\beta+\gamma)\right] \qquad (5\text{-}58)$$

which will induced a charge q_{cp} equivalent to a virtual voltage V_{cp}. Using the same reasoning, the command voltage $V'_{cp,-1}$ for drop #-1can be found from:

$$q_{-1} = -C_e V'_{cp,-1} - \alpha\, q_0 - \beta\, q_1 - \gamma\, q_2$$

$$-C_e V_{cp} = -C_e V'_{cp,-1} + \alpha\, C_e V_{cp,0} + C_e V_{ic}(\beta+\gamma)$$

$$V'_{cp,-1} = V_{cp}(1+\alpha) + V_{ic}(\beta+\gamma) \qquad (5\text{-}59)$$

Then by combining the same equation 5-55 &5-56 into 5-59 we get:

Drop #-1 command charging voltage

$$V'_{cp,-1} = \frac{1}{(1+\alpha+\beta+\gamma)}\left[V'_{cp,ss}(1+\alpha) + V'_{ic,ss}(\beta+\gamma)\right] \qquad (5\text{-}60)$$

Similarly, the command voltages for the following drops are:

$$V'_{cp,-2} = \frac{1}{(1+\alpha+\beta+\gamma)}\left[V'_{cp,ss}(1+\alpha+\beta)+\ \gamma V'_{ic,ss}\right]$$

$$V'_{cp,-3} = V'_{cp,ss} \qquad (5\text{-}61)$$

$$V'_{cp,N} = V'_{cp,ss} \quad \text{for N} = -3,\ -4,\ldots \text{ to last drop in sequence}$$

As mentioned before, the latter equations are valid only if straight lines sequences are printed.

Non-uniform charging pattern

In the event where the printing drop sequence is not straight or not continuous, a general compensation expression should be developed. To keep the same degree of accuracy as for the above equations, the general form will have to look nine drops forward instead of three. Those additional drops are necessary since there is no steady state induced charge as in the case of a uniformly charged sequence of drops. Nine drops is necessary in order to obtain a good accuracy similar to the one for straight line using three drops only.

The development of the general form involves lengthy algebra and will not be demonstrated here. The basic principles are the same as for the straight line printing except that in this case the charge q_{cp} or virtual voltage V_{cp} are varied in order to create curves or remove drops from a sequence.

As we know, the mathematical expression which relates the command charging voltage $V'_{cp,ss}$ to a particular deflected position is valid for a continuous sequence of equally charged drops. Since a non-uniformly charged sequence of drops does not reach a steady state, we can not used $V'_{cp,ss}$ as a direct function of the stream position. Instead, the stream position need to be represented its virtual voltage V_{cp} which is directly associated to the drop charge q_{cp}.

The general model will refer to the command voltage V'_{cp} by $V'_{c,n}$ instead. The more general charging command voltage $V'_{c,n}$ can represent any type of in-catch or printing charging voltage for the drop #n being charged.

Step one is to compute the command voltage $V'_{c,n,ss}$ that will deflect the entire stream to the desired position. This stream position represent also the desired position for the single drop n.

The second step is to derive the equivalent virtual charging voltage $V_{c,n}$ using equation 5-56.

$$V_{c,(n)} = V'_{c,(n),ss} \frac{1}{(1+\alpha+\beta+\gamma)} \qquad (5\text{-}62)$$

Now we can evaluate the compensated command voltage $V'_{c,n}$ that will provide drop #n with a charge q_c as a function of the 3 preceding drops.

$$V'_{c,(n)} = V_{c,(n)} + \alpha V_{c,(n+1)} + \beta V_{c,(n+2)} + \gamma V_{c,(n+3)}$$

$$V'_{c,(n)} = \frac{V'_{c,(n),ss}}{(1+\alpha+\beta+\gamma)} + \alpha V_{c,(n+1)} + \beta V_{c,(n+2)} + \gamma V_{c,(n+3)} \qquad (5\text{-}63)$$

However, the virtual voltage $V_{c,n+1}$, $V_{c,n+2}$ and $V_{c,n+3}$ also depends on the 3 drops preceding them. Therefore another set of equations of the form showed below can be done for each of the new virtual voltages.

$$\begin{aligned}
V_{c,(n+1)} &= V'_{c,(n+1)} - \alpha V_{c,(n+2)} - \beta V_{c,(n+3)} - \gamma V_{c,(n+4)} \\
V_{c,(n+2)} &= V'_{c,(n+2)} - \alpha V_{c,(n+3)} - \ldots\ldots \\
V_{c,(n+i)} &= \ldots\ldots \\
V_{c,(n+7)} &\approx V'_{c,(n+7)} - \alpha V_{c,(n+8)} - \beta V_{c,(n+9)} \\
V_{c,(n+8)} &\approx V'_{c,(n+8)} - \alpha V_{c,(n+9)} \\
V_{c,(n+9)} &\approx V'_{c,(n+8)}
\end{aligned} \qquad (5\text{-}64)$$

We have now (equation 5-64) 9 equations and 9 unknowns. Then, if we combined those new equations with equation 5-63, we will end up with an approximation of the general form for induced charge compensation of a random charging pattern. The general form is a function of the drop charging command voltages $V'_{c,n+i}$ that were applied on the drops preceding drop #n. The expression can be read as followed:

Induced charge compensation: general form

$$
\begin{aligned}
V'_{c,(n)} \equiv & \frac{1}{(1+\alpha+\beta+\gamma)} V'_{c,(n),ss} \\
& +\alpha\, V'_{c,(n+1)} \\
& +(\beta-\alpha^2) V'_{c,(n+2)} \\
& +(\gamma-2\alpha\beta+\alpha^3) V'_{c,(n+3)} \\
& -(2\alpha\gamma+\beta^2-3\alpha^2\beta+\alpha^4) V'_{c,(n+4)} \\
& -(2\beta\gamma-3\alpha^2\gamma-3\alpha\beta^2+4\alpha^3\beta-\alpha^5) V'_{c,(n+5)} \\
& -(\gamma^2-6\alpha\beta\gamma-\beta^3+4\alpha^3\gamma+6\alpha^2\beta^2-5\alpha^4\beta-\alpha^6) V'_{c,(n+6)} \\
& +(3\alpha\gamma^2+3\beta^2\gamma-12\alpha^2\beta\gamma-4\alpha\beta^3+5\alpha^4\gamma+10\alpha^3\beta^2-6\alpha^5\beta+\alpha^7) V'_{c,(n+7)} \\
& +\begin{pmatrix} 3\beta\gamma^2-6\alpha^2\gamma^2-12\alpha\beta^2\gamma-\beta^4+20\alpha^3\beta\gamma-6\alpha^5\gamma \\ +10\alpha^2\beta^3+15\alpha^4\beta^2+7\alpha^6\beta-\alpha^8 \end{pmatrix} V'_{c,(n+8)} \qquad (5\text{-}65) \\
& +\begin{pmatrix} \gamma^3-4\beta^3\gamma-12\alpha\beta\gamma^2+10\alpha^3\gamma^2+30\alpha^2\beta^2\gamma \\ -30\alpha^4\beta\gamma+7\alpha^6\gamma+5\alpha\beta^4-20\alpha^3\beta^3+21\alpha^5\beta^2-8\alpha^7\beta+\alpha^9 \end{pmatrix} V'_{c,(n+9)}
\end{aligned}
$$

The above expression can be easily implemented in the control software in order to compensate for induced charge effects for various charging sequence. Because some terms of the equation are rather small, the general form can be simplified by removing the terms with a power of 5 and above if necessary.

The basic assumption of the inductive coefficient ratio model is that induced charge is caused mostly by the three drops preceding the drop being charged. The assumption is based on the fact that the third drop influences the total induced charge by only 0.5% of its charge. The effect of a fourth drop would translate into an induced charge somewhere

around 0.0025% of its own charge which is already more accurate than the charging signal itself. This estimate of the fourth coefficient could be made since it relates to the square of its distance from the drop being charged. Since the third coefficient is in the vicinity of 0.5%, the fourth factor should be $(0.005)^2$x 100% = 0.0025%.

Effect of electrostatic forces on induced charge compensation accuracy

The above model is valid as long as drop interaction forces remain low. Problems arise when electrostatic forces become significant compared to the charging cell electric field force. In fact, if the charge differential between in-catch and printing drops is too large, inter-drop electrostatic forces will affect the flight path of the leading drop #0 and #-1. An excessive charge differential will create a strong electrostatic attraction force between drop #1, #2 and drop #0 and #-1 following Coulomb's law. This attraction force retards the deflection of both drop #0 and #-1 and causes the induced charge model to underestimate the required charge to reach the desired deflected position.

To judge whether or not the charge differential is too large, one can analyze the electrostatic merge curve for the desired charging condition (refer to section 5.8.2). If the graph of drop spacing (between drop #0 and #1) as a function of time of flight shows a decreasing drop spacing, it means that charge differential is too large.

Although it is possible to compensate for the electrostatic forces, it creates more steps and an additional source of error to our charge estimate. Therefore, it is easier to modify the printing condition in order to reduce, and even eliminate the problem. The solution is to increase the drop spacing by decrease the piezo resonator frequency, increase the flow rate or even using a narrower charging cell gap w_c.

5.6.4 Method to measure α, β, γ factor

The induced charge compensation method assumes we know the values of the three inductive coefficient ratios. The value of those ratios varies according to the printhead geometry, the flow rate and piezo resonator frequency. We have shown previously that modeling accurately such ratios, is not practical because of the complex geometry of the problem. Therefore, measuring the ratios is an elegant way to combine the complexity of the problem into few inductive coefficient ratio.

Since the ratios vary significantly with the flow rate and piezo resonator frequency, we must build a simple look up table for all the desired printing combinations. Since the range of jet stability is rather narrow the look up table remains small.

This section will describe the experimental method that was used successfully to determine the three inductive coefficient ratio.

Four drops method with charge collector instrument

The experiments relies on the principles discussed in section 5.6.3. It consists in four distinct steps where one, two, three and four drops, out of a sequence of 16 drops, are deflected onto the charge collector instrument. The total charge per drop sequence is recorded for each step and used to calculate the charging cell capacitance C_e and eventually the three inductive coefficient ratio.

For example, we start the experiment by deflecting one drop out of a 16 drop sequence on the charge collector instrument with a charging voltage V'_{cp} of 60 V. The fifteen other drops have no charge, therefore the single drop being deflected as no induced charge effect caused by other drops.

Since no induced charge effects affect the charge of the drop, the charging cell capacitance can be determined by:

$$C_e = \frac{-q_{1\,drop}}{V'_{cp}} \qquad (5\text{-}66)$$

The value of $q_{1\,drop}$ was determined by the expression relating the voltage read on the charge collector instrument to the charge on the drop. As a reminder, the equation is in this case:

$$q_{1\,drop} = \frac{V_{collector}}{GR_1 f_s} \qquad (5\text{-}67)$$

where G is the amplifier gain ≈ 104.65

R_1 is the feedback resistor ≈ 5.15 x10^6 Ohms

f_s is the sequence frequency which is the piezo frequency divided by the number of drops in the sequence = 76300/16 ≈ 4768 Hz

The second step is to deflect two drops onto the charge collector using the same charging voltage V'_{cp}. This time the second drops hold a lower charge because of induced charge effect by the leading drop. On the other hand, the leading drop still hold the same amount of charge as in step one. The value of α can be derived by adding the value of q_0 and q_{-1} and equating it to $q_{2\,drops}$, as follows:

$$q_0 = -C_e V'_{cp}$$
$$q_{-1} = -C_e V'_{cp} - \alpha q_0 = -C_e V'_{cp} + \alpha C_e V'_{cp}$$
$$q_{2\ \text{drops}} = q_0 + q_{-1} \qquad (5\text{-}68)$$

The value of the first inductive coefficient α is found to be:

$$\alpha = \frac{q_{2\,drops}}{C_e V'_{cp}} + 2 \qquad (5\text{-}69)$$

The next step is to deflect three drops onto the charge collector instrument. Using the same reasoning as above and our new ratio α, the second inductive coefficient ratio β is found as:

$$\beta = \frac{q_{3\ \text{drops}}}{C_e V'_{cp}} + 3 - 2\alpha + \alpha^2 \qquad (5\text{-}70)$$

And finally, by deflecting four drops onto the charge collector we can derive the third and last inductive coefficient ratio γ with:

$$\gamma = \frac{q_{4\ \text{drops}}}{C_e V'_{cp}} + 4 - 3\alpha - 2(\beta - \alpha^2) - \alpha^3 + 2\alpha\beta \qquad (5\text{-}71)$$

Optical method with linear camera

Another method which does not require any contact with the stream can be used to measure the inductive coefficient ratios. In this method a sequence of sixteen drops is used, out of which 8 drops are fully charged in-catch with charging voltage $V'_{ic,ss}$, and eight other drops are uncharged in-print charging voltage $V'_{cp,ss} = 0V$. The linear camera is focused on the uncharged sequence of drops. If no induced charge compensation is used the camera should see four peaks corresponding to four distinct levels of drop deflection in the stream due to induced charge effect on the 3 leading drops.

The task is to align the three leading drops with the rest of the stream by adjusting the charging voltage $V'_{cp,n}$ on the three leading drops (n=0,-1 and -2). The alignment is attained when the linear camera sees a single narrow peak (narrowest peak) which represents a train of 8 aligned drops. The charging voltages can be determined visually by iteration or from a software package which does it automatically. The results of the

following experiments are summarized as five charging voltage, $V'_{ic,ss}$, $V'_{cp,ss}$, $V'_{cp,0}$, $V'_{cp,-1}$ and $V'_{cp,-2}$. Then, the following set of three equations (5-69b to 5-71b) can be solved for α, β and γ.

$$\left(V'_{cp,0} - V'_{ic,ss}\right)\cdot\alpha + \left(V'_{cp,0} - V'_{ic,ss}\right)\cdot\beta + \left(V'_{cp,0} - V'_{ic,ss}\right)\cdot\gamma = V'_{cp,ss} - V'_{cp,0}$$

$$\left(V'_{cp,-1} - V'_{cp,ss}\right)\cdot\alpha + \left(V'_{cp,-1} - V'_{ic,ss}\right)\cdot\beta + \left(V'_{cp,-1} - V'_{ic,ss}\right)\cdot\gamma = V'_{cp,ss} - V'_{cp,-1}$$

$$\left(V'_{cp,-2} - V'_{cp,ss}\right)\cdot\alpha + \left(V'_{cp,-2} - V'_{cp,ss}\right)\cdot\beta + \left(V'_{cp,-2} - V'_{ic,ss}\right)\cdot\gamma = V'_{cp,ss} - V'_{cp,-2}$$

(5-69b to 5-71b)

where $V'_{cp,0}$ is the command voltage on drop 0
$V'_{cp,-1}$ is the command voltage on drop -1
$V'_{cp,-2}$ is the command voltage on drop -2
$V'_{cp,ss}$ is the command voltage on drop -3 and others
V'_{ic} is the command voltage for in-catch drop or drop 1, 2, ...
α, β and γ are respective the first, second and third inductive coefficient ratio

For example, the results of table 5.6 can be used to verify the validity of this method. For example, table 5.6 would give;

$V'_{ic,ss}$= 60 V,
$V'_{cp,ss}$ = 0V,
$V'_{cp,0}$= 8.035 V,
$V'_{cp,-1}$= 1.891 V and
$V'_{cp,-2}$= 0.236 V

When equations 5-69b to 5-71b are solved with the charging voltage values of table 5.6 to 5.8 we should get the same results for α, β and γ since all the measurement were done for same flow rate condition. (see table below):

From	Table 5.6	Table 5.7	Table 5.8
α=	0.128	0.124	0.123
β=	0.034	0.028	0.027
γ=	0.0045	0.006	0.0045

These numbers are also supposed to match the inductive coefficient ratio measured with the charge collector instrument in table 5.5. The above values were also used to

predict stream alignment charging voltage. When optically measured, the coefficient α, β and γ produced in general ***more accurate*** stream position alignment then when they were measured with the charge collector instrument. However, precautions should be taken with the printing conditions used. In fact, electrostatic repulsion and attraction forces between drops must be minimized to obtain good accuracy. To achieve that goal, drop charge should be kept to a minimum while deflection voltage V_d should be maximized.

Importance of centered jet

One factor often taken for granted is the alignment of the stream inside the charging electrode. However, alignment significantly affect the values of the three inductive coefficient ratios for a given flow rate and piezo resonator frequency. This variation is due to the variation in the electric field strength between the drops. The field will in fact decrease which as a result reduce the values of the inductive coefficient ratios.

Therefore, if a simple look up table of α, β and γ as a function of flow rate and piezo resonator frequency is used, we better make sure that the stream is well aligned inside the charging electrode. Otherwise, the measurement of the ratios α, β and γ should be done on a regular basis simultaneously with the printing. Typical values of α, β and γ are respectively about 0.15 to 0.20, 0.02 to 0.05 and 0.004 to 0.005.

5.6.5 Accuracy of model vs. experiment

The various methods to evaluate the level of induced charge were compared against the experimental results in order to establish their accuracy.

All the experiments were done with the same printhead and printing conditions showed in table 5.1.

Table 5.1: Experimental typical printing conditions.

Piezo resonator frequency [Hz]	76300
Orifice diameter [μm]	45
Charging electrode width wc [μm]	455
Charging electrode length lc [μm]	3000
Deflection cell width wd [μm]	1500
Charging voltage Vc [V]	60 & 80
Deflection cell voltage Vd [V]	2000 & 1000
Charge collector gain [xG]	104.65
Charge col. feedback res. [Ohm]	5.15 e6

Experiments with the method of image model

The experiment was to deflect all but 8 drops out of a sequence of 256 drops with a constant charging voltage V'_{ic}= 60 volts. The sequence of eight drops (i.e. drop #0 to drop #-7) were not charged or in other words, were charged by a grounded potential V'_n = 0 volt. Then, the charging voltage of drop #0 & #-1 were adjusted with V'_0 and V'_{-1} in order to compensate for induced charge and align the two leading drops with the rest of the sequence. The voltages were recorded (see table 5.2 column 3 and 5) and used to calculate the experimental overall induced charge on drop #0 [see table 5.2 column 6]. The overall induced charge effect x on drop #0 is caused by the summation of all the individual effects of the previous in-catch drops. The value of x corresponds to the fraction of the previous in-catch drop charges which appears in drop #0 as induced charge. If we refer to the ratio model, the overall induced charge can be determine as: $x = \sum(\alpha, \beta, \gamma, ...)$.

The percentage of the in-catch drops charge x induced on drop #0, was calculated from the following equation:

$$q_0 = C_e V'_0 - \alpha q_1 - \beta q_2 - \gamma q_3 - \ldots = 0$$
$$= C_e V'_0 - (\alpha + \beta + \gamma + \ldots) q_{ic} = 0$$
$$= C_e V'_0 - x q_{ic} = 0$$
$$= C_e V'_0 - x C_e V_{ic} = 0$$
$$= C_e V'_0 - \frac{x C_e V'_{ic}}{1+x} = 0 \qquad (5\text{-}72)$$

therefore

$$x = \frac{V'_0}{V'_{ic} - V'_0} \times 100\%$$

where q_0 is the desired charge on drop #0

V'_0 is the command voltage applied on drop #0 to compensated for induced charge, or in other words, to keep the charge $q_0 = 0$.

$q_1 = q_2 = q_3 = q_{ic}$ is the charge on the in-catch drops

V'_{-1} is the command in-catch voltage = 60 volts constant.

x% is the percent of charges q_{ic} that is induced on drop #0.

Since all the drops preceding drop #0 hold exactly the same charge q_{ic}, their respective inductive effect on drop #0 can be summed into the single value x.

Thereafter, the physical model using the method of images of section 5.5.3 was used to evaluate the steady state charge q_{ic} and the induced charge on drop #0. The modeled percent of induced charge [column 5 table 5.2] was then compared to the experimental one [column 6 table 5.2] to calculated the charging cell geometric coefficient K_{geo}.

$$K_{geo} = \frac{\text{Experimental\_ Induced charge } x_{exp}}{\text{Modeled\_ Induced charge } x_{model}}$$

Table 5.2 Induced charge on drop #0 evaluated by the physical model.

Flow rate [ml/min]	Model charging electrode cap. Ce [F]	Model steady state charge qic @ V'ic = 60 V	Model drop #0 induced charge Δq	Model x model induced charge on drop #0	Experiment x exp. induced charge on drop #0	Geometric coeff. Kgeo.
1.1	-4.20E-15	-2.01E-13	7.69E-14	38.3%	17.9%	0.467
1.2	-4.52E-15	-2.21E-13	7.97E-14	36.1%	15.5%	0.427
1.25	-4.68E-15	-2.30E-13	8.11E-14	35.2%	15.0%	0.427
1.26	-4.71E-15	-2.32E-13	8.13E-14	35.0%	14.3%	0.408
1.428	-5.22E-15	-2.65E-13	8.53E-14	32.2%	14.2%	0.440

For information only, the cube model described in Appendix C3 gave the following results for the induced charge coefficient x on the leading drop #0:

Table 5.2b: Results from the cube model described in Appendix C3.

Flow rate [ml/min]	Cube model induced x charged coeff. on drop #0
1.1	0.79
1.2	0.77
1.25	0.76
1.26	0.76
1.428	0.72

As it can be seen, the cube model is definitely not as accurate as other model described here, probably because the electric field model is too far from the reality.

The method of image model was also used to calculate the induced charge on drop #-1 (see table 5.3). In this latter case, drop #0's charge was the modeled induced charge of table 5.2 [column 4].

Table 5.3: Induced charge on drop #-1 evaluated by the physical model.

Flow rate [ml/min]	Model drop #-1 induced charge Δq	Model %q induced charge on drop #-1
1.1	5.97948E-15	3.0%
1.2	7.35392E-15	3.3%
1.25	8.00278E-15	3.5%
1.26	8.12684E-15	3.5%
1.428	1.01276E-14	3.8%

Knowing the geometric factor K_{geo}, we can now predict the charging command voltage V'_0 and V'_{-1} that will compensate for induced charge and align the sequence of 8 drops. The voltages were simply calculated with the following equation:

$$V'_0 = K_{geo} \frac{\Delta q_0}{C_{e,model}}$$

$$V'_{-1} = K_{geo} \frac{\Delta q_{-1}}{C_{e,model}}$$

where

Δq_0 is the modeled induced charge on drop #0 [table 5.2: column 4] and
Δq_{-1} is the modeled induced charge on drop #-1 [table 5.3: column 2].
and $C_{e,model}$ is the modeled charging cell capacitance.

The accuracy was calculated for the case of Q =1.2 ml/min flow rate by multiplying the potential difference between the modeled and measured command voltages by the

proportionality factor K_p. The proportionality factor (K_p = 2.17e-5 [m/volt]) was measured for a charging voltage of 60 Volts, 24 mm from the top of the deflection cell. The error estimate is showed for drop #0 and #-1 in table 5.4: column 6 &7.

Table 5.4: Modeled and experimental command voltage to print straight line with comparative accuracy using the method of images model.

Flow rate [ml/min]	Model drop #0 compensation voltage V'[0]	Exp. drop #0 compensation voltage V'[0]	Model drop #-1 compensation voltage V'[-1]	Exp. drop #-1 compensation voltage V'[-1]	Drop #0 placement accuracy [μm]	Drop #-1 placement accuracy [μm]
1.1	8.558	9.11	0.665	2.1	-	-
1.2	7.543	8.03	0.696	1.89	-11	-26
1.25	7.396	7.83	0.730	1.96	-	-
1.26	7.055	7.5	0.705	1.62	-	-
1.428	7.186	7.44	0.853	1.57	-	-

The accuracy of the charging voltage prediction V'[0] for drop #0 is acceptable [-11 μm]. However, the accuracy on the following drop is worst and about 2.5 times bigger [-26μm]. This discrepancy originates from the fact that the geometric factor K_{geo} was calculated for preceding drops with equal charge level. In the case of drop #-1, the preceding drops do not have the same charge since it is drop #0 which has very little charge compared to drop #1. Therefore the factor K_{geo} does not apply as well in this case because the electric field geometry as changed.

Induced charge experiment based on the voltage command readings V'[n] is not an accurate measure of the actual induced charge level. In fact, the command voltage is **not** directly related to the charge on the drops because of induced charge effects themselves. Since induced charge depends on the respective charge on each drops, a model which would measure directly the charge on the drops would be more accurate.

Induced charge compensation with the inductive coefficient ratio model

The following model separates the induced charge effect of the three preceding drops into three inductive coefficient ratio α, β & γ. Also, instead of modeling the charging cell capacitance C_e, it is measured.

The first step is to measure the capacitance as well as the three inductive coefficient ratio as mentioned in Section 5.6.4. The following table 5.5 shows the printing conditions and the charge collector voltage readings which were used to calculated the parameters.

Table 5.5: Charge collector experimental data.

Flow rate [ml/min]	1.2	**Charging volt. [Vc]**	60
Piezo frequency [Hz]	76300	**Ampl. gain [xG]**	104.65
Drops in sequence	16	**Fback res. [Ohmn]**	5.515 e+6
Drop diameter [µm]	79.4	**Drop spacing [µm]**	165
Deflection [m] @ Vc = 60 Volts & z=24 mm	0.0013	**Proportionality factor Kp [m/Volt]**	2.17E-05

# of deflected drop(s) per sequence	**Drop sequence per sec. [Hz]**	**Charge collector voltage [V]**	**Equivalent charge q [colomb]**
1 drop /16	4768.75	0.713	2.77409E-13
2 drop /16	4768.75	1.326	5.1591E-13
3 drop /16	4768.75	1.934	7.52466E-13
4 drop /16	4768.75	2.542	9.89022E-13

Ce	-4.62348E-15
alpha	0.140252454
Beta	0.026683374
phi	0.004725946

Notice that the measured value of the charging cell capacitance (C_e=-4.6e-15) is about 2% larger than what was expected from the model. Also, great care should be taken when measuring the voltage of the charge collector instrument for the 4 drops experiment. In fact, the calculation of the last coefficient γ is very sensitive and can vary by a few percent for a $\pm$ 10 mV error.

Several experiments were done in order to test the flexibility and accuracy of the method. The first one, similar to the one described above, deflects all the drops but 8 out of a sequence of 256 drops. The charging voltage of the sequence of 8 drops, originally 0 volt, was adjusted in order to align the leading drop #0, #-1 and #-2 with the other drops #-3 to #-7. The voltages were recorded for each drop [table 5.6, column 4] and also evaluated from the equation 5-58, 5-60, 5-61, using the parameters measured previously.

Table 5.6: Experiment with inductive coefficient ratio for V'_{cp} = 0 V and V'_{ic} = 60 V.

Print voltage V'cp	0				
In-catch voltage V'ic	60				
Drop number#	Desired printing virtual Vcp	Compensated command voltage model V'cp	Experimentai charging value V'cp	Voltage error ΔV	Computed position error Δx [μm]
#0	0	8.791	8.035	0.756	16
#-1	0	1.608	1.891	-0.283	-6
#-2	0	0.242	0.236	0.006	0
#-3	0	0.000	0.000	0	0
#-4	0	0.000	0.000	0	0
#-5 to #-8	0	0.000	0.000	0	0

In the case of table 5.6, the accuracy was calculated by multiplying the voltage error ΔV by the proportionality factor K_p calculated in table 5.5.

Another experiment was done where the base charging voltage of the sequence of 8 drops was changed from 0 to -30 volts. First, the steady state virtual charging voltage had to be calculated for the 8 drop sequence. Because the steady state command charging voltage is chosen to be -30 V, the applied command charging voltage of the leading drops will have to be adjusted in order produce the same virtual charging voltage of -25.6 on each drop of the sequence. This procedure is the equivalent to aligning the leading drop with the rest of the sequence for a given steady state command voltage.

Similar calculations were done to estimate the accuracy which appear to be slightly larger. This phenomenon can be explained by a larger charge differential between the in-catch and the printing drops. Since the compensated charging voltages are proportional to the inductive coefficient times the charge, so is the inherent error.

Table 5.7: Experiment with inductive coefficient ratio for V'_{cp} = -30 V and V'_{ic} = 60 V.

Print voltage V'cp	-30				
In-catch voltage V'ic	60				
Drop number#	Desired printing virtual Vcp	Compensated command voltage model V'cp	Experimental charging value V'cp	Voltage error ΔV	Computed position error Δx [μm]
#0	-25.605	-16.814	-17.784	0.97	21
#-1	-25.605	-27.587	-27.414	-0.173	-4
#-2	-25.605	-29.637	-29.6	-0.037	-1
#-3	-25.605	-30.000	-30.073	0.073	2
#-4	-25.605	-30.000	-30.073	0.073	2
#-5 to #-8	-25.605	-30.000	-30.073	0.073	2

For the case where the in-catch drops do not need to be deflected, the method was tested on a sequence of 8 drops charged with a V'_{cp} = 60 V. Therefore, instead of deflecting the drops to catch, we were deflecting the drops to print. The method showed a great adaptability to the new condition and generated a command voltage accuracy similar to the one in table 5.7.

Table 5.8: Experiment with inductive coefficient ratio for V'_{cp} = 60 V and V'_{ic} = 0 V.

Print voltage V'cp	60				
In-catch voltage V'ic	0				
Drop number#	Desired printing virtual Vcp	Compensated command voltage model V'cp	Experimental charging value V'cp	Voltage error ΔV	Computed position error Δx [μm]
#0	51.209	51.209	51.992	-0.783	-17
#-1	51.209	58.392	58.373	0.019	0
#-2	51.209	59.758	59.791	-0.033	-1
#-3	51.209	60.000	60.027	-0.027	-1
#-4	51.209	60.000	60.027	-0.027	-1
#-5 to #-8	51.209	60.000	60.027	-0.027	-1

Various charging patterns were experimented with similar accuracy results (see table 5.8 & 5.9). Notice that the error on drop #-1 is always smaller than error on drop #0 contrarily to the physical model performance showed earlier. The method responds very well to different printing conditions, which suggests that it could be used to print pattern other than straight lines on-off. In fact, it could be used for random charging sequences with the use of the general form of equation 5-65.

Table 5.9: Accuracy table for various charging patterns.

In-catch charging voltage V'ic	Printing charging voltage V'cp	Drop #0 Charging Accuracy Δx [μm]	Drop #-1 Charging Accuracy Δx [μm]
60	30	9	-1
60	0	16	-6
60	-30	21	-4
0	30	-12	0
0	60	-17	0
0	90	-16	4

The inductive coefficient ratios were measured for different binder flow rates. The results are showing that inductive ratios decrease as flow rate increases. The decrease is mainly related to the larger drop spacing caused by the higher flow rate, which was confirmed by the theory. The following table 5.10, could be considered as a simplified look up table that can be used to compensate for induced charge effect for any kind of charging patterns. The value were measured with the charge collector electrode method. The same value could also be measured from the optical measurement method which is expected to give a better accuracy than showed in table 5.9.

Table 5.10: Simplified look up table for induced charge compensation scheme.

Flow rate [ml/min]	Drop diameter [μm]	Drop spacing [μm]	Charging cell capacitance Ce [F]	α	β	γ
1.1	77.1	151	4.11 e-15	0.156	0.035	0.0036
1.2	79.4	164.8	4.62 e-15	0.14	0.0267	0.004
1.25	80.5	171.7	4.47 e-15	0.133	0.029	0.006
1.26	80.7	173	4.64 e-15	0.135	0.02	0.005
1.428	84.1	196	5.32 e-15	0.13	0.025	0.003

An interesting point to notice is the relationship between the three inductive coefficient ratios α, β & γ. From Coulomb's law we know that electrostatic effect are proportional to the inverse of the distance square. Since the distance between the drops is uniform, the coefficient β should be about the square root of the coefficient α and γ should be the square root of β or $1/\alpha^4$. For example, for Q=1.2 ml/min, if we apply the latter rule to calculate β and γ we get respectively 0.0196 and 0.0007 as compared to 0.0267 and 0.004 which can be considered as good first order estimate.

5.6.6 How to improve the model accuracy

Break off stability

The overall accuracy of the induced charge compensation method depends on the break off position stability. In fact, drift of the break off position will affect the charging efficiency as well as the inductive coefficient ratio. However, adding the break off position and alignment as parameter in the look up table would be prohibitive. Therefore, a sensible approach is to control the stream position such that it is always centered inside the charging cell. The other recommendation is to control the piezo signal frequency and amplitude such that the break up always happens about one third inside the charging cell. This position assures smaller induced charge effect while giving some shield protection against electric field interaction with the deflection cell.

Jet alignment inside the charging electrode should also be kept constant since it can seriously change the inductive coefficient ratios.

Lower charge

Keeping the charge level down on the drop will insure a better accuracy. In fact, by decreasing the average drop charge level, we decrease inter-drop electrostatic forces and charging voltage level which involves multiplicative offset errors.

5.7 Electrostatic deflection

5.7.1 Theory

Motion of an individual droplet is determined by the electrostatic field in the deflection cell zone. The electrostatic force on a charged droplet passing through a uniform field is given by:

$$F_{EX} = q\,E = q\,\frac{V_d}{w_d} \qquad (5\text{-}73)$$

where; q is the drop charge

E is the electric field inside the deflection cell

V_d is the potential difference between the two plates of the deflection cell

w_d is the deflection cell gap width

The field lines are perpendicular to the droplet velocity, so the x component of droplet acceleration along the field line is:

$$a_x = \frac{qV_d}{m_d w_d} = \frac{-C_e V'_{cp} V_d}{m_d w_d} \qquad (5\text{-}74a)$$

where; C_e is the charging cell capacitance [F]

V'_{cp} is the command charging voltage [volts]

m_d is the drop mass [kg]

If the value of C_e is unknown, we can substitute equation 5-8 & 5-21 which represents the charging capacitance model for parallel plate charging electrode:

$$a_x = \frac{-2\pi\,\varepsilon_0\,u_0\,V'_{cp}V_d}{m_d w_d f\left[0.244 + \ln\left(\frac{w_c}{d}\right)\right]} \qquad (5\text{-}74b)$$

In the region between the deflection plates, the charged droplet moves along a parabolic path and since there is no initial velocity of the droplet in the x direction, the displacement at point L_d is given by:

$$x_{Lc} = \frac{1}{2}a_x t^2 = \frac{a_x L_d^{\,2}}{2u_o^{\,2}} \qquad (5\text{-}75)$$

When the droplet leaves the deflection zone it travels on a straight line tangent to the parabola at the point L_d. The total deflection x_p observed at the powder bed level is then:

$$x_p = \frac{a_x L_d L_{dp}}{u_0^2} + \frac{a_x L_d^2}{2u_0^2} \qquad (5\text{-}76)$$

or:

$$x_p = \frac{-2\pi \varepsilon_0 L_d V'_{cp} V_d}{m_d w_d f u_o \left[0.244 + \ln\left(\frac{w_c}{d}\right)\right]} \left(L_{dp} + \frac{L_d}{2}\right) \qquad (5\text{-}77)$$

Equations 5-75 to 5-77 are true as long as drag forces are negligible. However, it will be showed later on that drag forces are significant and can not be neglected. Therefore, the above equation will usually underestimate the value of x_p and should be used only as a first estimate model.

5.7.2 Advantage of high Vd

The advantage of using a high potential value V_d are numerous and have been mentioned along the different sections of this chapter. The major advantage of a higher V_d is to allow a decrease of the average drop charge level. This charge decrease will minimize the electrostatic crosstalk between the drops making their flight path more predictable. In addition, a lower charge implies a lower charging voltage level which is less taxing for the amplifying electronics. In fact, a lower voltage level is less affected by the slew rate and accuracy of the amplifier.

For a given drop charge level, a higher V_d permits a shorter deflection cell. As we are going to see latter on, a shorter deflection cell will contribute to reduce the drop merging effect. (see section on merging) It also alleviates the design specification on the charging electrode by allowing a larger gap w_c for a given charge to deflection ratio. Although the advantage of a higher V_d is certain, its implementation is not as simple since there is a limit to the strength of the electric field after which arcing occurs. This limit is determined by the break down voltage which can be estimated from the ambient condition around the printhead.

5.7.3 Break down voltage

In its normal state a gas is almost a perfect insulator. However, when an electric field is established between two electrodes, of intensity dependent upon geometry and the gas properties, the gas can become a conductor. The transition from insulating to conducting states is an electrical discharge known as the electrical breakdown of the gas or spark. The critical potential difference is known as the breakdown potential Vs of the gas for a particular electrode system geometry.

In our particular application, two parallel electrode are separated by a distance w_d between which a static uniform field is kept. It was found that pressure has a significant effect on the breakdown potential V_S. As stated by Paschen's law, V_S can be expressed as a function of the product of the gap w_d and ambient pressure (see ref[71,72]). Or in other words, the law states that if the length of the discharge gap and the gas pressure are altered in such a way that their product is unchanged the magnitude of the breakdown voltage remains constant.

$$V_s = f(w_d * p) \qquad (5\text{-}78)$$

This function can be analytically determined from the two ionization coefficients α & γ defined by Townsend as part of its sparking criterion showed below:

$$\gamma e^{\alpha w_d} > 1 \qquad (5\text{-}79)$$

where α is the first coefficient of ionization, γ the second and the w_d the gap between the two electrodes. The Townsend criterion of equation (5-79) enables the breakdown voltage of a gap to be determined by reference to the appropriate curves relating α/p and γ with E/p, where p is the ambient pressure and E the electric field. Typical curves relating the breakdown voltage with the product of gas pressure times gaps length in several gases are compared in figure 5.27, where p_O is the gas pressure in mm.Hg (or kPa) reduced to 0° C. The breakdown voltage for each gas decreases as p_Od id reduced, reaches a minimum at a value of p_Od of the order of 1 to 10 mm.Hg x cm.(0.1 to 1.3 kPa), and then increases again..

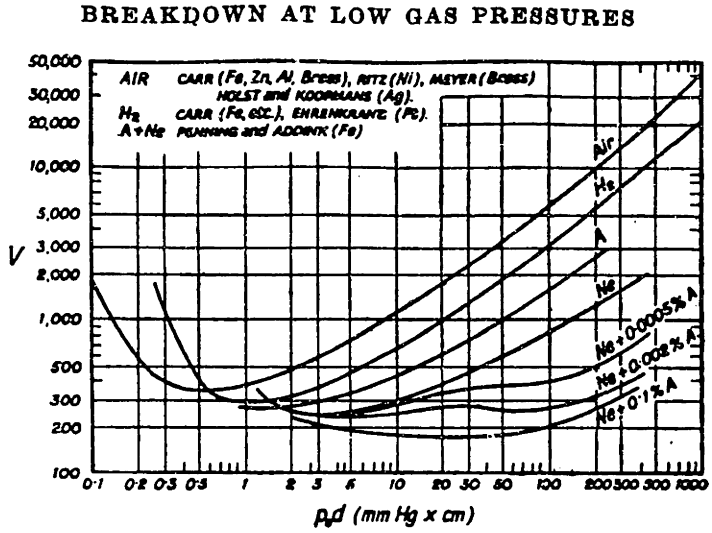

FIG. 2.2. Typical breakdown voltage curves for different gases between parallel plate electrodes. p_0 is the gas pressure in mm. Hg corrected to 0° C.

Figure 5.27: Typical breakdown voltage: Paschen's law, see reference [71]

For example, according to the above graph, our deflection electrode design with a 0.15 cm gap at ambient air pressure of 101.3 kPa (760 mm.Hg) would have a breakdown voltage of about 6000-6500 V. As a result, this breakdown voltage can be increased by a higher ambient pressure. For example, if the pressure is doubled to 202.6 kPa than breakdown voltage reaches about 10 kV.

Effect of printing environment

Spark-breakdown voltage is affected by the presence of impurities on the cathode surface such as oil, finger prints, oxide films, dust, and other insulating particles, as well as adsorbed gases. Therefore, the electrodes must be cleaned of impurities by washing off foreign materials with distilled water and need to be carefully polished to minimize the effects of sharp points.

Effectively, geometry plays a major role as to determined the breakdown voltage. In the case of our two parallel electrodes, special care should be taken to the shape of the outer edge of the electrode in order to avoid edge effects. Near the edge of plane electrodes the radius of curvature must be decreased very gradually so that at no point does the field become greater that in the center of the plane portion. Satisfactory profiles may be obtained by following Rogowski's extension of Maxwell's analysis of the electrostatic field due to a finite plane plate parallel to an infinite plate. This analysis can be reduced into simple mathematical expressions relating the coordinates x and y of the ideal shape of an electrode outer edge. (see Appendix C5, Calculating ideal electrode geometry)

As a note, the printhead charging electrode and deflection cell should have such a curved shape all around their periphery unlike what the design is actually. Sharp edges, such as the one showed as triangle in figure 5.28, reduces the theoretical breakdown voltage to a fraction of what it could be. Figure 5.28. shows the effect on the breakdown voltage in air for sharp and round edge with various polarity. As expected, for the same gap of 1.5 mm the breakdown voltage is only 2500 Volts in the case where the sharp edge is the cathode.

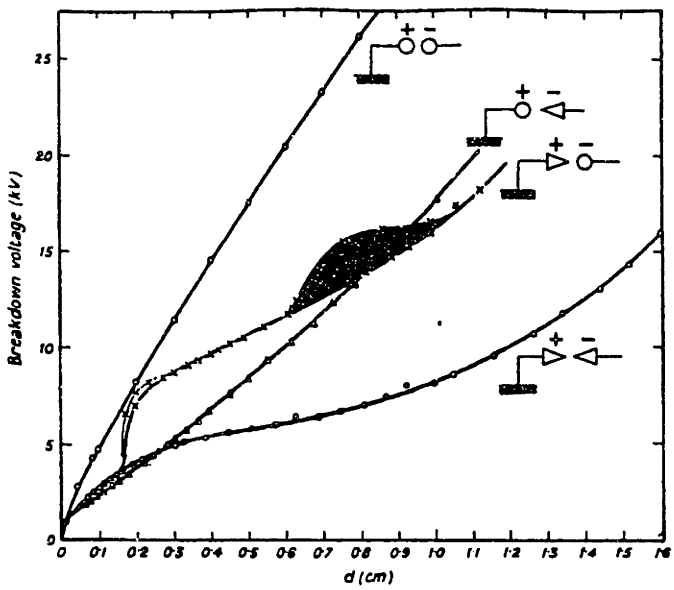

Fig. 7.19. D.C. breakdown voltage curves in air for various combinations of point and sphere electrodes. The sphere diameter is 5 cm.

Figure 5.28: Point charge and polarity effect on breakdown voltage: p322

In addition, breakdown voltage in air at atmospheric pressure is not affected by different electrode materials, such as copper, nickel or aluminum, provided that the surfaces are clean and smooth. Therefore, the nickel plating used on our printhead should be fine.

Finally, the use of insulating gases such as CCl_4, CCl_2F_2, SF_6 or a mixture of those in air can significantly increases the breakdown voltage by a factor 2 to 5 compared to open air. Nevertheless, implementing such an environment around a printhead should be done only in a last resort.

5.8 Inter-drop electrostatic attraction and repulsion

5.8.1 Coulomb's law

All of electrostatics stems from the quantitative statement of Coulomb's law concerning the force acting between charged bodies at rest with respect to each other. Coulomb showed experimentally that the force between two small charged bodies separated in air a distance large compared to their dimensions

(1) varied directly as the magnitude of each charge,
(2) varied inversely as the square of the distance between them,
(3) was directed along the line joining the charges,
(4) was attractive if the bodies were oppositely charged and repulsive if the bodies had similar charge level and polarity.

Furthermore it was shown experimentally that the total force produced on one small charged body by a number of small charged bodies placed around it was the vector sum of the individual two-body forces of Coulomb. Strictly speaking, Coulomb's conclusions apply to charges in vacuum or in media of negligible susceptibility.

If **F** is the force on a point charge q_1, located at z_1, due to another point charge q_2, located at z_2, then Coulomb's law is

$$F_C = k\, q_1\, q_2 \frac{(z_1 - z_2)}{|z_1 - z_2|^3} \qquad (5\text{-}81)$$

Note that q_1 and q_2 are algebraic quantities which can be positive or negative. The constant of proportionality k depends on the system of units used. For the metric system the expression becomes:

$$F_C = \frac{1}{4\pi\,\varepsilon_0} \frac{q_1\, q_2}{\lambda_{12}^{\,2}} \qquad (5\text{-}82)$$

where ε_0 is the permittivity of air 8.81 x 10^{-12} [F/m]
q_i is the drop charge in [coulomb]
λ_{12} is the distance between point charge 1 and 2.

When droplets are modeled as point charges, equation 5-82 is valid for most case as long as the following conditions are true:

(1) distance λ_{12} is large compared to the drop radius r,

(2) both drops are charged.

In the case where one of the conditions is not satisfied, Coulomb's law can not be applied directly because of polarization effect on the droplets. Polarization arises when the charges on an isolated drops are no longer distributed uniformly over its entire surface area. In fact, because of charge concentration one side of the drop becomes more positive or negative compared to the opposite side of the drop. A good example of drop polarization occurs when one of the drops has no charge. For example, for a given charge q_2, if q_1 is zero than according to equation 5-82 the force between the drops is zero as a result. However, because of charge polarization caused on the neutral drop there should be in fact an attractive force between both drops. This attractive force could be determined if the level of polarization of charge q_1 can be calculated.

A recursive method has been developed in order to tackle the problem. It refers to the theory described in Appendix C4 in order to find the image of a point charge inside the opposite droplet.

The method starts as follow:

Step #1: Say we have two drops facing each other at a distance λ_{12} with respective charge q_1 =0 and q_2 having a non-zero value.

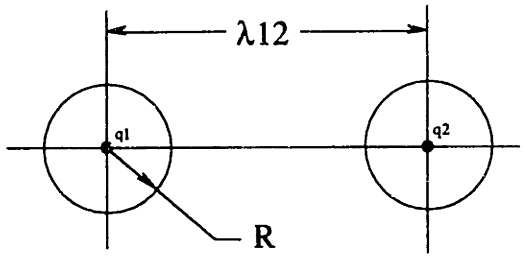

Step #2: The first procedure is to calculate the image charge of point charge q_2 inside droplet #1.

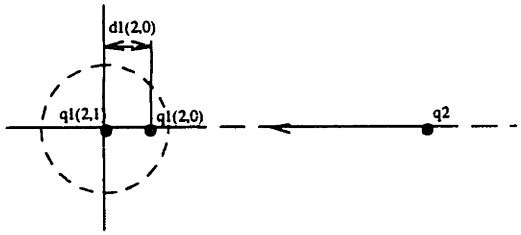

$$q_1^{2,0} = -\frac{R}{\lambda_{12}} q_2 \qquad d_1^{2,0} = \frac{R^2}{\lambda_{12}} \qquad (5\text{-}83)$$

$$q_1^{2,1} = q_1 - q_1^{2,0} \qquad (5\text{-}84)$$

Step #3: Then keep the two point charges generated in step #2 and find their images in droplet #2 which has a total charge q_2.

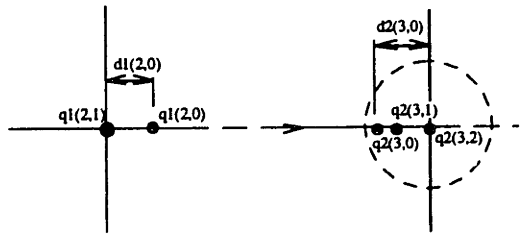

$$q_2^{3,0} = -\frac{R}{\lambda_{12}} q_1^{2,1} \qquad d_2^{3,0} = \frac{R^2}{\lambda_{12}}$$

$$q_2^{3,1} = -\frac{R}{\left(\lambda_{12} - d_1^{2,0}\right)} q_1^{2,0} \qquad d_2^{3,1} = \frac{R^2}{\left(\lambda_{12} - d_1^{2,0}\right)}$$

$$q_2^{3,2} = q_2 - q_2^{3,0} - q_2^{3,1}$$

Step #4: Then keep the three point charges generated in step #3 and find their images in droplet #1 which has a total charge q_1.

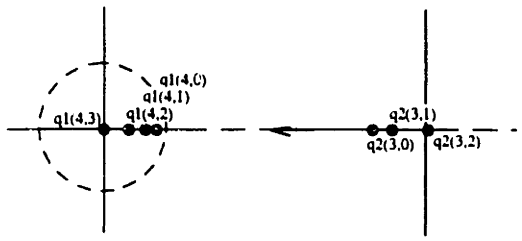

$$q_1^{4,0} = -\frac{R}{\lambda_{12}} q_2^{3,2} \qquad d_1^{4,0} = \frac{R^2}{\lambda_{12}}$$

$$q_1^{4,1} = -\frac{R}{\left(\lambda_{12} - d_2^{3,0}\right)} q_2^{3,0} \qquad d_1^{4,1} = \frac{R^2}{\left(\lambda_{12} - d_2^{3,0}\right)}$$

$$q_1^{4,2} = -\frac{R}{\left(\lambda_{12} - d_2^{3,1}\right)} q_2^{3,1} \qquad d_1^{4,2} = \frac{R^2}{\left(\lambda_{12} - d_2^{3,1}\right)}$$

$$q_1^{4,3} = q_1 - q_1^{4,0} - q_1^{4,1} - q_1^{4,2}$$

Step #5: Then keep the four point charges generated in step #4 and find their images in droplet #2 which has a total charge q_2. The iteration can be done N times until we get the desired number of point charges in each droplet. The position and the magnitude of the point charges represents the degree of polarization experienced by both drops. It was found that 5 iterations was sufficient since the smallest image charge is then in the range of 10^5 smaller than the original drop charge q_1 and q_2. Therefore, the resulting point charge pattern is as follows:

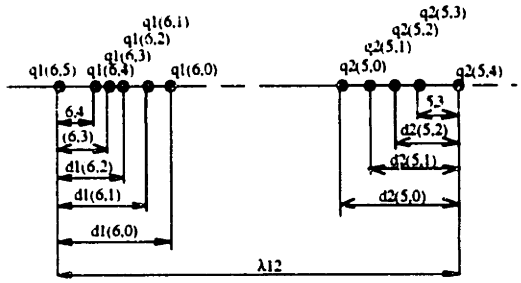

$$q_2^{5,0} = -\frac{R}{\lambda_{12}} q_1^{4,3} \qquad d_2^{5,0} = \frac{R^2}{\lambda_{12}}$$

$$q_2^{5,1} = -\frac{R}{\left(\lambda_{12} - d_1^{4,0}\right)} q_1^{4,0} \qquad d_2^{5,1} = \frac{R^2}{\left(\lambda_{12} - d_1^{4,0}\right)}$$

$$q_2^{5,2} = -\frac{R}{\left(\lambda_{12} - d_1^{4,1}\right)} q_1^{4,1} \qquad d_2^{5,2} = \frac{R^2}{\left(\lambda_{12} - d_1^{4,1}\right)}$$

$$q_2^{5,3} = -\frac{R}{\left(\lambda_{12} - d_1^{4,2}\right)} q_1^{4,2} \qquad d_2^{5,3} = \frac{R^2}{\left(\lambda_{12} - d_1^{4,2}\right)}$$

$$q_2^{5,4} = q_2 - q_2^{5,0} - q_2^{5,1} - q_2^{5,2} - q_2^{5,3}$$

$$q_1^{6,0} = -\frac{R}{\lambda_{12}} q_2^{5,4} \qquad d_1^{6,0} = \frac{R^2}{\lambda_{12}}$$

$$q_1^{6,1} = -\frac{R}{\left(\lambda_{12} - d_2^{5,0}\right)} q_2^{5,0} \qquad d_1^{6,1} = \frac{R^2}{\left(\lambda_{12} - d_2^{6,0}\right)}$$

$$q_1^{6,2} = -\frac{R}{\left(\lambda_{12} - d_2^{5,1}\right)} q_2^{5,1} \qquad d_1^{6,2} = \frac{R^2}{\left(\lambda_{12} - d_2^{5,1}\right)}$$

$$q_1^{6,3} = -\frac{R}{\left(\lambda_{12} - d_2^{5,2}\right)} q_2^{5,2} \qquad d_1^{6,3} = \frac{R^2}{\left(\lambda_{12} - d_2^{5,2}\right)}$$

$$q_1^{6,4} = -\frac{R}{\left(\lambda_{12} - d_2^{5,3}\right)} q_2^{5,3} \qquad d_1^{6,4} = \frac{R^2}{\left(\lambda_{12} - d_2^{5,3}\right)}$$

$$q_1^{6,5} = q_1 - q_1^{6,0} - q_1^{6,1} - q_1^{6,2} - q_1^{6,3} - q_1^{6,4}$$

Step #6: To calculate the electrostatic force between the two drops, we can apply Coulomb's law (equation 5-82) between each individual point charges. The summation of each individual electrostatic forces represents the total force between the two drops.

$$F_C = \frac{1}{4\pi\varepsilon_0} \sum_{i}^{N=6,4} \sum_{j}^{N=5,3} \frac{q_1^i q_2^j}{d_{ij}} \qquad (5\text{-}85)$$

where d_{ij} is the distance between charge point q_1^i and q_2^j,
and ε_0 is the permittivity of air 8.81 e-12 [F/m].

For each single point charge on one drop, we have to compute the force for all the point charge on the other drops. For example, the force between charge $q_1^{6,5}$ and $q_2^{5,4}$ should be summed with the force between $q_1^{6,5}$ and $q_2^{5,0}$, ... The summation continues for charge $q_1^{6,0}$ and all the q_2^i up to charge $q_1^{6,4}$ and $q_2^{5,3}$.

$$q_1^{6,5} \Rightarrow q_2^{5,4}, q_2^{5,0}, q_2^{5,1}, q_2^{5,2}, q_2^{5,3}$$

$$q_1^{6,0} \Rightarrow q_2^{5,4}, q_2^{5,0}, q_2^{5,1}, q_2^{5,2}, q_2^{5,3}$$

$$q_1^{6,1} \Rightarrow \text{"}, \text{"},\ldots$$

$$q_1^{6,2} \Rightarrow \text{"}, \text{"},\ldots$$

$$q_1^{6,3} \Rightarrow \text{"}, \text{"},\ldots$$

$$q_1^{6,4} \Rightarrow \text{"}, \text{"},\ldots$$

The summation of all the forces gives the total electrostatic force between the two drops. If the final value is positive, the force is repulsive, if negative the force is attractive. The following graph (figure 5.29) shows the difference between the force between two drops when calculated directly with Coulomb's law (equation 5-82) and the polarization method.

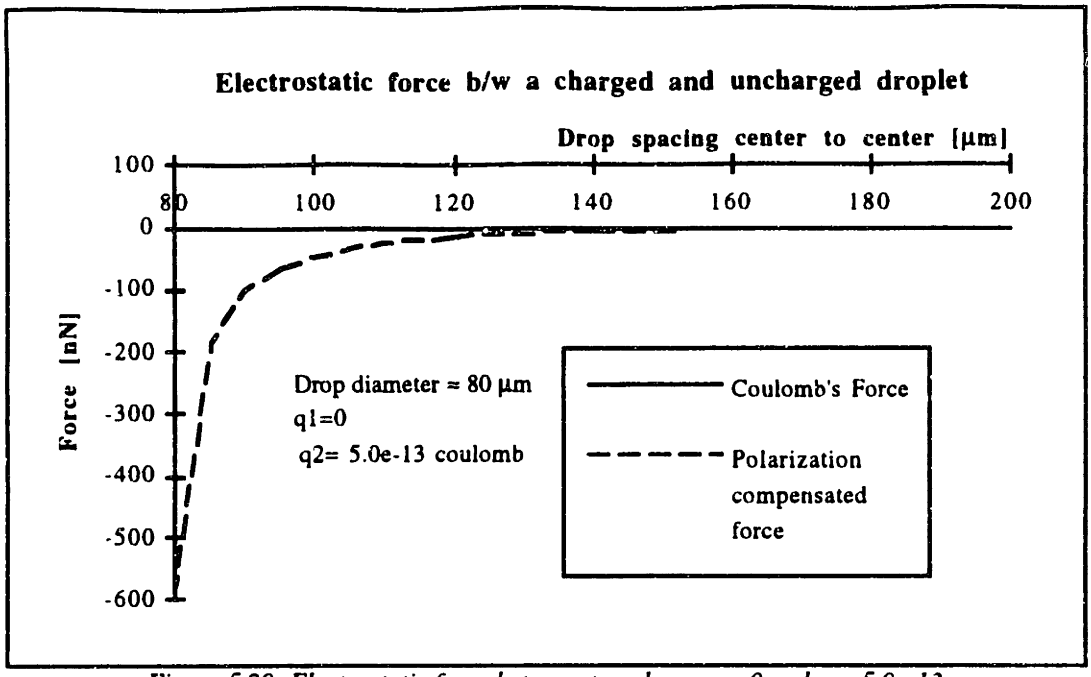

Figure 5.29: Electrostatic force between two drops q_1=0 and q_2=5.0e-13.

Coulomb's law is valid ($F_c = 0$) only down to a drop distance approximately equal to 2 drop diameters. For a distance smaller than 2 drop diameters, because of polarization, Coulomb's law is no longer valid since an attractive force is building up as the distance between the drops decreases. In this case the neutral drop becomes a dipole where one side is positive while the other negative. Because the drop is isolated, the dipole is just an effect of charge redistribution since the total charge of the drop remains neutral.

Another case where Coulomb's law fails to estimate the electrostatic force between two drops is when one drop as a small charge with same polarity compared to the other drop (see figure 5.30).

Figure 5.30, shows clearly that Coulomb's law predicts a small repulsive force when in fact because of polarization it is an attractive force instead.

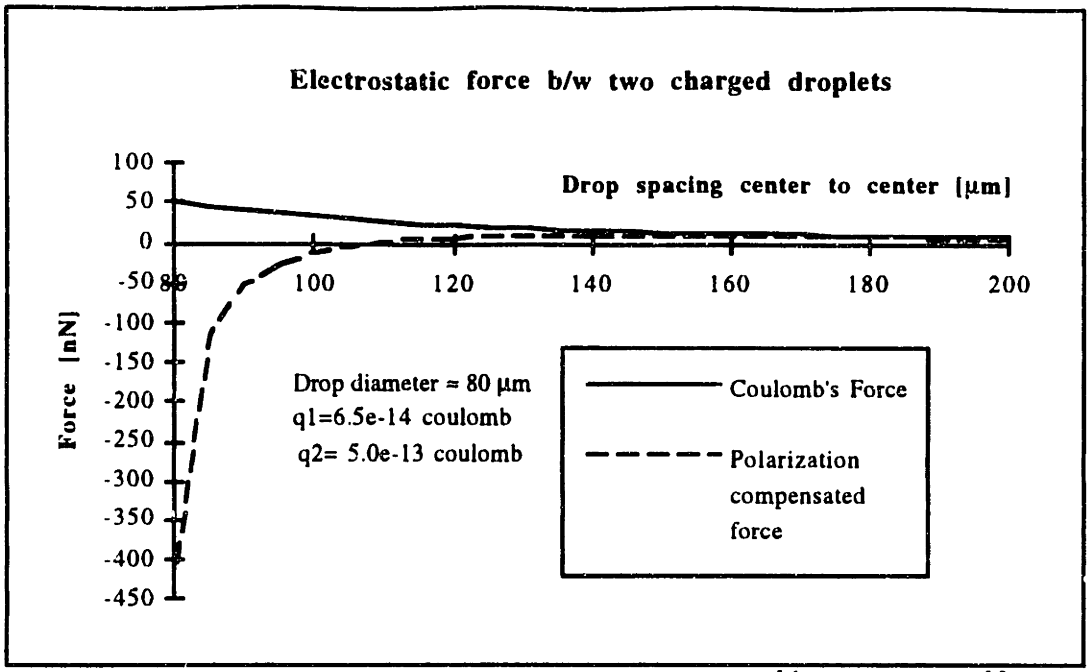

Figure 5.30: Electrostatic force between two drops q_1=6.5x10^{-14} and q_2=5.0x10^{-13}.

Finally, when both charge q_1 and q_2 are separated by a distance larger than the equivalent of 2 or 3 drop diameters, both models more or less coincide with each other. However, if the drop spacing is shorter, polarization occurs and should be accounted for in the calculations.

In summary, Coulomb's law should be used in most case, except when the drop spacing falls below 2 to 3 drop diameter. In such case, the polarization model should be used since polarization effect raises sharply as the drops gets closer.

5.8.2 In-flight drop interaction

The flight path of a charged drop should be defined by its charge and the strength of the deflection cell electric field. In some instance, because inter-drop electrostatic force are predominant over the deflection electric field, the drop flight path may be changed. The two major sources of error are found at both ends of a printing drop sequence.

Electrostatic merging

In fact, if the charge differential between the trailing in-catch drop #1 and the leading printed drop #0 is too large, the electrostatic attraction force may cause them to collide or in other word to merge into a single bigger drop.

The electrostatic merge curve graph of figure 5.31 & 5.32 shows two types of data: the drop spacing between drop #0 and #1 and the drop diameter. Electrostatic merging occurs when the distance between drop #0 and #1 is equal or smaller to one drop diameter. Therefore, merging occurs only if the drop spacing curve goes below the line defining the drop diameter. The graph shows also that once the drops have passed a critical minimum point, the deflection cell electric field take over the inter-drop attraction forces and deflect the drops according to their charges. If the drop spacing reaches a minimum without merging, then the deflection level will be retarded or decrease from its expected value. For accurate printing, it is then important to minimize the effect of electrostatic merging.

Electrostatic merging is sensitive to three basic parameters: the drop spacing, drop size, drop charge and distance L_{cd} between the charging electrode and top of deflection cell.

The flow rate affects electrostatic merging by changing the drop time of flight and drop spacing as well. Figure 5.31 shows the modeled drop spacing for three different flow rates. For the printing conditions used in the model ;

Orifice diameter = 45 μm
Piezo-resonator frequency = 76300 Hz
Distance L_{cd} b/w charging electrode and deflection cell = 2.5 mm
Stream break off position assumed to be centered in the charging electrode
Deflection voltage V_d = 1000 V
Deflection cell gap w_d = 1.5 mm
Charge on drop #0 = 0 in-print drops
Charge on drop #1 = $5x10^{-13}$ coulomb , in-catch drops

electrostatic merging occurred for both flow rate 1.0 and 1.1 ml/min while it did not happen for Q = 1.2 ml/min.

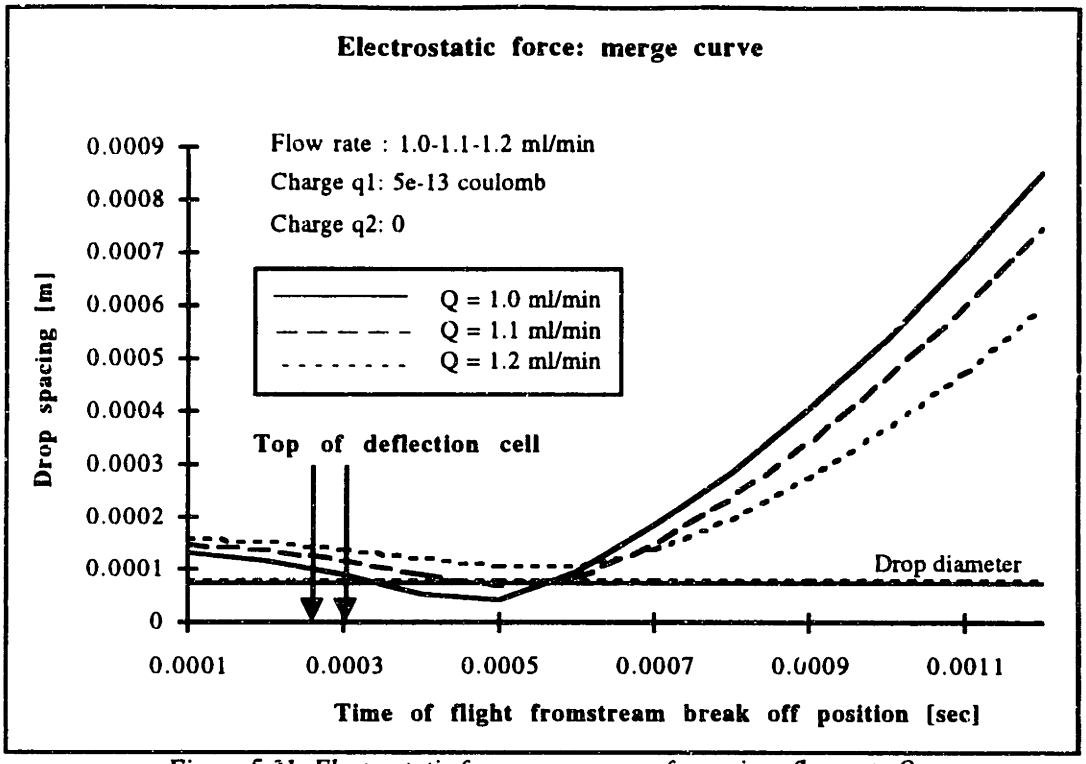

Figure 5.31: Electrostatic force merge curve for various flow rate Q.

Those same results were verified experimentally on the Diconix printhead. The charging level used in the experiment corresponded to the case of on-off printing were $q=5x10^{-13}$ coulomb is the charge necessary to deflect the drops in the catcher. For the case where the charge on drop #0 is of opposite polarity because of proportional deflection, electrostatic merging may occur for higher flow rates.

The effect of electrostatic merging is decreased as the flow rate was increased. This phenomenon can be explain by the longer drop spacing which decreased electrostatic force proportional to the square of the new distance. The larger drop spacing was also assisted by a higher drop velocity which left less time for the attraction force to react.

The distance L_{cd} between the charging electrode and the deflection cell also affect electrostatic merging its own way. In fact, the region of the printhead defined by the distance L_{cd} has in particular that the drops are fully charged but still not yet being deflected. Most drops are kept at a uniform spacing until two consecutive drop (drop #0 and #1) change the balance because of their significant charge differential. Therefore, the longer the two drops will remain undeflected, the more probable they are going to merge because of electrostatic attraction force. This phenomenon is shown in figure 5.32 where

the distance L_{cd} was change from 2, 3 to 4 mm at a constant flow rate Q =1.2 ml/min. (Other printing conditions are same as above)

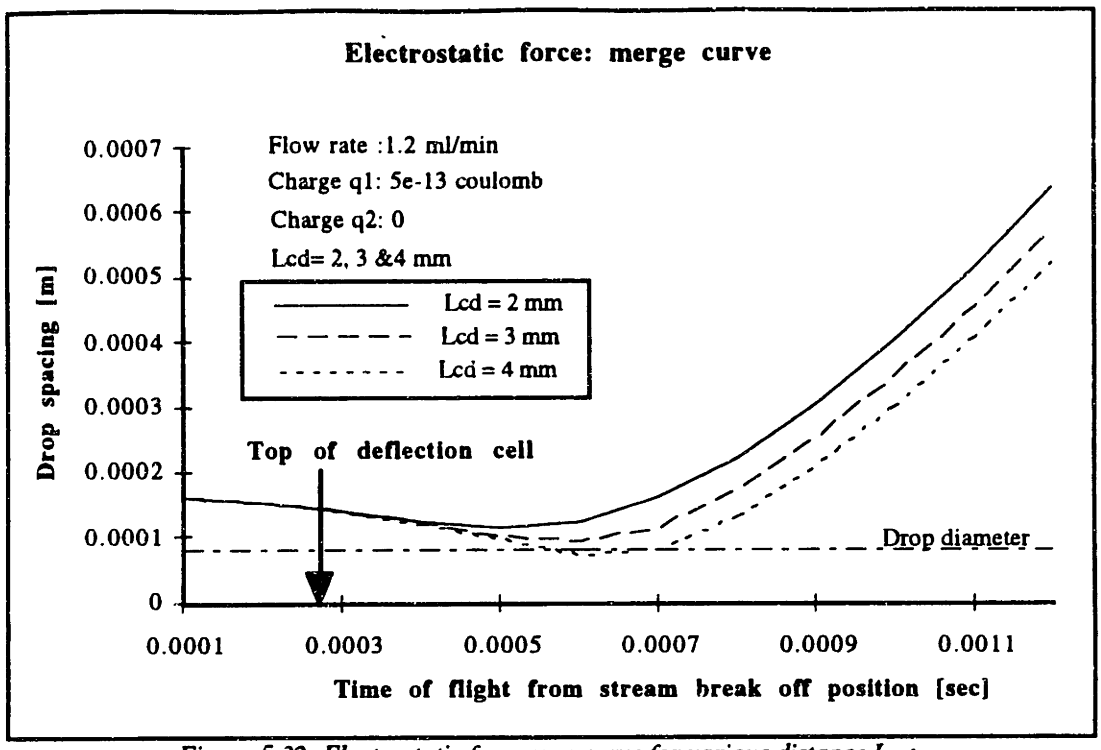

Figure 5.32: Electrostatic for merge curve for various distance L_{cd}.

The result shows clearly that for a larger value L_{cd}, electrostatic merging is more probable. In the case of our prediction, a printhead with a distance L_{cd} smaller than 3mm would be exempted from electrostatic merging.

Electrostatic merging is a caused of printing failure since the merged drop (drop #0,#1) is partially deflected and may impact at an undesired position on the catcher or powder bed. Therefore, it is essential to test a new printhead design against the worst charge sequence scenario and develop the design and printing condition accordingly.

Tail end effect & calculation

Another phenomenon related to inter-drop electrostatic force is seen at the trailing end of a printing drop sequence. Since a sequence of printed drops hold about the same charge and polarity, each drop repels each other within the sequence. Hence, the drop spacing remains the same since the repulsion forces are about equal, i.e. $F_{n+2,n+3} \approx F_{n+1,n+2} \approx$ ...(see figure 5.33). This repulsion force is beneficial for the leading drops since it works against the drag forces. However, following drops do not experience such air drag leaving the electrostatic forces acting alone. The problem arises when the repulsion forces are unbalanced at the last drop of a printing sequence (see schematic figure 5.33).

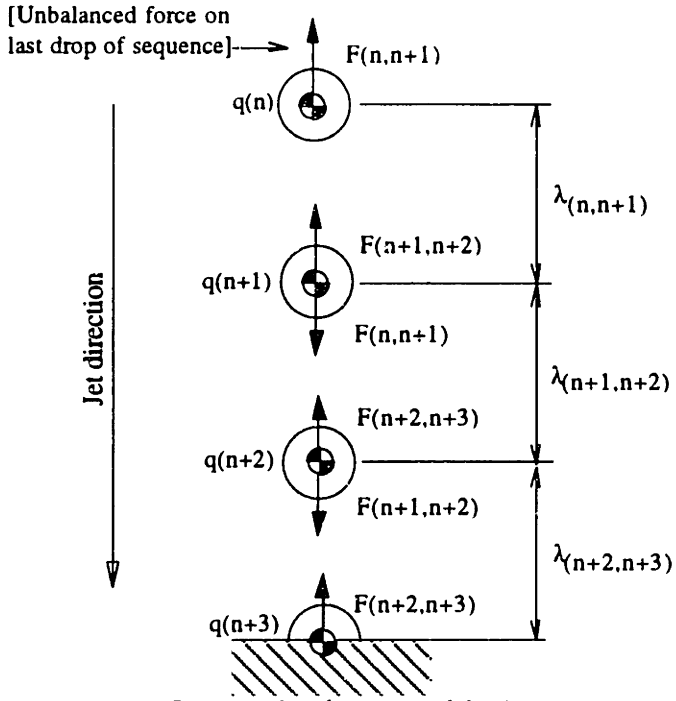

Figure 5.33: Tail end effect model schematic.

The force $F_{n,n+1}$ is not counterbalanced by any other forces since no drop are following behind because they were deflected in-catch. Because of the total force $F_{n,n+1}$, drop #n is pushed away from the drop sequence, increasing the distance $\lambda_{n,n+1}$ as a consequence. As a result, the magnitude of for $F_{n,n+1}$ is decreased proportionally to the square of the distance according to Coulomb's law. This reduction in force magnitude produces an unbalanced force on the next drop #n+1 this time. The overall effect continues until the trailing drops have a non-uniform drop spacing. This drop simulation was done using Coulomb's law in the equation of motion for each trailing drop. The model assumed that for our print distance range, (i.e. between 20 to 30 mm) a four drops model with the

first one anchored was sufficient. As it can be seen in figure 5.34, the model starts with a uniform drop spacing determined by the flow rate Q, the piezo frequency f and orifice diameter d_o. The parameter used in the simulation were;

Flow rate Q = 1.2 ml/min
Piezo frequency f = 76300 Hz
Orifice diameter d_o = 45 μm

The results showed that for a stream charged with $q=3x10^{-13}$ coulomb the drop sequence was stretched by ≈ 200 μm. The value of q was chosen such as it coincided with the maximum charge suitable for proportional deflection printing. Thus, the following results represent the worst case scenario for the given printing conditions. Other simulations for Q = 1.0 and 1.4 ml/min are showed in Appendix C6. In the case of Q = 1.0 ml/min the sequence was stretched by as much as 300 μm while it was 125 μm for Q = 1.4 ml/min. Notice that the drop relative position is given from the point of detachment (z_{pd} ≈ 5mm from top of deflection cell see figure 5.53) of tail end drops from the main stream. The point of detachment can be easily calculated using equation 5-132. Experimental results agreed very well with the above estimates. It was also observed that for uncharged printing drops, the drop spacing remains almost constant within the printing distance window of 20 to 30 mm from the deflection cell entry.

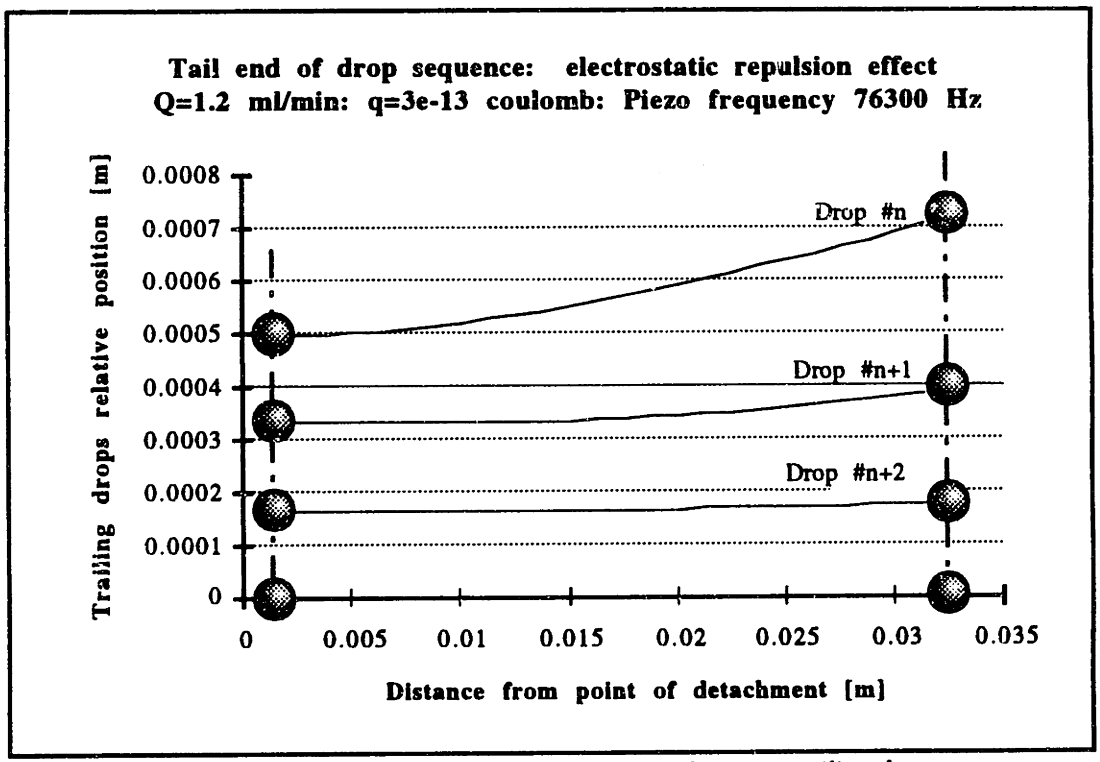

Figure 5.34: Tail end effect simulation for the last four trailing drops.

The printing error related to such effect can be seen as a longer printed line than expected from a uniformly spaced drop sequence.

From the model as well as from experimental observations, we can conclude that a higher flow rate as well as a lower printing charge level decrease the tail end effect. If the printing condition are chosen accordingly no compensation is required. However, if the printing conditions are not favorable, the print command should be re-evaluated. Say the uncompensated print command is start print at 11000 and stop print at 20000 μm. If the stream is estimated to stretch by $\Delta z = 200$ μm before it hits the powder bed, then it can be translated into a Δy compensation by:

$$\Delta y = \frac{\Delta z\, v_{y,scan}}{\lambda f} = \frac{\Delta z\, v_{y,scan}}{u_z} \cong \frac{\Delta z\, v_{y,scan}}{u_0} \qquad (5\text{-}86)$$

where Δz is the amount by which the stream has stretched

$v_{y,scan}$ is the printhead scanning speed = 1.5 m/s

λ is the average drop spacing ≈ 165 μm

f is the piezo resonator frequency = 76300 Hz

u_z is the droplet velocity @ the powder bed level ≈ u_0 = 12.5 m/s.

The printing command becomes; start printing @ 11000 μm and stop printing at $|20000 - 24|\mu m \approx 19980\ \mu m$ which is the closest integer multiple of 10 μm encoder ticks.

In most case however, the error introduced by the tail end effect is within the machine resolution which is defined by one encoder tick (i.e. 10 μm).

5.9 Air drag forces & boundary layer

In addition to the electrostatic forces acting on the charged droplets, another force due to drop aerodynamics should be considered. The magnitude of the aerodynamic drag can be as large as the deflection force. It is therefore essential to consider it in the drop flight path model in order to predict drop placement with suitable accuracy.

Two distinct drag forces can be determined within a sequence of printing drops: drag force on the leading drop and drag force on the following drops. Both forces have different magnitude because of their particular interaction with the surrounding air flow.

5.9.1 Drag on leading drops

The leading drop of a printing sequence (drop #0) is the only drop that flies in still air, while the other drops move in the wake of the preceding one. As a result, the drag force on the leading drop is higher and cause drop merging behavior as discussed in a later section.

The drag on most bodies is a combination of both form and friction drag. Drag due to pressure is called form drag because it depends on the shape or form of the body. Drag due to shear stress is called skin friction drag or friction drag. Friction drag depends primarily on the amount of surface in contact with the fluid.

The factor which determines whether drag is predominantly a pressure or a viscous force, is defined by the Reynolds number. The Reynolds number of a liquid drop can be calculated as follows:

$$\mathrm{Re} = \frac{u_z D}{\gamma_{air}} \qquad (5\text{-}87)$$

where u_z is the drop velocity [m/s]
D is the drop diameter [m]
and γ_{air} is the kinematic viscosity of air = 1.49×10^{-5} m^2/s

In our calculation, we assumed that the liquid drops of binder maintain an exact spherical shape with diameter D. In fact, drops of water, smaller than 100 μm in diameter, flying through air have no noticeable deformation because water surface tension dominates over gravity and air friction. Since the droplet diameters used in our printing application are usually smaller than 100μm, the drop can be modeled as a solid sphere.

The Reynolds number is a dimensionless value which indicates whether the flow characteristic around a drop is mostly laminar (Re < 100) or turbulent (Re > 1000). The Reynolds number can be seen also as the ratio of inertia force to viscous force in the fluid. Thus, for the flow around our droplet, *Re* indicates whether the drag is mainly a viscous force (Re <10) or a pressure force (Re > 1000). Depending on the magnitude of the Reynolds number, drag forces relates to different set of parameters as showed in table 5.11.

Table 5.11: Dependence of drag on various parameters in high Re and low Re flow.

Parameter	High Re number	Low Re number
Velocity (u_z)	u_z^2	u_z
Air density (ρ)	ρ	None
Air dyn. viscosity (μ)	≈ 0	μ
Drop diameter (D)	D^2	D

This sensitivity to different parameters is reflected in the way drag forces are computed for low and high Reynolds number.

$$F_{Drag}(\text{High Re}) = (\text{Constant})\left(\frac{1}{2}\rho_{air}u_z^2\right)\left(\frac{\pi D^2}{4}\right) \qquad (5\text{-}88)$$

$$F_{Drag}(\text{Low Re}) = (\text{Constant})(\mu_{air}u_z)(D) \qquad (5\text{-}89)$$

The constant value in equation 5-88 & 5-89 is referred as the drag coefficient C_D in the case of high *Re* and viscous drag coefficient C_D' for low *Re*.. The goal of this section is to find the best estimate of the drag coefficient C_D or C_D' for given printing conditions.

However, typical Reynolds number related to our printing conditions on the leading drop varies in the range 40 to 100. This range represents the transition between laminar and turbulent flow were both type of drag forces are present. Drop #0 experiences both types of drag, but the proportion between both force is unknown. Drag in the intermediate Reynolds number range (10 < Re < 1000) is most difficult to analyze, even qualitatively, because the boundary layer concept is not valid but the inertia forces are significant [ref 84]. Therefore, empirical solutions should be developed in order to evaluate the combined drag effects on drop #0.

Stoke's flow

A simple empirical solution was developed by Sir G. G. Stokes in 1851 for flow over a sphere at very low Reynolds number (i.e. Re < 1). Stokes found that the drag on a sphere at very low Reynolds numbers is given by:

$$F_{Drag} = 3\,\pi\,\mu_{air}\,D\,u_z \qquad (5\text{-}90)$$

where μ_{air} is the dynamic viscosity of air $\approx 1.8\text{x}10^{-5}$ [N x s/m^2]

D is the drop diameter [m]

u_Z is the drop speed or relative speed of air flow.

Equation 5-90 is called Stokes' law. The drag is not due to friction only; one third of the drag is due to pressure and two-third is due to friction. The streamline pattern around the sphere were assumed to be nearly symmetric with only a very thin wake (no separation). Although we know beforehand that the method is not tailored for our target Reynolds number range (40 -100), it gives a good first order estimate of the drag force. In principle, Stokes' law could be used for higher Reynolds number since laminar separation occurs at the rear end of the sphere for Reynolds number as high as ≈ 50. However, we should be aware that for such higher Reynolds number, the viscous force will be overestimated while inertial force underestimated.

The drag coefficient C_D for the sphere at very low Reynolds number (Stoke's flow) can be found by combining equation 5-88 and 5-90 to give:

$$C_D = \frac{F_{Drag}}{\frac{1}{2}\rho_{air}u_z^2\left(\frac{\pi D^2}{4}\right)} = \frac{24\mu}{\rho\,u_z D} = \frac{24}{\mathrm{Re}} \qquad (5\text{-}91)$$

Although Stoke's law is not a perfect match for Reynolds number in the range 40 to 100 because it underestimates the pressure drag, it could be considered as a good first order estimate.

Low Reynold's number model

Drag is difficult to analyze in the Reynolds number range (10<Re<1000) because it represents the transition region between laminar flow and turbulent flow. Information on drag in this range is based almost entirely on experiment. Data are usually presented in

terms of C_D as a function of Reynolds number *Re*. The drag coefficient for a smooth sphere is plotted in figure 5.35.

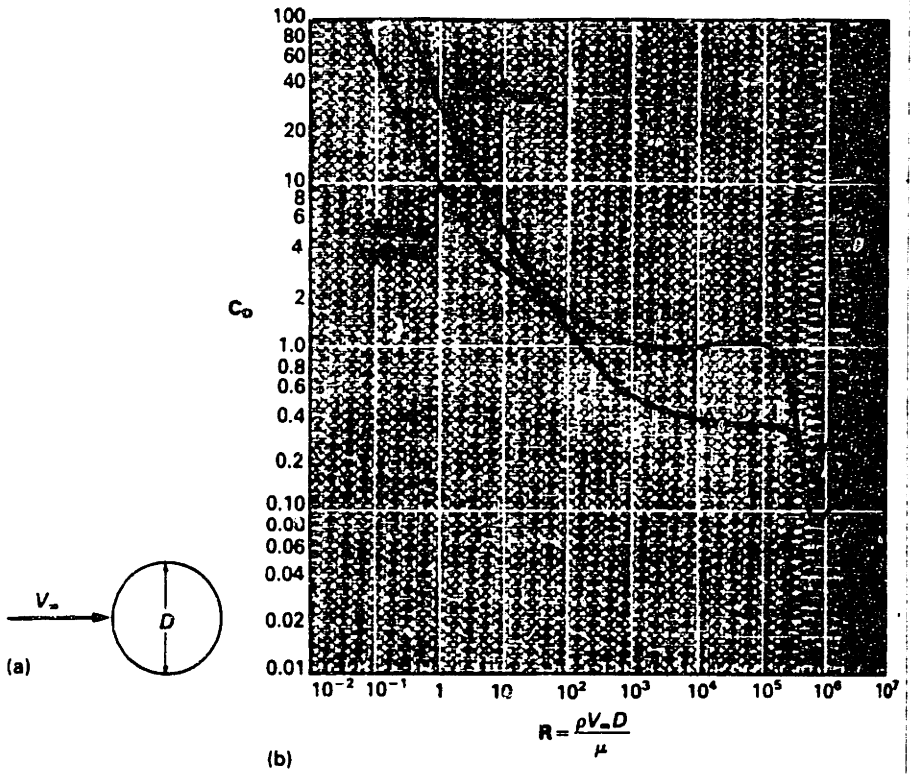

Figure 5.35 Drag of smooth body of circular cross section (cylinder or sphere) a) Schematic b) drag coefficients as a function of Reynolds number. (From fundamental of fluid mechanics p.522 ref [84])

A curve fit is also suggested to facilitate calculation.

$$C_{D,sph} \approx \frac{24}{\mathrm{Re}} + \frac{6}{1+\sqrt{\mathrm{Re}}} + 0.4 \ , \qquad \text{for } \mathrm{Re} < 2\times 10^5 \qquad (5\text{-}92)$$

At low Reynolds numbers, the sphere drag coefficient C_D varies with Reynolds number, decreasing as Reynolds number increases. This particular dynamics does not mean however, that the drag force decrease for low Reynolds number. To the contrary, drag increases because it is proportional to the square of the speed.

It is interesting to note the similarity between equation 5-91 and the Stokes drag coefficient in equation 5-92. By inspection, experimental data from curve fit would suggest that Stokes' law underestimates the drag coefficient C_D. This was expected since we have already predicted that Stokes' law underestimates the inertial force. The difference

between the two methods of calculation should stand out when compare with the measured data in section 5.10.2 in flight path model.

5.9.2 Drag on following drops (or stream)

The other type of drag force that was mentioned earlier is related to the drag on the drops following drop #0. Since the following drops flies in the wake of the preceding one, their drag characteristics are significantly different from the drag on the leading drop. Unlike a single drop moving in still air, the continuous stream of drops, when spaced closely enough, will trap the air between the drops and move it with the sequence of drops (see figure 5.36).

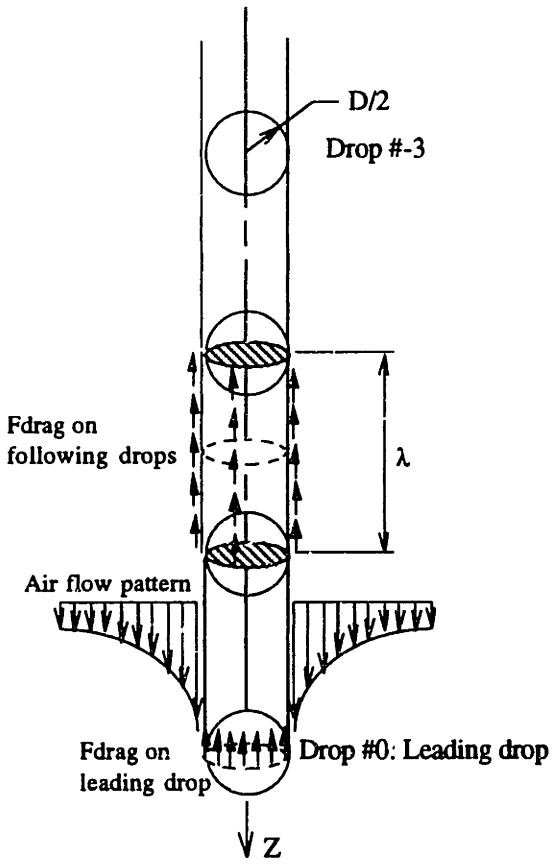

Figure 5.36: Schematic of drag force on following drops.

In our drag model, spheres are replaced by cylindrical slugs of the same diameter and of length equal to the drop spacing. The drag force is in this case a shear force, called also skin friction, acting on the surface of the cylindrical slug. The shear force is balanced by transferring momentum to the surrounding air to form a characteristic logarithmic shape air flow pattern around the jet.

Blasius solution

The shear force occurs at the interface between the boundary layer and the surface of the cylinder. The drag or shear force is determined from the velocity profile $u_{z,x}$ of the boundary layer as well as the kinetic viscosity γ_{air} of the ambient air. In 1908, Blasius found a simplified solution for a similar problem for an air flow over a semi-infinite flat plate.

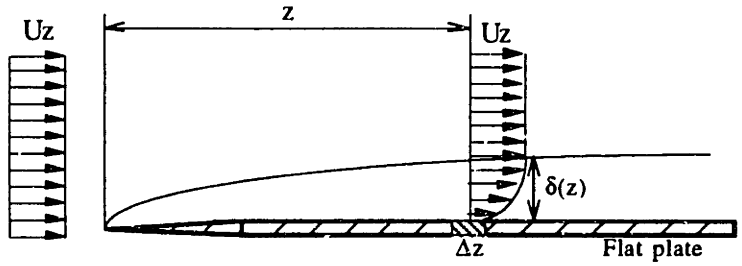

Figure 5.37: Schematic of Blasius laminar boundary layer over a flat plate.

Assuming a laminar boundary without separation from the plate, he derived the following expression for the friction coefficient C_f at a distance z from the tip of the plate.

$$C_f = \frac{\tau_w(z)}{\frac{1}{2}\rho_{air} u_z^2} = \frac{0.664}{\sqrt{\mathrm{Re}_z}} \qquad (5\text{-}93)$$

where $\tau_w(z)$ is the shear force [N/m^2] at a distance z from the tip of the plate

ρ_{air} is the air density $\approx$ 1.2 kg/m^3

u_z is the relative velocity of air or the drop velocity [m/s]

and $\mathrm{Re}_z = \frac{u_z z}{\gamma_{air}}$ is the Reynolds number at position z on the plate.

γ_{air} is the kinematic viscosity of air $\approx$ 1.58x10^{-5} [m^2/s].

Then the drag force F_d on a segment Δz of a plate of width b can be evaluated with the following expression:

$$F_D = \tau_w(z)\, b\, \Delta z = \left(0.664\ \mathrm{Re}_z^{-1/2}\right)\left(\frac{1}{2}\rho_{air} u_z^2\right)(b\, \Delta z) \qquad (5\text{-}94)$$

Which represent the force acting on only one side of the surface segment bΔz. The plate problem can be adapted to our jet stream if we bend the plate around itself parallel to the air flow in order to form a cylinder. The air flow is assumed to keep a similar velocity profile along the radial cross-section of the cylinder. Equation 5-94 can be modified by

simply replacing the surface bΔz by the surface of the cylindrical slug between the drop. The force on each drops is calculated by multiplying the shear force $\tau_w(z)$ at a distance z (measured from the orifice) by the surface area S of the cylinder formed by the drop diameter D and the drop spacing λ.

$$F_D = \tau_w(z)\,\pi\,\mathrm{D}\,\lambda = \left(0.664\ \mathrm{Re}_z^{-1/2}\right)\left(\frac{1}{2}\rho_{air}u_z^2\right)(\pi\,\mathrm{D}\,\lambda) \qquad (5\text{-}95)$$

This expression is valid for laminar flow only, which is characterized by a Reynolds number $Re_Z < 3.0x10^5$. Since the Reynolds number range in our application varies between $5x10^3$ and $25x10^3$, equation 5-95 can be applied to all the printing conditions. Most of the calculation done in the model developed in a next section make use of equation 5-95. The accuracy of this method relies on the validity of the assumption made about the similarity of the velocity profile nearby the plate versus the cylinder. A more accurate but also more complex method was developed at the IBM research centers by using the momentum and continuity theorem inside a control volume.

5.9.3 Stream boundary layer

This method tackles the problem by applying momentum conservation between the input and output of a control volume located at the exit of the printhead orifice (see figure 5.38). It differs from the Blasius method by modeling a cylindrical air flow geometry around the stream instead. Such an air flow model corresponds better to reality then the flat surface air flow depicted in the Blasius solution.

The input of the control volume is the jet stream at the orifice level. The output of the control volume is the stream as well as the air flow boundary layer at a distance z from the orifice.

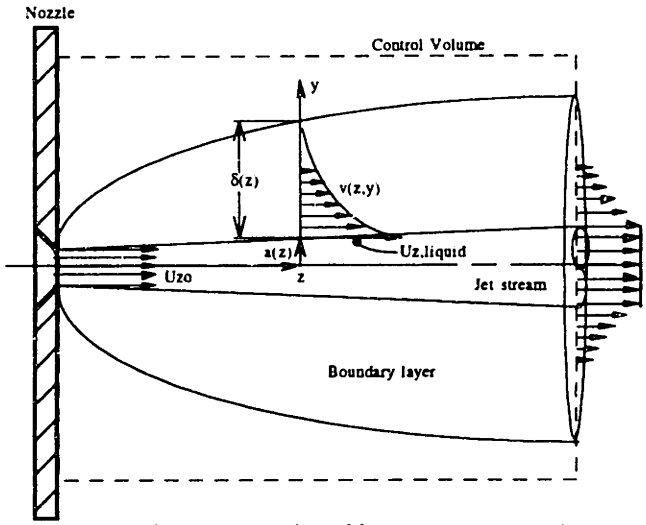

Figure 5.38: Boundary layer induced by a jet emerging from a nozzle.
(From Boundary Layer Around a liquid Jet, IBM reference [ ])

The momentum variation is derived by matching it with the momentum gain in the air flow and allowing the growth of the stream sectional area as the jet loses its momentum.

The method was used to calculate the boundary layer thickness $\partial_{0.99}$ as well as the drop speed u_z for predetermined printing conditions.

The boundary layer $\partial_{0.99}$ is an important result which is used to determine the region were a deflected droplet is still protected against direct drag force from still air. The drop speed on the other hand can be used to predict the ballistic effect on the powder bed or to compare the performance of various printing condition against drag effects.

Only the outline of the method will be described in this thesis. For more information the reader should refer to the paper cited in reference [63].

Because analysis of the stream of drops would be unreasonably complex, the method approximates the problem by replacing the drops with an equivalent section of cylindrical shape. It was showed (see ref[63]) that the analytically obtained momentum losses of liquid jets match experimental data on drop sequence very well.

With reference to figure 5.38, the momentum and continuity equations applied to a boundary layer of thickness $\partial_{0.99}$ and a liquid jet of radius a are

$$2\pi\rho_{air}\int_0^{\delta_{0.99}(z)}[a(z)+y]\,v^2(z,y)\,dy \;+\; \rho_{liq}\pi a^2(z)v_{liq}^2(z) = \rho_{liq}\,\pi\,a_0^2\,v_{liq,0}^2 \qquad (5\text{-}95)$$

$$\frac{d}{dz}\left[\rho_{liq}\,\pi\,a^2(z)\,v_{liq}^2(\bar{z})\right] = 2\pi\,a(z)\,\mu_{air}\left.\frac{dv}{dy}\right|_{y=0} \qquad (5\text{-}96)$$

$$\pi\,a^2(z)\,v_{liq}(z) = \pi\,a_0^2 v_{liq,0} \qquad (5\text{-}97)$$

Here, the coordinate z is in the jet direction, and y is measured radially from the surface of the liquid jet. Velocity, density, and dynamic viscosity are denoted by v, ρ, and μ, respectively, with subscripts *air* and *liq* for air and liquid. The subscript 0 denotes the initial values at the nozzle.

The first equation 5-95, represents the conservation of axial momentum, whereas (equation 5-96) matches the rate of momentum loss to the skin friction on the jet. Mass conservation, or the continuity of the liquid jet, is expressed in the last equation 5-97.

An approximate solution for a boundary layer equation in integral form such as equation (5-95) is normally obtained by assuming a velocity profile of the air flow v(z,y). From earlier experiments, it was observed that a logarithmic profile would be most appropriate, such as:

$$v(z,y) = v_{liq}(z)\left\{1-\frac{1}{\beta(z)}\ln\left[1+\frac{y}{a(z)}\right]\right\} \qquad (5\text{-}98)$$

where

$$\beta(z) = \ln\left[1+\frac{\delta(z)}{a(z)}\right] \qquad (5\text{-}99)$$

Then, substitution of equation (5-98) into equations (5-95 & 96) with elimination of a(z) and use the appropriate boundary conditions results in:

$$\bar{z} = \int_0^{\beta}\frac{\beta\left(1+e^{2\beta}\right)-\left(e^{2\beta}-1\right)}{\beta^2-\bar{\rho}\left[\beta^2+\beta-\frac{1}{2}\left(e^{2\beta}-1\right)\right]}\,d\beta \qquad (5\text{-}100)$$

where

$$\bar{z} = \frac{4}{\mathrm{Re}}\frac{z}{a_0}, \quad \mathrm{Re} = \frac{2a_0\rho_{air}v_{liq,0}}{\mu_{air}}, \quad \text{and} \quad \bar{\rho} = \frac{\rho_{air}}{\rho_{liq}}\frac{D^2}{d_0^2} \qquad (5\text{-}101)$$

where D and d_0 denote the diameter of the drops and orifice, respectively. The dimensionless density $\bar{\rho}$ had to be scaled by a factor $\frac{D^2}{d_0^2}$ in order to compensate for the larger volume of the cylindrical slug which replaced the spherical droplet shape.

Equation 5-100 can now be numerically integrated for a range of $\bar{z}$ values as a function of β. Afterwards, the stream velocity $v_{liq}(\bar{z})$, the stream radius a(z), boundary layer thickness $\partial_{0.99}(z)$, and air flow profile v(z,y) are obtained from equations 5-102 to 5-106 computed successively:

$$z = \frac{\mathrm{Re}\,a_0}{4} fct(\beta) = \frac{\rho_{air}\, v_{liq,0}\, a_0^2}{2\mu_{air}} fct(\beta) \qquad (5\text{-}102)$$

$$v_{liq}(z) = \frac{v_{liq,0}}{1-\bar{\rho}\left[1+\frac{1}{\beta}-\frac{1}{2\beta^2}\left(e^{2\beta}-1\right)\right]} \qquad (5\text{-}103)$$

$$a(z) = a_0\sqrt{\frac{v_{liq,0}}{v_{liq}(z)}} \qquad (5\text{-}104)$$

$$\delta_{0.99} = a(z)\left[e^{2\beta}-1\right] \qquad (5\text{-}105)$$

$$v(z,y) = v_{liq}(z)\left\{1-\frac{1}{\beta(z)}\ln\left[1+\frac{y}{a(z)}\right]\right\} \qquad (5\text{-}106)$$

The above equations were used to construct the next two graphs (see figure 5.39 & 5.40) of the boundary layer $\partial_{0.99}$ (z) and drop velocity v_{liq}(z) for three different flowrates. The three flow rates were chosen within the range of stable printing conditions defined by the Rayleigh's frequency.

The results showed (see figure 5.39) that the boundary layer is not significantly sensitive to the various flow rates. In fact, at a flight path distance of 25 mm the boundary layer $\partial_{0.99}(0.025)$ is within a window 3.2 μm ± 0.2 μm for the three flow rate. Compared to the drop diameters which varies between 75 and 85 μm, the boundary layer is relatively small for the flight path distance of a regular printhead design.

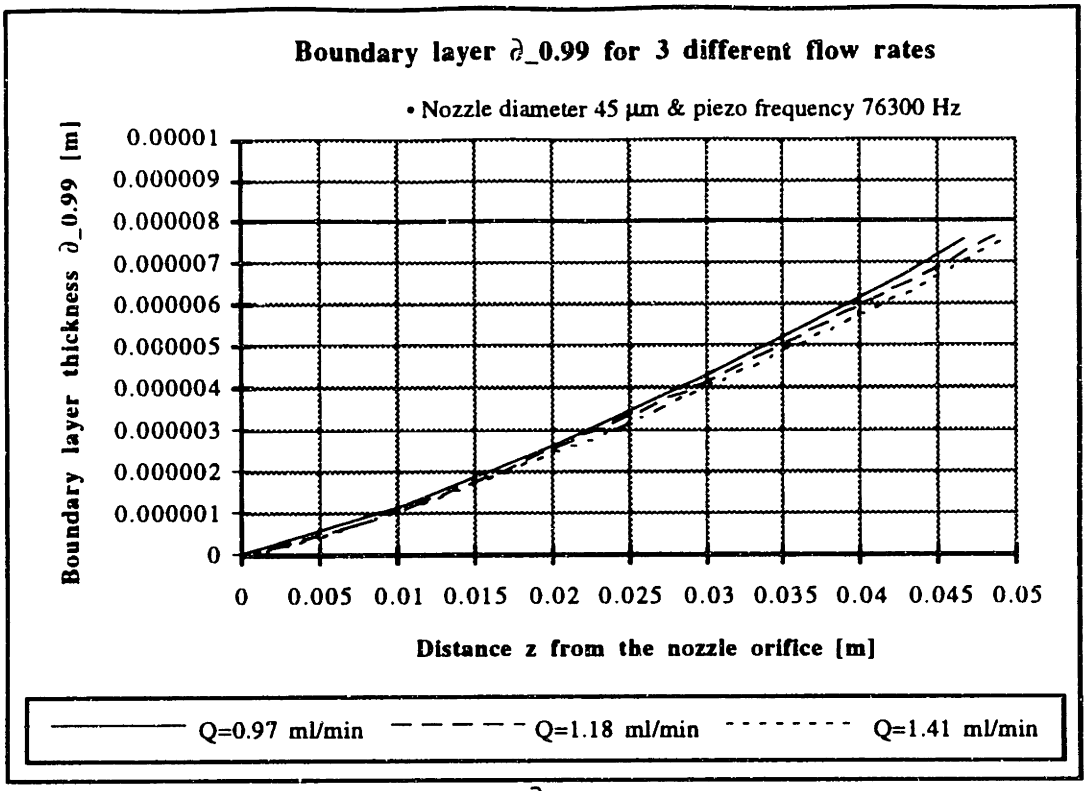

Figure 5.39: Boundary layer $\partial_{0.99}$ for three different flow rate.

The other graph (see figure 5.40) was done for the droplet velocity for the same three flow rates. An important observation can be done about the effect of different initial droplet velocity on the momentum loss. For example, the data from the graph shows initial speed of 14.7, 12.6, and 10.2 meter per second. Then, those respective velocity if measured 25 mm from the orifice would turn to be 12.87, 11.0, and 8.87, for and equivalent velocity loss of 12.4%, 12.7%, and 13.0%.

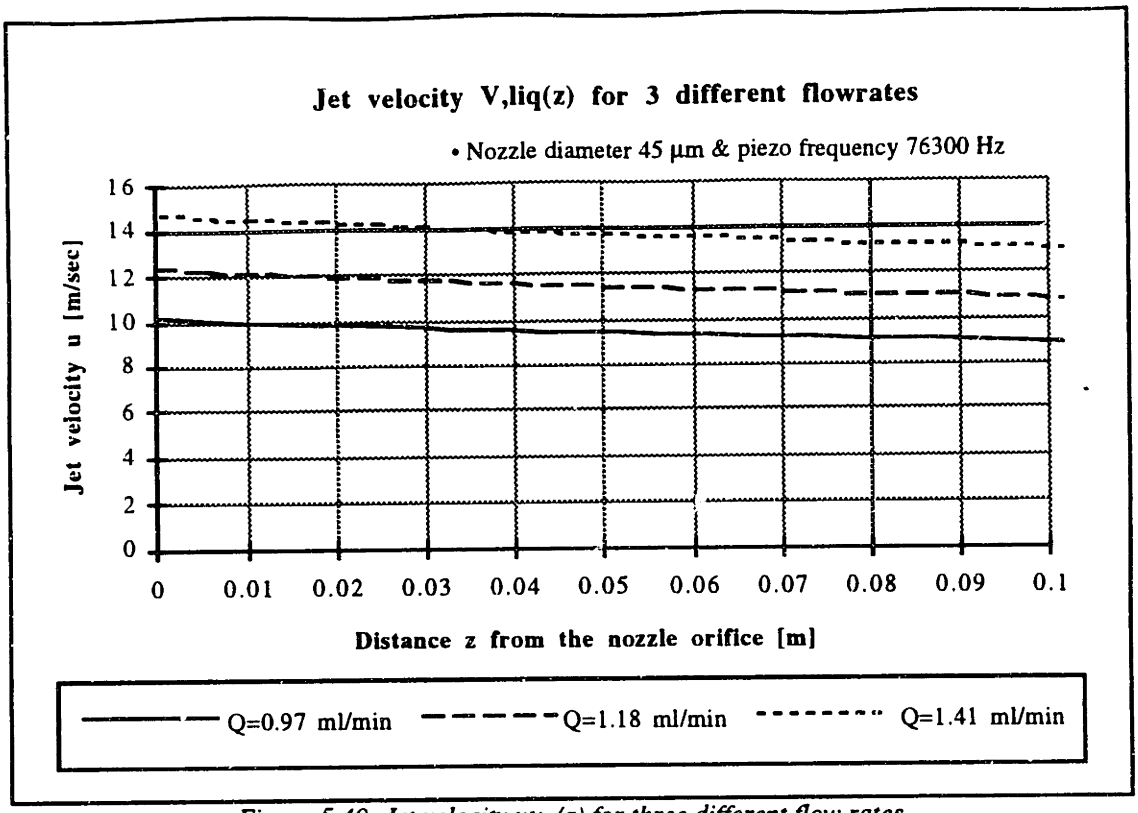

Figure 5.40: Jet velocity $v_{liq}(z)$ for three different flow rates.

This means that a lower flow rate will lose a larger proportion of its momentum compared to a higher flow rate or initial droplet velocity. In other words, a lower flow rate is more significantly affected by air drag forces. Therefore, this present study seems to indicate that, a higher jet velocity would be advantageous in order to minimize detrimental effects such as drop merging.

5.9.4 Slowdown effect & merging with subsequent drops

If, for example, a linear train of drops following each other moves through still air (figure 5.41 left), the leading drop is retarded most by air friction and therefore tends to merge with the drop behind it after a short time (see figure 5.41 right).

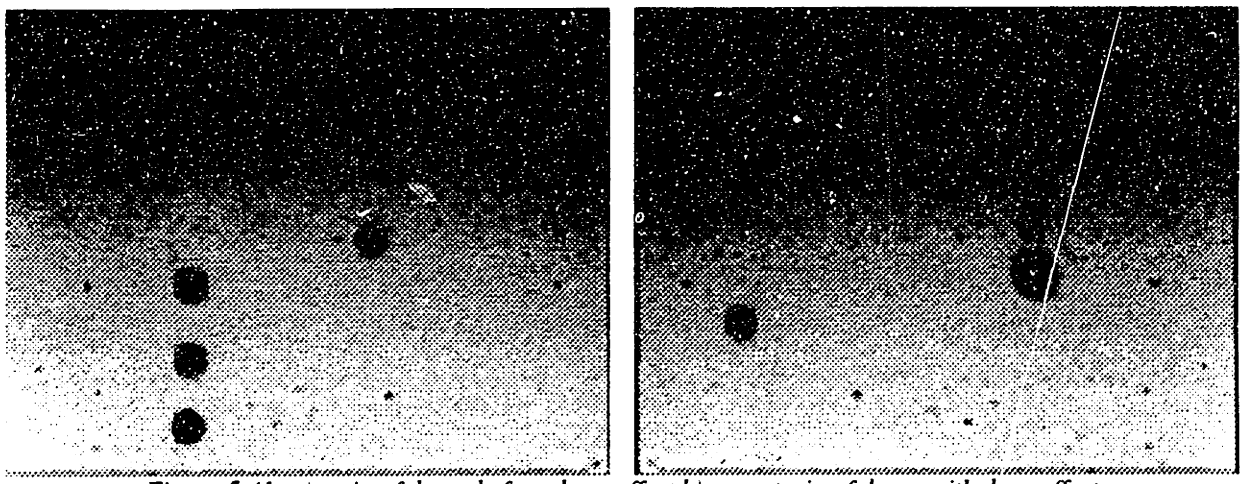

Figure 5.41: a) train of drops before drag effect b) same train of drops with drag effect

This process repeats itself until the entire train of drops has merged into a single drop (Mansson,1971). The situation becomes even more complex if closely spaced drops follow slightly different trajectories. Since the merging of drops is very undesirable for small printing features such as for surface macro-texture or contour snapping, adequate printing procedure should be observed. Techniques such as guard drops described in Hertz ref[62] can not be used, since 3D printing relies essentially on printing continuous uniform train of drops.

The question is that merging cannot be avoided but only postponed. It is therefore important to understand the drop dynamics in order to develop suitable printing techniques and conditions that will prevent or minimizing the negative impact of premature merge on the print quality.

Merging models as well as merge retarding methods will be described in a next section.

5.9.5 Effect of printhead scanning (fast axis) speed

As the printhead scans across the powder bed, the printing drop sequences have a relative speed $v_{y,\,scan}$ compared to the surrounding air. In other words, the drops are subjected to a cross wind of uniform velocity $v_{y,\,scan}$ perpendicular to their trajectory. The drag forces induced on the stream are about 50 to 100 times smaller than the drag forces

parallel to the stream axis. In fact, drag forces are proportional to the square of the air flow velocity, and the ratio jet velocity to scanning velocity varies between 7 to 10.

The effect of the perpendicular drag force is felt only an a portion of the stream. Depending on the printhead design, the stream will be shielded from the cross wind for a fraction of its flight path. In fact, the bulk of the printhead where the charging electrode and deflection cell are machined acts as wind shield in the Y-axis for about 50% of the flight path in the case of our printhead design.

Unlike other type of drag forces discussed earlier in this section, such a perpendicular drag force affect the drop positioning along the scanning Y-axis only. The final drop position along the Y-axis on the powder bed is essentially determined by the flight distance along the scanning or Y-axis. The drop flight distance along the Y axis is defined in theory by the printhead scanning speed $v_{y,\,scan}$ and the droplet time of flight t_f to the powder bed. The following expression is a direct way to calculate the distance y_f a drop travels along the Y axis before it hits the powder bed.

$$y_f = v_{scan,y}\, t_f \qquad (5\text{-}107)$$

where y_f is the flight distance taken from the drop forming point at the orifice
$v_{scan,y}$ is the fast axis scanning speed [m/s]
t_f is the drop time of flight from the point of drop formation

For example, say we are printing with the following typical printing conditions:

$Q = 1.2$ ml/min	Flowrate
$d_0 = 45\mu m$	Orifice diameter
$F = 76300$ [Hz]	Piezo-resonator frequency
$\lambda = 165$ [μm]	Drop spacing
$D = 80$ [μm]	Drop diameter
$u_z = 12.5$ [m/s]	Drop speed
$m_d = 3.1 \times 10^{-10}$ [kg]	Drop mass
$L_f = 25$ [mm]	Typical distance orifice to powder bed
$p_s = 50\%$	Percent of stream shielded from cross wind
$t_f = 0.002$ [s]	Typical drop time of flight
$v_{scan,y} = 1.5$ [m/s]	Printhead scanning speed
$Re_y = 7.5$	Reynolds number transversal to the stream
$C_D \approx 3.5$	Drag coefficient transversal to the stream (see graph in figure 5.35)

The drop flight distance y_f along the fast axis would be 0.0030 m. If the perpendicular drag force is added to the expression as:

$$y_f = v_{scan,y}\, t_f + \frac{1}{2} a_y \left(0.5 t_f\right)^2 \qquad (5\text{-}108)$$

where

$$a_y = \frac{-F_{D,y}}{m_d} = -\frac{C_D\left(\frac{1}{2}\rho_a v_{scan,y}^2\right)(\lambda D)}{m_d} \approx \; -200\ [\mathrm{m/s^2}] \qquad (5\text{-}109)$$

then y_f is equal to 0.0029 m which corresponds to a 3% or 100 μm decrease. The flight path y_f has a significant impact on the Y-axis accuracy for bi-directional printing. When the printhead prints in both direction along the Y axis, the flight path is used to compute a shift or offset compensation. An offset constant is added or subtracted from the printing command positions to compensate for the droplet speed component in the Y direction. The accuracy of this procedure depends strongly on the predictability of the scanning speed $v_{scan,y}$ as well as the time of flight measurements. For example, the standard velocity ripple on the fast axis is somewhere around ±1.5% above and below the average scanning speed $v_{scan,y}$. On the other hand, the time of flight t_f measurement can be done within ±0.25%. If we apply the propagation error theorem to the flight distance y_f for the above conditions, we find the following Y-axis accuracy:

$$\sigma_{total}^2 = \left(\frac{dy_f}{dv_{scan}}\right)^2\Bigg|_{\bar{p}} \sigma_{scan,y}^2 + \left(\frac{dy_f}{dt_f}\right)^2\Bigg|_{\bar{p}} \sigma_{t_f}^2$$

$$\sigma_{total} = \sqrt{v_{scan,y}^2 \sigma_{t_f}^2 + t_f^2 \sigma_{v,scan}^2} = 0.000045 \text{ m or } 45\ \mu\text{m} \qquad (5\text{-}110)$$

Therefore, since the expected error is smaller than the effect of drag ($\approx$100μm), it means that perpendicular drag force has a significant effect on the flight path. As a result equation 5-108 should be used instead of equation 5-107 in order to predict the printing offset compensation necessary for bi-directional printing.

However, if the velocity ripple on the fast scanning axis is larger, it may not be necessary to compensate for the perpendicular drag force. In this case, drag force compensation would be meaningless compared to error induced by the scanning velocity inconsistency.

It was observed that air flow in the range of 1.0 to 2.0 m/s perpendicular to the stream did not affect the drag parallel to the stream. In other words, if the motion of the leading drop #0 was frozen in space (20-25 mm from top of deflection cell) by using a strobe light, no cross wind in that range could change its vertical position. However, for high flow rate [>2.0 m/s], the drop was vibrating by about one diameter length.

Perpendicular drag does not have an effect on the leading drop #0 X-Z position, because it has no force component in the X-Z-axis. It will not affect drop #0 unless the perpendicular air flow velocity is large enough compared to the jet velocity. The binder jet velocity is usually in the order of 10 to 14 m/s. Therefore, as long as the scanning speed remains in the range 1 to 2 m/s, which is a factor 5 to 10 smaller, it should not affect significantly the X-Z position of drop #0. The latter experiment was done for various flow rates on binder drop of about 75-80 μm in diameter.

On the other hand, cross wind can have a small effect on the drop spacing. It was observed that a cross wind tends to reduce the drop spacing more rapidly. The effect was so small that it had to be measured over several drops. For example, a cross wind of 1.5 m/s, reduced a train of 120 drops by about 2 drop spacing for a flow rate of 1.2 ml/min with initial drop velocity of 12.5 m/s and 165 μm drop spacing. Which means that drop spacing was reduced by 2/120 or 1.7 % or about 2.7 μm, 20 mm from the printhead orifice. Although this effect seems small, when it is translated on the powder bed it may turn to be significant. In fact, it is the equivalent to remove 2 drops from the train of 120 drops (printed line 2.16 mm long) which convert into a powder bed error of -36μm along the fast Y-axis, if we print at f_{piezo} =76300 Hz with a scanning speed $v_{y,scan}$ = 1.5 m/s.

This drop spacing reduction is probably due to the cross wind pushing out the air trapped between drops, increasing by the same token the drag forces parallel to the stream axis. If drop spacing needs to be kept constant within 1%, then higher flow rate should be used. The experiment showed also that the drop spacing decrease is greatly reduced for smaller cross air flow velocity.

As a final note, if a wind shield is added in order to protect the entire flight path from the cross wind than drag force can be neglected along the Y-axis and equation 5-107 could probably be used with good accuracy. As a result drop spacing could also be considered constant.

5.10 Modeling single and train of droplet(s) flight path

Predicting and controlling the printing position is a task of combining all the forces and interactions on each single drops. Then applying those forces inside the equation of motion from the orifice to the powder bed level.

The largest sources of drop placement errors are deflection errors mainly caused by the drops aerodynamics and charging accuracy.

In order to make the drop placement analysis complete, 5 major topics need to be covered.

1- Aligning the drops or positioning each drop relative to other.
2- Model the combined forces on drops and predict drop position X-Z.
3- Understand and prevent merging.
4- Printing strategies
5- Printhead design restriction and recommendations.

The problem of aligning the drops was covered earlier in the compensation for induced charge section. Now our task is to predict accurately where an aligned train of charged drops is going to hit the powder and compare it with experimental values.

5.10.1 Model output is at best as accurate as input!

The general principle of any model is that output accuracy depends on the quality of the various assumptions which simplified our task of characterizing the problem. In addition, it also depends on the accuracy of the input parameters we are feeding the model with. The accuracy of the models will be assessed by using the theorem of error propagation, which is described more in details in the error budgeting chapter.

The basic expression:

$$\sigma_{f,total}^2 = \left(\frac{df}{da}\right)^2\Bigg|_{\bar{a},\bar{b},..} \sigma_a^2 + \left(\frac{df}{db}\right)^2\Bigg|_{\bar{a},\bar{b},..} \sigma_b^2 + \ldots\ldots \qquad (5\text{-}111)$$

where

f = *fct* (a,b,c,..).is the expression describing the flight path of a droplet.
a, b, c,.. are independent parameters needed to calculate the flight path.
and σ_x is the error standard deviation for the parameter *a, b, c,....*

will be used to quantify the accuracy for our complex non-linear model. The theorem assumes that each parameter $a,b,c,$ .. is independent from each other and have a normally distributed error. The total accuracy $\sigma_{f,total}$ will be computed from typical printing conditions labeled as $\bar{a}$, $\bar{b}$, $\bar{c}$,....

5.10.2 XZ drop trajectory model #1 (Physical model)

The following analysis will study the flight path of a single drop as well as of a continuous sequence of closely spaced drops. The purpose of analyzing the flight path for those two cases is to distinguish the effect of aerodynamics on a single leading drop compared to a continuous sequence of printing drops. These results will be used to predict the final position on the powder bed of a train of precisely charged drops. The conformity and accuracy of the model will be measured up against experimental results. In principle, the model should provide an accuracy which lie within the expected accuracy calculated from the input parameters.

Combining forces & other forces to be neglected

The major forces which determine the drops flight path are the aerodynamics drag force and the electric field force caused within the deflection cell limits.(see figure 5.42)

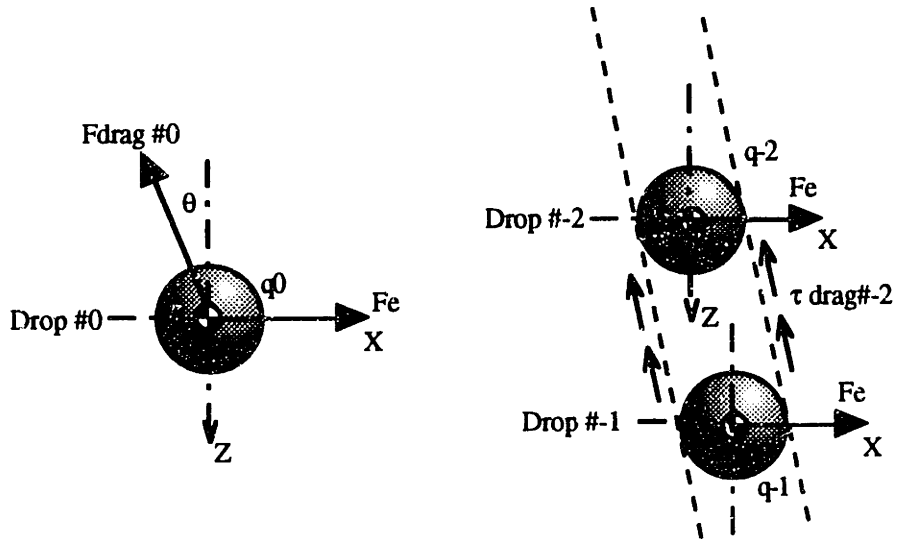

a) Leading drop b) Following drops

Figure 5.42: Free body force diagram of a) leading drop and b) following drops.

The velocity and charge of the drops will be varied in order to evaluate how the model reacts to changes. This actual model will neglect the electrostatic force interactions F_S between drops. This assumption is valid as long as the charge on the drops is minimized while the deflection voltage is held high near its break down value.

The first step in the model was to calculate the basic parameters describing the drops initial conditions such as:

$$\text{Initial drop speed: } u_0 = \frac{4Q}{\pi d_0^2} \text{ [m / s]}$$

$$\text{Initial drop spacing: } \lambda = \frac{u_0}{f} \text{ [m]}$$

$$\text{Drop diameter: } D = \sqrt[3]{\frac{6Q}{\pi f}} \text{ [m]}$$

$$\text{Drop mass: } m_d = \frac{\rho_{liq} Q}{f} \text{ [kg]}$$

We needed also a precise estimate of the charge q_n. The possibilities were to either calculate it using the techniques described in earlier sections, or simply to measure it. Since the initial goal was to evaluate the model without the need of on-line measurements, we calculated the q_n and verified it against the experimental charge measurements.

The model for the single drop #0 was calculated using the following expressions:

Drag force from equation 5-95 & 5.88:

$$F_{Drag\#0} = \tau_w(z)\,\pi\,\mathrm{D}\,\lambda$$

$$= \left(0.664\ \mathrm{Re}_z^{-1/2}\right)\left(\frac{1}{2}\rho_{air}u_z^2\right)(\pi\,\mathrm{D}\,\lambda)$$

$$\text{for } 0 \le z \le \left(\mathrm{L_{oc}} + L_{cd} + z_{pd}\right)$$

$$F_{Drag\#0} = (C_D)\left(\frac{1}{2}\rho_{air}u_z^2\right)\left(\frac{\pi D^2}{4}\right)$$

$$\text{for } z > \left(\mathrm{L_{oc}} + L_{cd} + z_{pd}\right)$$

$$C_{D,sphere} \approx \frac{24}{\mathrm{Re}} + \frac{6}{1+\sqrt{\mathrm{Re}}} + 0.4\ , \qquad \text{for } \mathrm{Re} < 2\times 10^5$$

Electric field force equation 5-73

$$F_{EX} = 0 \qquad \text{for } 0 \le z \le \left(L_{oc} + L_{cd}\right)$$

$$F_{EX} = q\,E = q\,\frac{V_d}{w_d} \qquad \text{for } \left(L_{oc} + L_{cd}\right) < z < \left(L_{oc} + L_{cd} + L_d\right)$$

Equation of motion along the X-axis:

$$x_0 = 0$$

$$u_{x,0} = 0$$

$$x_{i+1} = x_i + u_{x,i}\Delta t + \frac{1}{2}\left(\frac{F_E - F_D\sin\theta}{m_d}\right)\Delta t^2$$

$$u_{x,i+1} = u_{x,i} + \left(\frac{F_E - F_D\sin\theta}{m_d}\right)\Delta t$$

Equation of motion along the Z-axis:

$$z_0 = 0$$

$$u_{z,0} \equiv u_{z,0}$$

$$z_{i+1} = z_i + u_{z,i}\Delta t + \frac{1}{2}\left(\frac{-F_D \cos\theta}{m_d}\right)\Delta t^2$$

$$u_{z,i+1} = u_{z,i} + \left(\frac{-F_D \sin\theta}{m_d}\right)\Delta t$$

where

L_{oc} is the distance from the orifice to the top of the charging electrode

L_{cd} is the distance from the top of the deflection electrode to the entry of the deflection cell.

L_d is the length of the deflection cell parallel to the Z-axis

z_{pd} is the point of detachment distance measured from the deflection cell entry.

$$z_{pd} \equiv u_{z0}\sqrt{\frac{2\, x_{pd}\, m_D w_d}{q_{01} V_d}} + r_d \qquad (5\text{-}112)$$

The various forces acting on the drops can be applied only for certain region of the drop flight path. For example, the deflection force F_{EX} is valid only within the deflection cell limits as defined above. The same is true for the drag force on the leading drop which changes from drag on following drop to drag on leading drops as the drops reach the point of detachment z_{pd}.

The model for the following drops is quite similar except for the drag force calculation which stays as the drag on the following for the entire flight path. Therefore equation 5-113 should be used instead of 5.95 & 5.88, without consideration for the limits.

$$F_D = \tau_w(z)\, \pi\, D\, \lambda = \left(0.664\ \mathrm{Re}_z^{-1/2}\right)\left(\frac{1}{2}\rho_{air} u_z^2\right)(\pi\, D\, \lambda) \qquad (5\text{-}113)$$

The above set of equations will be used in the model which will attempt to predict the drops path measured in the following experiment.

Description of experiment

The goal of this experiment was to assess the accuracy of our drop flight path models for two different printing situations: 1) on a single drop, 2) on a continuous sequence of closely spaced drops.

The experiment begun by deflecting all the drops by charging them with a constant charge level q_n. The charge q_n was measured with the charge collector instrument to make sure charge q_n was kept constant. The flight path X-Z of the deflected drops was recorded in order to be compared with the modeled X-Z flight path.

The second part of the experiment was to deflect only a single drop. In order to visualize and measure the drop position X-Z, a single drop was deflected for each sequence of 256 drops. Therefore, 255 drops would remain uncharged while one drop would hold the same charge q_n as before in order to be deflected. The flight path X-Z of the single drop was recorded, and also modeled, up to a distance of $z \approx 25$mm from the orifice. One concern was that air turbulence from a preceding drop would affect the air flow on the following drop. Such a condition would be inappropriate for this experiment since our goal is to measured the X-Z flight path of a drop in still air. However, as stated in the IBM journal ref[63], 255 drop spacing is sufficient to prevent any air disturbance from one drop to the other.

Expected accuracy

Two distinct accuracy can be estimated in order to evaluate the experiment performance; the accuracy of the model and the repeatability of the experiment.

The accuracy of the model depends on the accuracy and precision of the input parameters. Those parameters consists basically in **all** the input parameters including the constant values (such as printhead dimensions) as well as all the other input variables. The accuracy of the parameters are both dependent on the long term steady state error as well as the short term error such as mid-frequency noise in a voltage amplifier.

Unlike the accuracy of the model, the repeatability of the experiments depends only on the parameters subject to short term changes. Their accuracy is determined from the equipment stability specifications such as the power supply voltage ripple error for example. Therefore, steady state error or drift with long term change should not be included.

Both types of accuracy are calculated by applying the theorem of error propagation (see section 6.3.2) to the set of equation showed above. The accuracy was expected to be different for the X and Z axis since they are characterized from a different set of equations.

The calculations were done based on the typical operating conditions of the printhead, as showed in the following table:

Table 5.12: Typical value of parameters and accuracy used for model error estimate.

INPUT PARAMETERS (MODEL)	TYPICAL VALUE	$\pm\sigma_n$
Jet position x_0 [μm]	0	10
Flow rate Q [ml/min]	1.2	1%
Piezo resonator frequency [Hz]	76300	50
Charging electrode width w_c [μm]	450	10
Deflection cell width w_d [mm]	1.5	15μm
Deflection cell high voltage V_d [V]	1000	0.1%
Charge collector voltmeter Vr	10	0.05%
Charge collector gain G	100	0.1%
Charge collector resistor R1 [MOhmn]	5.15	0.2%
time of flight t_f [s]	0.0025	0.25%
Air density [kg/m^3]	1.19	0.025
Binder density [kg/m^3]	1180	10
Kinetic viscosity [m^2/s]	$1.55\text{x}10^{-5}$	$2.5\text{x}10^{-7}$

Calculations were conducted with a mathematical software package "*Mathematica*" because of the complexity and number of equations. Using the above calculation methods, the accuracy of the model was determined as: **X ± 40 μm** and **Z ± 240μm**. The deflection accuracy along the X axis represents the error introduced by the printhead parameters only and are independent of the rest of the 3D printing machine. On the other hand, the Z-error is larger since it is very sensitive to flow rate fluctuations (jet velocity).

The same method was used to calculate the repeatability of the experiment. Notice the smaller number of parameters, which is directly related to the smaller number of mid-range frequency error sources in the system.

Table 5.13: Typical variables value and accuracy for experiment repeatability estimate.

INPUT PARAMETERS (Experiment)	TYPICAL VALUE	$\pm\sigma_x$
Jet position x_0 [μm]	0	0.25%
Flow rate Q [ml/min]	1.2	0.25%
Piezo resonator frequency [Hz]	76300	5
Charging voltage V_c [V]	80	0.03
Deflection cell high voltage V_d [V]	1000	0.05%
Charging cell capacitance C' [F]	$4.5\text{x}10^{-15}$	2%

Table 5.13 shows some parameters similar than in table 5.12 but with smaller error magnitude since the steady state error has been neglected. For example, the charging cell capacitance was determined based on a stream off-centered position of ±5% inside the cell (se figure 5.18).

Using those new values, the repeatability of the experiment was estimated to be: **X ± 1.3 μm** and **Z ± 60 μm**. The X-axis deflection accuracy is excellent and is mainly due to the quality of the equipment used in the set up.

On the other hand, the error along the stream axis or Z-axis still appears to be large. Just by itself the Z error does not mean anything. However, the Z error does have an effect on the drop flight distance along the Y-axis. Using a similar method, the repeatability along the fast Y-axis was estimated to be **Y ± 45 μm**, assuming a scanning speed $v_{scan,y}$ = 1.5 m/s with 1.5% velocity ripple (using equation 5-114 below).

$$y_f = v_{scan,y} \frac{z_f}{u_z} \qquad (5\text{-}114)$$

where z_f is the distance between the orifice and powder bed [m]

u_z is the drop speed [m/s]

This error could be greatly improved if we had a better control over the scanning velocity of the printhead. For example, if the scanning velocity is controlled within 0.5% instead, then the repeatability along to the fast Y-axis would improved to **±18 μm**.

XZ Model vs Experiment

The drop path was experimentally measured and then estimated with our model for different printing conditions. The graph of figure 5.43 is a typical example of a comparison analysis that can be done for a particular set of printing conditions.

The Z-axis is centered on the jet axis and has its zero reference located at the top of the deflection cell. This particular reference position is justified since no electrostatic deflection along the X-axis occurs upstream from that position. However, the model does initiate right at the exit of the printhead orifice in order to account for the drop deceleration between the orifice and the top of the deflection cell. On the other hand, the X-axis represents the level of drop deflection away from the jet center line or Z-axis. In the region between the deflection plates (i.e. from Z=0 to Z≈0.0095 m on the graph) the charged droplets move along a parabolic path. When the droplets leave the deflection zone, they travels approximately along a straight line depending on the drag force level (see figure 5.43).

Each graph includes five pieces of information or curves in which three of them are the model (MODEL in the legend) and two experimental set of data points (EXP in legend).

The main printing parameters that were used to perform the experiment and modeling are showed in the table just above the graph. For example, the first graph (see figure 5.43), was done for a typical flow rate of 1.25 ml/min with a charging voltage V_c=20V for

an equivalent drop charge $q_n = 7.22 \times 10^{-14}$ C. This particular charging pattern is typical for proportional deflection since the deflection level is approximately 200 μm (or one line width) at the powder bed level.

Main printing conditions

Nozzle diameter [m]	4.50E-05
Flow rate [ml/min]	1.25
Piezo frequency [Hz]	76300
Drop diameter [m]	8.04906E-05
Charging voltage [Vc]	20
Charge q [Coulomb]	7.22E-14
Deflection voltage [Vd]	1000
Deflection cell width [m]	0.0015
Deflection cell length [m]	0.0095
Drop mass [kg]	3.22193E-10
Exit jet velocitu [m/s]	13.10
Z-Offset for exp. data [μm]	9500
Point of detach zpd [m]	0.012

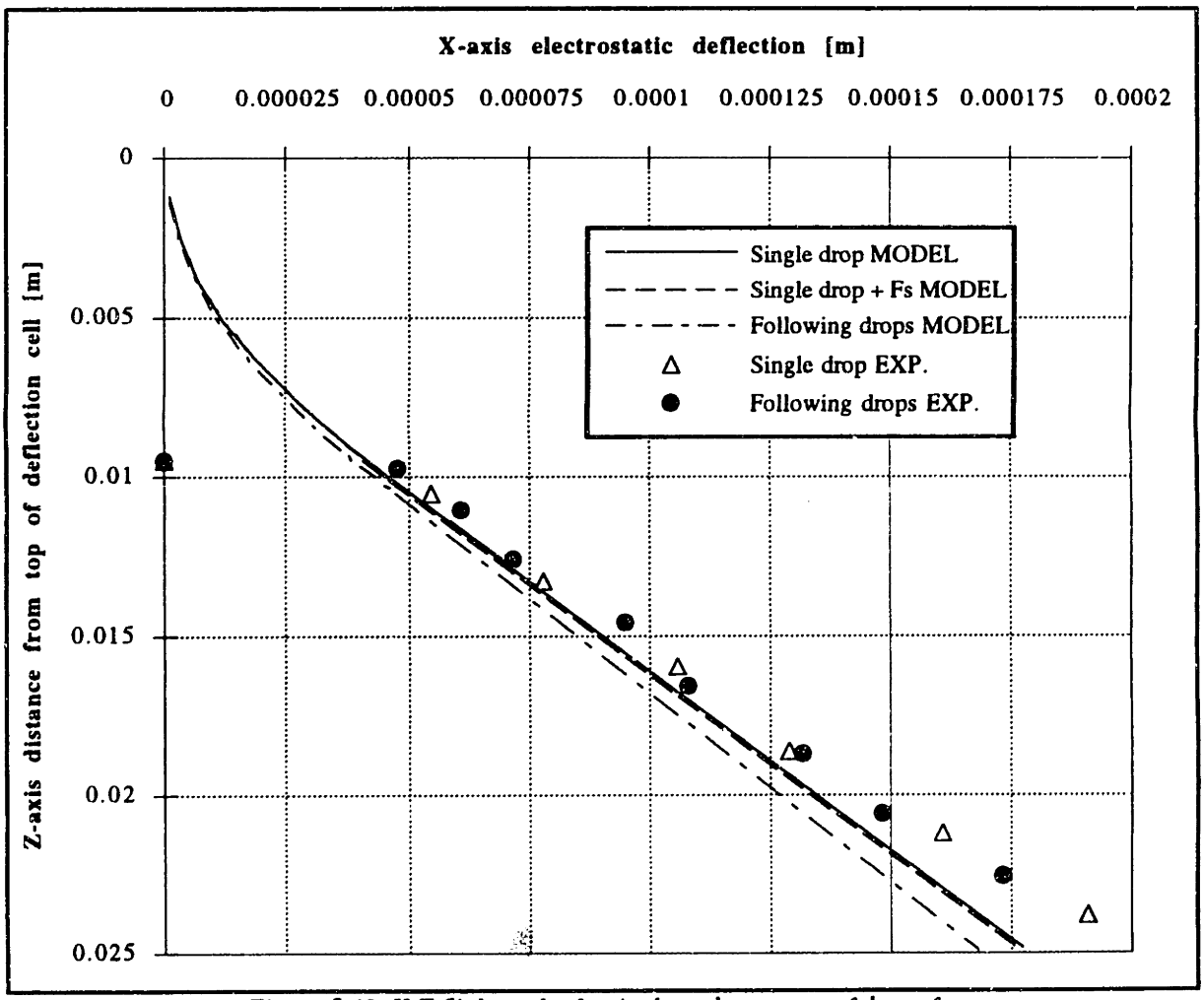

Figure 5.43: X-Z flight path of a single and sequence of drops for Q=1.25 ml/min, q_n=7.22x10^{-14} C, and V_d = 1000 V.

Because of the different scale on both X and Z axis, the deflection appears exaggerated. For example, in the case of figure 5.43, the angle between the deflected stream and the jet axis is a only 0.5°.

The general trend in the modeled curves of figure 5.43 and 5.44 is that the single drop MODEL always deflect more than the continuous stream of drops which certainly hold the exact same charge q_n. Two physical characteristics of the system can explain this phenomenon. First, since a single drop undergoes a larger drag force, the single drop travels slower and remains a longer time inside the limits of the deflection cell. Therefore, the drop has more time to be deflected. Along the same line, since the drag force is mainly along the Z-axis, the X-component of the speed has also more time to build up distance

However, the EXPERIMENTAL data do not always corroborate the fact that the single drop deflects more the following drops (see figure 5.43 & 5.44). In fact in both graph, the single drop path and following drop path is about the same. On the other hand, figure 5.45 & 5.46 show a clear difference between the single and following EXPERIMENTAL drop path.

The difference between the two first and the two last graphs is the strength of the electric field E (caused by V_d) in the deflection cell. In the first case, the electrostatic attraction force F_S on the single drop is strong enough to retard its deflection. To understand more about the force F_S see the section on electrostatic merging. If the strength of the electric field is increased as in figure 5.45 & 5.46, the force ratio is proportionally increased in favor of the deflection cell electric field. As a result, the single drop path is not influenced as much by inter-drop electrostatic force, making the model more reliable.

A third curve including the effect of electrostatic force F_S was added to the single drop path MODEL. This new curve was modeled by combining the electrostatic inter-drop force equation (see section 5.8.2) with the actual set of equation for the single drop. Needless to say, this latter model adds complexity and more sources of error.

To conclude, the clear advantages of using a higher electric field in the deflection cell is to make the MODELed drop path more predictable and accurate by overcoming the back ground noise such as the inter-drops electrostatic forces .

Nozzle diameter [m]	4.50E-05
Flow rate [ml/min]	1.237
Piezo frequency [Hz]	76300
Drop diameter [m]	8.02106E-05
Charging voltage [Vc]	80
Charge q [Coulomb]	1.53E-13
Deflection voltage [Vd]	1000
Deflection cell width [m]	0.001524
Deflection cell length [m]	0.0095
Drop mass [kg]	3.18842E-10
Exit jet velocitu [m/s]	12.96
Z-Offset for exp. data [μm]	9500
Point of detach. zpd [m]	0.009

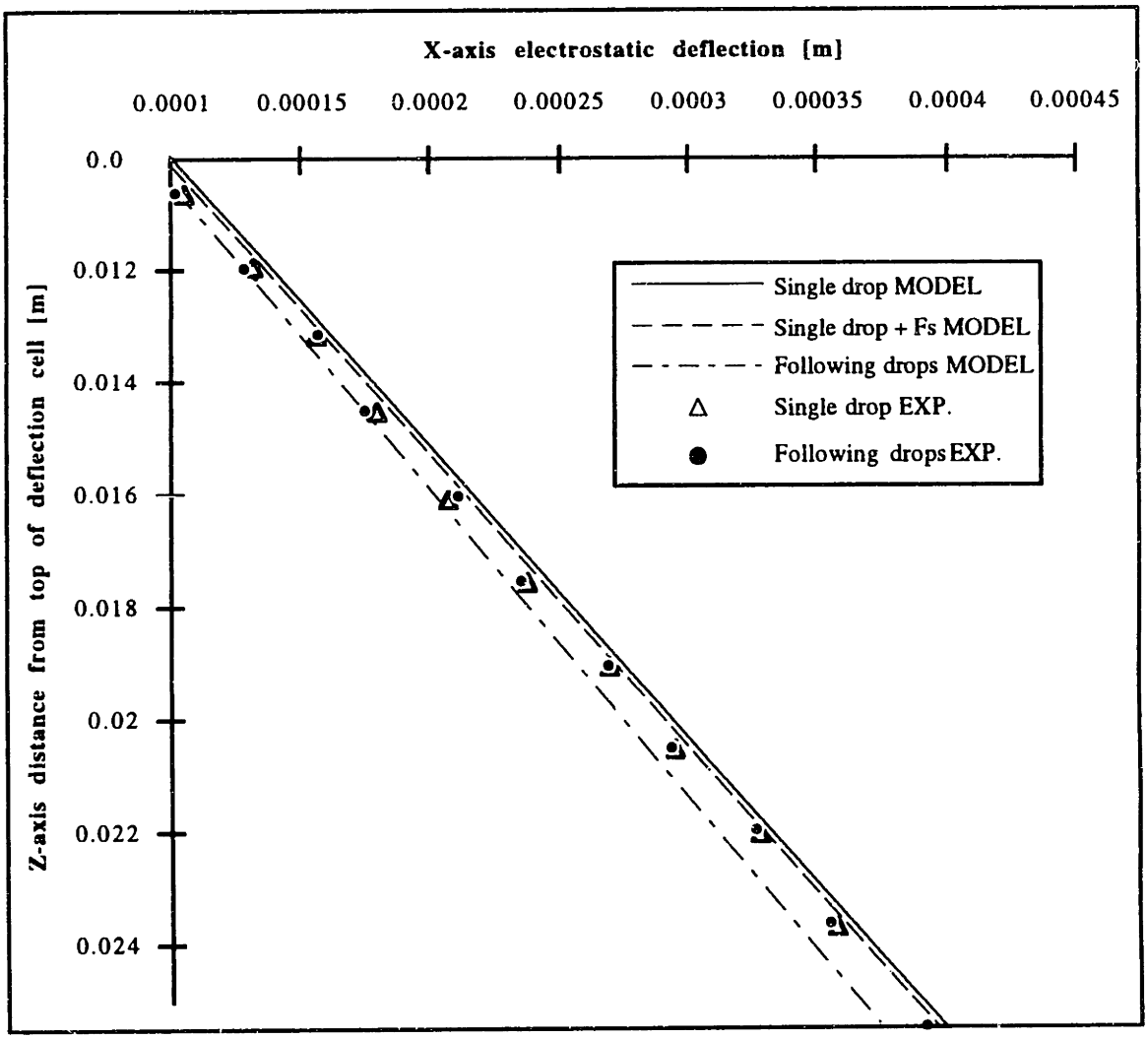

Figure 5.44: X-Z flight path of a single and sequence of drops for Q=1.24 ml/min, q_n=1.5x10^{-13} C, and V_d = 1000 V.

Nozzle diameter [m]	4.50E-05
Flow rate [ml/min]	1.265
Piezo frequency [Hz]	76300
Drop diameter [m]	8.08113E-05
Charging voltage [Vc]	60
Charge q [Coulomb]	2.33E-13
Deflection voltage [Vd]	2000
Deflection cell width [m]	0.0015
Deflection cell length [m]	0.0095
Drop mass [kg]	3.26059E-10
Exit jet velocitu [m/s]	13.26
Z-Offset for exp. data [μm]	9500
Point of detach. zpd [m]	0.005

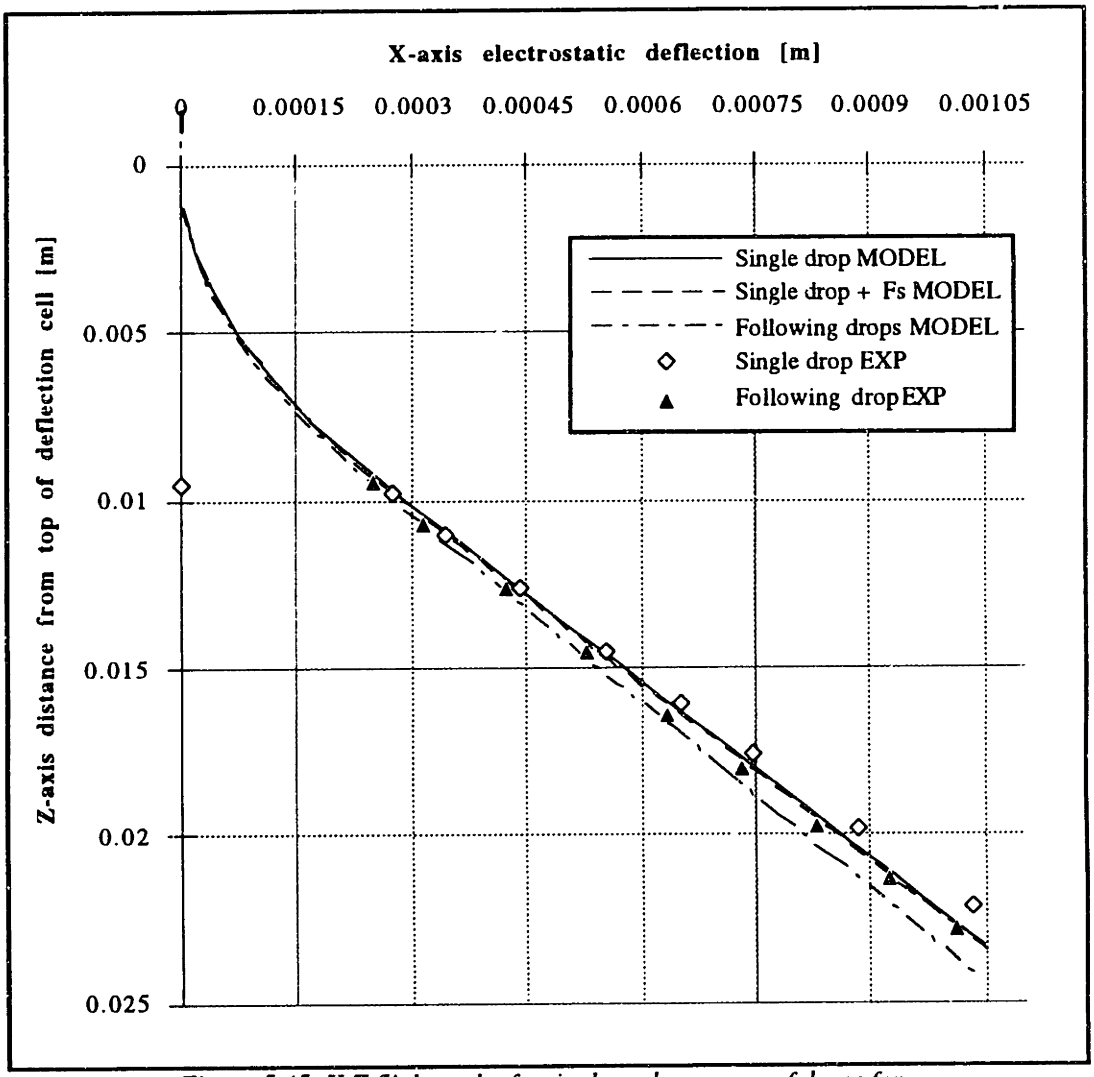

Figure 5.45: X-Z flight path of a single and sequence of drops for Q=1.26 ml/min, q_n=2.3x10^{-13} C, and V_d = 2000 V.

Nozzle diameter [m]	4.50E-05
Flow rate [ml/min]	1.411
Piezo frequency [Hz]	76300
Drop diameter [m]	8.38078E-05
Charging voltage [Vc]	60
Charge q [Coulomb]	2.79E-13
Deflection voltage [Vd]	2000
Deflection cell width [m]	0.0015
Deflection cell length [m]	0.0095
Drop mass [kg]	3.63692E-10
Exit jet velocitu [m/s]	14.79
Z-Offset for exp. data [µm]	9500
Foint of detach. zpd [m]	0.006

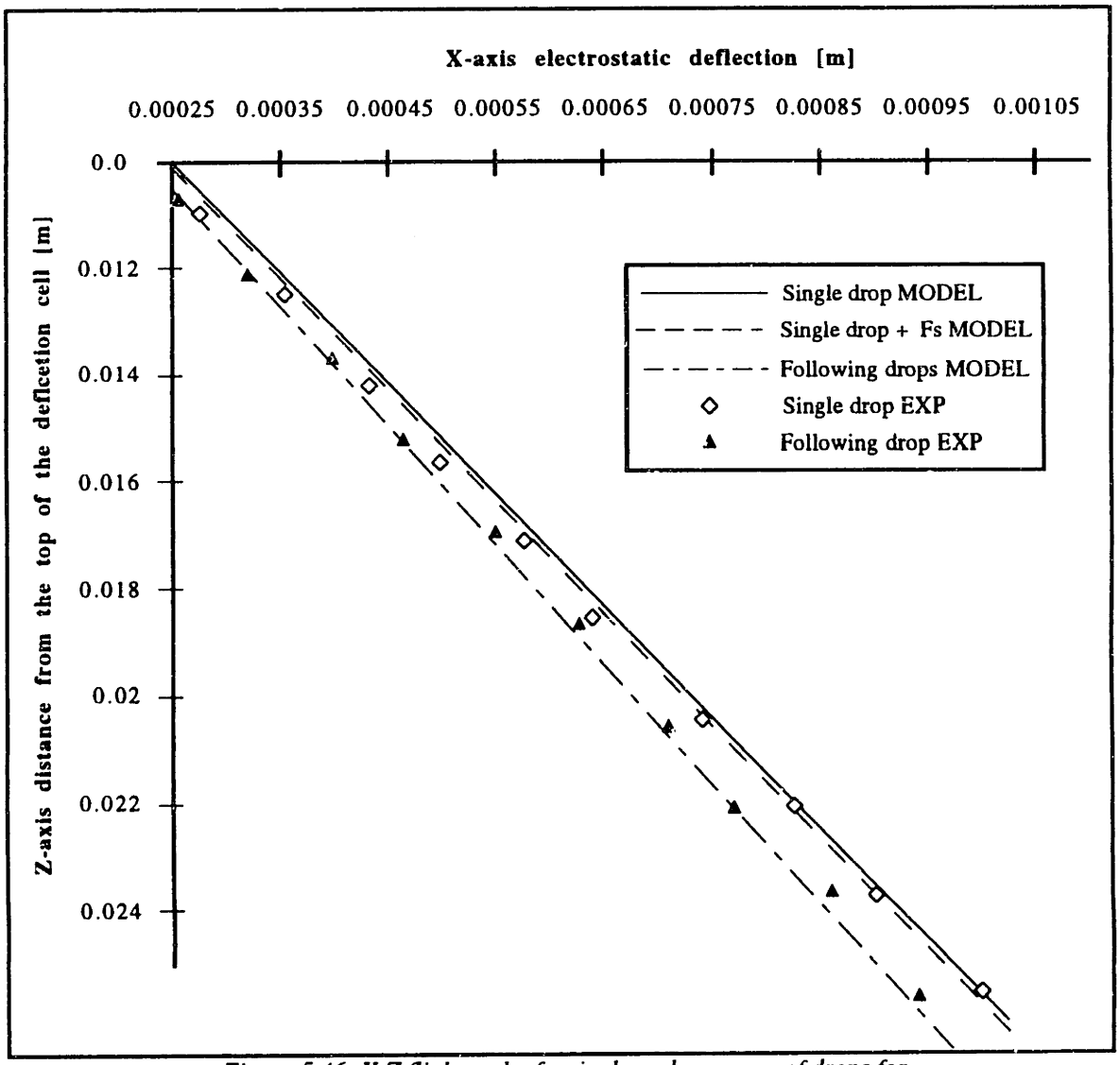

Figure 5.46: X-Z flight path of a single and sequence of drops for Q=1.4 ml/min, q_n=2.8x10^{-13} C, and V_d = 2000 V.

The accuracy of the MODEL predictions was measured compared to the experimental values. According to the graphs of figure 5.43 to 5.46, the positioning accuracy was recorded for the four printing conditions at Z = 25 mm which represents the powder bed level.

Table 5.14: Accuracy of MODEL compared to EXPERIMENTAL results.

Graphs	Single drop MODEL X accuracy [μm]	Following drops MODEL X accur. [μm]
Figure 5.43	-17	-25
Figure 5.44	-10	-20
Figure 5.45	-40	-45
Figure 5.46	0	-10

These results (Table 5.14) are more or less within the accuracy expected from our propagation error analysis done earlier which predicted an accuracy along the X-axis of ±40 μm. This accuracy however may not be satisfactory for precision printing. The obvious explanation for this lack of precision is the model dependence on several variables or in other words, error sources.

In the following sections, the aerodynamic model of the single drop and following drops will be combined in order to predict the behavior of a continuous train of drops. The predicting methods will be simplified in order to decrease the number of variable and increase the accuracy of our drop positioning model.

5.10.3 XZ trajectory MODEL #2

The following stream positioning methods are useful and simple to use, but should be applied carefully in order to minimize error. The best way to use properly those methods, is to understand their limits or the neglected parameters involved in their calculations.

Model based on stream position measurements (Proportionality factor)

A simple method to help calculate the deflected position of a train of charged drops is the proportionality factor method. The validity of the factor relies on the fact that deflection is proportional to the charge assigned to a set of drops.

The method consists in measuring the deflected position d1 of a stream at the powder bed or printing level for a reference charging voltage Vref. It can be showed that if the printing conditions remains unchanged, i.e. the flow rate, break off and stream alignment position inside the charging electrode, the charge is itself proportional to the charging voltage applied at the cell. Therefore, by knowing the position and the reference voltage required to obtain that deflection, one can calculate the proportionality factor Kp as shown below.

$$K_p = \frac{d1}{Vc} \text{ [m / volt]} \qquad (5\text{-}115)$$

In order to minimize the error caused by this approximation, the reference charging voltage should be chosen accordingly. Since the error is multiplicative, one should minimize the distance between the reference and the various positions to be evaluated. This can be accomplished by choosing a voltage which is midway between the maximum proportional deflection and ground for the case of a centered printhead (see next section for more details).

Once the factor Kp is known, the deflected voltage that will provide a given stream deflection d2 can be evaluated simply by the equation (5-116).

$$V_{c.d2} = \frac{d2}{K_p} \qquad (5\text{-}116)$$

The proportionality factor should be evaluated regularly throughout the printing session, since it is sensitive to the break off location, stream alignment and flow rate.

The advantage of this method is its simplicity. Only one measurement is needed and the same factor can be used to predict the required voltage on both side of the stream center

line. The sign (±) of Kp should be switched depending on the desired stream position (left or right) relative to the jet center line.

The main disadvantage of this method is its accuracy. In fact, the proportionality factor does not take in account the slight changes in drag forces occurring on the stream as it is deflected away from the undeflected position. Since drag forces have a significant effect on the stream position, calculated positions will consistently be underestimated when above the reference position and overestimated when below. (a comparison table is provided in accuracy section)

Two-point measurements or second order modeling of drag effect

The proportionality factor Kp assumes the triangle formed by p1-d0-d1 showed in figure 5.47, will scale with the same proportions to triangle p2'-d0-d2' for a larger deflection. However, since drag forces fluctuate for different deflection level, the triangle proportion deviates to give the triangle p2-do-d2 instead. In fact, it was experimentally shown that drag forces increase for larger deflection. Model #1 (method of images) showed very clearly that drag forces get larger since larger deflection increases drop velocity and distance between the drops.

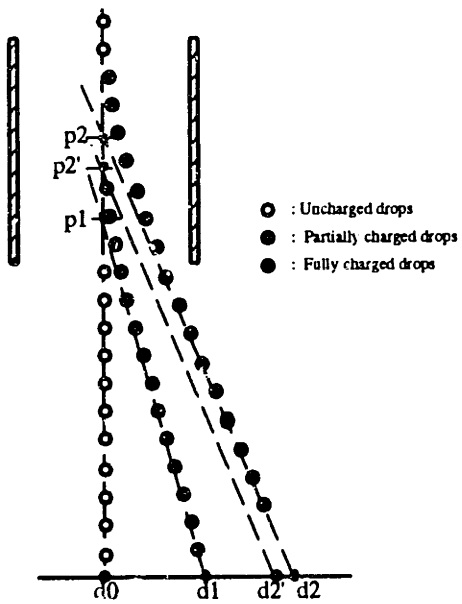

Figure 5.47: Sketch of pivot point position for different charging level.

For example, with an initial jet velocity of v_z=12.5 m/s excited at 76.3 kHz, if a train of drop with unit charge q = 1.35×10^{-13} Coulomb/drop is accelerated through a deflection electrode (V_d=1000V) than, the final absolute velocity would be about v_1=12.51 m/s and the drop spacing ≈ 164 µm (see figure 5.48).

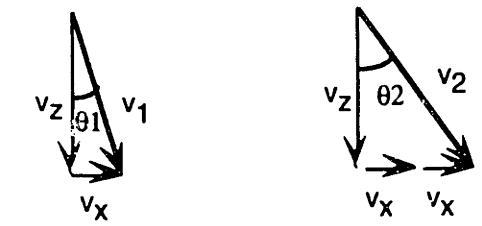

a) drop velocity

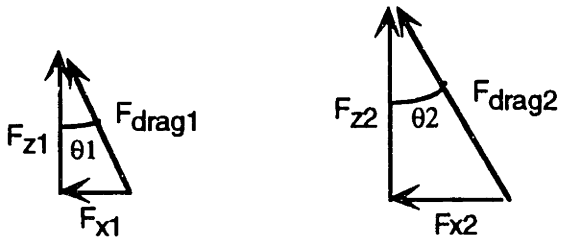

b) drag force on drops

Figure 5.48: Velocity and drag force vector on drop charged with $q=1.35x10^{-13}C$ (case 1) and 2q for case 2.

On the other hand, if the charge is doubled to 2q with the same printing conditions, than the final absolute velocity v_2 and drop spacing are 0.2 % larger. Because drag force can be simplified to the following expression:

$$F_{Drag} \propto Cte \ \bar{u}^2 \lambda$$

, it means that drag force F_{drag1} would increase to F_{drag2} by about 0.4 to 0.5%. The increase is explained by the drag dependence on the absolute speed to the square (see figure 5.48b). Thus, drag force F_{z2} increases as well, and if integrated over the entire drop path it increases also the total deflection by about 1 to 1.5%. In other words, it translates to a positioning error varying between 10 and 25 μm if a proportionality factor is used to interpolate the positions. These numbers slightly varies depending on the printing conditions.

Experimental measurements have shown that the change in stream position has effectively a small second order behavior which accounts for the change in drag forces as deflection increases (see parabola figure 5.49).

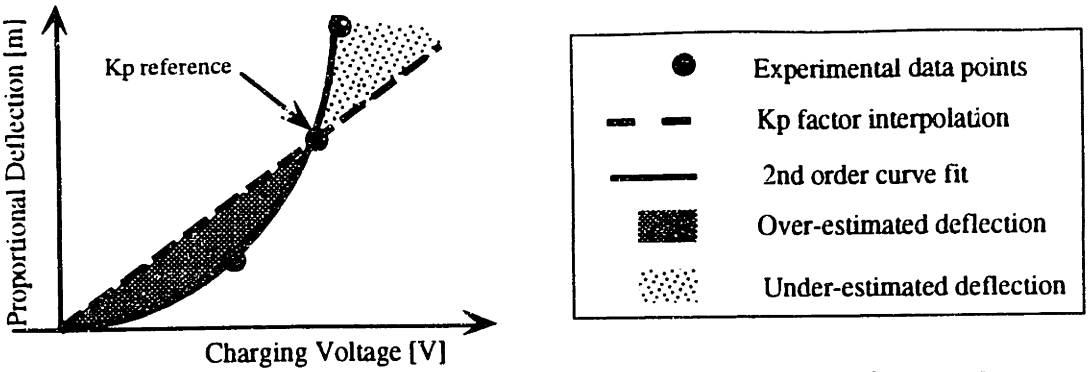

Figure 5.49: Error due to linearization with Kp factor versus second order curve fit.

The idea of using 2 data points instead of one for Kp, combined with the de facto data point (0,0) will allow for the calculation of a second order regression expression or best fit.

Calculation of the second order terms is showed in equation 5-117. A non-uniform data point spacing is preferred in order to minimize error. In the following example, the first data point is chosen at 1/3 of the full deflection range and the other one at the full deflection.

Improved model #2

- First data point: V_0=0V Deflection x_0=0
- Second data point: V_1=0.33 V_{max} Deflection x_1
- Third data point: V_2=V_{max} Deflection x_2
- V_{max} corresponds to the applied charging voltage providing the maximum proportional deflection distance.

$$\begin{bmatrix} 3 & 1.33\,V_{max} & 1.11\,V_{max}^2 \\ 1.33\,V_{max} & 1.11\,V_{max}^2 & 1.027\,V_{max}^3 \\ 1.11\,V_{max}^2 & 1.027\,V_{max}^3 & 1.0081\,V_{max}^4 \end{bmatrix} \bullet \begin{bmatrix} a_0 \\ a_1 \\ a_2 \end{bmatrix} = \begin{bmatrix} x_1 + x_2 \\ V_{max}(0.333x_1 + x_2) \\ V_{max}^2(0.111x_1 + x_2) \end{bmatrix} \quad (5\text{-}117)$$

Proportional Deflection: $$x_i = a_0 + a_1 V_i + a_3 V_i^2 \text{ or } \pm V_i = \frac{a_1}{2a_2}\left(-1 + \sqrt{1 + 4\frac{a_2 x}{a_1^2}}\right)^* \quad (5\text{-}118)$$

*Note: For simplicity factor x_i and a_i should keep their + sign whether or not the stream is deflected on left or right of the jet center line. Changing the polarity of V_i is much more straight forward for the case of a centered printhead only.

Even though the non-linear term a_2 is very small, it adds a significant value to the expression in order to compensate for the drag fluctuations. Also, if the fit is well behaved the term a_0 should be ≈0 since for V=0 we want the jet centered.

The non-linearity factor a_2 depends strongly on the ratio u_x/u_z between deflection speed u_x and the jet speed u_z. The smaller this ratio is, the more linear our deflection model becomes. In other words, if the ratio u_x/u_z is small enough (< 0.01), the drag fluctuations can be neglected and the proportionality factor Kp could provide adequate accuracy. For example, a typical ratio u_x/u_z such as the one used in this research is in the order of 0.1 which means that deflection is non-linear.

Accuracy

A simple experiment was conducted in order to verify the above statement about the non-linearity of the drop deflection behavior for different charging voltage. The experiment consisted in charging the entire drop stream at three predetermined voltages. Their deflected x position away from the jet center line was then recorded at the same distance z (25 mm) below the top of the charging cell. This latter distance represents a likely position of the printing plane or powder bed.

Table 5.15: Linear vs Second order deflection level prediction model

Reference Charging Voltage [V]	Measured deflection x [μm] @ 25 mm	Factor Kp [μm/Volts]	Linear Model with Kp	2nd order Model	Linear Model Error [μm]	2nd order Model Error [μm]
0	0	-	0	0**	0	0
30	642	21.4	653	642**	11	0
60	1306	*21.77	1306	1300	0	-6
90	1974	21.93	1959	1974**	-15	0

*Note: Kp @ 60V used for the calculation.
**Note: 0, 30 and 90 where the nodes used in the curve fit calculation.

Notice that the linear model overestimated the measured deflection when below the reference (Vref = 60V) and underestimated above the reference as expected.

The coefficients a_0, a_1 and a_2 of equation (5-117 & 5-118) where respectively -7.69×10^{-22}, 2.113×10^{-5} and 8.89×10^{-9}. The offset coefficient a_0 can be obviously rounded off to 0 to give the simplified expression that was used to calculate the deflection in Table 5.15. Only three nodes where used in the second order regression calculation of equation 5-118. More data points could have used, but would compromise the printing duty cycle of the machine since each stream position measurement takes a few seconds.

5.11 Drop merging model

5.11.1 What is merging?

If a uniformly spaced train of drops following each other moves through the air, the leading drop is retarded most by air drag and therefore tends to merge with the drop behind it after a short time. This phenomenon is called merging. Drop merging is not only detrimental for the print quality because of larger drops, but also affects the dimensions of the parts being printed. Hence, there is a need to understand the drop merging dynamics in order to predict the merging occurrence and if possible to develop printing conditions that will prevent or circumvent the bad effects.

5.11.2 Description of the merging dynamics

The drop merging model is not intended to produce excessively accurate estimate of the merging position. The model is nevertheless, a very good tool to evaluate the number of merged drops for various distances and printing conditions. Also, it will help compare which printing scheme delays merging distance the most.

The two significant forces influencing the merge distance are air drag and electrostatic repulsion. A delicate balance exists between the aerodynamic forces that tend to merge the drops and the electrostatic repulsion that tend to scatter them (see Force diagram figure 5.50)

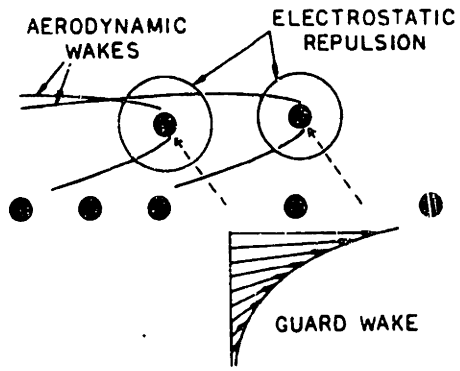

Figure 5.50: Diagram of aerodynamic and electrostatic forces interaction between droplet.. (from Aerodynamics of Ink Jet Printing p.84 ref[57])

The decreased velocity of a stream of drops due to predominant air drag forces eventually causes the drops to merge. Calculations of aerodynamic effects are complicated

by the fact that only the first drop in the stream is traveling through still air, while the second drop traveling in the wake of the first, experiences a smaller drag force. If this difference in drag is not sufficiently counteracted by electrostatic repulsion forces, the second drop is eventually overtaken by the first and merge into a single oversized drop.

The drag on the leading drop has been evaluated earlier using the C_D of equation 5-88. Drag coefficient for the second following drop however is more difficult to evaluate since it does not behave like a leading drop nor a following drop yet. Earlier research conducted by Hendricks (see ref[57]) on drag on uniformly spaced spheres in water demonstrated a good correlation with small liquid drops in air for matching Reynolds numbers. The result is summarized in the graph (see figure 5-51) showing relative drag on a following drop as a function of the drag on the leading one for different drop spacing at a constant Reynolds's number of 84. (see figure 5.51) This latter Reynolds's number [Re=84] represents more or less a flow regime similar to the one around our printing drops.

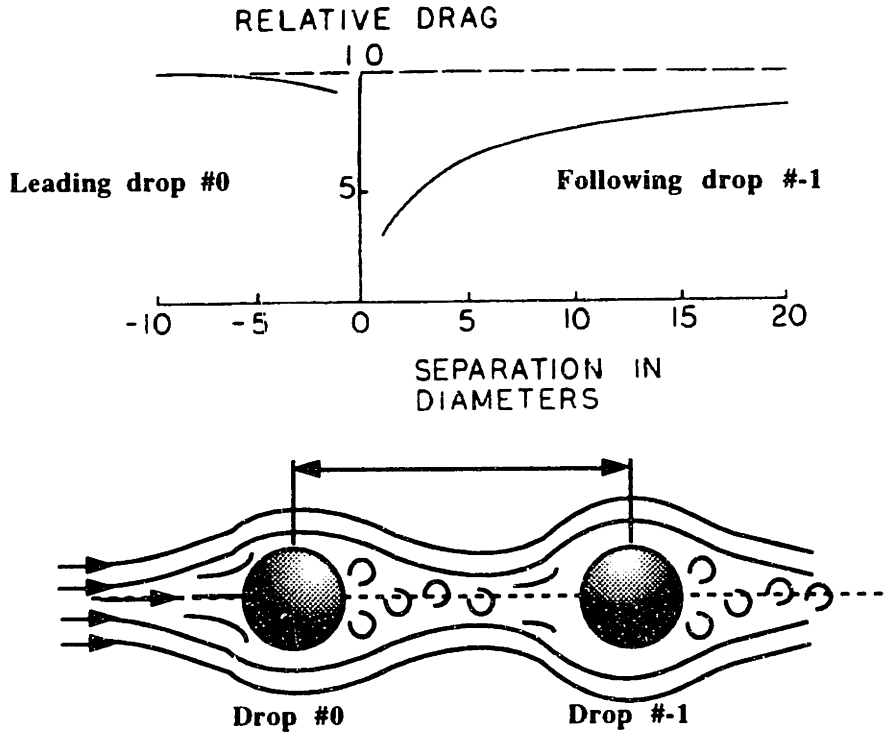

Figure 5.51: Drag of a droplet as a function of non-dimensional distance tp a leading (right part), or lagging (left part) droplet. For a Reynolds number of 84 in a water channel.

The graph of figure 5.51 refers to the situation in which two identical droplets move together, one behind the other, at various separation distances, expressed in number of droplet diameters. Plotted vertically is the non-dimensional drag of one of the droplets,

using the drag of a single isolated droplet as reference. For positive values of separation, the curve depicts the drag of the trailing droplet #-1; for negative values, the drag of the leading droplet #0 is shown (see figure 5.51). Note that the leading droplet #0 also undergoes a small drag reductions as it approaches the following droplet #-1. In fact, as the drop spacing gets smaller the laminar flow pattern which usually creates a low pressure as it closes behind the first drop, does not in this instance. Instead, as the two drops get closer, the air flow goes around them almost as if they were a single body. As a result, the laminar flow going around drop #0 closes behind the following drop #-1. Thus, the air gap between drop #0 and #-1 remains at a higher pressure pushing the leading drop forward or in other words reducing the total drag on the leading drop #0 (see figure 5.51 left).

Drag on the third and subsequent drops is modeled with the Blasius expression for skin friction on a jet stream. As mentioned previously, we assume that air, trapped between the drops, travels at the same speed as the drops. The drag or skin friction acting on each of those drops is applied on the surface formed by a cylinder with a length equal to the drop spacing, with the same diameter as the drops.

Using the standard drag and electrostatic equations discussed earlier in this thesis, combined with the latter material, we can now attempt to model drop merging for various printing conditions and drop sequences.

5.11.3 The drop merging model

The drop merging model accounts for the drag forces which tends to merge the drops, and electrostatic repulsion and deflection cell electric field which tends to scatter them.

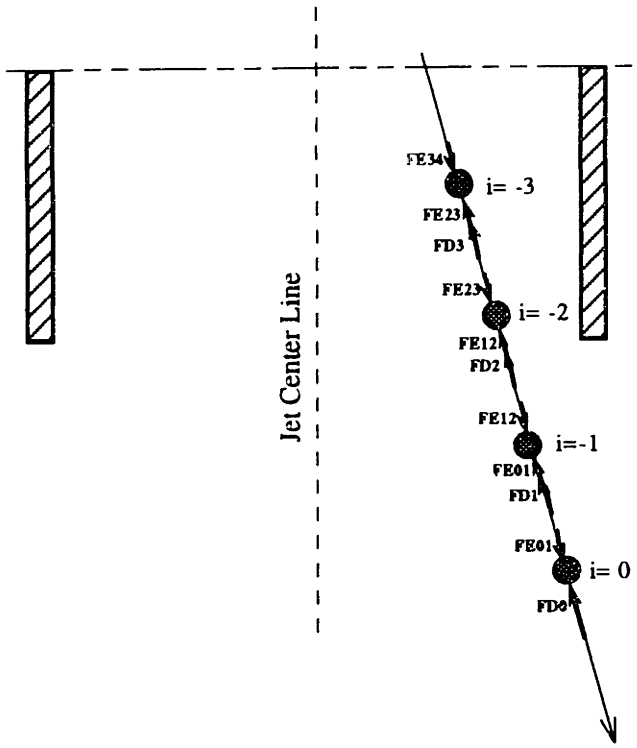

Figure 5.52 Free-body diagram of first second and third leading drops.

The following model (see equations next) assumes that the stream of drops has been deflected out of the main stream boundary layer with drops bearing approximately the same charge. The schematic of figure 5.52 shows how the different forces are distributed.

Equation of motion [i: drop number, n: increment number]

Z-Drop velocity: $$u_{Z\,i,n+1} = u_{Z\,i,n} + \left(g + \frac{F_{Ei} - F_D}{m_d} \right) dt \qquad (5\text{-}119)$$

Drop displacement: $$z_{i,n+1} = z_{i,n} + \left(u_{Z\,i,n}\, dt \right) + \frac{1}{2}\left(g + \frac{F_{Ei} - F_{Di}}{m_d} \right) dt^2 \; * \qquad (5\text{-}120)$$

Equations specifically related to the leading drop [i=0].

Reynolds number: $$\mathrm{Re} = \frac{u_{z0} D_d}{\nu_{air}} \qquad (5\text{-}121)$$

Drag coefficient: $$C_d = \frac{24}{\mathrm{Re}} + \frac{6}{\left(1 + \sqrt{\mathrm{Re}}\right)} + 0.4 \qquad (5\text{-}122)$$

Drag force: $$F_{D0} = \tfrac{1}{2}\, C_D\, \rho_{air}\, u_{z0}^2 \left(\tfrac{\pi D_d^2}{4} \right) \qquad (5\text{-}123)$$

Electrostatic force: $$F_{E01} = \frac{1}{4\pi\varepsilon_0} \frac{q_0^2}{\lambda_{01}^2} \quad \text{(or see polarization section)} \qquad (5\text{-}124)$$

Additional equations related to the second drop [i=-1].

Drag force: $$F_{D1} = \mathrm{Re}\textit{lative drag\%} \times F_{D0} \qquad (5\text{-}125)$$

Electrostatic force: $$F_{E\,i,i+1} = \frac{1}{4\pi\varepsilon_0} \frac{q_0^2}{\lambda_{i,i+1}^2} \quad \text{(or see polarization section)} \qquad (5\text{-}126)$$

Equations related to the third and subsequent drops [i=-2,-3,...].

Reynolds number: $$\mathrm{Re} \cong \frac{u_{z0}\, z_i}{\nu_{air}} \; ** \qquad (5\text{-}127)$$

Drag coefficient: $$C_D = \frac{1.328}{\sqrt{\mathrm{Re}(z_i)}} \qquad (5\text{-}128)$$

Drag force: $$F_{Di} \cong \tfrac{1}{2}\, C_D\, \rho_{air}\, u_{z0}^2\, \pi\, D_d\, \lambda_{i,i+1} \qquad (5\text{-}129)$$

Electrostatic force: $$F_{E\,i,i+1} = \frac{1}{4\pi\varepsilon_0} \frac{q_0^2}{\lambda_{i,i+1}^2} \quad \text{(or see polarization section)} \qquad (5\text{-}130)$$

Note: Most of those equations are just showed as a review of previous sections
*Displacement origin z=0 @ point of detachment from the rest of the jet (see next section for calculation).
** zi is measured relative to the top of the deflection cell.

The model categorizes the stream into three distinct regions which are the drop #0, the second drop #-1 and the other drops. The leading drop (i=0) is distinct since it is the only one which travels through almost still air and is exposed to maximum drag. The following drop (i=-1) experiences a drag which represents a fraction of the drag of droplet #0 since it move in the wake of the latter. The value of this relative drag varies between 0.3 to 0.7 depending on the drop spacing and Reynolds number (see graph 5.51). And finally, the other drops are slowed down by another kind of drag, called skin friction explained earlier in section 5.9.2.

What makes the drop merging model complex, is the fact that all the forces are simultaneous and interdependent. For example, as the distance between the drops is closing because of their deceleration, the electrostatic repulsion force which was small compared to drag forces earlier, increases significantly pushing away the surrounding drops proportional to the inverse of the distance square. Meanwhile, the drag forces undergo radical changes as the air flow pattern between the drops is affected by drop velocity, spacing and increased drop size as they merge.

The following graph 5.53 represents the combination of all those forces as the drops fly down toward the powder bed. Each line represents the flight path of a drop which is part of a train of seven drops. In the top left corner, the lower line represents the leading drop #0 and each successive line above, represents a following drops. In this example, the 7 drops are uniformly separated by the typical drop spacing determined by the jet speed u_{z0} and piezo resonator frequency F. As each individual drops slows down at different rate along the z abscissa (vertical component), the initial drop spacing changes until the leading drops start merging with the following ones.

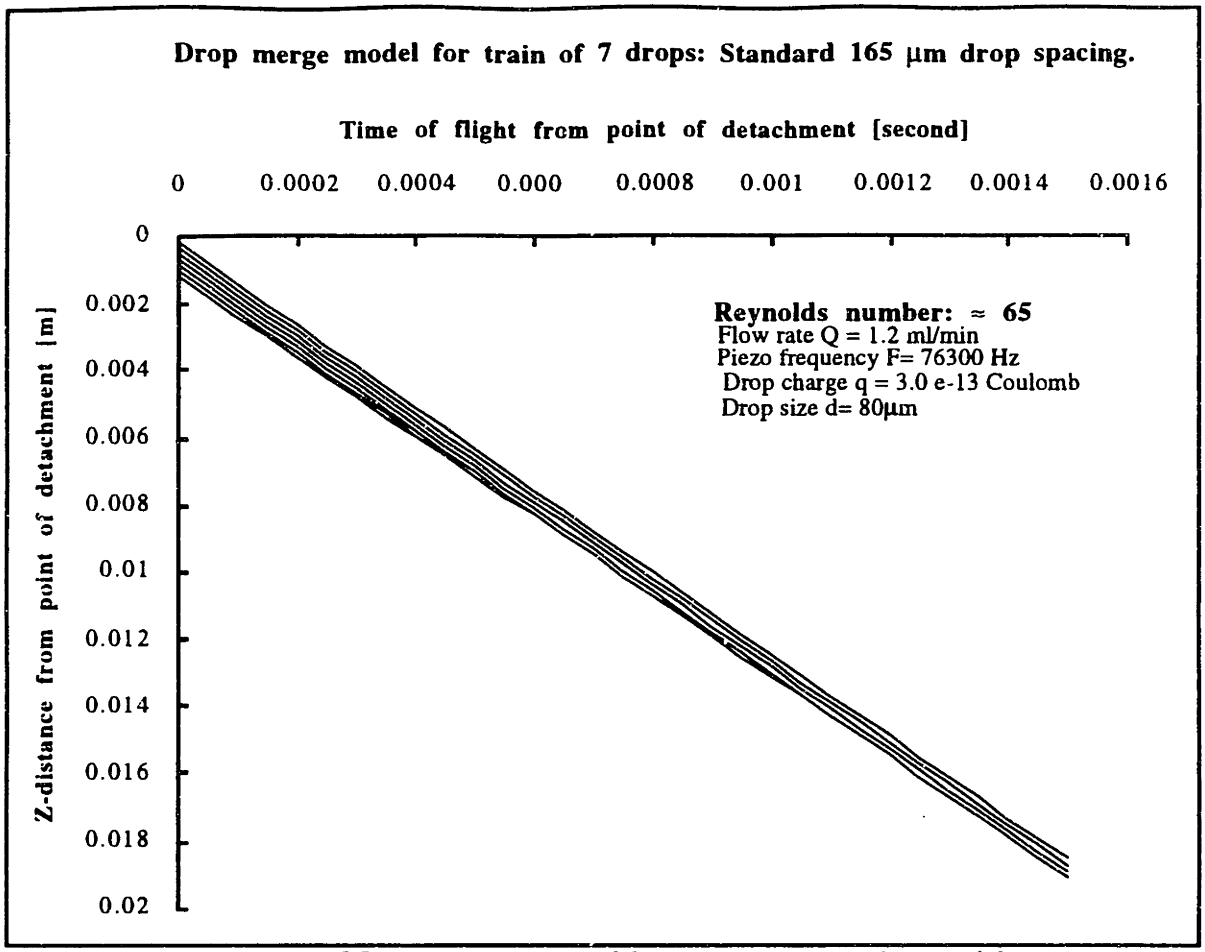

Figure 5.53: Drop merging model for a train of uniformly spaced drops.

On the graph of figure 5.53, we can read that the first two drops are merging first, at about 5 mm from the point of detachment of the jet. This distance, however does not state where merging occurs with respect to the printhead body, because it represents a distance calculated from the point of detachment on the stream.

This point of detachment z_{pd} can be defined as the distance between the top of the deflection cell and the position where the leading printing drop #0 and the trailing catch drop #1 comes apart by a predetermined distance x_{pd} (see shaded drops figure 5.54). The distance x_{pd} is determined as the position where the deflected leading drop #0 (top drop) is pulled out enough to clear off the boundary layer created by the preceding drops #1, #2,..(bottom drops). As seen in figure 5.54, the value of x_{pd} is the sum of the drop diameter and the boundary layer around the preceding drops (see equation 5-131)

$$x_{pd} = Dd + \partial_{0.99} \approx Dd + 5\ \mu m \qquad (5\text{-}131)$$

For various printing condition, the boundary layer around the stream $\partial_{0.99}$ varies only between 3 and 5 microns. Since the calculation for the boundary layer is tedious, we can assume a constant value $\partial_{0.99}$=5 μm without incurring significant errors.

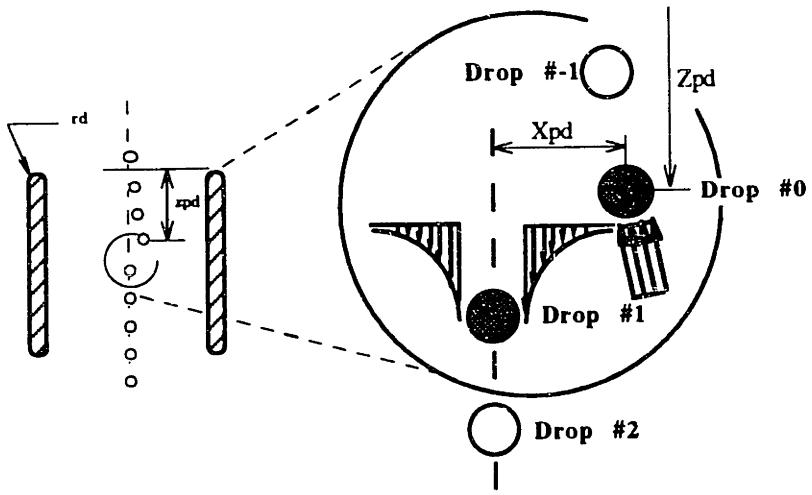

Figure 5.54: Schematic of point of detachment z_{pd} where direct drag start acting on the newly deflected drops.

Once the value of x_{pd} is known, the point of detachment distance z_{pd} can be determined from the equation of motion for charged drops inside a uniform electric field as seen in equation 5-72. Equation 5-75 can just be transformed into:

$$z_{pd} \equiv u_{z0}\sqrt{\frac{2\,x_{pd}\,m_D w_d}{q_{01} V_d}} + r_d \qquad (5\text{-}132)$$

to give directly the point of detachment distance z_{pd} measured from the top of the deflection cell. The value r_d represents the radius of curvature machined around the deflection cell to prevent sparking. The electric field in this region is not as strong as between the parallel planes of the cell (see figure 5.54), thus does not contribute to the electrostatic deflection in the x-direction.

It should be noticed that the value of q_{01} corresponds to the differential charge of drop #0 with respect to drop #1. For example, if the charge q_0 is -1.5e-13 coulomb and q_1 is 5.0e-13, then the differential charge q_{01} is 6.5e-13 coulomb. This procedure makes sure that equation 5-132 is still valid in the case where both printed and in catch drops have to be charged and deflected in opposite directions. It is the equivalent to transfer all the charges on one set of drops in order to keep their relative deflection (i.e. printed relative to in-catch) intact in equation 5-132.

For the example of figure 5.54, the value x_{pd} has been evaluated to 85 μm for a drop diameter D= 80 μm. Combined in equation 5-132, it gives a point of detachment z_{pd} of 5.6 mm from the top of the deflection cell. By adding the latter value to the first merge distance of graph 5.53 (5.5 mm), the first merge distance can be estimated as 11.1 mm from the top of the deflection cell. Using similar technique, the second merge distance would be at about 13 mm. As a comparison, the first merge distance was experimentally measured at 2.4 mm below the bottom of the charging cell. Since the charging cell length is 9.5 mm long it gives a comparable first merge distance of 11.9 mm.

5.12 Merging Model vs. Experimental results

In order to understand the drop merging phenomenon and validate our drop merging model as well, a set of drop merging experiments were conducted for different printing conditions.

The merge distance was measured using a CCD camera, a synchronized strobe light and a X-Z positioning table showed in the experimental set-up described in section 5.3.1. The experiments were to measure the distance of the merging point between two leading drops relative to the bottom of the deflection cell. The merging point is defined as the position where two drops are merging or necking to form a single unit. The accuracy of the measurement is related to the repeatability and stability of the drop merging occurrence. Unfortunately, because of air turbulence and very slow approach velocity between the drops, the point of contact could deviate by as much as ± 0.5 mm; which represents basically the accuracy of the following experimental results.

5.12.1 Sensitivity to flow rate

This experiment was to deflect most of the drops away from the jet center line, while keeping a train of drops undeflected on which was measured the first merge position for different flow rates. In more detail, it consists in a sequence of 256 drops out of which 246 were deflected away. The 10 other drops, on which the merging position was recorded, remained uncharged to avoid undesired electrostatic forces. It was therefore assumed that a distance of 246 drop spacing between each train of 16 drops was sufficient to isolate each train of 16 drops from the drag of the previous one in order to prevent any air disturbances on the leading drops.

A set of merge positions were measured for different flow rates. The flow rates were chosen within the drop formation stability criterion defined by Rayleigh as:

$$3.5 < \frac{\lambda}{d_0} < 7.0 \qquad (5\text{-}133)$$

From this criteria, three flow rates 1.0, 1.2 and 1.4 ml/min were chosen to perform the experiments. Those flow rate represents the lower end of the stability window with the Rayleigh frequency flow rate (1.45 ml/min) as the higher limit. Table 5.16 shows the results gathered by this experiment.

Table 5.16: Flow rate vs merge distance: model and experiments

Flow rate [ml/min]	Jet velocity [m/s]	Reynolds Number Re	**Measured** Drop charge [Coulomb]	MODEL Point of detachment z_{pd} [m]	MODEL Merge from z_{pd} [m] see App.C7	MODEL Merge distance model [m]	**Experiment** Merge distance [m]
1.0	10.5	51	3.0e-13	0.00545	0.004	0.0095	0.0106
1.2	13.1	68	4.5e-13	0.00625	0.005	0.0113	0.0126
1.4	14.7	79	5.2e-13	0.0069	0.007	0.0139	0.0145

The merge distance (model) was calculated by adding the value of the point of detachment z_{pd} with the merge distance read from the merge graph of Appendix C7. The variables used for the calculation are showed in Table 5.16. Other parameters such as deflection cell spacing (w_d=1.5 mm), deflection cell radius of curvature (r_d =0.65 mm), deflection cell potential difference (V_d =1000 V) and charging voltage (V_{cc} = 120 V & V_{cp}=0V) were kept constant.

The results showed clearly that merging is affected by the deflection level as well as by the flow rate. Deflection level affects the merge distance by changing the point of detachment distance. By inspection of the value of the point of detachment z_{pd}, we can conclude that for higher deflection (lower flow rate) the merge position decreased by the same amount as z_{pd}. On the other hand, flow rate affects the merge distance point by changing the equivalent Reynolds number characterizing the printing conditions. For example, as the flow rate increases the Reynolds number increases causing the merge distance (see graphs in App. C7) to occur farther from the deflection cell.

In other words, a higher Reynolds number means larger drops or higher jet velocity or both. This upscale make the stream less sensitive to drag effect as well as electrostatic effects. In addition, longer drop spacing which is the result of a higher flow rate increases the merging distance since the drops have a longer stretch before merging.

It should be noticed that the model consistently underestimates the experimental values of merge distance. This discrepancy is probably due to the value z_{pd} which has been calculated with a simplified expression. In fact, for sake of simplicity, the model does not take in account electrostatic attraction forces between the deflected and undeflected drop as well as previous drag effects from the stream above.

5.12.2 Sensitivity to deflection & charge

Drop merging distance is also a function of the charging level on the drops being printed. The charge affects merging distance in two distinct ways: electrostatic repulsion and point of detachment position.

Since successive printed drops carry more or less the same charge level and polarity, they repulse each other according to Coulomb's law (see equation 5-82). This electrostatic repulsion force retards drop merging since it works against drag forces. According to theory, a higher drop charge will increase the repulsion forces and extend the merge distance even farther from the deflection cell. However, if the charge is increased, the deflection level is also increased which makes the point of detachment occur earlier. As we know by now, a shorter point of detachment distance means also a shorter merge distance.

Therefore, drop charging level tends to increase merging distance by repulsion forces but at the same time it affects the point of detachment promoting premature drop merging. One way to analyze drop behavior under such force interaction was developed in the IBM research centers as part of an effort to design a new breed of ink-jet printer (see reference [56] on printhead). They developed a characterization methods called merge curves which eventually help understand drop interactions to a higher level.

Merge curves were generated by the following experiments: Two drops in a stream of otherwise uncharged drops are charged such that both follow the same deflection trajectory. Since the second drop is traveling in the wake of the first, it experiences a smaller drag force. If this difference in drag is not sufficiently counteracted by electrostatic repulsion forces, the second drop eventually overtakes the first and they merge into a single oversized drop. A merge curve is defined as the set of coordinates at which merging occurs. A different merge curve can be obtained for each initial spacing of the two drops. (See merge curve example in figure 5.55)

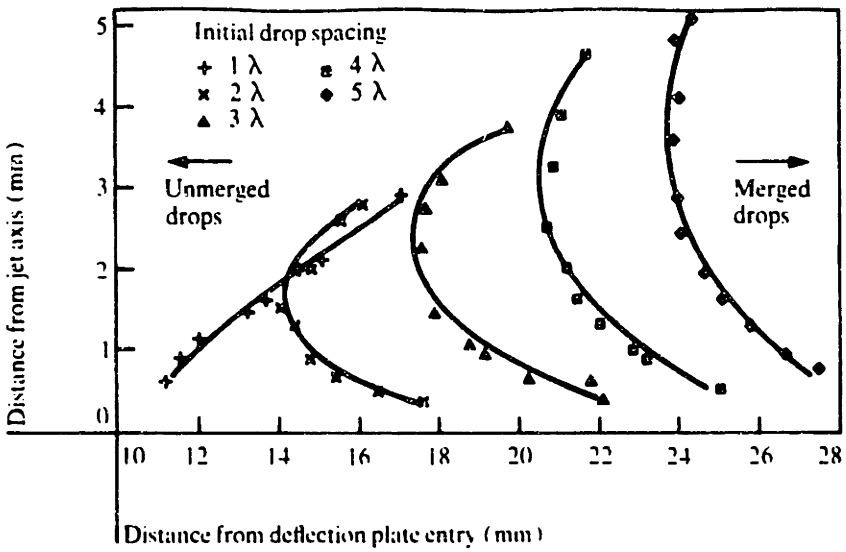

Figure 5.55 Merge curves for train of two drops (IBM Journal of research and development, January 1977).

Because the wake of the undeflected stream reduces the differential drag of the two drops, the merge curves bend sharply to the right near the abscissa. As drop charge is increased, electrostatic repulsion between the drops becomes increasingly significant, causing the bending to the right at large deflections. The curves end abruptly at very large deflections, when the electrostatic forces become strong enough to prevent merging. One additional characteristic worth noting is the crossing of the curves for different initial spacing. The aerodynamic forces fall off less rapidly than the $1/d^2$ electrostatic force. It is therefore possible for two drops separated by several wavelength to build up a relative momentum that cannot be overcome by the electrostatic force, whereas this same electrostatic force is more than sufficient to prevent merging when the drop are initially separated by some smaller distance. As a result, we can not claim that increasing the drops separation always prevent merging.

The usefulness of the merge curves is not limited to providing an understanding of the important parameters associated with drop merging. The area beyond the curves (merged drops arrow) represents a region in which a train of drops can not be deflected without merging.

The curves (see figure 5.55) are based on a train of two-drop experiments which does not apply directly to train of multiple drops used to print continuous lines. For longer train of drops the several following drops cannot be moved up and down as freely as for a single following drop. As a result, the drag differential between the leading and trailing drops causes the merging point to occur earlier in the case of longer train of drops

Effect of drop deflection on merge distance

Two experiments were developed in order to understand the effects of drop deflection and charging level on the merge distance. The first experiment was designed to isolate the effect of deflection without any electrostatic disturbances. A voltage pattern was cycled through a sequence of 256 drops in order to allow a strobe light to freeze the stream motion for visual measurements of the merging occurrence. Out of 256 drops, 246 were charged to achieve different in-catch deflection level. The 10 remaining drops, on which the merging distance was measured, were kept undeflected for the entire experiment. As a result, the change in the in-catch deflection level was varying the point of detachment from the mainstream (or undeflected position). In other words, the in-catch drops, acting as guard drops, were protecting the train of undeflected drops from direct air drag for a distance equivalent to the point of detachment position z_{pd}.

The results are showed in figure 5.56 for a uniformly spaced train of drops (left curves) and also for a similar train of drop with the second drop (drop #-1) removed. In the following example, the charging voltage was varied between 50 and 120 Volts for the 246 in-catch drops while the 10 other drops were kept uncharged.

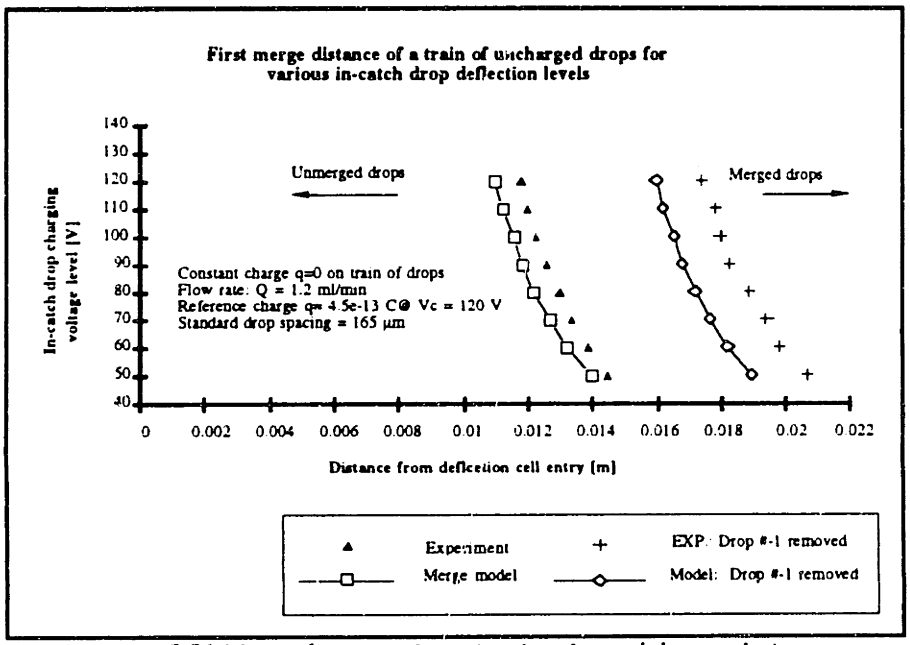

Figure 5.56:Merge distance of a train of uncharged drops relative to deflection cell entry for various in-catch drop deflection levels.

The drop merging model agreed with sufficient accuracy with the experimental values, although it consistently underestimated the experimental results because of simplifications discussed earlier in the merge modeling section. Both drop sequence configurations showed the same trend as the merge distance decreased as the in-catch drop deflection was

increased. In fact, for larger deflection the point of detachment measured from the deflection cell entry is shorter, thus in-catch drops do not guard the undeflected drops from direct air drag for as long. Since drag forces affect the train of drop earlier on, its cumulative deceleration effect causes shorter merging distances. In summary, one can say that increasing the deflection distance between in-catch and printing drops position, will produce a shorter merging distance for a given print distance.

The graph of figure 5.56 shows also two sets of curves corresponding to two distinct drop sequences. The left curve represents a uniformly spaced train of drop with a drop spacing of λ that has a merge distance varying between 11 and 14 mm from the top of the deflection cell. The other set of data (right side) represents a train of 9 drops out of which the second drop (drop #-1) has been deflected in-catch. This procedure created a gap of two regular drop spacing (or 2λ) between the two new leading drops (drop #0 and drop #-2). Since the two leading drops have now a bigger distance to cover before merging, it delays their merging distance by about 45% (or up to 16 to 19 mm) for this particular flow rate.

For example, one of our current printhead design has a distance between the top of its deflection cell and the powder bed of about 23 mm. If the same printing condition as of the above graph were to be used with this printhead, two assertions could be made. First, more than one drop merging would occur before the powder bed for the case of regular drop spacing. On the other hand, if the second drop is removed only one merging would occur. Therefore, if merging is unacceptable because of lower print quality, a new set of printing conditions as well as printhead design should be investigated. This development work could be done by predicting the merge distance associated with different parameter using the model described in this section.

Effect of drop charge on merge distance

Positioning drops on the powder bed by accurately controlling their charge is an elegant way of improving printing quality. A printing technique called "proportional deflection" makes use of this method in order to print curves, snap to geometric features as well as improving the general surface finish of 3D printed parts.

The following experiment is meant to measure the combined effect of charging and deflecting drops on the merge distance. Contrary to the previous experiment where the train of drop was uncharged, this experiment explored the effects of charging the drops, causing additional electrostatic forces to interact with drag forces.

As we know by now, consecutive drops about to be printed must have more or less the same charge since printed lines need to be continuous. Such a sequence of charged drops will create electrostatic repulsion forces between each individual drops. Therefore as drops repel each other, it forces the merge distance further down. However, as the charge is increased, so is the deflection which concurrently decreases the merge distance. The combination of both phenomenon has been captured in the graph of figure 5.57.

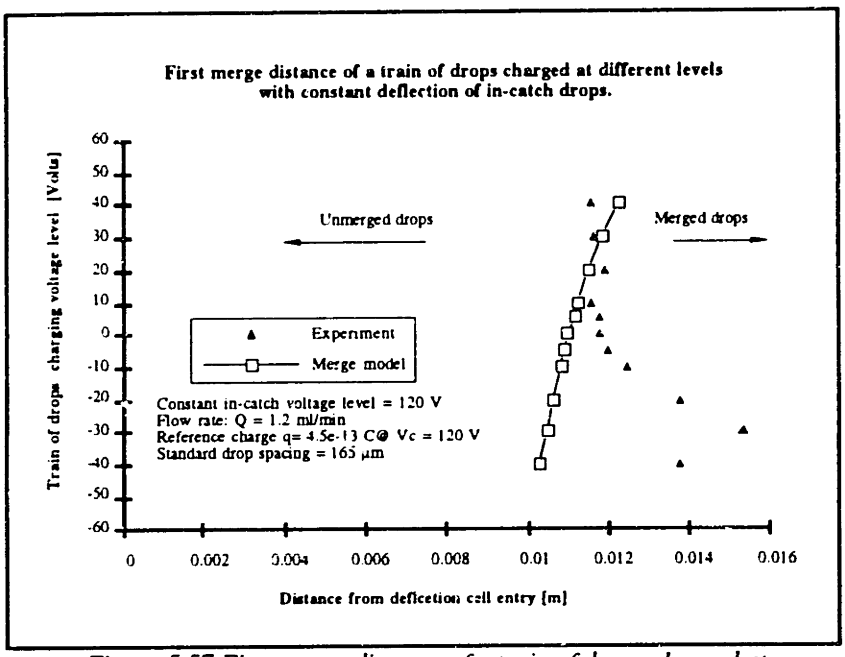

Figure 5.57 First merge distance of a train of drops charged at different levels with constant in-catch deflection .

The experiment consisted in deflecting in-catch 246 drops, out of a sequence of 256, with a constant charging level. The other 10 drops were charged with the same voltage levels corresponding to an exact deflected position located on both side of the jet center line. The 246 in-catch drops were charged with a constant +120 Volts while the remaining 10 drops were charged with a voltage range varying between -40 to +40 volts. As a reference, when the drops were charged with 0 Volts the drops were aligned with the jet center line axis.

The merge model showed a good fit with the experiment for charging voltage value varying between +40 and 0 Volt. This represented the lower half of the deflection differential between the 246 in-catch drops and the train of 10 drops. However, as the drops were deflected further away on the opposite side of the jet center line, the experimental values diverted steeply to the right to give higher merging distances then expected. The justification for this divergence came obviously from a phenomenon that

was not considered in the merging model, but that was covered in the section on electrostatic merging. In fact, since the 246 in-catch drops had a very strong negative charge (V_{cc}=+120 Volts) while the printing drops had an increasing positive charge (V_{cp}=0 to -40 volts), a strong electrostatic attraction force was created between the leading printing drop (drop #0) and the trailing in-catch drop (drop #1).

As a reminder, if the charge differential between in-catch and printing drops is too strong, the two drops (#0 and #1) will merge mid-way between the in-catch and printing position causing printing failure (see section 5.8). This attraction force which has been acting on the drops since they left the charging electrode, caused both drop #0 and #1 to approach each other and change the drop spacing between drop #0 and #-1. Thus, when the two drops (#0 & #1) entered the deflection cell, they were already closer to each other while #0 and #-1 were further apart. As a result, drop #0 had a new longer distance to cover before merging with drop #-1. Moreover, since drop #0 has been closer to drop #1 for part of its flight path, the total drag acting on drop #0 was reduced, giving drop #0 a slight drag advantage over other drops. Therefore, because of the combined effect of a larger drop spacing between drop #0 and #-1 plus a slight drag advantage given to drop #0 compared to other drops, merge distance was increased as the charge differential built up.

In principle, merge distance will decrease as the charge is increased up to a certain charge differential. If the charge on the printing drop is really large, than a merge distance will increase again as electrostatic repulsion force prevails over drag force. One can predict if electrostatic forces are significant by running the electrostatic merging graph seen in a previous section for the specific charging condition . If it is found that the drops are on the edge of merging electrostatically it means that the merging distance can be extended as far but no farther than for the case where the second drop was removed (see figure 5.56). Otherwise, using the model directly will give the user a conservative estimated about the merge distance.

The new drop separation is a function of the charge differential between the two drops as well as the distance L_{cd} between the charging electrode and the top of the deflection cell. For example, if the distance L_{cd} can be decreased by redesigning the printhead, it should make the model more accurate. However, it may not be necessary to decrease the distance L_{cd} for that only reason, since merge distance has been improved for the actual printhead geometry.

Comments

The consequences of drop deflection and charging level on merge distance discussed above, can be either amplified or reduced depending on the printhead design configuration: i.e. jet centered in print position or off-centered in-catch position. In either case, it should be noted that the required deflection is the same whether the jet is centered or not. However, in the case of an off-centered printhead, the average charge level on the printing drops is much larger than for the centered case. Our later analysis would than suggest that an off-centered printhead design would be a better choice as far as merge distance is concerned. However, other criteria enters in the choice of the optimal printhead design. This topic will be further developed in a next section on optimum printhead design.

5.12.3 Summary of drop merging dynamics

The effect of flow rate on the merge distance might as well be generalized by using the drop Reynolds number. As the flow rate of a particular printhead is increased, so is the drop Reynolds number. We can then say that for a larger Reynolds number, merging occurs farther from the deflection cell entry. By analogy, one can say also that increasing the drop velocity, drop diameter, or decreasing the ambient gas viscosity μ_{air} [Ns/m^2] will also increase the merge distance. For example, if graph of figure 5.53 is redone for a printhead printing in Helium He compared to air:

Density	$\rho_{He} = 0.18\ {}^{kg}/_{m^3}$	$\rho_{air} = 1.19\ {}^{kg}/_{m^3}$
Viscosity	$\mu_{He} = 1.67\times10^{-5}\ {}^{Ns}/_{m^2}$	$\mu_{air} = 1.83\times10^{-5}\ {}^{Ns}/_{m^2}$
Kinematic viscosity	$\nu_{He} = 9.29\times10^{-5}\ {}^{m^2}/_{s}$	$\nu_{air} = 1.55\times10^{-5}\ {}^{m^2}/_{s}$

the merge distance would be increased by 4mm (from ≈11mm to 15mm) or 36% increases according to the merge model. Other gases such as water vapor have very low density and viscosity or SF_6 (hexafluoride) with high dielectric constant (to prevent sparking) could be used. Although, in the case of SF_6, merging would occur earlier since it is a heavier gas than air. In any case, implementing such controlled environment around the printhead should be done only in last resort.

Another aspect of a higher flow rate is the longer drop spacing caused by the higher drop velocity while keeping a constant piezo resonator frequency. Longer drop spacing

will increase also the merging distance not only because the drops have a longer distance to cover before merging, but also because it increases the drag on the drops following the first few leading ones.

Finally, if the drop sequence is altered by removing one or more drops from a uniformly spaced train of drop, it should increase the merge distance. More details will be provided on this issue in the printing strategy section.

Summary of parameter affecting merging distance

- Higher droplet Reynolds number postpones merge distance.
    - Larger drops postpones merge distance.
    - Higher drop velocity postpones merge distance.
    - Lower viscosity μ_{gas} postpones merge distance.
- Larger deflection alone shorten merge distance.
- Larger deflection and charge may affect merging both ways depending on the conditions.
- Longer drop spacing increases merge distance.
- Removing drops increases merging distance to different degrees depending on the number and location of the drops removed.

5.12.4 Printing errors caused by merging

The first merge position is an important characteristic used to optimize the printing conditions of a particular printhead design. Another useful feature of the drop merging model is to predict the total number of merged drops N. This information is useful in order to evaluate the printing command compensation Δy .

If the printing conditions lead to a multiple drop merging situation, printing accuracy will be affected. For example, if 4 leading drops of a sequence of 20 drops merged just before hitting the powder bed, the total length of the sequence is not 19 drop spacing (19λ) anymore, but rather 16 λ . Therefore the length of the line printed on the powder bed is shorter than expected by an amount proportional to N-1 drops. More specifically, the downsize is proportional to N-1 drops times the distance between each drop on the powder bed. Since the distance between two successive printed drops on the powder bed is equal to the printhead scanning speed $v_{y,scan}$ divided by the piezo resonator frequency f, the printing compensation can be expressed by : (see equation 5-134)

$$\Delta y = \frac{(N-1)\, v_{y,scan}}{f} \qquad (5\text{-}134)$$

The value Δy represents the size reduction of a printed line compared to its expected length. Δy represents also the amount by which the printing command should be expanded in order to compensate for the merging effect. For example, if the printing command for a 1000 µm long printed line segment is: START print at 1500 µm and STOP print at 2500 µm and we know that 4 merged drops occur for this particular printing conditions ($v_{y,scan}$=1.5 m/s, f=76300 Hz). According to equation 5-134, Δy would be 58.9 µm (≈60 µm), thus the printing command should be changed to (START 1440µm, STOP 2500 µm) in the case where the printing is done with ascending encoder position.

This latter calculation assumed that the stream started as a uniformly spaced sequence of drops. It also assumed that the larger drops generated after a few merge will have more or less the same ballistic effect on the powder. However, in many instance this last assumption can not be applied, especially if the number of merge is larger than two. Figure 5.58 shows examples of printed line with three or four merge drops showed on the right edge or the leading edge of the drop sequence.

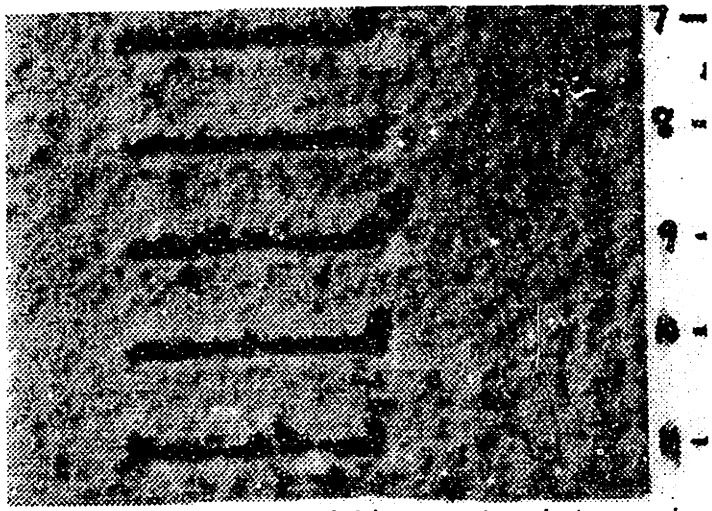

Figure 5.58: Picture of crater left by approximately 4 merge drops forming the leading end of a 5mm long printed line.

The larger crater formed by the merged drops (right edge) is unacceptable for accurate printing. In this case, the Δy compensation do not apply since the correction does not take in account the larger diameter of the crater. This diameter could be determined by using the drop-powder ballistic model developed by Tailin Fan (see reference 93).

If a non-uniform drop spacing is used instead, in order to prevent multiple merging, then the number of merged drop N can not be used as is in equation 5-134 since drops have

been removed. Instead, N is the number of merged drops, added to the number of drops removed within the sequence forming the merged drops.

For example, if a sequence is formed by removing every second and third drops from the standard stream to make the sequence: drop #0,#-3,#-6,#-9,... Then, if two merged drops (drop #0 and #-3) have been estimated at the powder bed level , it means that N equal 2 drops (#0 and #-3) plus the two removed drops (#-1 and #-2) which used to be in between, to give a corrected value of N=4. This new value of N can than be used in equation 5-134 to calculate the compensation value Δy for a non-uniform drop sequence.

5.13 Optimal printing conditions

Some basic rules can be applied to improve printing quality. Those rules range from printing strategy to prevent drop merging, to printing conditions to minimize drop placement errors. The next section will present some of the options which can be used to accomplish the task.

5.13.1 Printing strategy to prevent merging

It should be understood that any kind of drop merging prior to the powder bed is unacceptable for accurate printing. Figure 5.58 showed clearly the damage caused to a printed line which had at least 3 or 4 merged drops on its leading edge.

Following, different printing strategies are evaluated based on the drop merge model seen previously.

Drop removal method

One remedy to postpone drop merging is to remove some of the drops following the leading drop #0. As seen in figure 5.56, merge distance can be significantly improved when the second drop #-1 is removed from the train of drops. Other printing schemes have been investigated to determine the best combination of drop removal which will postpone merging beyond the powder level. Those printing schemes have been experimentally measured and modeled as well for standard printing conditions as follow:

Flow rate Q= 1.25 ml/min
Orifice diameter d_0= 45 μm
Piezo frequency f = 76300 Hz
Drop charge q = $3.0x10^{-13}$ Coulomb
Deflection voltage V_d = 2000 V

Table 5.17: Merge distance from the deflection cell entry for various printing patterns.

Drops removed	First 2 drops to merge	Measured merge distance [mm]	Modeled merge distance [mm]
NONE	#0 & #-1	12.9	11.6
drop #-1	#0 & # -2	16.6	14.6
drop #-1, #-3	#-4 & #-5	17.4	-
drop #-1, #-2	#-3 & #-4	15	16.8
drop #-1,#-2,#-4	#-5 & #-6	18	-
drop #-1,#-3,#-5	#0 & #-2	17.8	19.1

* See Appendix C8 for modeled merge distance curves

As it can be seen, the merging distance can be stretched significantly by removing drops from the stream. The model (see section 5.11) gives a good comparative approximate which can be useful to determine which strategy gives better result relative to each others.

An interesting point to notice is when every other drops are removed from the stream (ex: #-1,#-3,#-5,..), merging can be extended up to 18mm comparatively to 12.9mm when no drop is removed (see table 5.17). Although it appears that removing every other drops reduces the printing duty cycle, it is not the case if the removed drops are used for printing too. This is possible if the stream is split in two sequences of drops by charging them accordingly. ***A split stream really emerges as the optimum printing strategy to prevent drop merging.*** If a split stream is not appropriate, the second best option would be to use either one of the other options with a preference on removing drop #-1 only for print control simplicity.

Printing with exits only

Another option to conceal merge drop effects without preventing it, is to print with exits only. If we refer to figure 5.58, this means that we would print with the left side of the printed lines. Since the left side is neat and free of merged drops, we can use it to define the edges of our parts while hiding the merged drops in the middle of each printed lines. As a result, to print a single line will necessitate two printhead passes instead of one. This method significantly reduces the print duty cycle by doubling the print time. In addition, it can not be used to print fine surface texture since the small printed line segment which are formed by 10 to 20 drops could not absorb the two merge effects involve in the middle section of the line.

The decision associated to the choice of printing strategy depends solely on the compromise we are ready to make. Printing strategy are a means to escape the merging problems without attempting to act at the source of the error. Therefore, it seem that redesigning the printhead to prevent or decrease the effect of drop merging is the most logical step in our design effort. Then only, should we use one or the other techniques described above.

5.12.2 Design rule to achieve printing quality

The first design actions towards preventing drop merging and improve the print quality of the 3D printer should be built into the printhead configuration itself.

Redesign printhead for shorter drop path

For example, the printhead should be designed such as the drop flight path is minimized. A minimum flight distance provides the benefit of reducing the effect of drop merging as well as increasing the printing accuracy.

The single most important factor involved in reducing the drop flight path without affecting the printing duty cycle is the deflection cell voltage V_d. As seen in section 5.7, the deflection cell voltage V_d controls the amount of deflection experienced by charged drops. A significant proportion of the drop flight path is due to the deflection cell length l_d required to achieve a prescribed drop deflection. To shorten the deflection cell length l_d we can either increase the drop charge q, the deflection cell voltage V_d or both. Because of electrostatic forces between drops (see section 5.8), the drop charge q should be kept to a minimum as much as possible. Therefore, a very elegant way to keep drop charge to a decent level and reach our target drop deflection while decreasing the flight path, is to increase as much as possible the deflection voltage V_d at the limit of the break down value (see section 5.7).

Centered in print or off-centered in-catch jet axis

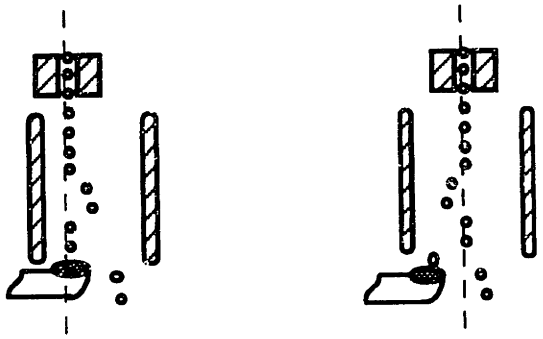

Figure 5.59: Two different printhead arrangement; a) Off-centered In-catch no-charge stream, b) Centered In-print no charge stream.

Since we are not planning to use look up tables, the arrangement that will provide the best accuracy is the one which minimize electrostatic interaction between drops and drag fluctuations, or in other words the most predictable. In this discussion, prediction of the stream position will always be done from a reference position of the stream measured in real time. This position as well as the charging voltage necessary to obtain it are recorded and used to compute the proportionality factor Kp [m/Volts]. Predicting stream position strictly from the physical model was ruled out since it does not provide adequate accuracy.

The off-centered in-catch design (see figure 5.59a) has the advantages of reducing induced charge effects since the in-catch drops are uncharged. In addition, since the drop are all charged with the same polarity for the all range of deflection, the risk of potential electrostatic merging is lower. On the other hand, as the stream is pushed further from the initial position to its printing position, the drag force on the stream constantly increases. As a result, drop deflection is no longer proportional to the drop charge q because of the non-linearity of the drag force. Therefore, prediction of drop position can no longer be done with a proportionality factor K_p but with a curve fit instead. In-addition, since drag forces are higher in the print region, it increases the probability of drop merging problem.

The centered in-print design (see figure 5.59b) has the advantages of reducing the amount of deflection to reach the required printing position. Since the positioning error is multiplicative because of the proportionality term, the centered in-print design should be more accurate than the other design. The smaller required deflection also minimized the effect of drag force on the drops, making the relation drop charge to position more linear and predictable. Although proportionality is appropriate, a curve fit provides a better accuracy (see section 5.10.3). On the other hand, since drop positioning involves bipolar charging, the risk of electrostatic merging is higher then in the case of the off-centered design. However, if the printing condition are carefully chosen, merging or electrostatic attraction force should not affect the drop flight path. Finally, since the in-catch drops hold a strong charge, induced charge effect can be seen on the leading printing drops. Therefore, induced charge compensation is necessary while it is not in the case of the other design.

In conclusion, it seems that a in-print centered design is a better choice since it can provide an improved drop placement accuracy. However, its application should be done carefully by adjusting the printing conditions accordingly in order to avoid electrostatic merging and induced charge effects.

Other important parameters

Merging can also be reduced by using appropriate printing conditions. For example, we mentioned before that increasing the drops Reynolds number reduces the effect of drag which is the cause of merged drops. However, increasing the Reynolds number implies to either increase the jet velocity or printing larger drops. Both actions goes to the opposite of what is needed in 3D printing which is to reduce ballistic effect and improve resolution. Although increasing the Reynolds number seems to create more problem than it solves, does not mean it should not be considered. Instead, it should be used as a design parameters as part of the decision making to determine the optimum printing conditions.

Chapter 6 : Simplified error budget

6.1 Introduction

We have now covered all the fabrication steps necessary to produce a finished cast part with surface textures directly from a CAD model. Each processing step starting from the initial concept to the finished part was evaluated for their dimensional limits and accuracy. The geometric information which was transferred from one step to the other was subjected to those dimensional limits and variations inherent to each fabrication process. In order to understand the contribution of each fabrication steps to the total error, we had to keep track of the magnitude and type of variation at each steps.

Because of the anisotropic nature of 3D printing, the magnitude of the errors, or in other words the accuracy, had to be determined for the three main axes of the machine. Statistical calculations over several test samples were used to quantify the average dimension and accuracy (standard deviation). In addition, since the fabrication process involves control parameters with different magnitude of time constants, accuracy of a parameter may affect different features of a part, such as its surface finish, shape or dimension.

Therefore, a method is needed to keep track of all those errors in an organized fashion, known as error budget, in order to help analyze and understand dimensional variations. The goal of this chapter is not to provide a complete error budget of the 3D printing machine, but to use the error budget principles as a tool to explain and differentiate the effects of specific error sources on the final product. The task was then to properly classify an error source of interest into its particular subgroups related by their orientations in space and time constant.

6.2 Error Budgeting

An error budget is a systems analysis tool, used for prediction and control of the total error of a system at the design stage, for systems where accuracy is an important measure of performance. The budget subdivides the overall problem into a number of smaller steps, thereby providing a more systematic approach as well as a greater degree of scrutiny of the various details. Two basic error budget frameworks can be conceived, the predictive or the control mode. The predictive mode consists of evaluating the error contributions of

existing subsystems design leading to a predicted overall system error, while in the control mode, error budget sets individual subsystem error limits and balances the level of difficulty among subsystems in order to achieve a predetermined target accuracy. For our case, the predictive approach will be used since most sub-system are already designed.

Any manufacturing process has inherent error sources that can be the result of subsystem perturbations deviating over time (temporal errors) or over position (dimension or spatial errors). Besides, the same perturbations can be additive or multiplicative as well, meaning they can be finite or varying in amplitude over time or dimension. Each error source should be classified into one of these classes and conferred with a frequency of variation. In fact, error sources can be associated with a wavelength or frequency of variation affecting the workpiece exactness with specific patterns. Depending on the frequency range, an error source could affect surface finish without altering the form or size of the workpiece.

For example, a lathe spindle turning at 1200 rpm with a feedrate of 0.15 mm/rev has a feed speed of 3 mm/s. If surface finish is defined as a wavelength shorter than 0.75 mm along the workpiece surface, then the temporal cut-off frequency in the surface finish category will have to be (3mm/sec)/(0.75mm), or 4 Hz. Any control parameter affecting the workpiece with a frequency higher than 4 Hz will affect the surface finish, while any lower frequency would contribute to form or dimension error.

Workpiece attributes like surface finish, form and dimension are then defined as error categories influenced only by a range of error frequencies out of which no effect is noted. Therefore, by knowing the frequency of variation of an error source and the transition frequencies demarcating error categories, one could deduce directly how error sources affect the workpiece.

6.3 Basic Assumptions

6.3.1 Introduction

For sake of simplicity, the error budget is valid for a predetermined window of normal operating conditions defined by the general variable $\bar{p}$ or by individual parameters, $\bar{a}$, $\bar{b}$, $\bar{c}$,... . A list of the different parameters related to the fabrication process is available in chapter 3,4 and 5 based on which most equations are computed in this chapter, unless otherwise stated. The error budget can be described as the book keeping of the variations around the normal operating conditions. However, in some instances, some of the parameters are considered constant since they have no major effect on the workpiece accuracy. Such parameters are the powder size uniformity, gravity, ...etc.

On the other hand, some error sources are not well characterized since they are coupled and difficult to measure independently (ex. part Δshrinkage, tool offset, drag). Therefore, to some extent such coupled errors will be combined into the same generic error source.

6.3.2 Error specifications

The combination of different errors into an overall result is achieved by using the root mean square [RMS or σ_A] amplitude errors in order to perform standard statistical treatment of the data. Otherwise, the alternative solution is to sum arithmetically each individual Peak-to-Valley [PV or Δn] errors ensuing an extremely conservative result, due to the very low probability of all N errors being at a maximum simultaneously.

Most of the subsystems of a machine are rated with peak-to-valley (PV) performance specifications, requiring a need to convert PV into RMS amplitude. Nevertheless, those two amplitudes can be connected by an equation of the form

$$PV_i = K \cdot RMS_i \qquad [6\text{-}1]$$

where K is a numerical factor depending on the probability distribution of the error signal between the bounding lines. The value of K for three distributions; a pure sinusoid, a signal with uniform probability density and ±sigma Gaussian or Normal, are 2.83, 3.46 and 4.0 respectively. It appears that the two latter could describe the error distribution of physical system quite accurately, although mechanical subsystem do not necessarily show a

central tendency. Therefore, the uniform density assumption would be a more conservative and realistic choice (K=3.46) in order to convert the PV specifications into RMS values.

Most machine subsystem errors are due to the variation of a single parameter that can be associated directly to a dimensional variation on the workpiece by using a simple linear transfer function. Other more complex subsystems have an error contribution that depends on one or several independent parameters with their individual variation that can not be related directly or linearly to a workpiece error. For example, a machine subsystem has a workpiece dimensional output parameter Q, that depends on several parameters a, b, c, ... such as:

Q = f(a,b,c,...) for a, b, c, ... independant

In this case the theorem of propagation of errors (see Young) could be used in order to combine and translate each RMS independent variation (σ_a, σ_b, ...) into a well defined workpiece error (σ_Q) as shown below:

$$\sigma_Q^2 = \left(\frac{\partial Q}{\partial a}\Big|_{\bar{a},\bar{b},..} \right)^2 \cdot \sigma_a^2 + \left(\frac{\partial Q}{\partial b}\Big|_{\bar{a},\bar{b},..} \right)^2 \cdot \sigma_b^2 + \ldots$$

where the derivatives have to be computed with the normal operating parameters ($\bar{a}$, $\bar{b}$, ...) of the machine.

6.4 Structural and Metrology Loops

6.4.1 Structural loop

To find the errors contributors of the error budget, one considers the chain of all elements connecting the tool (printhead) to the workpiece (powder bed) through the machine. In fact, there are two such chains connecting the tool to the workpiece. One such chain consists of all machine elements which provide mechanical support for the printhead and the powder bed. This loop is referred to as the structural loop. The second chain includes both some structural supports and those components which are used to measure or control the position of the printhead. This chain is referred to as a metrology loop.

For example, the structural loop for the 3D printer (see figure 6.1) is shown with the structural chain between the powder bed and the jet of binder with an unusual split branch which are required to define the reference position of the top and bottom part of the loose powder bed.

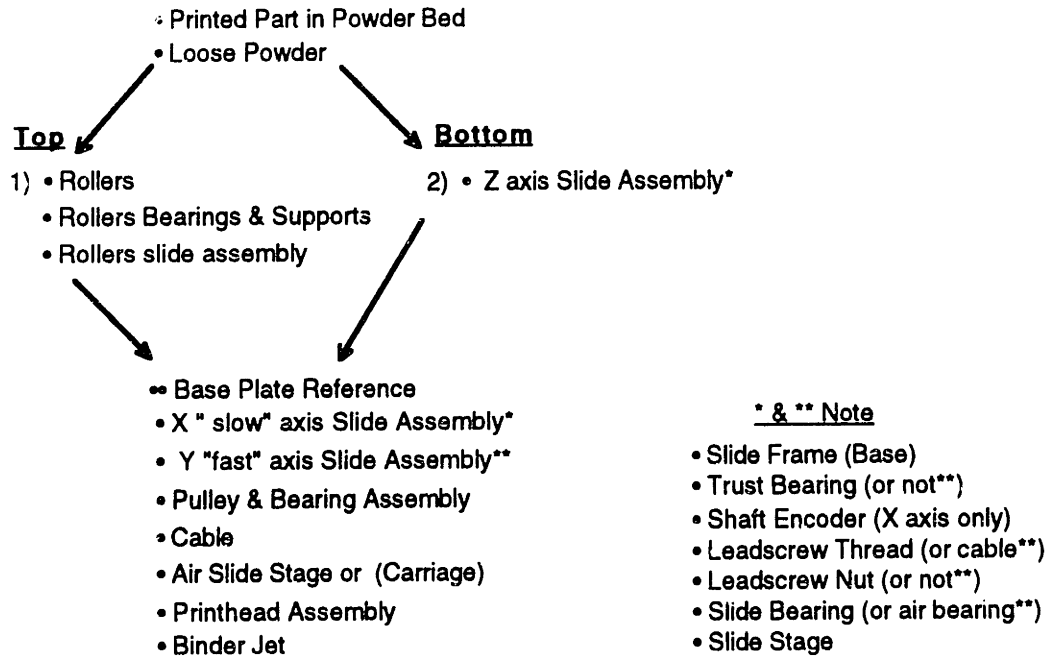

Figure 6.1: 3D printer structural loop

The X, Y and Z slides assembly can be subdivided into their own structural loop (see note*) incorporated within the machine loop. Their effects on the error budget, depends on the quality of the design and accuracy of the components.

6.4.2 Metrology loop

The machine is designed so that the Y "fast" and Z "vertical" axis position are measured directly from a linear position encoder. In fact, it is possible to remove structural loop elements from the metrology loop by inserting a metrology element in parallel (linear encoder).

For example, the Y and Z axis are designed using a linear positioning system attached between the slide stage and the slide frame. With this added element, the thrust bearing, shaft encoder, lead screw & nut (or cable and pulley assembly) can be replaced in the metrology loop by the position transducer. Even though these elements are still part of the structure producing the motion, they are no longer a factor in the positioning accuracy. Otherwise, like in the case of the X "slow" axis with its rotary encoder, the accurate positioning of the slide stage depends on machine elements which can introduce additional variation such as the one caused by temperature fluctuation, wear, backlash, ...etc. The metrology loop shown in figure 6.2 is the revised version of the structural loop using linear encoder on the Y "fast axis" and the Z axis.

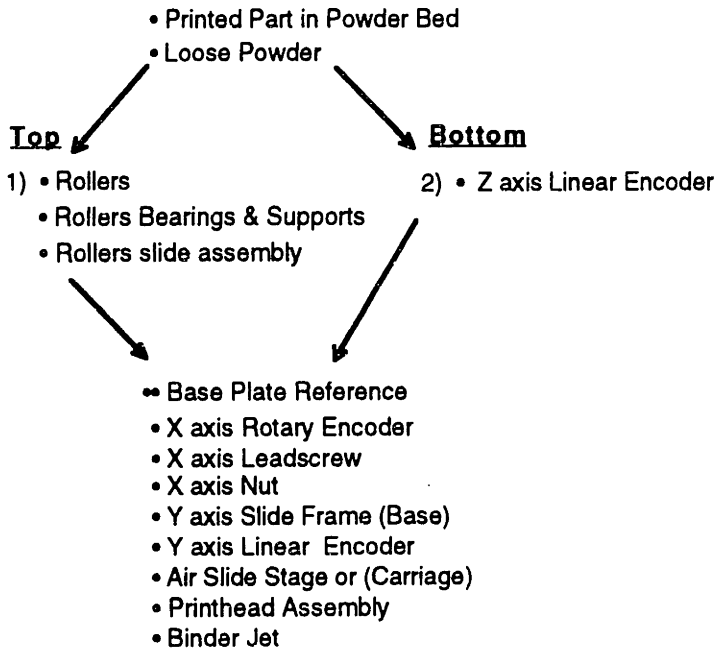

Figure 6.2: 3D printer metrology loop

6.5 Error flow Chart

Figure 6.3 shows the overall process of properly generating an error budget from the process sources of error on the left to the dimensional errors on the workpiece on the right. Distinct logical steps should be followed to efficiently keep track of the various errors from their causes to their effects on the workpiece.

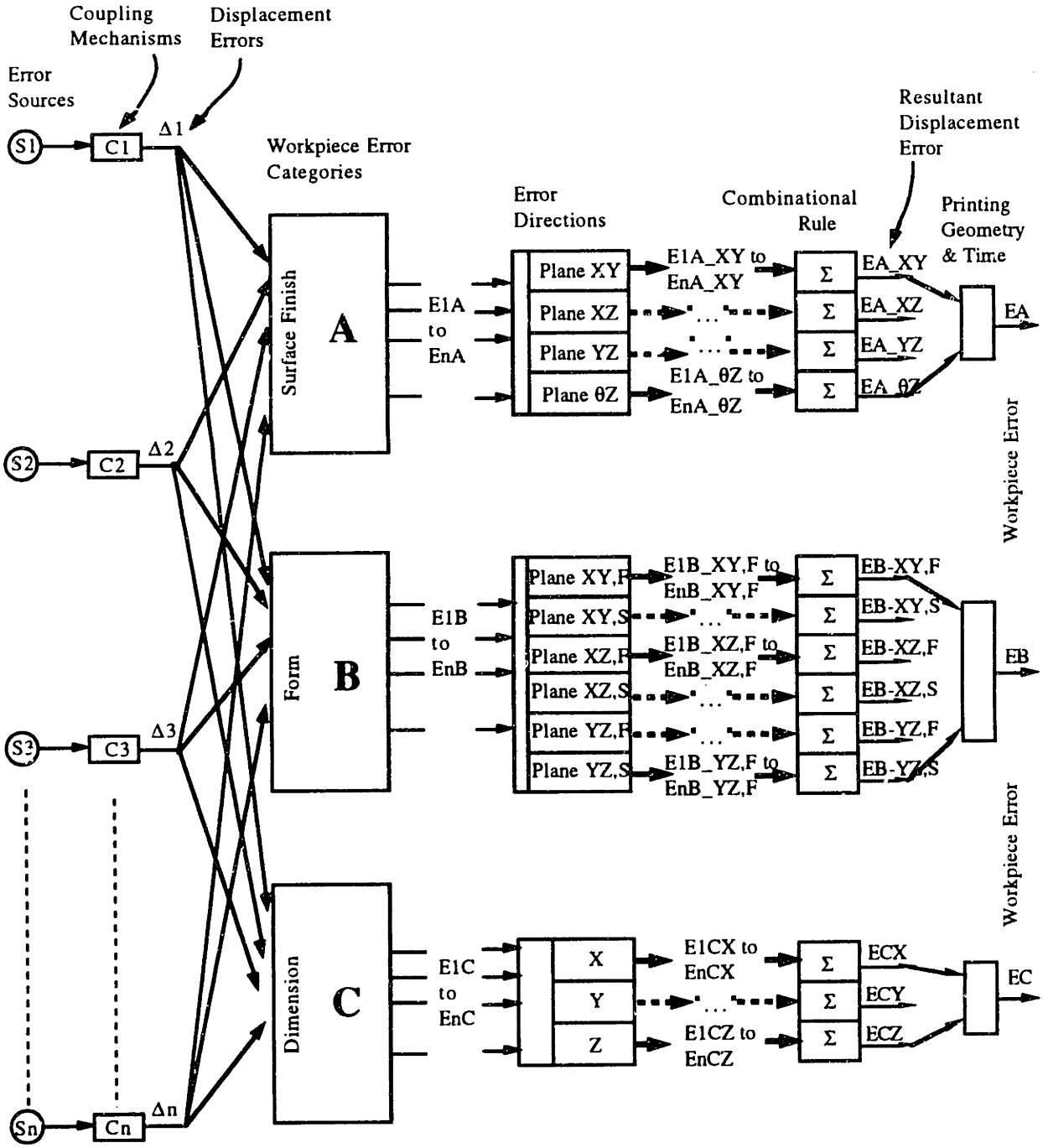

Figure 6.3: Generic error flow chart for generating an error budget. Taken from ref.[54].

The displacement errors Δn appearing at the left of the chart, corresponds to the distances between the surfaces of an actual and an ideal (perfect) workpiece. The displacement errors are always measured in the sensitive direction, i.e., normal to the ideal workpiece surface which are the X, Y, and Z direction. The error sources are the physical cause of a displacement error, and the coupling mechanism is the physical factor that connects the two. The coupling mechanism is in general a transfer function or mathematical expression that couples the variation of a process parameter to a displacement error on the workpiece. The transfer function may range from an elementary, such as a simple multiplier, to a more complex multivariable polynomial of degree n. The transfer functions were developed previously into various models based on the physics of the particular component (chapter 3,4 and 5).

Three error categories are usually used in an error budget: A) surface finish error, B) form error and C) displacement or dimensional error. The categories are separated according to the spatial frequency of variation along the workpiece surface. For example the average dimensional type C errors are "dc" (zero frequency) term, while surface finish type A has the most rapidly varying spatial frequency and form errors being in between. The cut-off frequency which delimits each category are calculated for 3D printing in the next section.

After generating a list of displacement errors for each category, the list is then subdivided into error directions X, Y and Z along the main machine axis. The amount of detail available on the set of errors will dictate which combinatorial rule should be implemented. The indicated choices are either to sum the individual PV (Peak-to-valley) displacement-error amplitude arithmetically or to convert the bounded errors into RMS amplitudes in order to conduct statistical treatment of the data. The appropriate choices made for this particular error budget are discussed in more details in the next sections.

6.6 Workpiece Error Categories

Because three dimensional printing is an additive manufacturing process that produces anisotropic parts, it is important to choose a set of error categories that reflects the intrinsic characteristics of the material and, are meaningful for the intended end use of the workpiece as well.

The expected choice of category would be surface finish, form and size, since the process must comply with tight specifications in regard to those latter physical features. Nevertheless, because of the anisotropic nature of the final product and also the particular build time history, each category should be refined into sub categories that will consider plane orientation (see Table 6.1).

Table 6.1: Cut-off frequency for the three error categories and sub-categories for the 3D Printing machine.

Category A: Surface finish		*Transition cut-off Frequency*
1) Plane X-Y with proportional deflection		
Top & Bottom surface.....	X axis	2 Hz
	Y axis	7500 Hz
2) Plane X-Z.....	X-axis	2 Hz
	Z-axis	DC-0.01 Hz
3) Plane Y-Z.....	Y-axis	7500 Hz
	Z-axis	DC- 0.01 Hz
Category B: Form		
1) Plane X-Y		
A- Flatness	[DC to 2 Hz or 7500 Hz]	
B- Squareness	[DC]	
2) Plane X-Z		
A- Flatness	[≈0.5 to 2 Hz]	
B- Squareness	[DC to ≈0.5 Hz]	
3) Plane Y-Z		
A- Flatness	[DC to 0.5Hz or 7500Hz]	
B- Squareness	[DC]	
Category C: Size		
1) "X" (slow) axis	[DC]	
2) "Y" (fast) axis	[DC]	
3) "Z" (piston) axis	[DC]	

As mentioned before in section 6.1, each category A, B and C is sensitive to a range of error frequency obtained from the normal printing conditions. The calculation of those frequencies is described in this next section.

6.6.1 Surface finish category

The surface finish category (A) is subdivided into three sub-sections that represent the 3 orthogonal planes perpendicular to the 3 major X, Y and Z axes of the machine. Each plane has two main axis along which two different surface characteristics can be defined. The surface finished differs depending on whether the surface was shaped by the top, bottom, sides or edges of a printed lines. The build rate of a plane along its two main axis will prescribe the surface finish cut-off frequencies which will differentiate a surface finish displacement error from a form error.

First, we need to define the minimum spatial wavelength which distinguishes a surface finish problem from a form problem. Since the primitive size on alumina powder is about 200 µm, we will consider that any dimensional disturbance smaller than $\lambda_{spatial}$=200 µm is considered as a surface finish attribute. In addition, we assume that the line spacing L_S and layer spacing Lay_S are kept constant at 175 µm. The fast Y-axis scanning speed $v_{,scan}$ = 1.5 m/s will be assumed constant over a travel length of $T_L \approx$ 0.6 m. Finally, a cube of side b= 50mm will be considered as a reference part size to evaluate the average build time.

Plane X-Y (Slow-Fast axis)

The surface finish of plane X-Y is defined as a high frequency dimensional variation in the Z-direction along either the X or Y axis. The surface finish is determined by the top surface of a printed line located by the powder spreading roller's reference. The cut-off frequency f_c can be calculated from the build rate of the part along the desired axis. The build rate of the printed X-Y layer is determined by the scanning speed $v_{y,scan}$ along the fast Y-axis, and the slow axis speed v_x along the slow X-axis. We assume the Z-axis positionner to remain at a constant position.

The cut-off frequency along the fast axis $f_{c,Y}$ is defined as:

$$f_{c,Y} \approx \frac{\dot{Y}_{\text{Build rate}}}{\lambda_{spatial}} = \frac{v_{y,scan}}{\lambda_{spatial}} = \frac{1.5 m/s}{200 \times 10^{-6} m} = 7500 \text{ Hz} \qquad (6\text{-}2)$$

Therefore, any process parameters which influences the Z-dimension along the fast Y-axis, will affect the surface finish only if its frequency of variation is larger than 7500 Hz. Otherwise, that same parameter will contribute to either the form or dimension error of the part along the Z-axis.

Along the same line, the cut-off frequency $f_{c,X}$ along the slow X-axis is determined by:

$$f_{c,X} \approx \frac{\dot{X}_{\text{build rate}}}{\lambda_{\text{spacing}}} = \frac{v_{y,scan}\, L_s}{\lambda_{\text{spacing}}\, T_L} = \frac{1.5 m/s \cdot 175 \times 10^{-6} m}{200 \times 10^{-6} m \cdot 0.6 m} = 2 \text{ Hz} \qquad (6\text{-}3)$$

The same principle applies for the X-axis but for a much lower cut-off frequency of 2 Hz. Very few parameters can affect the surface finish on the plane X-Y. In fact, binder drop size and velocity are part of the few which can affect the surface finish in the Z-direction, but their time constant are high enough (low frequency) to make those parameters more damageable for the form or dimension of a part.

The top and bottom X-Y planes experience the same transition frequency even though their visual aspect is not the same due to different error sources sensitivity.

Plane X-Z (Slow-vertical axis)

The surface finish on the X-Z plane is defined as a high frequency dimensional variation in the Y-direction along either the X or Z axis. The surface X-Z is determined by both ends of the printed lines.

The cut-off frequency along the X-axis $f_{c,Y} \approx 2$ Hz remains the same as the one calculated in the case of plane X-Y. However, the cut-off frequency along the Z-axis have to be calculated with the following expression:

$$f_{c,Z} \approx \frac{\dot{Z}_{\text{build rate}}}{\lambda_{\text{spatial}}} = \frac{Lay_s \cdot L_s \cdot v_{y,scan}}{b \cdot T_L \cdot \lambda_{\text{spatial}}} = \frac{(175 \times 10^{-6} m)^2 \cdot 1.5 m/s}{0.05 m \cdot 0.6 m \cdot 200 \times 10^{-6} m} = 0.008 \text{ Hz} \approx \text{DC} \qquad (6\text{-}4)$$

This cut-off frequency was calculated for a part with an average section of 50mm W x 50 mm L. A bigger part would make the cut-off frequency $f_{c,Z}$ even smaller or closer to DC. This result means that the surface finish of plane X-Z is sensitive to almost any process variation frequency which affect the Y dimension. On the other hand, if such a process variation has a very low time constant (high frequency) the error may average itself (aliasing) to give a decent surface finish.

Plane Y-Z (Fast-vertical axis)

The surface finish of plane Y-Z is defined by the sides of a printed lines. The cut-off frequencies $f_{c,Y}$ and $f_{c,Z}$ were calculated previously and applies to the same rule as presented in the two previous cases, but for dimensional variation in the X direction.

Note: If multiple nozzles are used on the printhead, the effect would be to increase the cut-off frequency along the X and Z axis since the build rate would be increased.

6.6.2 Form & Dimension category

The form category (B) is subdivided about the three orthogonal planes with flatness and squareness as the two distinct criteria. Both criteria are sensitive to frequency lower than the surface finish transition frequencies in their respective directions. Flatness will usually be affected by error frequencies near the cut-off frequency while squareness is closer to DC. In other words, squareness can be used as a diagnostic to identify slow drifts in the fabrication process parameters, while flatness indicate a faster drift.

The form category is therefore bounded by the surface finish cut-off frequency and the dimensional category (A) which is usually a DC of 0 Hz frequency. Such a frequency is characteristics of friction, offset error or any type of steady state error in a control system.

6.7 Error sources of fabrication process

Error sources can be regrouped under three main categories: static, quasistatic, and dynamic error. The static errors are determined by the dimensional accuracy and quality of assembly of the machine subsystems. It means that once the machine is assembled, the errors are set and definitive. The quasistatic errors, are caused by physical phenomenon such as: deflection caused by weight, thermal expansion, ...etc, that affect the accuracy of the machine by varying amplitude over time or position. Finally, the dynamic errors are caused by the kinetic of machine subsystem such as velocity controller, vibration, subsystem acceleration & deceleration, or simply electrical noises.

The major source of errors in the 3D printing machine are dynamic errors, since static and quasistatic errors are usually consistent and can be compensated for.

Here is the list of the seven areas of error sources in the fabrication process of CoCr castings using 3D printing:

1- Geometric Machine Accuracy
2- Positioning and other controllers errors
3- Printing controller errors
4- Powder & Binder Chemistry and Interaction variation
5- Environment variation
6- Casting errors
7- Post-processing errors

Out of all the error sources present in the process two sources predominate: 1) printhead velocity control and 2) printing controller errors. This statement assumes that static and quasistatic errors have been compensated for in the design and assembly of the machine as well as in the chemistry of the materials.

The error introduced by the printhead velocity controller was mentioned in section 5.10.2 of chapter 5. The printing errors caused by the controller have been discussed thoroughly in chapter 5 and Appendix C9, where more details are available on drop charging and positioning error.

6.8 Error analysis using error budget

6.8.1 Introduction

The accuracy of the final cast part is associated with the dimensional variation introduced from each fabrication step. Among the steps used to produced surface macro-texture on metal casting, only a few predominates in determining the total casting accuracy.

6.8.2 Major error contributors

As mentioned before, the major error sources of the process are caused from the velocity and printing controller of the actual 3D printing machine. Other error sources such as the positioning controllers of the 3D printing machine have a repeatability of about 5 μm, which is only a small portion of the final castings displacement error. Likewise, the casting process errors are minor as well because of the very small size of the cast features. In fact, the ceramic mold dimensions hold very well to the high temperature and metal pressure stresses to transfer predictable casting dimensions. In fact, little dimensional variation (aside from shrinkage effects) was introduced between the ceramic molds and casting (see section 3.8.2). Although shrinkage was noticeable, it can be compensated for with relatively good accuracy (within ≈0.2 to 0.3% of the dimension).

Finally, the chemistry of the powder and binder have been optimized (see ref.[90]) to produce uniform and reproducible point and line primitives size, which do not add variability to the ceramic mold dimensions. Although in some specific instances, such as for the bottom layer or specific printing conditions, binder and powder interaction can have a small effect on surface finish. However, these problems are outside the scope of this research. As a result, since the printing controller relies on several control parameters, it made the sub-system more complex to control accurately. Therefore, a lot of effort was invested in order to reduce the initial printing accuracy of ± 100 μm down to ±20 μm or lower.

6.8.3 Accuracy in flow of geometric information

The concept of accuracy is no longer attached to a single digit which prescribed the accuracy in all the direction of a part. As seen previously, accuracy can be subdivided into three categories, (surface finish, form and dimensions) which all have three sub-group for

the three orthogonal axes of the 3D printing machine. Keeping track of all the error sources was done by assessing the drop placement accuracy, and measuring mold and casting dimensions. The flow of geometric information can be traced as followed.

Dimensional variation is introduced first by the positioning slides X-Z and structure of the 3D printing machine. The process variation at this point are about:

$$\sigma_{\text{slow X-axis}} \approx \pm 5\ \mu\text{m}$$
$$\sigma_{\text{fast Y-axis}} \approx \pm 5\ \mu m$$
$$\sigma_{\text{vertical Z-axis}} \approx \pm 5\ \mu m \qquad (6\text{-}5)$$

The accuracy of the printhead controller was also measured (see section 5.10) and the results were:

$$\sigma_{\text{slow X-axis}} \approx \pm 15\ \mu\text{m}$$
$$\sigma_{\text{fast Y-axis}} \approx \pm 40\ \mu m \qquad (6\text{-}6)$$

Those numbers were achieved with the regular printhead control scheme used with a minimum of error compensation. As we know by now, those numbers can be reduced by applying compensation procedures described in previous chapters. As a reminder, the value $\sigma_{\text{slow X-axis}}$ can be reduced to ±6 μm (see table 5.15), if the second order model is applied instead of the linear one. Along the same line, $\sigma_{\text{fast Y-axis}}$ can be reduced to ≈±20 μm if the flow rate and fast axis velocity ripple are minimized (see section 5.10.2). In addition, drag force and drop merging account for the major portion of the error along the fast axis. Solutions to counteract those effects were evaluated in section 5.10.

The mold dimensions which are a combination of the machine, printhead controller errors and binder-powder interactions were measured as:

$$\sigma_{\text{slow X-axis}} \approx \pm 26\ \mu\text{m}$$
$$\sigma_{\text{fast Y-axis}} \approx \pm 23\ \mu m$$
$$\sigma_{\text{vertical Z-axis}} \approx \pm 30\ \mu m \qquad (6\text{-}7)$$

The molds dimensions were measured optically with a high magnification microscope. As a result, the measurements included the three categories of errors into one number. The

dimensional variations were calculated as the standard variation σ of the measurements made on 20 ceramic molds along the main axis X-Y and Z of the machine. Because of occlusion inherent to optical measurements of granular materials (described in ref.[90] p.196) the accuracy of the measurements themselves were also affected by about half a grain size ±14-15 µm. The standard deviation along the fast axis $\sigma_{\text{fast Y-axis}} = \pm 23$ µm seem to be underestimated, since the mold should have a variation of at least ±40 µm because of the printhead controller. However, if the occlusion problem is accounted for, $\sigma_{\text{fast Y-axis}}$ is indeed within the limits.

Finally, the dimensions on the castings were measured, and their dimensional variations were measured as:

$$\sigma_{\text{slow X-axis}} \approx \pm\ 20 - 30\ \mu\text{m}$$

$$\sigma_{\text{fast Y-axis}} \approx \pm\ 60\ \mu m$$

$$\sigma_{\text{vertical Z-axis}} \approx \pm\ 10\ \mu m \qquad (6\text{-}8)$$

The dimensional measurements were done with a caliper which combined the surface finish, form and dimension errors into each reading. The standard deviations were calculated from the experimental measurements of 16 castings sample (see section 3.8.2). Since the occlusion problem is non-existent in this case, the values obtained should be more representative of reality.

The accuracy of the slow axis was determined partly from the printhead controller with its $\sigma_{\text{slow X-axis}} = \pm\ 15$ µm. The other error contributors were a combination of machine error and powder-binder interaction causing a rough finish on one of the casting surface.

The results obtained on the fast axis seemed unreasonably high. According to the error introduced by the printhead and machine, $\sigma_{\text{fast Y-axis}}$ should be at most ± 40-45 µm.

Two phenomena can explain this result: drop merging and missing or additional printed drop. The surface finish of the plane X-Z has the roughest finish compared to all the other casting surfaces. This rough finish is due to inadequate control of the printed drops at the edges of a printed lines. In fact, the 2 or 3 leading drops forming the start of a printed line merge into a bigger drop just before the powder bed if no compensation is applied. The merge effect caused by air drag force not only produces bigger drops with a different ballistic characteristics, but also shorten the length of a printed line (see section 5.10).

In addition, the printhead charge synchronization circuit was designed in such a way that the drop forming either end of a printed line can be omitted or duplicated. This effect

would aggravate the surface finish locally and generate and error of about ±20 μm depending on the printing conditions. Isolated surface irregularities and tiny metal studs were created on the plane X-Z of the castings because of this effect.

In summary, the value $\sigma_{\text{fast Y-axis}} = \pm 60$ μm is due to dimension and surface finish error, both of which can be compensated for with the methods suggested in this thesis.

The casting accuracy can be broken down into surface finish, form and dimensional accuracy. The values stated above did not distinguished between the three categories. The following section is meant to clarify that point.

6.8.2 Surface Finish error Budget

According to table 6.1, the surface finish on the casting will be affected by process parameters only if their error frequency is above 2 Hz , 7500 Hz and DC along the X, Y and Z axis respectively.

Plane Y-Z

For example, the surface finish of plane Y-Z is affected by displacement error in the X-direction along both the Y and Z axis. Along the Y axis, the only error which has an effect in the X-direction with a frequency higher than 7500 Hz is the charging electrode. More precisely, the digital-to-analog converter and amplifying stage of the electronic circuit have to regulate voltages at frequencies similar to the piezo frequency in most extreme cases (i.e. ≈ 70-200 kHz). The combined error due to this part of the electronic can be attribute to a variation of at most ± 1 μm.

Along the Z-axis, all the process parameters with an effect in the X-direction can affect the surface finish since the cut-off frequency is DC. However, because of the very slow drift of most of those process parameters (see table 6.2), it is not probable that those parameters would affect surface finish.

Table 6.2: Process parameters with a displacement error in the X-direction.: (or proportional deflection direction)

INPUT PARAMETERS (Experiment)	TYPICAL VALUE	frequency [Hz]	time constant	$\pm\sigma_x$
Jet position x_0 [μm]	0	≈DC	30 min	0.25%
Flow rate Q [ml/min]	1.2	≈DC	30 min	0.25%
Piezo resonator frequency [Hz]	76300	≈DC	1 hour	5
Charging voltage V_c [V]	80	70-200kHz	5-15μs	0.03
Deflection cell high voltage V_d [V]	1000	1 Hz	1 s	0.05%
Charging cell capacitance C' [F]	4.5×10^{-15}	≈DC	30 min	2%

The time constants are so large (very low frequency) that surface finish could be affected only for very large part which necessitate a very long printing time. In summary,

no process parameters other than powder-binder interaction really affects the surface finish on the plane Y-Z.

Plane X-Z

The story is different for plane X-Z for which surface finish is affected by displacement errors in the Y direction. Since the cut-off frequency of the X and Z axis are 2 Hz and DC respectively, most process parameters with an effect along the Y-axis would affect surface finish in that particular plane. In this case, the scanning velocity ripple with a frequency of about 50 to 1000 Hz and the printhead controller with a 70-200 kHz have a significant effect on surface finish. Another source of error originates from inaccurate offset compensation for bi-directional printing. Such an error can account for as much as 25 µm or more of the surface finish problem if not adjusted properly. In fact, most of the casting displacement error $\sigma_{\text{fast Y-axis}} = \pm 60$ µm is under the surface finish category. The latter errors account for more than 85% of the total error.

Lots of development is needed to improve the surface finish in the Y-direction. It corresponds indeed to the worst surface finish on the 3D printed mold.

Plane X-Y

As mentioned before, very few parameters have displacement error in the Z-direction which can affect the surface finish of plane X-Y. In fact, the most important one being the binder flow rate and Z positioning stage which all have very high time constant (low frequency). Those low error frequencies can not affect significantly the surface finish or even the form of the part.

6.8.3 Form Error Budget

According to table 6.1, intermediate frequencies between DC-2 Hz, DC-7500 Hz and DC-DC can affect the form in the planes X-Y, X-Z and Y-Z. If we look at the problem from the error sources stand point, three main sources of errors can affect the form of a cast part: the machine alignment, binder flow rate drift and jet shift. At the beginning, we assumed the machine axis to be satisfactorily aligned and orthogonal to each other. The binder flow rate however, could still affect the shape of a printed part. Thus, as a precaution the binder flow rate was measured and recorded during the entire printing period for all the ceramic mold produced in the experiment.

In addition, the jet shift can influence the form of a part in two manners. First, a jet which slow drift in position can cause squareness errors in the Y-Z and X-Z planes. Second, a shifted jet inside the charging electrode changes the electrode capacitance (increases capacitance) and causes proportional deflection errors by changing the constant

of proportionality. The 3D printing machine is actually equipped with instruments to measure the jet position at regular intervals also.

Since no drift was actually measured in either the flow rate nor the jet position, we can conclude that the displacement errors (results 6-8) have no form category component.

6.8.4 Dimensional Error Budget

Finally, the displacement errors are all caused by DC or steady state displacement errors in the process parameters. Many parameters can be included in this category. Among the most notable are the three axis positioning controller which have an approximate repeatability of about ±5 μm on all the axes of the machine.

X-dimension

The displacement errors in the X-direction is mainly due to the proportional deflection errors. The magnitude of the error depends on the interpolation method used to predict the position for a given charging voltage V_C. If the linear proportionality factor is used, a dimensional error of ±15 μm can be seen. If compared to the casting displacement error $\sigma_{slow\ X-axis} = \pm 20\text{-}30\ \mu m$, the dimension component corresponds to a significant portion of the displacement error while surface finish would account for the balance of the error.

If the second order jet positioning method (see section 5.10.3) is used instead, it would reduce the proportional deflection error to about ±6 μm, which in turn could improve the X-axis accuracy to $\sigma_{slow\ X-axis} \approx \pm 15\text{-}20\ \mu m$ depending on the amount of deflection required.

Y-dimension

Dimension Y has two sources of DC displacement error: air drag force on drops and electrostatic repulsion on drops. Air drag force causes the leading drops of a train of printing drops to slow down faster then the rest of the train. This effect causes drop merging, but also reduce the length of the expected printed line. The phenomenon is repeatable and cause the part to be consistently shorter than initially expected from the print command. The magnitude of effect on the Y-dimension is estimated to about -40 to -60 μm depending on the printing conditions used (see section 5.10). The error caused by air drag is not included in the measured casting dimensional variation (result 6-8) since it is a DC error. However, if not compensated for in the printing command, it should be accounted for in the shrinkage compensation.

On the other hand, electrostatic repulsion increases the length of a printed line by 20 to 30 μm depending on the drop charge level. Most of the printing done in this research was

performed with uncharged drop which means that electrostatic forces had no effect on the part dimension.

Z-dimension

The dimension Z displacement error is mainly associated to a dimensional error since the surface finish and form are determined by the roller and machine reference. For this same reason, the Z dimension is the most precise of all the displacement error with a ± 10 μm accuracy.

Conclusion

- Accuracy in X-axis is dominated by dimension and form displacement error.
- Accuracy in Y-axis is dominated by surface finish after drag force on drops has been compensated.
- Accuracy in Z-axis is dominated by dimension displacement error if binder-powder interaction are optimized for smooth surface finish.

6.8.5 Estimate of best achievable accuracy on castings

Eventually, current error sources seen in the 3DP manufacturing process could be lowered or even counteracted by implementing different compensation method seen earlier. As our expertise on the machine improves and the different compensation method are implemented, it is estimated that the 3D printing could realistically achieve the following overall accuracy on small castings.

$$\sigma_{\text{slow X-axis}} \approx \pm\ 10 - 15\ \mu\text{m}$$

$$\sigma_{\text{fast Y-axis}} \approx \pm\ 20 - 25\ \mu m$$

$$\sigma_{\text{vertical Z-axis}} \approx \pm\ 10 - 15\ \mu m$$

This estimate may vary depending on the size of the part being printed as well as the compensation procedure being used or modification to the printhead design. However, it is a good estimate of what can be achieve in a relatively short term with the available equipment. The fast axis is the less accurate until the printing controller is modified with a smoother scanning velocity and tighter drop charge control.

Chapter 7: Conclusion

7.1 Design rules for accurate surface macrotextures

The ultimate goal of this research was to fabricate CoCr castings with accurate surface macro-textures from a 3D printed ceramic mold. To reach that goal, the fabrication process was broken into fabrication steps (see figure 1.7) which were analyzed in order to establish their constraints on the flow of geometric information.

This summary of design rules often refers to sections of the thesis where the specifics are covered in more detail in order to keep the list concise.

7.2 Summary of design rules

The following is a list of rules which summarizes the capabilities and limits of the fabrication process to produce CoCr castings with accurate surface macro-textures. The corollaries are meant to be used as a reference to create future texture designs, but also as a tool to improve the quality of the final product. The rules are subdivided in the major fabrication process steps described earlier in detail in this thesis.

The design rules are not absolute since for example, the minimum feature size required from one fabrication step may be overridden by a minimum features required from another fabrication procedure.

Most of the process rules are meant to be as general as possible and can be applied to other mold and casting materials. Other rules are suitable only for the process of printing colloidal silica binder in 30 μm alumina powder. The binder is assumed to be optimized in order to minimize bleeding and give adequate strength to the ceramic. Therefore, some design rules may apply only to the specific printing conditions and material system used. A range of printing parameters for which most rules apply is showed as follows:

- Powder material: 30 μm average size Alumina powder + gelling additives
- Binder: Colloidal silica with 50 nm silica particle size
- Nozzle orifice diameter: 45 μm
- Drop frequency: between 50 and 100 kHz
- Flow rates: between 0.5 and 2.5 ml/min

7.2.1 CAD model and rasterizing algorithm

1) Feature snapping in the slow X-axis is key to assure conformity to CAD model for millimeter size features. (Feature snapping should be done with proportional deflection control) (see also section 4.2)

2) Feature snapping in the vertical Z-axis is needed to assure conformity to CAD model for millimeter size features.
(Feature snapping should be done by either changing the layer thickness within a certain window of non-bleeding operation or adjust the CAD model dimensions to be an integer number of constant layer thicknesses. Small negative offset can be used also (see section 4.2))

3) Drop or tool offset compensation should be used to compensate for the primitive size in the X-Y-Z direction

4) Proportional deflection should be used to make smoother surface feature on the ceramic mold and seal adjacent printed lines to prevent metal infiltration during casting.

7.2.2 Machine, Printhead control and performance

1) 3D printing machine has a repeatability of about ±5 to ±10 μm (depending on the size of the part) for the 3 main axis of the machine assuming adequate squareness and parallelism.

2) Printhead control accuracy is about ±15 μm for slow X-axis with proportional deflection and ± 40 μm for fast Y-axis. If proper control procedure is used, those numbers can be improved to ±6 μm for slow axis and ±20-30 μm for the fast axis when appropriate printhead control is applied (see section 5.10 and App. C9).

3) Printing in one direction minimizes dimensional error on the fast Y-axis.

4) Several methods to determine the charging voltage can be used in order to control drop position. (see section 5.10)

5) Induced charge compensation methods should be used to print accurate features (see section 5.6)

6) Merged drop should be prevented using printing strategies described in section 5.11)

7.2.3 Printing process of ceramic mold and powder removal

1) Binder saturation level must be controlled to prevent bleeding and assure material uniformity.(see section 4.4.1)

2) The minimum printable positive (protrusion) feature size along the fast Y-axis is about 300 μm long or the equivalent of 5 printed drops. (depends on the printing conditions shown above)

3) The minimum printable positive feature size along the slow X-axis is ≈ 200 μm long, which represents the width of a single printed line.

4) The minimum positive feature size along the vertical Z-axis is 150-200 μm long which represents the minimum layer thickness plus some ballistic and bleeding effects.

5) The minimum cavity size in the slow-fast X-Y axis plane must be at least 3 to 5 grain diameter which represents a minimum cavity width varying between 150 and 250 μm. (see section 4.3)

6a) The minimum cavity depth on the vertical Z-axis is related to the layer thickness but also to the ballistic effect and particle size used. For example, a 175 μm layer thickness would create a cavity height around 165 μm high.

6b) The maximum cavity depth is not determined but we know for a fact that it can be made up to a Depth/Width ratio D/W 12:1 in the case of a cavity with section 150μm W x 400μm L x 1800 μm Deep. If any moisture or any other kind of powder bed binding additive is used, the figures mentioned above about the cavity minimum dimension can be affected. In the case of powder misted with water the ratio D/W goes down to 5.

7a) The minimum free standing positive feature size that will sustain powder removal has a stress ratio $H^2/LW^3 < 1000$ [1/mm^2] for single line (200μm W x 400 μm L) features and at least 200 [1/mm^2] for two printed lines (350 μm W x 400 μm L) cantilever shaped features. The latter value is probably much more than 200 [1/mm^2] in the case of 170 μm layer thickness since the stress limit was not reached in our particular experiments. (see section 4.3.2)

7b) If the positive features are somehow interconnected with other features by a bridge then the ratio H^2/LW^3 could go up higher than 1000.
(For example, a feature size could be 350 μm wide x 3000 μm high)

8) Feature of size 500 μm and less should be considered as square shaped features in the CAD model since any kind of curvature cannot be properly generated at that scale. Unless proportional deflection is used in which case the minimum radius can be cut by half to 250 μm.

9) Square edges on the CAD model must be smoothed down to 80-100 μm radius to reflect the minimum achievable radius of a printed primitive.

7.2.4 Casting Process and Mold Removal

1) Minimum freestanding ceramic mold feature should have a L/W ratio of at most 20 to sustain metal pouring stresses. Another useful ratio proportional to the stress at the base of a feature could be L^2/HW^3 which should be smaller than ≈ 450 [1/mm^2].

2) Minimum casting cavity dimension which can be infiltrated by metal should be determined by surface tension of the liquid metal. (see section 3.2.4)

3) Casting freezing time should be kept approximately around 10-20 seconds (using Shvorinov's rule) which can be determined from the casting conditions and mold design (see section 3.2.5).

4) Minimum casting cavity for mold removal should have a ratio D/W smaller than 20:1 for minimum cavity size of 350 μm wide x 10 mm deep cavities (using regular

sodium hydroxide sol'n). The ratio D/W could go larger than 20 for bigger cavities. If more than 2 post-dips are used, those figures can be reduced by about half.

5) Square edges on the CAD model of the metal casting must be smoothed down to about 100-175 μm radius due to molten metal surface tension.

6) Achievable accuracy on the casting is between 20 to 30 μm along the slow X-axis, ±60 μm along the fast Y-axis and ±10-15 μm along the vertical Z-axis. Those figures can be reduced to 10-15 μm, 20-30 μm and 10-15 μm respectively if proper printhead control is applied. (see section 6.8.5)

7) Casting oxide layer removal may decrease the casting dimension by as much as 25 μm when aggressive chemical method such as the one described in section 3.7.3 is used.

7.3 Future work

We know that surface macro-texture with geometric features parallel to the main axes of the machine can be produced with adequate quality. Several orthogonal texture designs can be done in this fashion. With the use of drop proportional deflection, even more texture design possibilities can be achieved with added features such as curved lines and smooth geometry. Along the same line, proportional deflection is also necessary if a multiple nozzle printhead is used. In fact, since the spacing between nozzle is fixed, proportional deflection is essential in order to provide edge feature snapping; unless only one of the nozzle is used at a time. As mentioned before, feature snapping is necessary to assure part conformity with the CAD model.

For those reasons, development of proportional deflection printing scheme, which was not fully implemented in this research, should lead to improved texture designs and quality.

Another important parameter to optimize will be the layer thickness. Thinner layer thickness should be used in order to minimize the stair stepping effect which is particularly damaging for sub-millimeter surface textures. Combined with thinner layer, a new printing strategy will have to be developed in order to avoid bleeding. Techniques such as selective printing of a layer as opposed to printing the entire layer should be investigated in more detail. As mentioned before, post-dipping the ceramic mold in a solution of refractory in suspension may solve the problem. However, if it could be solved right from the printing process, it would significantly reduce the number of post-process manipulations.

Here are some other topics that could be considered as a continuation of the present research:

- A feature snapping scheme combined with variable layer thickness will be necessary to keep the integrity of the surface texture on inclined planes. One strategy would be to selectively print on a particular layer only the features that snap to the edge of surface features. The work would involve using thin layer, proportional deflection as well as a smart slicing and control algorithms.

- Considering the fact that surface textures are made from very small printed line segments, printing with exits only to avoid the effects of drop merging is practically hopeless. However, techniques to eliminate drop merging can be used to print

important details with the leading drops. Various techniques were proposed in this thesis, but few could be tested since the machine controller was not updated soon enough to provide the necessary drop control at the time of the experiments.

- Printing using proportional deflection should improve the surface finish of the cast texture itself. Combined with bimodal or spherical ceramic powder the cast surface quality can be improved. A better surface finish could be achieved while reducing the occurrence of ceramic grain mechanical pick up.

- Some printing angles will have to be avoided to optimize our control over surface finish. The work will be to discover the range of angles in order to optimize the texture quality by playing with the printing orientation of the part.

7.4 Final note

This research showed that accurate surface macro-textures, suitable for orthopaedic applications, could be done using the 3D printing technology. Pore size in the range of 200 to 1200 μm with bulk porosity varying between 20 and 80 % were successfully produced on cobalt-based alloy castings.

As a result, two hundred dog implant castings were produced in order to be tested both mechanically and in-vivo against the FDA, ASTM and Johnson & Johnson requirements (see figure 7.1). Four promising texture designs offering a range of porosity, pore size and re-entrant geometric features were chosen from several other configurations as our first test samples (see figure 7.2 and chapter 1).

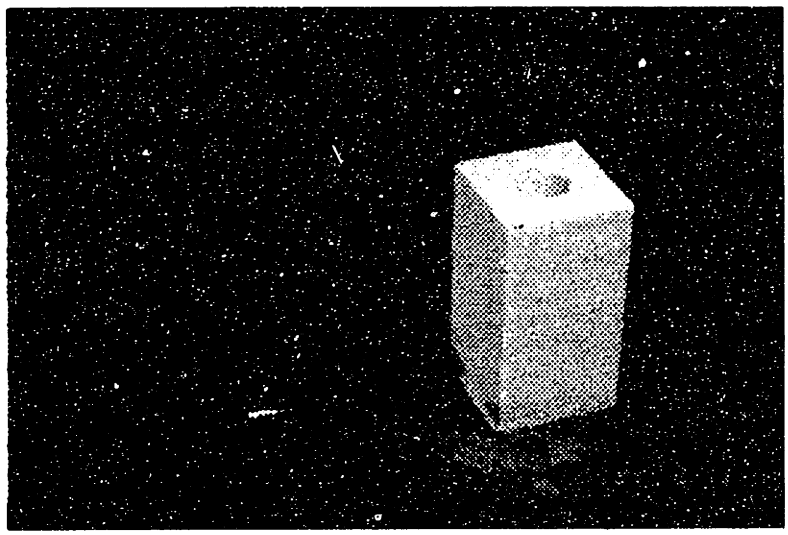

Figure 7.1: F75 Cobalt-Chrome dog implant casting and 3D printed mold with customized surface texture.

Preliminary mechanical tests on the four texture designs showed results which easily exceeded standard requirements set by the medical industry.

Figure 7.2: F75 Cobalt-Chrome dog implant casting showing f our different surface texture design and properties.

A set of design rules and machine control strategies were developed in order to help future texture design improvements to be done efficiently and accurately. Those rules determined the dimensional limits of the process in order to be able to reliably fabricate ceramic mold and cast them without any defects. Several process control models were developed in order to predict and control the dimensions of the mold and metal casting.

The printhead controller was investigated in details since it was the major source of error in the process. Sources of printing errors such as, induced charge, air drag and inter-drop electrostatic forces were analyzed, and printing control strategies were developed to counteract their effects. Induced charge between drops significantly affected the desired charge level of the drop being charged. Physical models and methods to measure and counteract the effect were proposed in this research. Air drag caused leading drops to merge and change the drop flight path in combination with electrostatic forces. Models based on the physics of the problem were used to understand and predict merging and stream position for different printing conditions.

It was found that physical models were not accurate enough. More accurate models, using simplified look up tables or on-line measurements, were also developed in order to improve drop placement and as a result the fabrication process accuracy to within ±10 to ±30 μm. The analysis of the printhead leads also to some printhead design recommendations which could improve printing accuracy and minimize secondary effects such as the ones mentioned above.

The work remaining to be done is to implement the various design rules into a CAD system in order to automate and simplify the design process of new textures. The machine

control strategy should be as well implemented in the 3D printing machine design and control software to assure accuracy and integrity with the CAD model. In other words, assure the "WYSIWYG" or What you see is what you get!.

Because of the various advantages of 3D printing over other surface texture processes, orthopaedic industry should benefit from the latest developments. Other industry will also benefit, since such low cost, reliable and accurate surface textures process can find other applications such as adhesive bonding, heat transfer, promoting fluid flow turbulence, and chemical reaction.

Appendix A: Orthopaedic Application

Appendix A1: 2D renderings of potential textures.

Design 1A

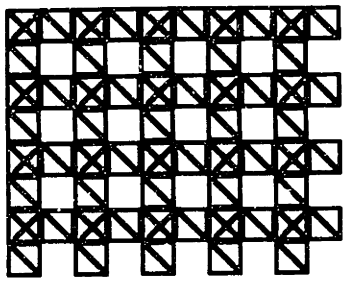

Design 1B

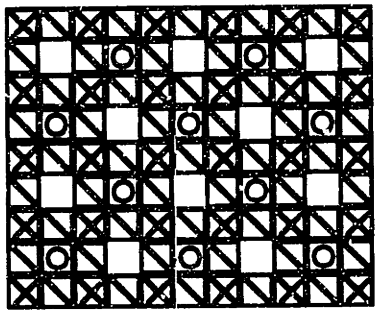

Design #4

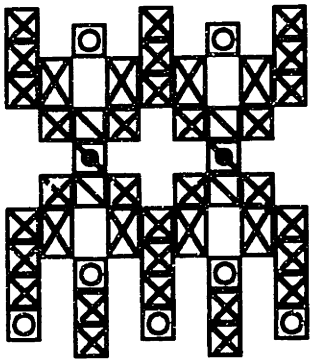

Design 2A

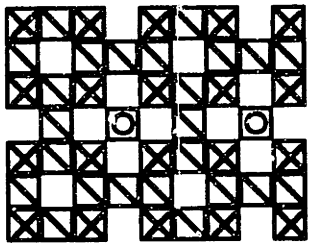

Design 3

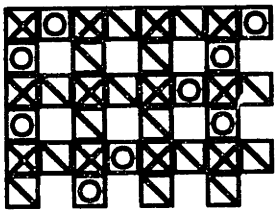

Design 2B

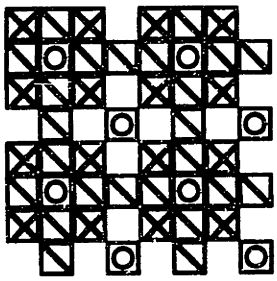

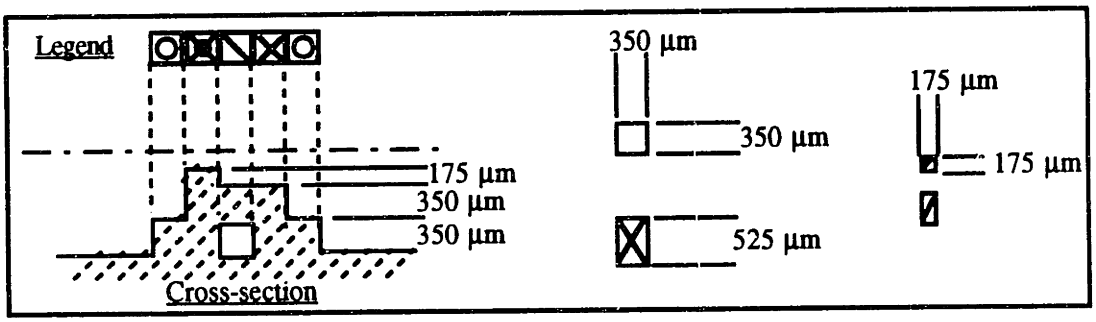

Appendix A1: 2D renderings of potential textures continued.

Design #5

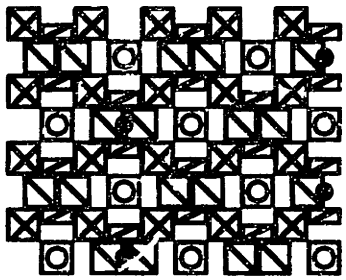

Design 6

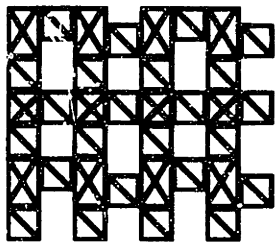

Design #7A

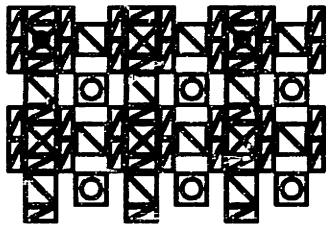

Design 8

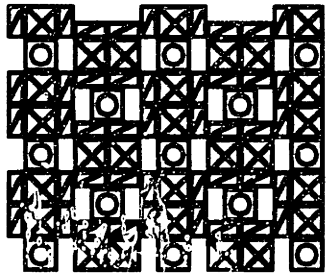

Design 9

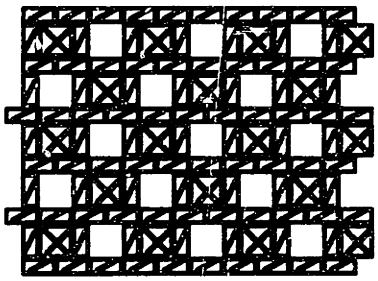

Design #10

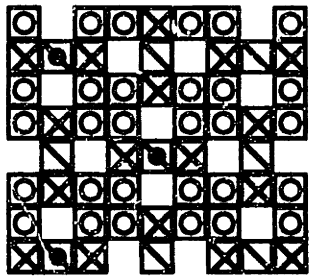

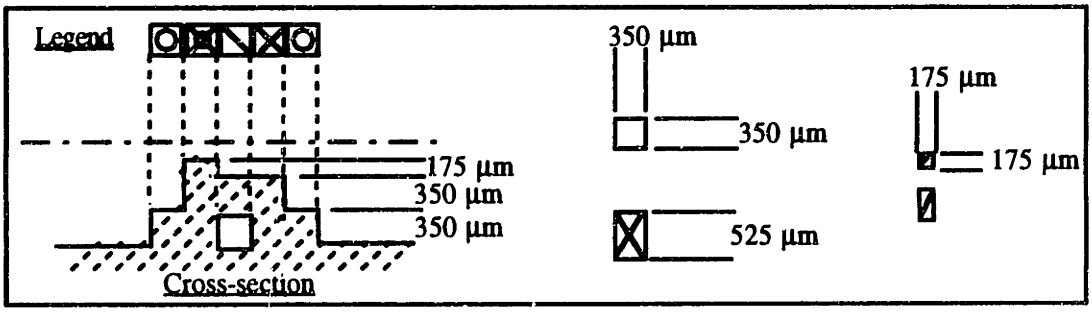

Appendix B: Casting

Appendix B1:Thermal conductivity of AL_2O_3 Alumina [W cm^{-1} K^{-1}]

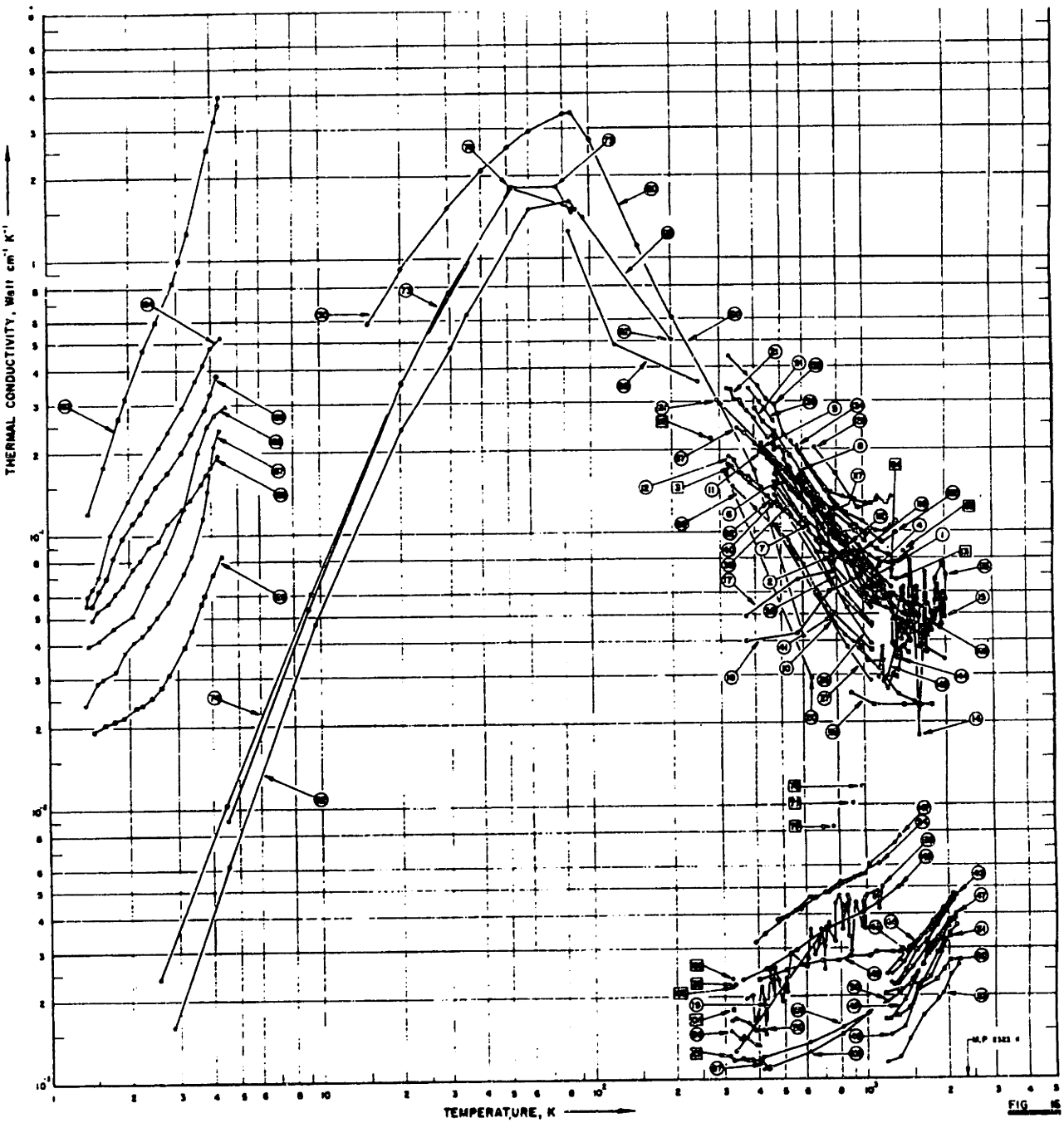

*3D printed mold material is similar to material in curves: 119, 147, 14

Appendix B2: Dog implant ASTM F75 casting experiment.

		Mold condition					Casting Conditions					
		A	B	C	D	E	1	2	3	4	5	Comments
Part #	Texture design # (layer 180 µm)	1 post-dip	2 post-dip	3 post-dip	1 post-dip + JJ prime coat*	1 post-dip + colloidal alumina**	Standard Cast 2800 F air (Exp. 3.1a)	Cast 2750 F air (Exp. 3.1b)	Cast 2800 F + protective atm. (Exp. 3.1c)	Cast 2750 F + protective atm. (Exp. 3.1d)	Cast 2700 F + protective atm. (Exp. 3.1e)	
11	4	x					o					good quality, oxyde
12	5	x						o				good quality, some oxyde
13	7a	x					o					good quality, oxyde
14	10	x						o				bad porous mold, oxyde
15	1	x										very few defects, oxyde
16	4		x				o					good quality, oxyde
17	5		x				o					good quality, oxyde
18	7a		x					o				good quality, oxyde
19	10		x				o					bad porous mold, oxyde
20	1		x					o				few defects, oxyde
21	4			x				o				good quality, oxyde
22	5			x				o				good quality, oxyde
23	7a			x			o					good quality, some oxyde
24	10			x				o				bad porous mold, oxyde
25	1			x				o				few defects, oxyde
26	4				x			o				defects, no oxyde
27	5				x			o				some defects, no oxyde
28	7a				x			o				some defect, no oxyde
29	10				x		o					bad porous mold, no oxyde
30	4					x	o					good quality, some oxyde
31	5					x	o					little defects, ceramic left, some oxyde
32	7a					x	o					good quality, some ceramic left, some oxyde
33	10					x	o					bad porous mold
44	4	x										lost
45	5	x									o	very few defects, some oxyde
46	7a	x									o	good quality, some oxyde
47	10	x								o		bad porous mold, no oxyde
48	1	x								o		few defects, no oxyde
49	4		x							o		good quality, no oxyde
50	5		x						o			few defects, no oxyde
51	7a		x						o			good quality, no oxyde
52	10		x									bad porous mold, oxyde
53	1		x								o	some defects, some oxyde

Appendix B2: Dog implant ASTM F75 casting experiment (continued).

Implant samples cont'd

		Mold condition					Casting Conditions					
		A	B	C	D	E	1	2	3	4	5	Comments
Part #	Texture design # (layer 180 µm)	1 post-dip	2 post-dip	3 post-dip	1 post-dip + JJ prime coat*	1 post-dip + colloidal alumina**	Standard Cast 2800 F air (Exp. 3.1a)	Cast 2750 F air (Exp. 3.1b)	Cast 2800 F + protective atm. (Exp. 3.1c)	Cast 2750 F + protective atm. (Exp. 3.1d)	Cast 2700 F + protective atm. (Exp. 3.1e)	
54	4			x								good quality, ceramic left, no oxyde
55	5			x								???
56	7a			x							o	good quality, some oxyde?
57	10			x							o	bad porous mold, some oxyde
58	1			x						o		defects, no oxyde
59	4				x					o?		incomplete, no oxyde
60	5				x							???
61	7a				x							???
62	10				x					o		bad porous mold, no oxyde
63	4					x				o		good quality, powder left, no oxyde
64	5					x					o	
65	7a					x					o	good quality, no oxyde
66	10					x				o		bad porous mold, no oxyde

Appendix B3: Cube & fin test sample ASTM F75 casting experiment.

Cubes

		Mold condition					Casting Conditions					
		A	B	C	D	E	1	2	3	4	5	Comments
Part #	Layer thickness [µm]	1 post-dip	2 post-dip	3 post-dip	1 post-dip + JJ prime coat*	1 post-dip + colloidal alumina**	Standard Cast 2800 F air	Cast 2750 F air	Cast 2800 F + protective atm.	Cast 2750 F + protective atm.	Cast 2700 F + protective atm.	
1	170	x					o					fin 1, cav. 1, Surface 2, oxyde on fin
2	180	x						o				fin 3, cav. 1, Surface 3, oxyde on fin
3	170		x					o				fin 1, cav. none, surface 2, oxyde on fin
4	180		x					o				fin 2, cav. 2, surface 1, oxyde on fin
5	170			x				o				fin 1, cav. 3, surface 2, oxyde on fin
6	180			x			o?	o				fin 3, cav. 3, surface 2, oxyde on fin
7	170				x							Lost
8	180				x		o					fin 4, cav. 2, surface 1, oxyde on fin
9	170					x	o					fin 2, cav. 3, surface 1, oxyde on fin
10	180					x	o					fin 2, cav. 4, surface 2, oxyde on fin
34	170	x									o	fin 1, cav. 1, surface 2, no oxyde
35	180	x									o	fin 2, cav. 1, surface 2, no oxyde
36	170		x								o	fin 1, cav. 2, surface 2, no oxyde
37	180		x							o		fin 2, cav. 2, surface 2, no oxyde
38	170			x						o		fin 2, cav. 2, surface 3, no oxyde
39	180			x						o?		fin 4, cav. 3, surface 1, no oxyde
40	170				x							Lost
41	180				x							Lost
42	170					x						Mold was damaged no fin, Lost
43	180					x						Mold was damaged no fin, smaller section

* JJ prime coat: JJPI prime coat diluted 1:5 in water, pH 8, [2 coats dipped 2 min. each and dried in between]

**Colloidal alumina: 2.5%vol. 0.7µm alumina & 2.5% vol. 50nm alumina , pH 4, [2 coats dipped 1 min., dried in between

Note:

Grade	fin	cavity	surface finish
1	no defects	clean	very smooth ≈ ± 15 µm
2	tiny defect	75% clean	smooth
3	few defects	50 % clean	medium ≈ ± 50 µm
4	damaged	25 % clean	medium rough ≈ 200 µm
5	almost inexistent	filled	rough >200 µm

Appendix B4: Cube mold & casting dimensional measurements

Casting part # [mm]	Layer thickness [μm]	Dimension A [mm]	Dimension B [mm]	Dimension C [mm]	Dimension D [mm]	
9	170	9.71	9.66	0.34	2.45	
36	170	9.76	9.84	0.33	2.46	sand blast
5	170	9.69	9.78	0.36	2.47	
1	170	9.7	9.72	0.37	2.45	sand blast
34	170	9.74	9.72	0.34	2.45	
3	170	9.69	9.76	0.34	2.46	
38	170	9.68	9.69	0.39		
		9.71	9.7385714	0.3528571	2.4566667	
		0.029	0.060	0.021	0.008	
4	180	9.72	9.76	0.34	2.35	sand b.
10	180	9.78	9.77	0.36	2.44	
2	180	9.77	9.75	0.39		
35	180	9.62	9.71	0.37	2.42	sand b.
37	180	9.7	9.75	0.39	2.49	
		9.718	9.748	0.37	2.425	
		0.064	0.023	0.021	0.058	
Mold dimension [mm]	Layer	Slow Axis	Fast Axis	Slow Axis	Z axis	
theory	170	9.775	9.4	0.325	2.52	
noise	170	0.0186	0.023	0.0193	0.03	
theory	180	[illegible].775	9.4	0.325	2.484	
noise	180	[illegible].0201	0.0258	0.0195	0.024	

Appendix B5: Cavity & protrusion mold measurements

170 μm
no mist #1

Cavity length [μm]	400	400	400	400	400	400	400	400	400
Offset [μm]	0	20	40	0	10	20	30	40	50
1	381	400	398	398	387	428	410	418	432
2	363	349	426	365	367	387	410	421	464
3	317	397	412	360	379	401	447	413	423
4	330	392	423	332	382	409	398	413	428
5	353	391	453	343	357	366	402	433	410
6	346	425	465	356	364	389	416	418	455
7	373	437	429	363	357	392	379	415	417
8	343	473	472	357	357	387	456	456	443
Cavity width [μm]	175	175	175	350	350	350	350	350	350
Offset [μm]	0	10	20	0	10	15	20	25	30
1	142	211	230	320	357	413	427	435	457
2	153	208	232	341	362	358	424	426	448
3	157	218	198	339	380	397	402	424	407

170 μm
no mist #1

Protrusion length [μm]	400	400	400	400	400	400	400	400	400
Offset [μm]	0	-20	-40	0	-10	-20	-30	-40	-50
1	409	376	347	447	425	403	378	359	436
2	386	366	347	450	438	437	447	390	442
3	437	380	324	486	479	463	418	421	408
4	413	378	390	444	482	485	423	430	448
5	435	394	349	468	493	484	447	455	448
6	420	427	327	509	498	438	452	434	425
7	446	353	314	473	487	444	438	431	449
8	432	369	343	522	493	484	444	454	406
Protrusion width [μm]	175	175	175	350	350	350	350	350	350
Offset [μm]	0	-10	-20	0	-10	-15	-20	-25	-30
1	228	238	236	379	373	355	367	346	358
2	221	210	221	384	369	356	340	375	350
3	237	211	200	364	366	381	328	358	338
4	222	229	208	372	358	339	349	351	346
5	233	247	220	403	385	365	361	353	369
6									
7									
8									

Appendix B5: Cavity & protrusion mold measurements

170 μm
mist #2

Cavity length [μm]	**400**	**400**	**400**	**400**	**400**	**400**	**400**	**400**	**400**
Offset [μm]	**0**	**20**	**40**	**0**	**10**	**20**	**30**	**40**	**50**
1	324	416	491	305	382	396	403	440	426
2	349	393	453	334	388	412	408	410	466
3	359	442	431	339	376	403	387	432	496
4	321	410	424	356	373	438	427	457	424
5	344	426	449	367	359	364	402	442	444
6	359	402	447	372	379	394	416	445	428
7	349	420	426	363	373	400	401	434	409
8	353	416	475	398	364	387	462	512	478
Cavity width [μm]	**175**	**175**	**175**	**350**	**350**	**350**	**350**	**350**	**350**
Offset [μm]	**0**	**10**	**20**	**0**	**10**	**15**	**20**	**25**	**30**
1	141	193	221	309	355	362	377	393	429
2	151	192	229	336	362	365	381	395	412
3	153	210	227	327	348	353	382	404	422
4	148	186	217	355	377	359	385	397	438
5	151	184	213	347	342	362	356	362	410

170 μm
mist #2

Protrusion length [μm]	**400**	**400**	**400**	**400**	**400**	**400**	**400**	**400**	**400**
Offset [μm]	**0**	**-20**	**-40**	**0**	**-10**	**-20**	**-30**	**-40**	**-50**
1	380	399	389	478	480	447	450	472	450
2	411	395	399	476	464	444	450	465	427
3	409	378	365	463	470	467	452	468	399
4	396	361	397	490	471	444	462	453	416
5	432	378	344	431	467	467	458	441	442
6	412	388	358	485	481	447	449	449	450
7	454	378	359	494	481	490	454	445	439
8	434	371	390	495	495	475	457	423	430
Protrusion width [μm]	**175**	**175**	**175**	**350**	**350**	**350**	**350**	**350**	**350**
Offset [μm]	**0**	**-10**	**-20**	**0**	**-10**	**-15**	**-20**	**-25**	**-30**
1	204	204	203	392	369	350	339	334	341
2	220	213	233	296	389	350	359	379	360
3	226	227	212	370	357	372	343	343	327
4	222	219	200	397	363	375	340	379	340
5	244	211	220	400	394	363	357	358	353
6	223	231	229	388	367	359	388	358	355

Appendix B5: Cavity & protrusion mold measurements (continued)

170 μm
no mist #3

Cavity length [μm]	**400**	**400**	**400**	**400**	**400**	**400**	**400**	**400**	**400**
Offset [μm]	**0**	**20**	**40**	**0**	**10**	**20**	**30**	**40**	**50**
1	318	408	404	329	327	400	381	427	427
2	327	380	434	312	333	405	396	391	456
3	341	405	370	369	342	366	394	424	413
4	348	374	437	367	352	410	394	422	422
5	357	410	472	338	362	387	377	453	422
6	349	391	456	310	355	366	370	394	413
7	359	394	407	362	332	380	364	409	437
8	319	411	449	309	416	363	422	414	455
Cavity width [μm]	**175**	**175**	**175**	**350**	**350**	**350**	**350**	**350**	**350**
Offset [μm]	**0**	**10**	**20**	**0**	**10**	**15**	**20**	**25**	**30**
1	111	199	205	349	336	362	377	405	418
2	131	184	204	344	321	350	373	394	423
3	130	186	208	318	372	374	369	377	410
4	159	195	217	322	241	386	359	453	399
5									

170 μm
no mist #3

Protrusion length [μm]	**400**	**400**	**400**	**400**	**400**	**400**	**400**	**400**	**400**
Offset [μm]	**0**	**-20**	**-40**	**0**	**-10**	**-20**	**-30**	**-40**	**-50**
1	439	368	354	525	502	478	480	454	424
2	443	436	352	497	503	472	406	443	397
3	397	360	352	505	485	466	443	422	406
4	393	409	376	504	488	472	443	429	414
5	409	396	347	489	476	478	435	446	385
6	412	373	381	503	489	478	424	432	400
7	391	376	371	491	491	447	428	416	408
8	442	402	369	503	485	462	435	427	406
Protrusion width [μm]	**175**	**175**	**175**	**350**	**350**	**350**	**350**	**350**	**350**
Offset [μm]	**0**	**-10**	**-20**	**0**	**-10**	**-15**	**-20**	**-25**	**-30**
1	226	211	219	400	388	378	359	344	326
2	230	229	206	373	386	366	344	352	337
3	221	212	209	383	386	370	358	361	335
4	226	231	215	398	369	374	373	359	335
5	237	236	223	403	373	379	355	357	346
6	257	228	221	394	384	371	361	366	341

Appendix B5: Cavity & protrusion mold measurements (continued)

180 μm
no mist #4

Cavity length [μm]	400	400	400	400	400	400	400	400	400
Offset [μm]	0	20	40	0	10	20	30	40	50
1	291	364	439	365	341	365	370	414	409
2	339	401	453	364	364	382	363	389	427
3	321	374	447	333	358	389	383	383	416
4	355	395	411	353	385	388	365	419	398
5	347	430	427	354	362	383	358	393	435
6	288	380	413	361	368	382	356	416	421
7	332	409	443	378	345	362	391	415	427
8	372	414	444	377	342	360	391	397	444
Cavity width [μm]	175	175	175	350	350	350	350	350	350
Offset [μm]	0	10	20	0	10	15	20	25	30
1	157	201	201	353	346	345	350	386	393
2	158	186	228	338	330	350	381	384	423
3	181	196	233	341	323	326	382	400	405
4	178	177	232	333	348	375	377	395	405
5	161	168	229	340	348	375	402	404	421
8									

180 μm
no mist #4

Protrusion length [μm]	400	400	400	400	400	400	400	400	400
Offset [μm]	0	-20	-40	0	-10	-20	-30	-40	-50
1	449	411	392	508	440	400	416	389	380
2	436	397	410	465	436	435	403	400	348
3	438	400	377	438	462	406	393	409	358
4	410	404	322	455	479	418	394	397	383
5	427	411	374	473	471	407	405	379	366
6	408	387	355	495	457	426	389	389	364
7	403	425	384	490	493	412	367	347	357
8	394	432	366	499	477	432	369	400	356
Protrusion width [μm]	175	175	175	350	350	350	350	350	350
Offset [μm]	0	-10	-20	0	-10	-15	-20	-25	-30
1	213	192	191	369	337	356	340	325	316
2	210	202	200	361	343	335	361	338	337
3	241	214	209	369	378	330	359	322	318
4	236	197	215	390	368	338	339	345	326
5	233	221	218	381	370	350	341	347	330
8									

Appendix B5: Cavity & protrusion dimensions statistics

Cavity length [μm]		
Offset [μm]	Mean	Standard dev.
0	341.5	21.6
20	404.0	24.2
40	436.9	25.4
0	352.8	23.5
10	363.4	19.1
20	388.8	19.2
30	396.8	26.8
40	422.5	25.2
50	433.3	21.9
Cavity width [μm]		
Offset [μm]	Mean	Standard dev.
0	150.7	16.9
10	193.8	13.1
20	219.1	12.1
0	336.0	12.9
10	344.0	31.6
15	365.4	20.4
20	382.6	21.1
25	402.0	22.1
30	418.8	17.0
Protrusion length [μm]		
Offset [μm]	Mean	Standard dev.
0	418.7	20.4
-20	389.9	21.8
-40	363.3	24.1
0	482.8	24.1
-10	476.2	19.6
-20	450.3	27.1
-30	428.4	29.0
-40	424.0	31.1
-50	408.3	31.8
Protrusion width [μm]		
Offset [μm]	Mean	Standard dev.
0	227.7	11.8
-10	218.8	14.1
-20	214.0	11.5
0	380.3	23.0
-10	371.5	14.5
-15	359.6	15.1
-20	352.8	13.9
-25	352.3	15.2
-30	340.2	13.7

Appendix B5: Mold cavity dimension along the Z axis.

Z-axis

Cavity width [μm]	340	360
Layer thickness [μm]	170	180
	280	325
	314	305
	298	297
	295	311
	280	313
	278	317
	292	304
	277	318
	279	304
	277	340
	341	340
	329	340
	341	350
	367	366
	289	325
	297	
	299	
	297	
	305	
	282	
	308	
	280	
	317	
	266	
	297	
	331	
	367	
	353	
	363	
	313	
	357	

	average	Standard dev.	Offset
170 μm	308.7	30.27	201.3
180 μm	323.7	19.77	216.3

Appendix B6: Texture design #5 Mold cavity dimensions.

Expected [µm]	760	695	380	345
	A	B	C	D
1	1.2	1.1	0.4	0.5
	1.1	1	0.4	0.4
	1.1	1	0.5	0.45
	1.15	1	0.35	0.4
	1.1	1.05	0.4	0.35
	1.1	1.05	0.47	0.4
	1.1	1.05	0.5	0.4
	1.15	0.95	0.4	0.5
	1.1	0.9	0.5	0.45
	1.1	1	0.5	0.4
	1.15	1	0.6	0.5
	1.122727273	1.009090909	0.456363636	0.431818182
	0.034377583	0.053935989	0.07242551	0.051345532
Scaled average	0.741	0.666	0.301	0.285
Scaled deviation	0.023	0.036	0.048	0.034
Scale factor	30mm=>2mm			

Appendix B7: Cast texture design #4 & #5 pore dimensions

Design #4 casting: Top surface pore dimensions

Stats [mm]	Pore area [mm2]	Max.Dia.	Min.Dia.	Ave.Dia.
Minimum	0.332	0.853	0.35	0.577
Maximum	0.813	2.204	2.204	2.204
Range	0.481	1.351	1.855	1.628
Mean	0.573	1.411	0.891	1.122
Std.Dev	0.166	0.47	0.67	0.558
Sum	11.462	28.226	17.82	22.439
Samples	20	20	20	20

Design #4 casting: Bottom surface pore dimensions

Stats [mm]	Pore area [mm2]	Max.Dia.	Min.Dia.	Ave.Dia.
Minimum	0.064	0.389	0.249	0.337
Maximum	0.128	0.541	0.33	0.386
Range	0.064	0.152	0.081	0.049
Mean	0.102	0.436	0.296	0.36
Std.Dev	0.016	0.046	0.023	0.016
Sum	1.019	4.359	2.963	3.601
Samples	10	10	10	10

Design #5 casting: Top surface pore dimensions

Stats	Pore area [mm2]	Max.Dia. [mm]	Min.Dia. [mm]	Ave.Dia. [mm]
Minimum	0.169	0.556	0.331	0.456
Maximum	0.303	0.709	0.543	0.603
Range	0.134	0.153	0.212	0.147
Mean	0.231	0.644	0.423	0.526
Std.Dev	0.032	0.033	0.046	0.035
Samples	40	40	40	40

Design #5 casting: Bottom surface pore dimensions

Stats [mm]	Pore area [mm2]	Max.Dia. [mm]	Min.Dia. [mm]	Ave.Dia. [mm]
Minimum	0.057	0.32	0.205	0.288
Maximum	0.128	0.599	0.333	0.396
Range	0.072	0.279	0.128	0.108
Mean	0.093	0.43	0.251	0.335
Std.Dev	0.025	0.083	0.039	0.042
Sum	1.025	4.726	2.764	3.686
Samples	11	11	11	11

Appendix B7: Cast texture design #7 & #10 pore dimensions

Design #7 casting: Top surface pore dimensions

Stats [mm]	Pore area [mm2]	Max.Dia. [mm]	Min.Dia. [mm]	Ave.Dia. [mm]
Minimum	0.175	0.605	0.419	0.536
Maximum	0.448	0.954	0.651	0.733
Range	0.273	0.349	0.232	0.197
Mean	0.311	0.737	0.521	0.617
Std.Dev	0.057	0.082	0.054	0.053
Samples	37	37	37	37

Design #7 casting: Bottom surface pore dimensions

Stats	Pore area [mm2]	Max.Dia.	Min.Dia.	Ave.Dia.
Minimum	0.104	0.592	0.106	0.359
Maximum	0.153	0.663	0.26	0.45
Range	0.05	0.071	0.153	0.09
Mean	0.126	0.617	0.173	0.422
Std.Dev	0.018	0.027	0.053	0.029
Sum	0.88	4.316	1.214	2.953
Samples	7	7	7	7

Design #10 casting: Top surface pore dimensions

Stats [mm]	Pore area [mm2]	Max.Dia.	Min.Dia.	Ave.Dia.
Minimum	0.336	0.741	0.533	0.633
Maximum	0.569	0.994	0.809	0.836
Range	0.234	0.253	0.276	0.202
Mean	0.447	0.883	0.619	0.737
Std.Dev	0.054	0.065	0.061	0.047
Sum	15.188	30.037	21.037	25.062
Samples	34	34	34	34

Design #10 casting: Bottom surface pore dimensions

Stats	Pore area [mm2]	Max.Dia.	Min.Dia.	Ave.Dia.
Minimum	0.098	0.389	0.267	0.339
Maximum	0.126	0.537	0.537	0.537
Range	0.029	0.148	0.27	0.198
Mean	0.114	0.456	0.354	0.404
Std.Dev	0.013	0.054	0.108	0.079
Sum	0.455	1.826	1.417	1.616
Samples	4	4	4	4

Appendix C: Printhead

Appendix C1: Printhead controller schematics

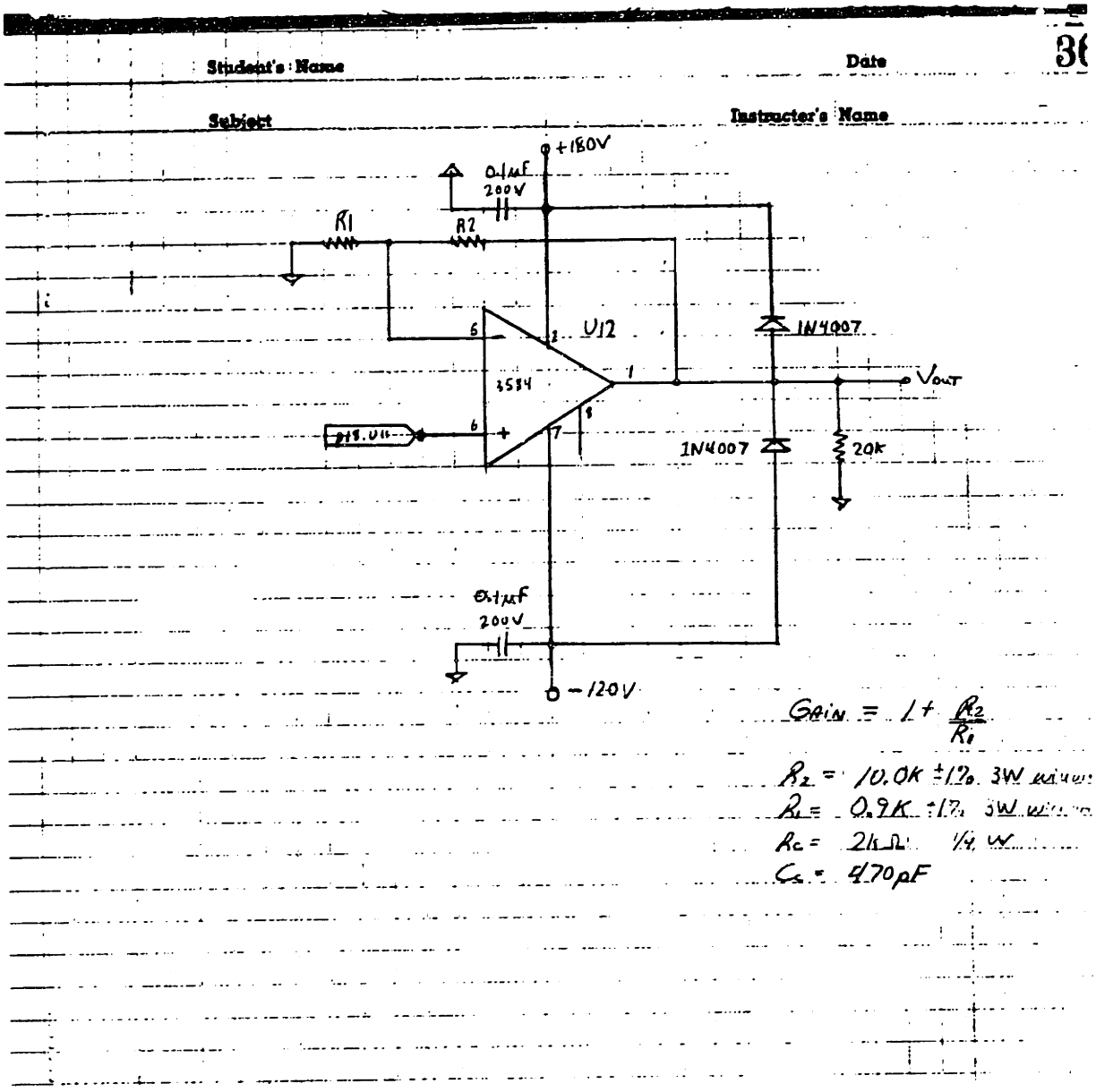

Appendix C1: Printhead controller schematics (continued)

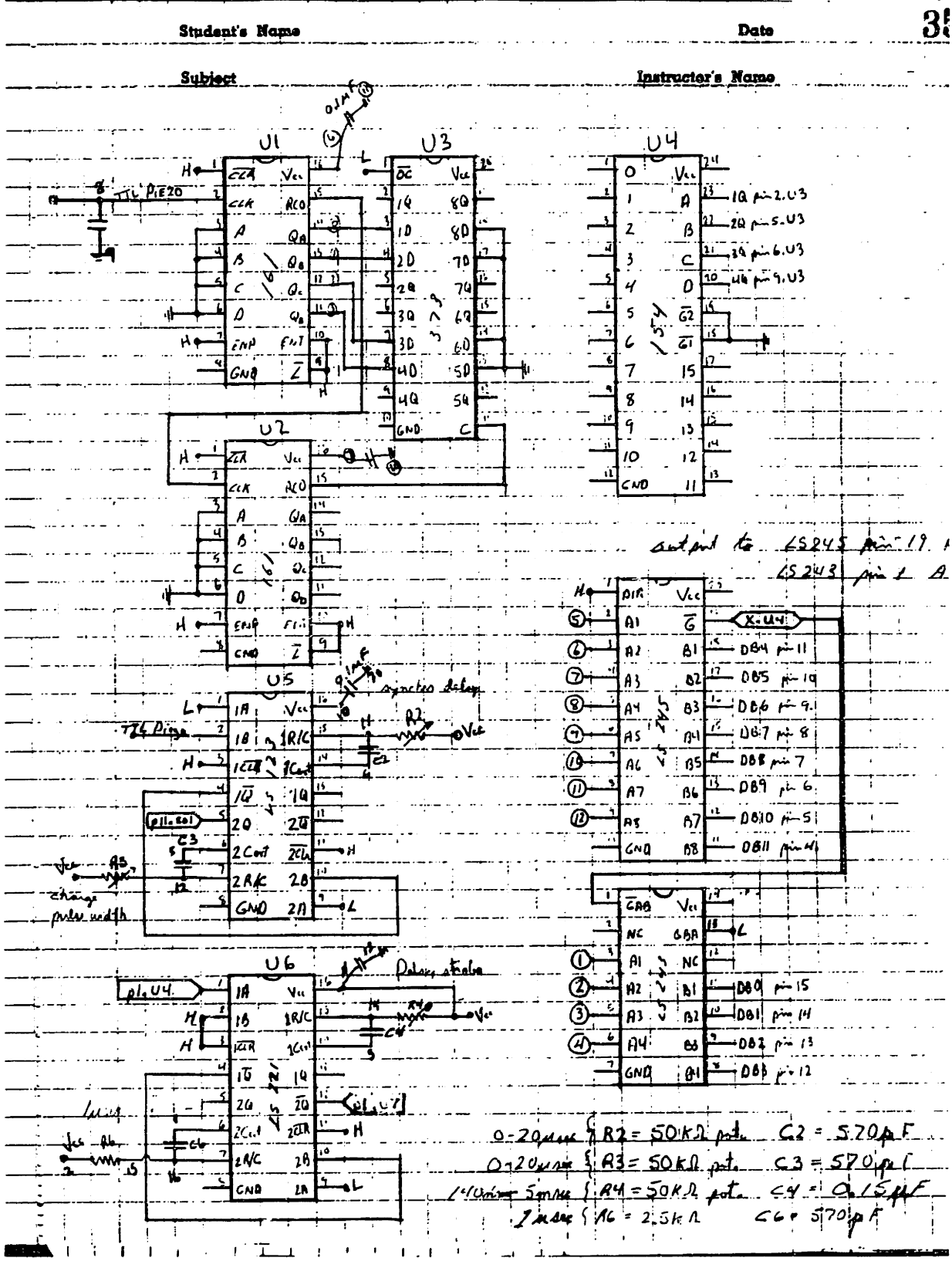

Appendix C1: Printhead controller schematics (continued)

Student's Name | Date | 3(

Subject | Instructor's Name

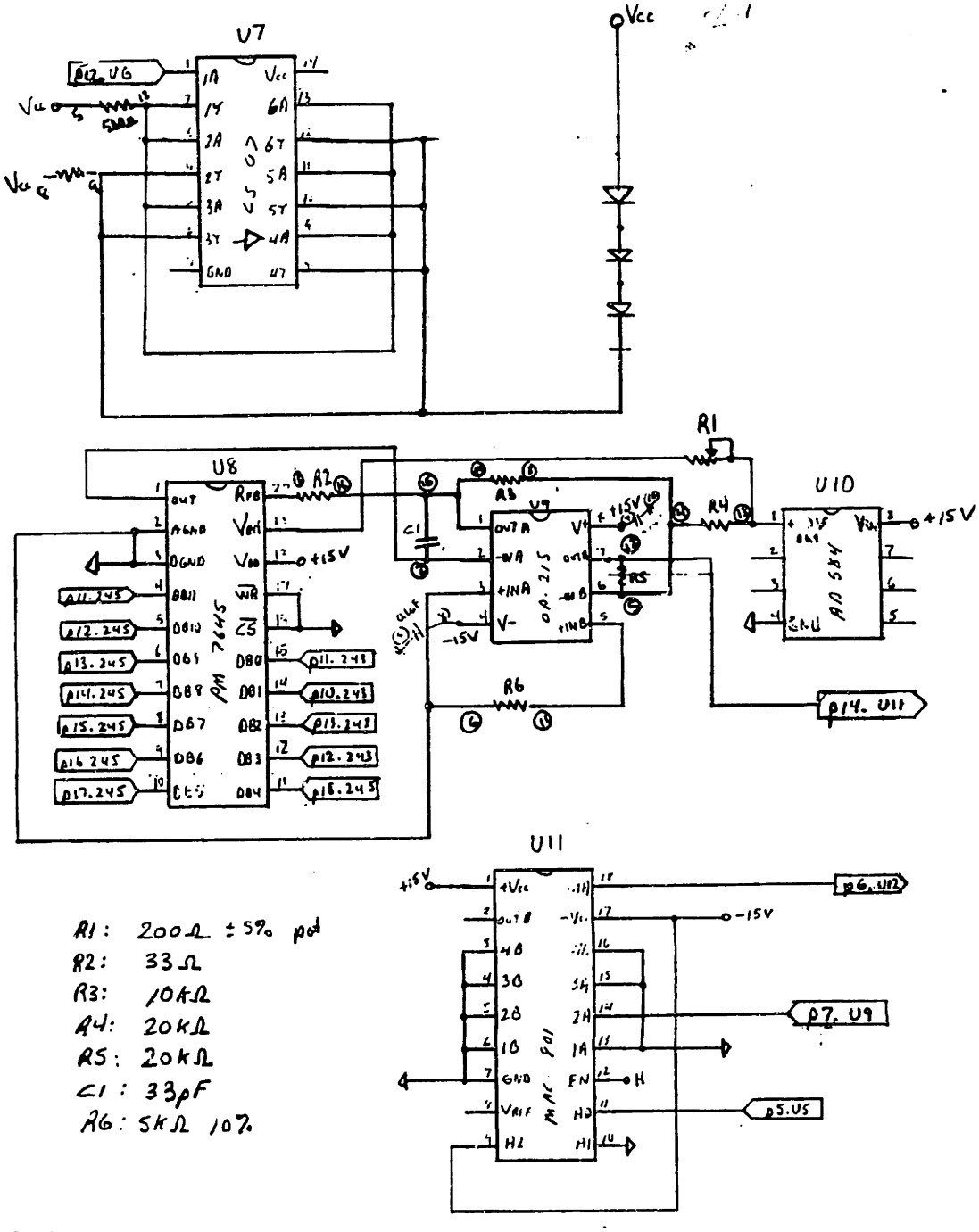

R1: 200Ω ± 5% pot
R2: 33Ω
R3: 10kΩ
R4: 20kΩ
R5: 20kΩ
C1: 33pF
R6: 5kΩ 1%

Appendix C2: Charging electrode capacitance for a sphere between two plates.

Electric field around a point charge

$$E = \frac{1}{4\pi\varepsilon_0}\frac{q\,dr}{r^2}$$

Distance from the point charge

$$r = nw_c - x$$

Electric field from one point charge image n

$$E_n = \frac{q}{4\pi\varepsilon_0(nw_c - x)^2}$$

Electric field from all the image point charge

$$E = \sum_{n=-\infty}^{\infty} \frac{(-1)^{n+1} q}{4\pi\varepsilon_0(nw_c - x)^2}$$

Potential between a sphere of diameter d and charging electrode of width w_c

$$V_{12} = \int_{\frac{1}{2}}^{w_c - \frac{1}{2}} E\,dx = \frac{q}{2\pi\varepsilon_0}\sum_{n=-\infty}^{\infty}(-1)^{n+1}\frac{(w_c - d)}{w_c(2n-1)(2nw_c - d)}$$

Capacitance of a sphere centered between two plates

$$C_{12} = \frac{q}{V_c} = \frac{2\pi\varepsilon_0}{\sum_{n=-\infty}^{\infty}(-1)^{n+1}\frac{(w_c - d)}{w_c(2n-1)(2nw_c - d)}}$$

Appendix C3: Charging electrode cube model.

Multiple Terminals and mutual capacitance
Drop Charging in ink jet printers (taken from reference [69])

The geometry in an actual ink jet printer is fairly complex, involving the charging electrode, roughly spherical drops undergoing oscillations, and the disturbed jet connected by a thin ligament to the forming drop. To illustrate the method, we drastically simplify the geometry to the form shown in figure C3.1 and neglect fringing fields. Just at the point of drop breakoff, there are four charge-carrying electrodes in the system. These are the drop which is just forming, identified by the subscript d, the previous drop p, the jet j, and the charging electrode e, which consist of an upper and lower part. The two drops are modeled as cubes, and the remaining electrodes are assumed to have the corresponding rectangular shapes shown in the figure.

The charge on the forming drop is the primary concern here. It is given by Gauss' law as

$$q_d = \oint_{A_d} D \bullet dA \qquad \text{(C3-1)}$$

The electric fields at the surface of this drop depend on the potentials of the neighboring electrodes as shown in figure C3.2, where s is the drop separation and c is the distance to the charging electrode. These fields are directed as shown in the figure and have the magnitudes

$$E_c = \frac{v_d - v_e}{c} \qquad \text{(C3-2)}$$

$$E_p = \frac{v_d - v_p}{s} \qquad \text{(C3-3)}$$

$$E_j = \frac{v_d - v_j}{s} \qquad \text{(C3-4)}$$

Using these fields in Gauss' law gives the net charge on the drop as

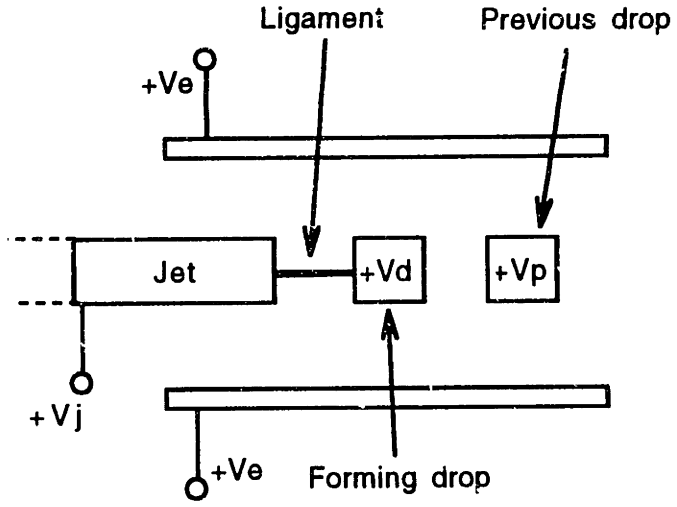

Figure C3.1: Simplified charging geometry for ink drop.

$$q_d = \frac{2\varepsilon d^2(v_d - v_e)}{c} + \frac{\varepsilon d^2(v_d - v_p)}{s} + \frac{\varepsilon d^2(v_d - v_j)}{s} \qquad \text{(C3-5)}$$

which has the form

$$q_d = C_{dd}v_d + C_{dp}v_p + C_{de}v_e + C_{dj}v_j \qquad \text{(C3-6)}$$

Just at the point of breakoff, the jet and the new drop are connected by a conducting ligament, so they will be at the same voltage. Since we are allowed to pick one voltage level as reference, the work that follows is simplified by assuming that the jet and the forming drop are both at the reference level (i.e. ground).

$$v_j = v_d = 0 \qquad \text{(C3-7)}$$

This simplifies the charge expression for the drop to

$$q_d = C_{de}v_e + C_{dp}v_p \qquad \text{(C3-7)}$$

As anticipated, the charge on the drop depends on the charging voltage, but also on the voltage on the previously formed drop.

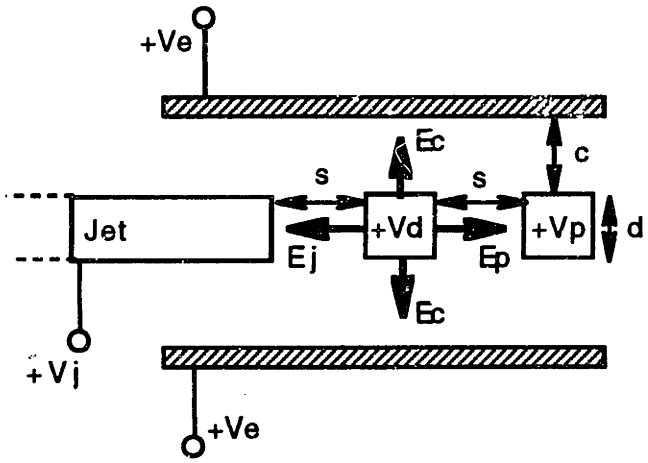

Figure C3.2: Electric fields around the charging drop.

This voltage Vp is not known in advance. Rather, the charge on the previous drop has been fixed, so we have to convert this charge into the corresponding voltage. This can be done with the terminal relation for the previous drop, which is found in the same manner by integrating Gauss' law over the drop surface. After integrating and using the same voltage constraints on the jet and new drop, the charge on the previously formed drop is given by

$$q_p = \frac{2\varepsilon d^2(v_p - v_e)}{c} + \frac{\varepsilon d^2(v_p - v_d)}{s} \qquad \text{(C3-9)}$$

or, in terms of the capacitance coefficients and the known charge,

$$q_p = C_{pp}v_p + C_{pe}v_e \qquad \text{(C3-10)}$$

when Vd = 0 as before. Solving this equation for Vp and substituting into the charge expression for the new drop gives the charge on the new drop as

$$q_d = C_{de}\left(1 - \frac{C_{pe}C_{dp}}{C_{de}C_{pp}}\right)v_e + \frac{C_{dp}}{C_{pp}}q_p \qquad \text{(C3-11)}$$

$$q_d = -\frac{4\varepsilon d^2}{c}\left(\frac{s+c}{2s+c}\right)v_e - \frac{c}{2s+c}q_p$$

As expected, this charge depends on both the charging voltage and the charge on the previous drop. To charge the new drop accurately, the charging voltage must be controlled to account for the disturbance introduced by the previous drop.

Appendix C4: The image of a point charge on a conducting sphere. (from references 69 & 73)

The image charge is not necessarily equal and opposite to the true charge. For example, consider the case of a point charge q at a point P outside a conducting sphere of radius r, as shown in figure. C4.1.

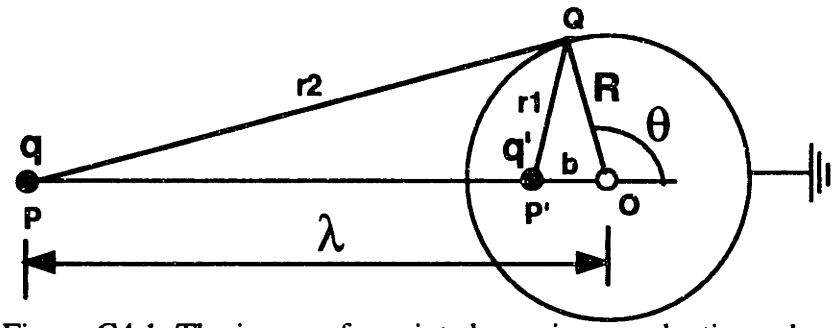

Figure C4.1: The image of a point charge in a conducting sphere

By symmetry, the image charge must lie on the line joining the center of the sphere and the point charge. Let the value of the image charge be q' and its position be defined by the point P'. The potential at point Q on the surface of the sphere is then

$$V = \frac{1}{4\pi\varepsilon_0\varepsilon_r}\left(\frac{q'}{r_1} + \frac{q}{r_2}\right)$$

$$V = \frac{1}{4\pi\varepsilon_0\varepsilon_r}\left(\frac{q'}{\left(R^2 + b^2 + 2\,R\,b\,\cos\theta\right)^{1/2}} + \frac{q}{\left(R^2 + \lambda^2 + 2\,R\,\lambda\,\cos\theta\right)^{1/2}}\right) \quad \text{(C4-1)}$$

It is only possible to make V=0 over the whole surface of the sphere if the functions in the denominators are similar functions of θ. Therefore b must be chosen so that

$$\frac{b}{R} = \frac{R}{\lambda} \quad \text{(C4-2)}$$

When P and P' are related by these distances, they are called the inverse points of the sphere. It can be seen that the triangles POQ and P'OQ have a common angle. From equation (C4-2), the adjacent sides of these triangles are similar and it follows that

$$\frac{b}{R} = \frac{R}{\lambda} = \frac{r_1}{r_2} \quad \text{(C4-3)}$$

Appendix C4: The image of a point charge on a conducting sphere. (continued)

The potential at Q due to point charges at P and P' is

$$V = \frac{q + \left(\lambda/R\right)q'}{4\pi\varepsilon_0\varepsilon_r\left(R^2 + \lambda^2 + 2R\,\lambda\,\cos\theta\right)^{1/2}} \qquad \text{(C4-4)}$$

This will be zero if we make

$$q' = \frac{R}{\lambda}q \qquad \text{(C4-5)}$$

Therefore the image of a charge q in an earthed conducting sphere is a charge $-\frac{R}{\lambda}q$ at the inverse point in the sphere.

If the sphere is an isolated conducting sphere and initially uncharged, its total charge must remain zero. In this case there must be a second charge -q', at a position such that the surface remains an equipotential, i.e. -q' must be at the center of the sphere.

Appendix C5: Calculating ideal electrode geometry.

The determination of the desired surface profile is facilitated by means of the curves obtained by Stoerk of which the $\psi = \pi/2$ and $\psi = 2\pi/3$ curves are plotted in Fig. C5.1a.

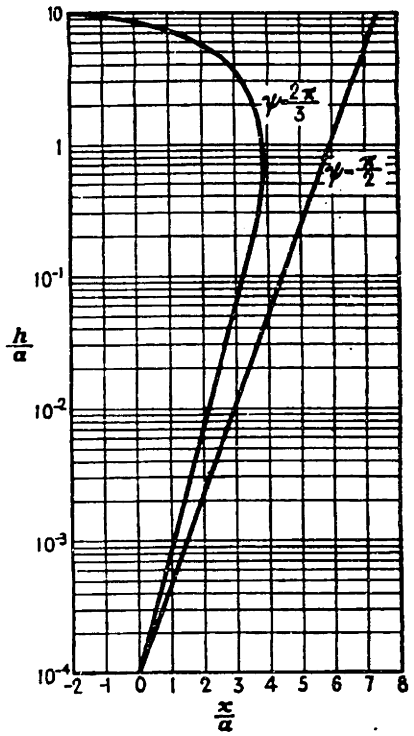

FIG. 7.23.—Construction data for Rogowski type electrodes: $x = \frac{a}{\pi}(\phi + e^{\phi}\cos\psi)$; $y = \frac{a}{\pi}(\psi + e^{\phi}\sin\psi)$; $h = y - a$.

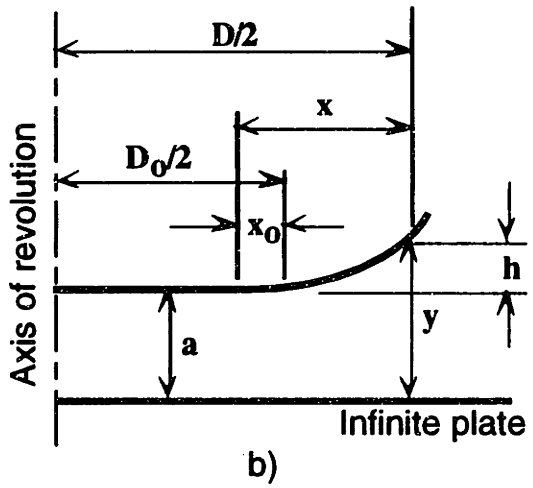

Figure C5.1: a) Construction data for rogowski type electrodes.b) Electrode cross section layout.

$$x = \frac{a}{\pi}\left(\phi + \varepsilon^{\phi}\cos\varphi\right);\quad y = \frac{a}{\pi}\left(\phi + \varepsilon^{\phi}\sin\varphi\right);\quad h = y - a$$

In these equation, ψ represents equipotential surfaces and ϕ lines of force, both of which may take on various constant values, and x and y are the coordinates. In figure C5.1b, a is the gap between the infinite plane and the finite plane electrode, the x = coordinates is in the direction of the infinite plane, and h is the elevation of the curved portion of the finite plane above its plane portion, as in Fig. Cxb. The diameter of the revolved section D, and D_0 is the diameter of the plane portion. In using the data of Fig. C5.1a, consider the following example for a $\psi = \pi/2$ surface: Assume a separation of

Appendix C5: Calculating ideal electrode geometry. (continued)

electrode and infinite plane a = 5 mm., Fig. C5.1b, and a diameter D_o of 50 mm. for the plane portion of the electrode surface. To determine a point on the curved portion of the electrode, assume an initial value of h = 10^{-1} mm., or h/a = 0.2 x 10^{-1}, as the least value that is practical, for which case $\psi = \pi/2$ (Fig. C5.1a) gives x_o/a = 3.4 and x_o = 17 mm. Let this value correspond to the diameter D_o , that is, to the point from which all values of x are measured. This reference point is $D_o/2 - x_o$ distant from the axis of rotation. For another point h=2.5, h/a = 0.5 , x/a is 5.43, or x = 27.15. The diameter corresponding to this value is

$$D = D_0 + 2(x - x_0), \quad \text{or} \quad 50 + 2(27.5 - 17) = 70.3 \text{ mm.}$$

Other points for the profile of the electrode are found in a similar way. In use a second identical electrode is placed at a distance 2a from the first.

Appendix C6: Tail end effect simulations for Q=1.0 and 1.4 ml/min

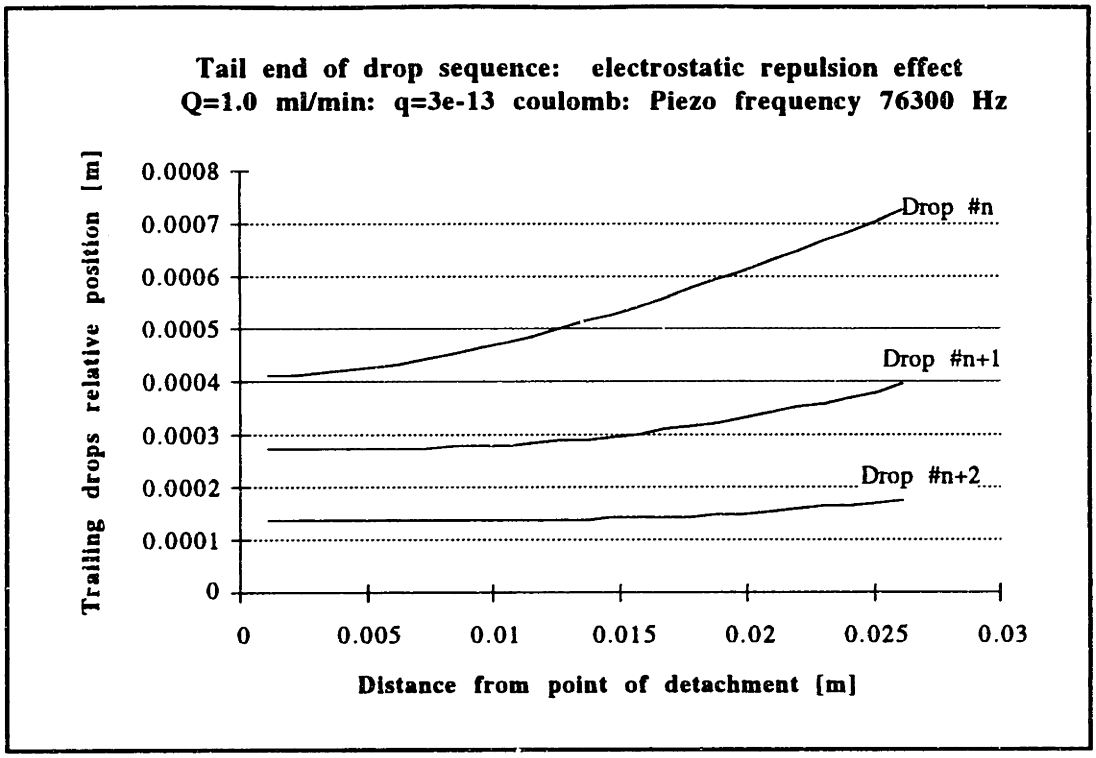

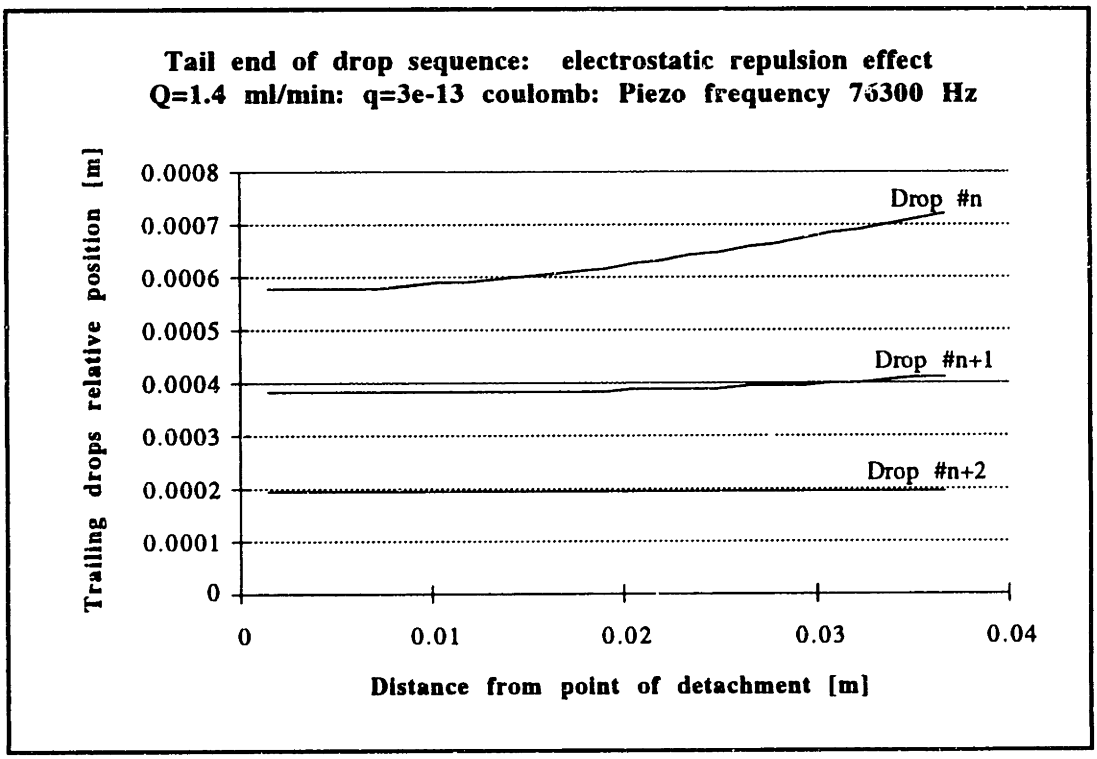

Appendix C7: Merge distance from point of detachment (MODEL) for Re=50 & 64

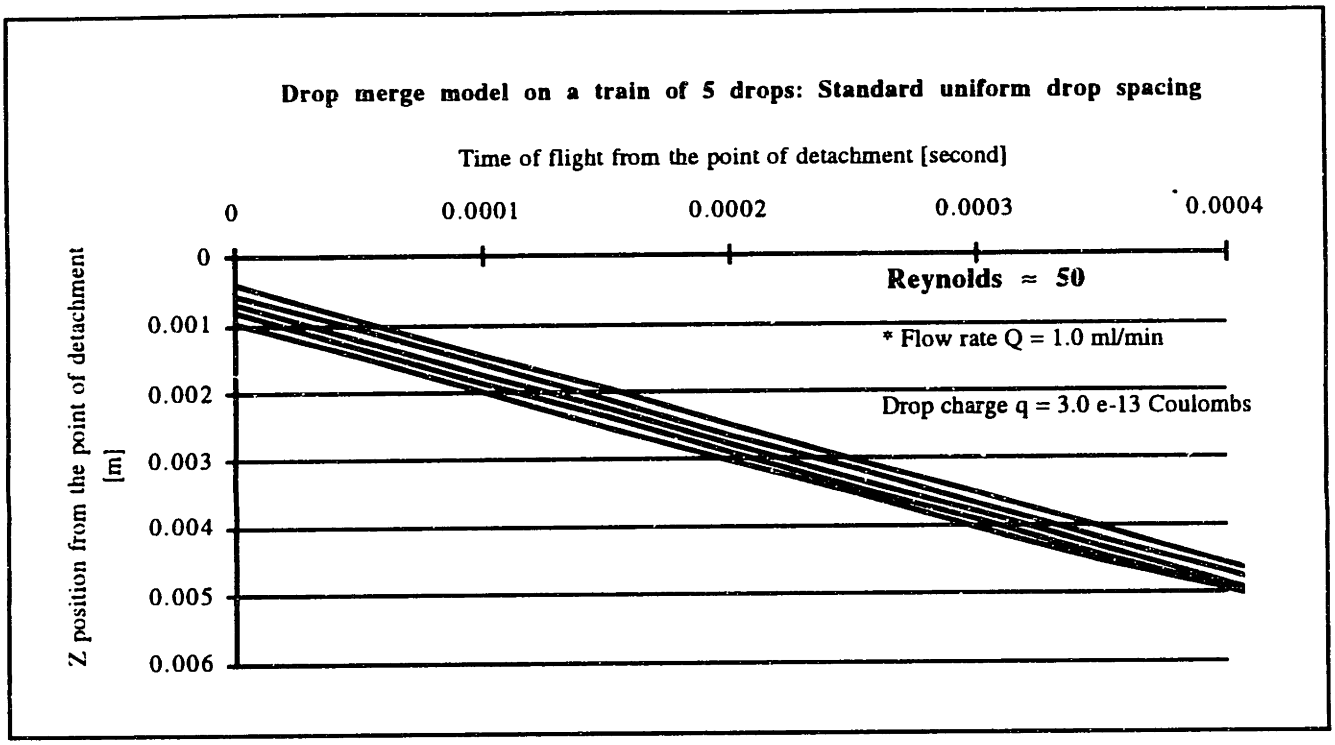

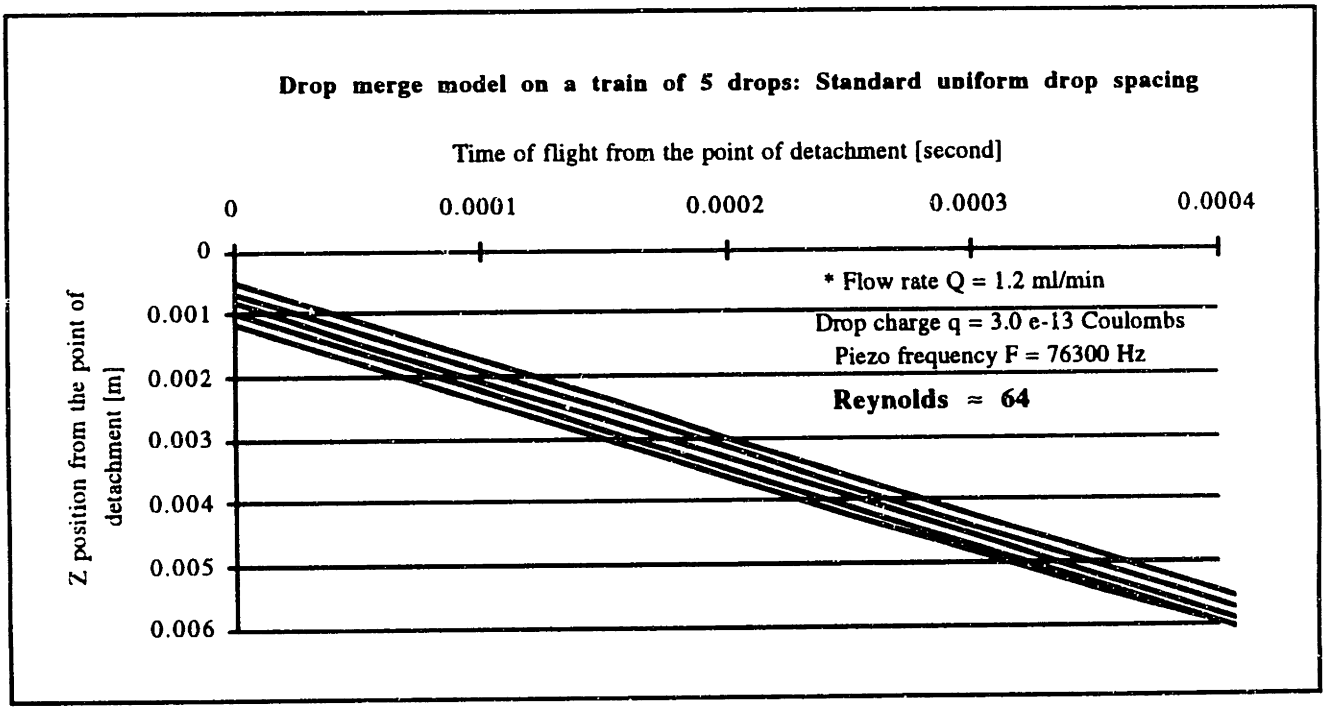

Appendix C7: Merge distance from point of detachment (MODEL) for Re= 80 (continued)

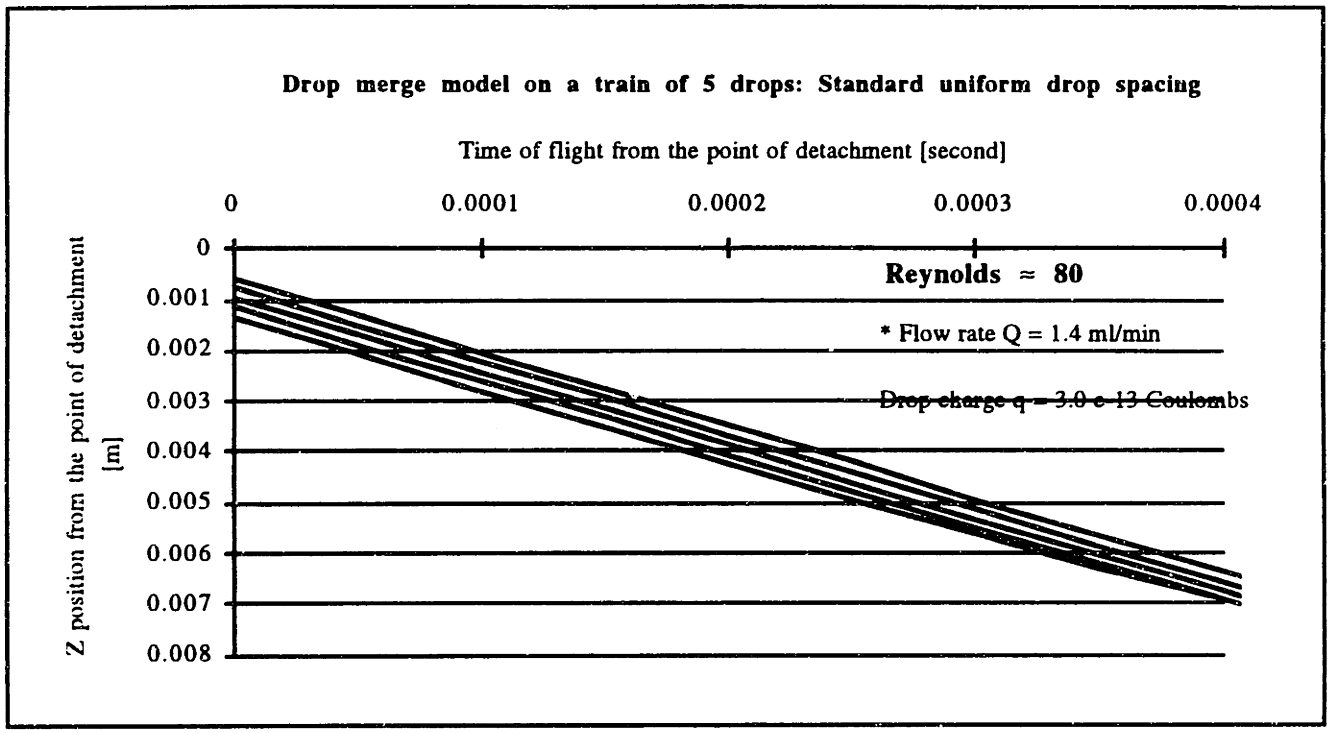

Appendix C8: Merge distance from point of detachment (MODEL) Different printing strategy

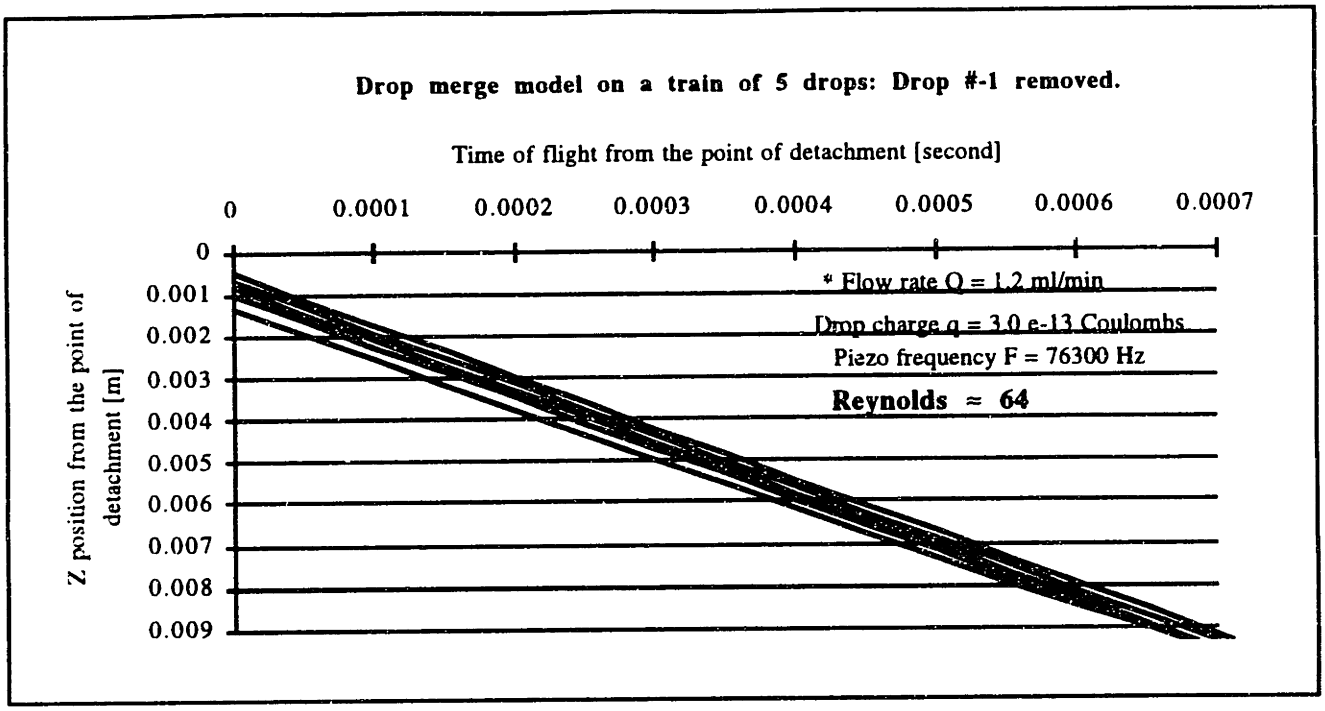

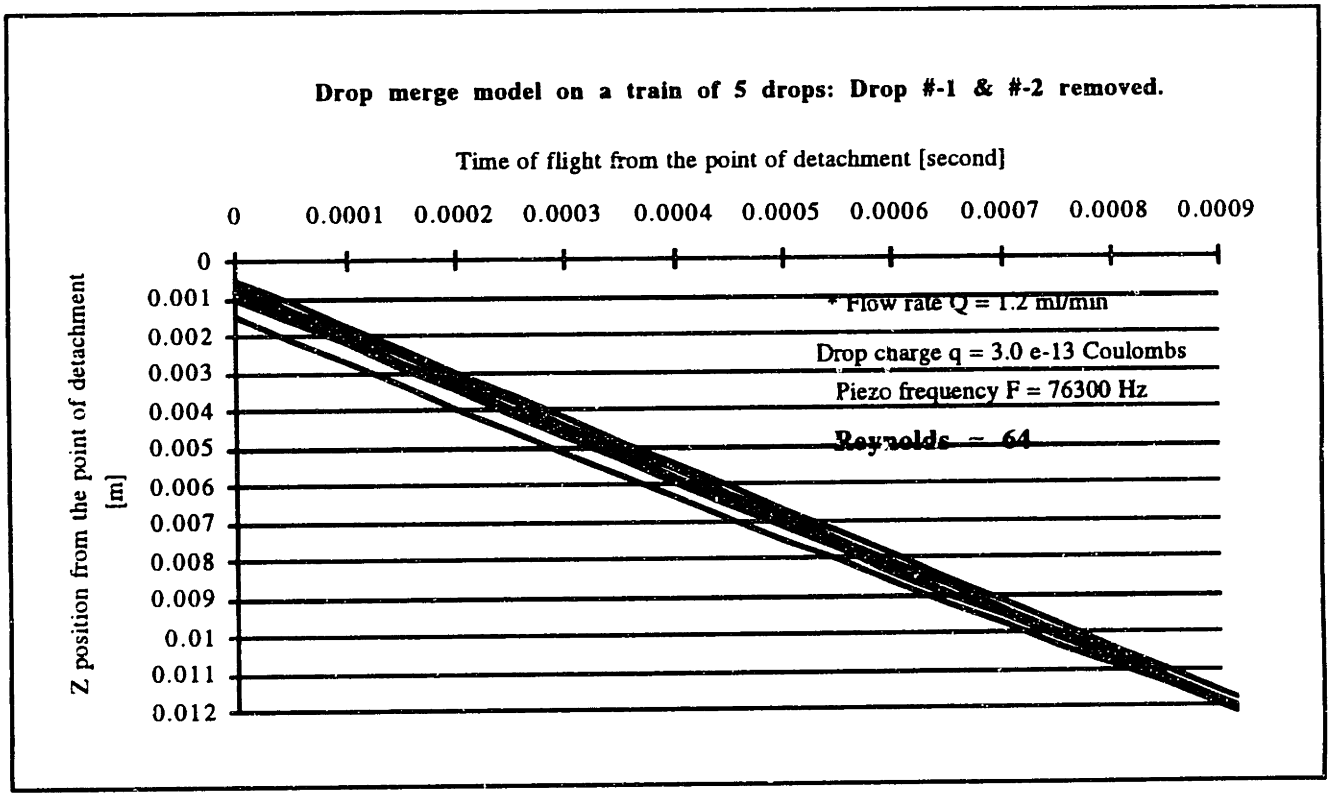

Appendix C8: Merge distance from point of detachment (MODEL) Different printing strategy (continued)

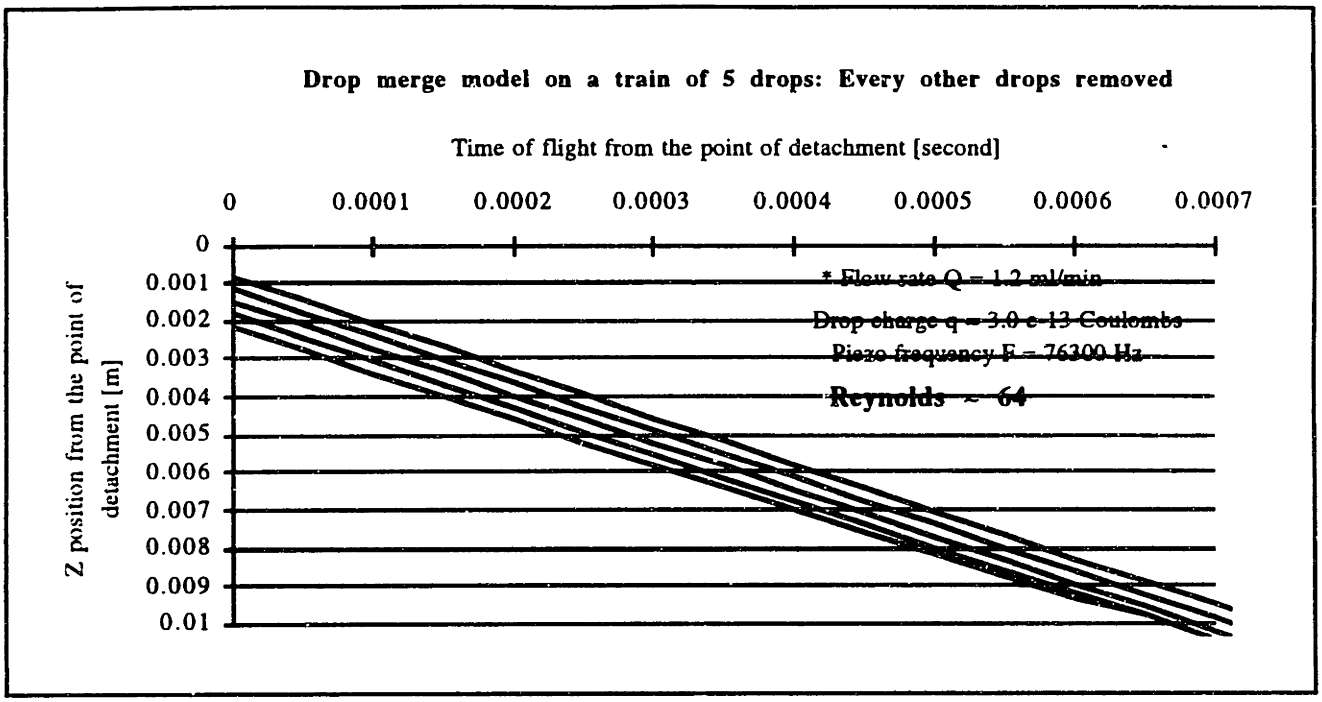

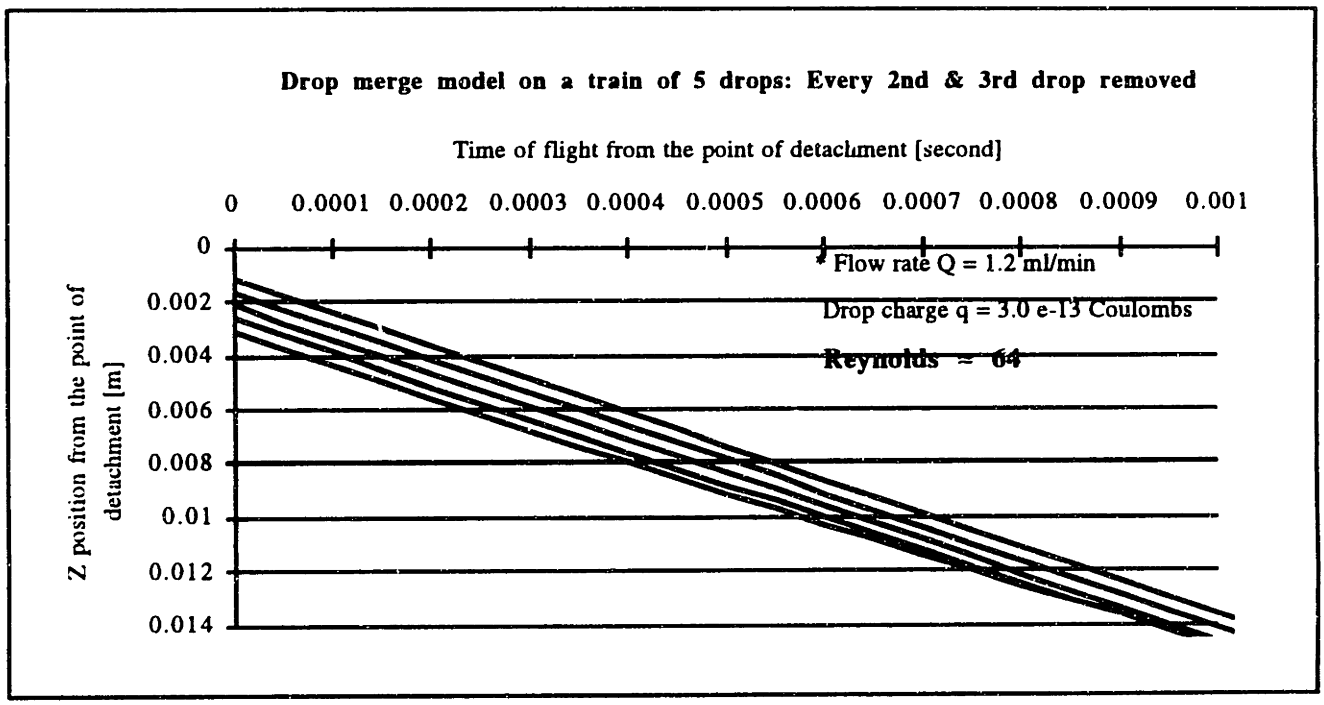

Appendix C9: Droplet generator-Position Encoder error caused by asynchronous timing

The synchronization controller uses both the fast axis position encoder and piezoelectric drop generator signals to insure a proper charge on droplets generated from a jet of binder. In fact, a discrete voltage must be present at the charging electrode for each droplet formed. This level must be applied for a sufficient interval prior to drop breakoff for the charge to build up its desired value. This interval is called also the charging transient window CTW.

This level must be maintained until the drop breaks off. Some time period is also required to change the voltage level to the new value required for the next droplet (voltage transition delay or VTD), but the voltage must not change until the original drop has broken off from the stream. Both value can be combined into a single one t_{nc} , which represent the time before break off charging voltage V_c can not be changed.

The absolute position of the fast Y-axis linear position encoder is fixed relative to the machine reference. Therefore, the encoder signal f_{enc} has always the same phase relationship with the machine reference. However, the relative position of the regularly spaced printed droplet is determined from the piezo signal f_{piezo}. Since the phase of f_{piezo} compared to f_{enc} is not constant, the position of a printed line relative to the fixed encoder grit may vary (see figure C9.1).

Appendix C9: Droplet generator-Position Encoder error caused by asynchronous timing (continued)

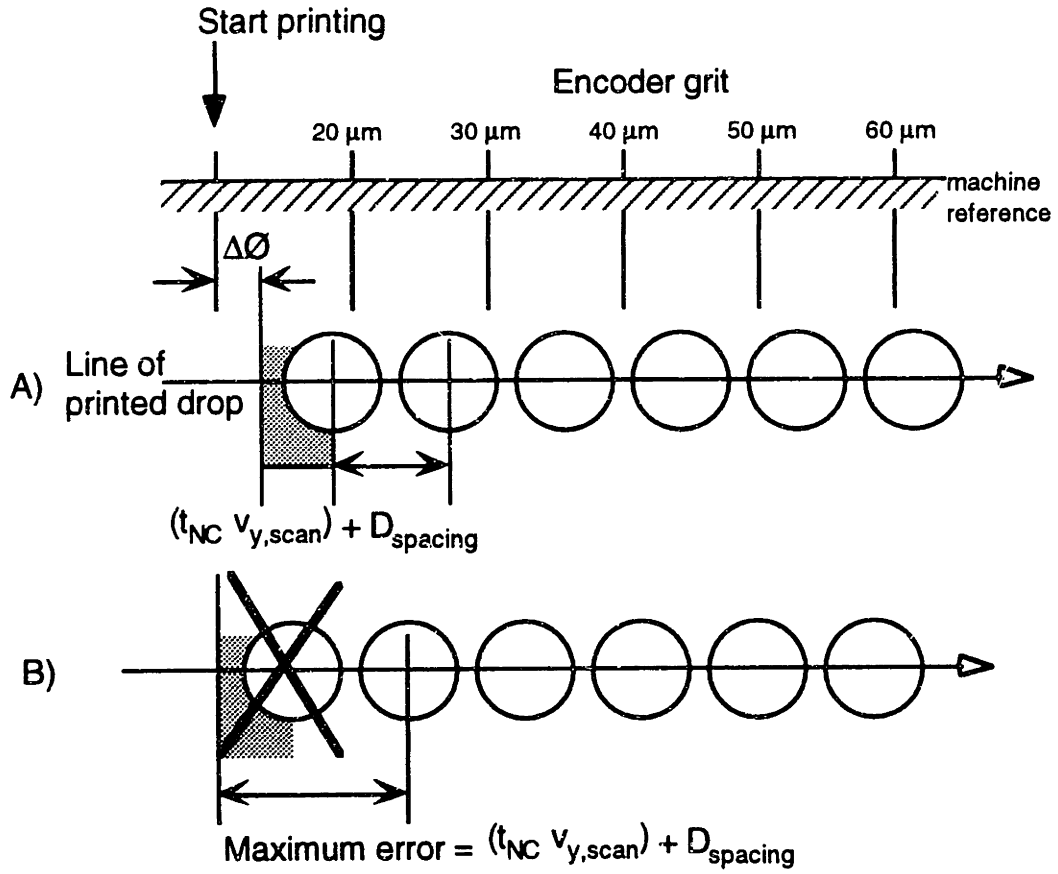

Figure C9.1: Phase relationship between fast axis linear encoder and drop powder bed position.

Both signals f_{enc} and f_{piezo} have a random phase (asynchronous) relative to each other, causing adjacent printed line of drops to not necessarily align with each other on the fast Y-axis. Thus, the induced Δy peak-to-valley error is in the order of:

$$\begin{cases} +0.000 \\ -\left(D_{spacing} + t_{NC} \cdot v_{y,scan}\right) \end{cases}$$ at the printed line starting point

Appendix C9: Droplet generator-Position Encoder error caused by asynchronous timing (continued)

and the same is true at the line exit, except that it is a positive error instead.

$$\begin{cases} +\left(D_{spacing} + t_{NC} \cdot v_{y,scan}\right) \\ -0.000 \end{cases}$$ at the exit of the printed line.

where t_{nc} is the no change charging signal period $\approx 0.25\ T_{enc}$

$v_{y,scan}$ is the fast Y-axis scanning speed.

$D_{spacing}$ is the powder bed droplet spacing defined by:

$$D_{spacing} = \frac{v_{y,scan}}{f_{piezo}} \cdot 10^6\ [\mu m]$$

The value $t_{nc}\ v_{y,scan}$ represents the distance traveled by the printhead during a no change charging voltage period t_{nc}.

Since the occurrence of this type of error is between 2Hz and $f_{piezo}/2$, surface finish of plane X-Z is affected only. The average error induced on the total length of a printed line converted in RMS is about $\sigma = \pm(D_{spacing} + t_{nc}v_{y,scan})$.

Depending on encoder resolution, printhead scanning speed and piezo droplet generator frequency, three scenarios can determine the probability of occurrence of such error.

Appendix C9: Droplet generator-Position Encoder error caused by asynchronous timing (continued)

1) $f_{encoder} > f_{piezo}$

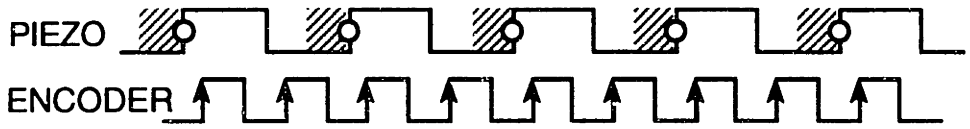

2) $f_{encoder} \approx f_{piezo}$

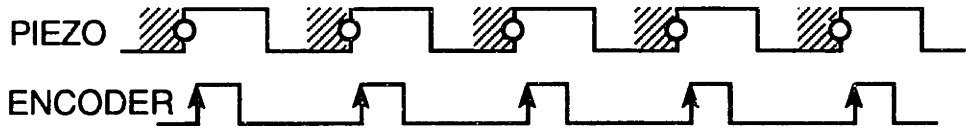

3) $f_{encoder} < f_{piezo}$

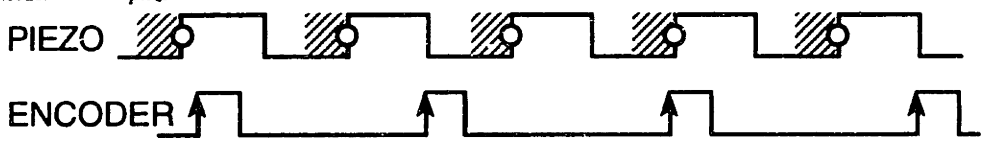

▨ is the t_{nc} region

○ is the drop break off point

Appendix C9: Droplet generator-Position Encoder error caused by asynchronous timing (continued)

For example, for the given printing conditions:

$v_{y,scan} = 1.5$ m/s

$\Delta x = 10$ μm (encoder resolution)

$f_{enc} = 150\,000$ Hz

$f_{piezo} = 80\,000$ Hz

For $t_{nc} \approx 3$ μs, the maximum error would be about ± 23 μm.

The error can be reduced by simply decreasing the powder bed drop spacing by minimizing scanning speed $v_{y,scan}$ or maximizing the piezo frequency f_{piezo}.

Bibliography & References

Medical

[1] Albrektsson, T., Branemark, P.I., Hansson, H.A., Linstrom, J., " Osseointegrated Titanium Implants", Acta Orthop. Scand. 52, pp. 155-170, 1981

[2] Cook, Stephen D., Walsh, Kimberly A., Haddad Jr., Ray J., "Interface Mechanics and Bone Growth into Porous Co-Cr-Mo Alloy Implants", Clinical Orthopaedics and Related Research, Number 193, March 1985, pp 271- 280

[3] Cook, S., Barrack, R., Thomas, K.A.,..."Tissue Growth into Porous Primary and Revision Femoral Stems", The journal of Artroplasty Vol. 6 Supplement pp.S37-@46, October 1991

[4] Bobyn, J.D., Pilliar, R.M., Cameron, H.U., Weatherly, G.C., "The optimum Pore Size for the Fixation of Porous-Surfaced Metal Implants by the Ingrowth of Bone", Clinical Orthopaedics and Related Research, p. 263, Number 150, July-August 1980

[5] Jensen, L.N., Lund, B., Gotfredsen, K.,"Bone growth into revised porous-coated patellar implant", Acta Orthop Scand 1990; 61(3):pp.213-216

[6] Kossovsky, N., "Biological Interfacial Phenomena", from CRC Surface Modification Engineering Vol. I, Chapter 5 Technological Aspects

[7] Kossowsky, R., Kossovsky, N., "Surface Engineering of Materials for biological and medical applications", from CRC Surface Modification Engineering Vol. II, Technological Aspects, pp 3-24

[8] Soballe, K., Hansen, E.S.,..."Fixation of Titanium and Hydroxyapatite-coated Implants in Arthritic Osteopenic Bone",The journal of ArthroplastyVol. 6 No. 4 pp. 307-316, December 1991

[9] Spector, Myron, Ph.D., "Historical Review of Porous-Coated Implants", The Journal of Arthroplasty, Vol. 2 No. 2 June 1987, pp. 163-177

[10] "Guidance document for testing orthopaedic implants with modified metallic surfaces apposing bone or bone cement.", Division of General and Restorative Devices, U.S. FDA (Food and Drug Administration), April 1, 1993

[11] "Standard Specification for Porous-surfaced Femoral Prostheses", American Society for Testing and Materials, ASTM F04.03.02, 04/21/1993

[12] "Test Method for Tension Testing of porous Metal coating", American Society for Testing and Materials, ASTM F 1147

[13] "Test Method for Shear testing of Porous Metal Coating", American Society for Testing and Materials, ASTM F 1044

[14] "Specification for Cast Cobalt-Chromium-Molybdenum Alloy for Surgical Implant Applications", American Society for Testing and Materials, ASTM F75

[15] "Specification for Thermomechanically-Processed Cobalt-Chromium-Molybdenum Alloy for Surgical Implants", American Society for Testing and Materials, ASTM F 1044

[16] International patent PCT/US91/02672,"Porous Metal Surface And Method Of Production", October 31, 1991

[17] United States Patent # 4,636,219 "Prosthesis Device Fabrication", Jan. 13, 1987

[18] United States Patent # 3,605,123 "Bone Implant", April 29, 1969

[19] United States Patent # 4,550,448 " Bone Prosthesis with porous coating", Nov. 5, 1985

[20] United States Patent #5,152,791,"Prosthetic Artificial Bone Having Ceramic Layers of Different Porosity", Oct. 6, 1992

[21] United States Patent #5,139,528,"Method of Securing a Mesh to a Metal Substrate for a Bone Implant", Aug. 18, 1992

[22] United States Patent #4,261,063,"Titanium Or Titanium Alloy Pin To Be Fixed In Long Bones", April 14, 1981

[23] United States Patent #3,808,606,"Bone Implant With Porous Exterior Surface", May 7,1974

[24] United States Patent #3,905,777,"Composite And Porous Metallic Members Which Can Be Used For Bone Prosthesis", Sept. 16, 1975

[25] United States Patent #3,906,550,"Prosthetic Device Having A Porous Fiber Metal Structure", Sept. 23, 1975

[26] United States Patent #4,017,911,"Heart Valve With A Sintered Porous Surface", April 19, 1977

[27] United States Patent #4,722,870,"Metal-Ceramic Composite Material Useful For Implant Devices", Feb. 2, 1988

[28] United States Patent #5,108,435,"Cast Bone Ingrowth Surface", Apr. 28, 1992

[29] United States Patent #4,089,071,"Material For Making Bone Endoprosthesis Of Said Material", May 16, 1978

[30] United States Patent #3,855,638,"Surgical Prosthetic Device With Porous Metal Coating", Dec. 24, 1974

Materials

[31] "CRC Handbook of Basic tables for chemical analysis",Thomas J. Bruno,, Paris D.N. Svoronos, CRC Press p.4 QD78.B78 1989

[32] "CRC Handbook of chemistry and physics", David R. Lide 74th edition pp 93-94, pp6-191 1993-94 QD65 .H235

[33] "Des Matériaux", Palissy, Edition de l'École Polytechnique de Montréal,1980

[34] "CRC Handbook of Chemistry and Physics", David R. Lide, 76th Edition 1995-1996, QD65 .H235 1995-1996

[35] "Thermophysical Properties of High Temperature Solid Materials",Volume 2: Non ferrous alloys, Research Center, Purdue University, Y.S. Touloukian, Editor, TA407 .P985 V.2 pt.2 c.2 1967

[36] "Thermal Expansion, Metallic Elements and Alloys", Y.S. Touloukian, TA418 .52 .P985 V.12

[37] "Thermophysical Properties of Matter", Vol.5, Specific Heat, Nonmetallic solids, Y.S. Touloukian editor, TA418 .52 .P985 V.5 pt.1

Casting

[38] Bird, Charles R., "Precision Casting Methods for Iron, Nickel and Cobalt-based Alloys", Advanced Casting Technology, Conference Proceedings, ASM International 1986 pp. 53-61

[39] Chhabra, R.P. "Surface Tension of Liquid metal: a predictive approach.".\, High Temp.-High Press., 1990 pp 171-175 ISSN-0018-1544

[40] Flinn, Richard A.,"Fundamentals of Metal Casting", Addison-Wesley Publishing Company, TS230, .F622

[41] Hwang, Weng-Sing, "Flow Pattern Prediction of Molten Metal in Thin Section Castings", Advanced Casting Technology, Conference Proceedings, ASM International 1986 pp.71-80

[42] Kalpakjian, Serope, " Manufacturing Engineering and Technology", 2nd edition

[43] Lyashchenko N. N., "Effect of gaseous medium on the microconfiguration of the surfaces of castings",SOVESHCHSNIE po teorii liteinykh protsessov. 9th, Moscow, 1963, pp. 224-229

[44] Obolentsev, F.D. , "Quality of cast Surfaces", Moscow 1961

[45] Okazaki M., Takahashi, J., Kimura H., and Ida K.,"Estimation of Solidification Time during Casting by use of Heat Transfer Model", J. Dent. Res., Oct. 1982, 61, (10) pp.1188-1191

[46] "Advanced Casting Technoogy", ASM International, Proceedings of International Conference on Advanced Casting Technology, Michigan, USA 12-14 November 1986, Easwaran, J., TS228, .99, .I584 1986

[47] "Analysis of Casting defects", American Foundrymen's Society,TS236, .A512 1966

[48] "Applied Science in the Casting of Metals", Edited K. Strauss, Pergamon Press, 1970, TS230, A652

[49] "Casting Cobalt-Based alloys", T. Klemp, Cannon-Muskegon, Mod. Cast., Dec 1988, TS .M688

[50] "Casting Design Hanbook", American Society for Metals, Metals Park, Ohio, TS233, .A517

[51] "Fundamentals of Metal Casting", Addison-Wesley Publishing Comp., Chap.2, pp 33-37

[52] "Fundamentals of Classical Thermodynamics",Wylen, V., Sonntag, Desrochers, 2nd edition, John Wiley & Sons, Inc.,1981

[53] "Precision Casting methods for irons, nickel and Cobalt-Based alloys", C.R. Bird, Advanced Casting Technology [Proc. Conf.], Kalamazoo, 12-14 Nov. 1986, ASM International, Metals Parks, Ohio, pp53-61, TS228.99.I584 1986

Machine & Printhead

[54] Donaldson R, R., "Error Budget, Large Optics Diamond Turning Machine Project", Lawrence Livermore National Lab., Technology of Machine Tools, Robert J. Hooken (ed), Machine Tool Task Force, U.S. Dept. of Commerce National Technical Information, Service Report UCRL-52960-5, October 1980

[55] Duhamel, D., Auvray, M., Chatton F.,"Study and Development of a System for the Measurement of Print Quality", Centre National d'Études des Télécommunications, Lannion, France

[56] Fillmore, G.L., Buehner, W.L., West, D.L., "Drop Charging and Deflection in an Electrostatic Ink Jet Printer", IBM Journal of research and development, Vol. 21, No.1, p.p 37-47, January 1977

[57] Hendriks, F.,"Aerodynamics of Ink Jet Printing", Journal of Applied Photographic Engineering, Vol 6, Number 3, June 1980

[58] Kruth, J.P., "Material Incress Manufacturing by Rapid Prototyping Techniques", Universiteit Leuven/Belgium, 1992

[59] Plummer, W.T., "Precision: How to achieve a little more of it, even after assembly", Fifth International Symposium on Robotics and Manufacturing, Maui, Hawaii, August, 1994

[60] Slocum, Alexander H.,"Precision Machine Design",MIT, Prentice Hall , chap.2.2 p.61

[61] "Advances in Ink Jet Control Systems", Elaine Pullen, Linx Printing technology plc, IMI second annual Ink Jet Printing Worksop, March 1993

[62] "Ink-Jet Printing", J. Heinzl, C.H. Hertz, Advances in Electronics and Electron Physics, Vol. 65, pp91-171, Academic Press, 1985

[63] "IBM Journal of research and development", IBM J. Res. Develop., Vol. 21, No. 1, pp. 1-96, January 1977

[64] "Ink-Jet Printing", J. Heinzl, C.H. Hertz, Advances in Electronics and Electron Physics, Vol. 65, Academic Press, pp. 91-171, 1985

[65] "Machinery's Handbook", 24th edition, Industrial Press Inc.,1992

[66] "Principles of Nonimpact Printing", second edition, Jerome L. Johnson, Palatino Press, Copyright 1992

Statistics

[67] "Introduction to Statistics", Third Edition, Ronald E. Walpole, Macmillan Publishing Co., Inc. 1982

[68] "Statistics for Experimenters:An Introduction to Design, Data Analysis, and Model Building", George E.P. Box, William G. Hunter, J. Stuart Hunter, John Wiley & Sons,1978

Electrostatics

[69] "Electrostatics Principles, Problems and Application", J.A. Cross, Adam Hilger,Chap #7, QC571 .C75 1987

[70] "Electromagnetic Field, Theory and Applications" Vol. I- Mapping field , Ernst Weber, Wiley & sons, QC670 .W373 1965

[71] "Electrical Breakdown of Gases" by J.M. Meek and J.D. Craggs, Oxford, Clarendon Press, 1953: QC711 .M494 c.3

[72] "Electrical Breakdown and Discharges in Gases" Part A, Fundamental Processes and Breakdown, by Erich E. Kunhardt, Lawrence H. Luessen, Plenum Press pp. 1-18

[73] "Fundamentals of applied electrostatics", Joseph M. Crowley,WIley-Interscience Publication, 1986, Part II,Chap.#4, QC571 .C76 1986

Surface post-processes

[74] Sachs, E., Curodeau, A., Gossard, D., Haeseong, J., Cima, M., Caldarise, S., "Surface Texture by 3D Printing", SFF Solid Freeform Fabrication symposium proceeding, Austin, Texas, August 1994

[75] "Chemical Milling, the technology of cutting material by etching", William T. Harris, Clarendon Press TJ1191 .H37 1976

[76] "Electrochemical Machining ", A.E. DeBarr, D.A. Oliver, Macdonald & Co Ltd., TJ1191 .D286 1968

[77] "Electrospark Machining of Metals" (volume 2) Translated from russian, B.R. Lazarenko, Consultant Bureau 1964, TJ1191, .A3131 V.2

[78] "Practice and Theory of Electrochemical Machining", John F. Wilson, Wiley-Interscience, TJ1191 .W749, 1971

[79] "Understanding EDM Surface Integrity", AGIE USA LTD, Form No. 1012-587-5

Others

[80] Catmull,"A Subdivision Algorithm for Computer Display of Curved Surfaces", Ph.D. Thesis, Department of Computer Science, Univ. of Utah, December 1974.

[81] Crawford,"Solid Freeform Fabrication Technologies and Sources of Geometric Data", 3rd SIAM Conference on Geometric Design, Tempe, Arizona, November, 1993.

[82] Peachey, D., "Procedure Texture" SIGGRAPH '93 COURSE 44 NOTES: Procedure Modeling and Rendering Techniques, Chapter 2. 1993

[83] Sachs, E., Cima, M., Cornie, J , Curodeau, A., "Three Dimensional Printing: Ceramic Tooling and Parts Directly from a CAD Model", Proceeding of the National Conference on Rapid Prototyping, Dayton Ohio, June 4-5 1990

[84] "Fundamentals of Fluid Mechanics", Philip M. Gerhart, Richard J. Gross, Addison-Wesley, 1985

[85] "Fluid Mechanics", Merle C. Potter, John F. Foss, Great Lakes Press, Inc., 1982

[86] "La transimission de la Chaleur", André B. De Vriendt, Vol 1, Tome 1-2, Gaetan Morin éditeur, 1984

[87] "The art of Electronics", Paul Horowitz, Winfield Hill, Second édition, Cambridge University Press,1989

[88] US Patent # 5,204,055 "Three-dimensional Printing techniques", April 20, 1993

[88] US Patent # 5,387,380 "Three-dimensional Printing techniques",February 7th, 1995

3D Printing Theses

[89] Brancazio, David, "Development of a Robust Electrostatically Deflecting Printhead for Three Dimensional Printing", MS Thesis, MIT 5/91.

[90] Bredt, Jim F.,"Binder Stability and Powder/Binder Interaction in Three Dimensional Printing", PhD Thesis, Mech. Eng., MIT 1/95

[91] Curodeau, Alain, "Three Dimensional Printing: Machine Control from CAD Model to Nozzles", MS Thesis, Mech. E., MIT 8/91.

[92] Esterman, Marcos, "Characterization of the Powder/Binder Interaction in the Three Dimensional Printing Process", MS Thesis, Mech. E. MIT 8/90

[93] Fan, Tai-lin,"Droplet-Powder Impact Interaction in Three Dimensional Printing", PhD Thesis, Mech. Eng., 9/95

[94] Harris, Christopher, "Characterization of Dimensional Variability and Part Bleeding Using the Three Dimensional Printing Process" SB Thesis, Mech. E., MIT 5/91

[95] Lee, Sang-Joon John,"Powder Layer Generation for Three Dimensional Printing" MS Thesis, Mech. E., MIT 5/93

[96] Lauder, Alan, "Microstructure and Particle Arrangement in Three Dimensional Printing", MS Thesis, Mat'ls Sci., MIT 9/92

[97] Milner, Jill, "Time of Flight Controller and Stream Position Compensation System for the Three Dimensional Printing Process", MS Thesis, Mech. E., MIT 5/93

[98] Shutts, Christopher J.,"Development of a Reliable Electrostatic Multijet Printhead for Three Dimensional Printing", MS Thesis, Mech. Eng. 5/95

[99] Williams, Paul, "Three Dimensional Printing: A New Process to Fabricate Prototypes Directly from CAD Models", MS Thesis, MIT 5/90